

TOMOGRAPHIC IMAGING IN CIVIL ENGINEERING INFRASTRUCTURE

by

Farshad Gheslaghi

A thesis
presented to the University of Waterloo
in fulfillment of the
thesis requirement for the degree of
Doctor of Philosophy
in
Civil Engineering

Waterloo, Ontario, Canada, 1997

© Farshad Gheslaghi 1997



**National Library
of Canada**

**Acquisitions and
Bibliographic Services**

**395 Wellington Street
Ottawa ON K1A 0N4
Canada**

**Bibliothèque nationale
du Canada**

**Acquisitions et
services bibliographiques**

**395, rue Wellington
Ottawa ON K1A 0N4
Canada**

Your file Votre référence

Our file Notre référence

The author has granted a non-exclusive licence allowing the National Library of Canada to reproduce, loan, distribute or sell copies of his/her thesis by any means and in any form or format, making this thesis available to interested persons.

The author retains ownership of the copyright in his/her thesis. Neither the thesis nor substantial extracts from it may be printed or otherwise reproduced with the author's permission.

L'auteur a accordé une licence non exclusive permettant à la Bibliothèque nationale du Canada de reproduire, prêter, distribuer ou vendre des copies de sa thèse de quelque manière et sous quelque forme que ce soit pour mettre des exemplaires de cette thèse à la disposition des personnes intéressées.

L'auteur conserve la propriété du droit d'auteur qui protège sa thèse. Ni la thèse ni des extraits substantiels de celle-ci ne doivent être imprimés ou autrement reproduits sans son autorisation.

0-612-21349-8

The University of Waterloo requires the signature of all persons using or photocopying this thesis. Please sign below, and give address and date.

ABSTRACT

This research was to assess the potential of tomographic imaging in a variety of geotechnical processes, with emphasis on matrix-based inversion algorithms. While most prior research in tomography has been based on simulated data, this research centers on case histories gathered under well-controlled, yet realistic field conditions. The goal is to invert a velocity image which reflects the state or evolution of a given soil parameter (e.g., stress, pore pressure, ion concentration) using a set of picked travel times.

Among inversion methods, matrix inversion methods are versatile and robust. However, efficient storage and computation are required. The sparsity of matrices involved in tomographic problems enable us to employ efficient storage and solvers.

In general, it is assumed that "picked travel times" correspond to paths of shortest travel path (Fermat's principle). If the velocity contrast in the medium is more than 15 to 20 percent, rays bend toward higher velocity regions. In this case, entries in the coefficient matrix depend on a prior estimate of the velocity field. Therefore, the relation between pixel velocities and travel times is non-linear in general. This non-linear inversion problem can be solved by employing iterative solutions with ray tracing.

Ray tracing methods can be categorized as: one-point methods, two-point methods, and whole-field methods. The computational time demand for ray tracing methods for each category is evaluated based on the number of segmental travel time calculations. The computational efficiency of the ray tracing methods is also compared for fundamental cases. Some evidence of the accuracy needed in ray tracing to solve the inversion problem, within the context of other errors in CE-tomography, are given.

Prior experience with simulated data has shown that the quality of inversion is unrealistically good when compared to inversions with real data. In part, this reflects the compatibility of forward simulation algorithms with hypotheses made in the inversion stage. A central goal of this thesis is to assess the potential of inversion with real data. A database of case histories has been compiled for this purpose. Part of this study is dedicated to the testing of pre-processing strategies in each case history. It is shown that data pre-processing can be employed to provide foresight about the medium, and help the selection of proper constraints. Distribution and amount of information, presence of accidental and systematic errors, degree of heterogeneity and anisotropy, and analysis of shadows are analyzed for all case histories.

A tomographic program based on sparse matrix algorithms was encoded as part of this study. The selected tomographic inversion methods are based on matrix analyses. Data structures are used to take advantage of the sparsity of the coefficient matrix and to avoid high memory and computational demand. Sine-arc ray tracing and straight rays are two possibilities. The program is in structured form to facilitate future additions and modifications.

Tomographic data are usually mixed-determined and ill-conditioned. Damped Least squares (DLSQ) and regularization add information in the form of constraints in order to decrease the ill-conditioning of the problem. The optimum damping or regularization coefficient gives the best solution. Optimal damping or regularization coefficients should be determined in an inversion process. In this study, several guidelines are proposed to determine optimal damping or regularization coefficients.

Inverted images for all case histories in this study are given in Appendix F. The results indicate the ability of the method to invert large size, ill-conditioned, and noisy problems.

ACKNOWLEDGMENTS

Thanks to the God Almighty for giving me support through my entire life.

I would like to express my sincere gratitude to my supervisor and friend Professor J.C. Santamarina for all of his thoughtful help, time, and support during every single day of this study.

I also want to acknowledge Prof. M. Polak (who leads the surface-waves complement to this study), Prof. E. Matyas, Prof. M. Dusseault, Prof. P. Calamai, and Prof. G. Rix for giving me the opportunity to gain knowledge from their insight.

Thanks to the people who provided data for this research: Ontario Hydro and MDC Geological Consultants for Crack and Concrete column data, Prof. R. Rehtien for Korean Demilitarized Zone data, Prof. J. Rhazi for Chute Hemmings Dam data, and A. Tallin and T. Wakim for Balloon and Kosciuzko bridge data.

Distinguished recognition to my loving wife Nafiseh for providing me with all the support and encouragement through these intense and successful years. She was always there when I needed her. And to my daughter Yasmine for her sweet smiles!.

Finally, I would like to recognize the Ministry of Higher Education of the Islamic Republic of Iran and the International Institute of Earthquake Engineering and Seismology (IIEES) for providing funding for this research.

Dedication

To those who I love the most

**My wife Nafiseh,
my little princess Yasmine,
and my parents**

TABLE OF CONTENTS

TITLE PAGE	i
AUTHOR'S DECLARATION	ii
BORROWER'S PAGE	iii
ABSTRACT	iv
ACKNOWLEDGMENTS	vi
DEDICATION	vii
TABLE OF CONTENTS	viii
LIST OF TABLES	xiii
LIST OF ILLUSTRATIONS	xiv
LIST OF MATHGRAMS	xxiii
NOTATIONS	xxiv
CHAPTER I: INTRODUCTION	1
1.1 Physical Issues	2
1.1.1 Penetration vs. Resolution.....	2
1.1.2 Scanning and Geometry.....	3
1.1.3 Testing Difficulties	3
1.1.4 Wave Propagation Effects.....	3
1.2 Mathematical Issues	4
1.3 Organization of the Thesis	5
CHAPTER II: INVERSION	8
2.1 The CE-Tomographic Problem	8
2.2 Matrix Inversion Methods	9
2.2.1 Least Squares Method.....	9
2.2.2 Minimum Norm Method.....	11
2.2.3 Damped Least Squares Method.....	11

2.2.4	Regularization and Data Errors	12
2.2.5	Singular Value Decomposition (SVD).....	13
2.3	Iterative Methods	14
2.4	Transform Methods	16
2.4.1	High Frequency Illumination - Fourier Slice Theorem	17
2.4.2	Diffraction: Fourier Diffraction Theorem	20
2.5	Other Methods	26
2.5.1	Fuzzy Logic (Backprojection and min-max)	26
2.5.2	Probability-Based	26
2.5.3	Parameteric Characterization of the Unknown Space	26
2.6	Summary and Conclusions	27
 CHAPTER III: RAY THEORY & RAY TRACING		35
3.1	Introduction	35
3.2	Ray Theory-Eikonal Equation	35
3.2.1	Eikonal Equation: Derivation, Importance and Limitations ..	37
3.3	Ray Tracing Methods	41
3.3.1	One-Point Methods.....	42
3.3.2	Two-Point Methods.....	46
3.3.3	Whole-Field Methods	51
3.4	Summary and Conclusions	56
 CHAPTER IV: SOFTWARE FOR CE-TOMOGRAPHIC STUDIES (DESIGN		
DECISIONS		70
4.1	Introduction	70
4.2	Numerical Issues in Inversion Algorithms	70
4.3	Computational and Physical Issues in Ray Tracing	71
4.3.1	Assumptions and Fundamental Cases	72
4.3.2	Other Comments.....	77

4.3.3	Accuracy in Travel-Time Measurements and Ray Tracing	77
4.4	WATom-I: General Approach	79
4.4.1	Ray Tracing	79
4.4.2	Matrix Inversion	80
4.4.3	WATom-I: Structure	82
4.5	Summary and Conclusions	85

CHAPTER V: DATA BASE OF CASE HISTORIES	105	
5.1	Introduction	105
5.2	Case Histories	105
5.2.1	High Velocity Circular Anomaly - Acoustic Waves	105
5.2.2	Concrete Block - Well Controlled Features	108
5.2.3	Kosciuzko Bridge - Very Noisy Environments	109
5.2.4	Chute Hemmings Dam - Asymmetric Structure	109
5.2.5	Korean DMZ - Heterogeneous, Anisotropic Background	110
5.3	Summary	110

CHAPTER VI: DATA PRE-PROCESSING STRATEGIES	118	
6.1	Purpose	118
6.2	Distribution of Information Content	119
6.3	Systematic and Accidental Errors	119
6.4	Analysis of Shadows	120
6.5	Heterogeneity and Anisotropy	120
6.6	Case Histories and Pre-Processing	121
6.6.1	Balloon 1	121
6.6.2	Balloon 2	123
6.6.3	Balloon 3	124
6.6.4	Balloon 4	125
6.6.5	Crack in Concrete (Side-to-Side Shootings)	125

6.6.6	Crack in Concrete (Top-to-Left Side Shootings).....	126
6.6.7	Crack in Concrete (Top-to-Right Side Shootings)	127
6.6.8	Column of Aggregate.....	128
6.6.9	Kosciuzko Bridge Pier	129
6.6.10	Chute Hemmings Dam.....	130
6.6.11	Korean Demilitarized Zone.....	131
6.7	Discussion and Conclusions	131

CHAPTER VII: INVERSION OF CASE HISTORIES - OPTIMAL INVERSION

	STRATEGIES	173
7.1	Introduction	173
7.2	Null Space and Singular Values (Global Information).....	174
7.3	Damped Least Squares Solution - Optimal η.....	175
7.4	Regularization Solution - Optimal λ.....	176
7.5	Damped Least Squares vs. Regularization - Noisy Data	176
7.6	Regularization - Straight and Bent Rays	177
7.7	Optimal λ in Real Situations (Unknown Solution)	178
7.8	Statistical Parameter Estimation - Maximum Likelihood	179
7.9	Tomographic Inversion of Case Histories - Procedure.....	182
7.9.1	Balloon 1.....	183
7.9.2	Balloon 2.....	183
7.9.3	Balloon 3.....	184
7.9.4	Balloon 4.....	184
7.9.5	Crack in Concrete (Side-to-Side Shootings).....	185
7.9.6	Crack in Concrete (Top-to-Left Side Shootings).....	185
7.9.7	Crack in Concrete (Top-to-Right Side Shootings)	186
7.9.8	Column of Aggregate.....	186
7.9.9	Kosciuzko Bridge Pier	187
7.9.10	Chute Hemmings Dam.....	187

7.9.11 Korean Demilitarized Zone	188
7.10 Summary and Conclusions	188
CHAPTER VIII: SUMMARY AND CONCLUSIONS.....	222
8.1 Summary	222
8.2 Conclusions.....	228
REFERENCES.....	230
APPENDIX A: Ray Paths and Direction Cosines.....	236
APPENDIX B: Lytle and Dines's One-Point Method ALGOL	239
APPENDIX C: General Algorithms and Flowcharts in WATOM-I	241
APPENDIX D: WATOM-I Software	245
APPENDIX E: Corresponding Input Files For All Case Histories	269
APPENDIX F: Corresponding Inversion Mathcad Files For All Case Histories	305

LIST OF TABLES

Table 2.1 Matrix Inversion Methods	10
Table 3.1 Ray Tracing Methods	58
Table 4.1 Computation of total number of travel times, assuming straight rays.....	73
Table 4.2 An estimate of the number of calculations in multiple segmentation two-point method.....	76
Table 5.1 Case Histories	106

LIST OF ILLUSTRATIONS

Figure 1.1	Definition of notation. The unknown region between source and receiver boreholes is divided into pixels.	7
Figure 2.1	Filtering kernels for different types of regularization smoothing	28
Figure 2.2	Parallel beam projections are taken by measuring a set of parallel rays for a number of different angles	29
Figure 2.3	Equi-distance fan beam projections	30
Figure 2.4	Equi angular fan beam projections.....	31
Figure 2.5	Equi-distance and equi-angular fan beam projections.....	32
Figure 2.6	The Fourier slice theorem relates the Fourier transform of a projection to the Fourier transform of the object along radial line..	33
Figure 2.7	The Fourier diffraction theorem relates the Fourier transform of a diffracted projection to the Fourier transform of the object along a semicircular arc.....	34
Figure 3.1	Head waves from a horizontal refractor (layer 2). Head waves begin at the critical distance and overtake the direct waves at the crossover distance	59
Figure 3.2	Arrival time-distance curves for diving waves. Starting angles= 0°, 10°, 20°, and 30°; velocity gradient is (a) continuous velocity gradient; (b) velocity gradient interrupted by a low-velocity zone from z_1, z_3 resulting in a shadow zone	60
Figure 3.3	Shadow zone in the presence of a high impedance region	61

Figure 3.4	The first Fresnel zone: Interaction between a wave front and the interface between two media	61
Figure 3.5	Fresnel zone and different size bodies	62
Figure 3.6	One point method in 2D - A schematic representation	63
Figure 3.7	An example of perturbing rays in bending methods.....	63
Figure 3.8	Three-point perturbation scheme in three dimensions.....	64
Figure 3.9	Two approaches to perturb ray paths	64
Figure 3.10	Perturbing the ray path by mid-point method.....	65
Figure 3.11	Two-dimensional simplex BWO illustrating the four mechanisms of movement: reflection (R), expansion (E), contraction (C), and shrinkage(S).....	65
Figure 3.12	An example of the Simplex moving on the response surface contour plot	66
Figure 3.13	True wave surface and approximating wave surface F. For each direction of the ray; e is taken as indicative of goodness of fit.....	66
Figure 3.14	The source grid point A and the eight points in the ring surrounding point A.....	67
Figure 3.15	Cell organization of a network, (a) Dashed lines: cell boundaries. Black circles: nodes. Solid lines: connections. (b) Shortest path from one node to others in a homogeneous model.....	67
Figure 3.16	Forward process in the LTI method	68

Figure 3.17	A ray path crosses segment AB at point C and reaches point D in a cell.....	68
Figure 3.18	Rays from a seismic Huygens' source toward sixteen grid points	.69
Figure 3.19	Example of initial and modified ray paths in Sassa's method69
Figure 4.1	A region divided by 4x4 pixels87
Figure 4.2	A source and receiver pair connected by different paths.....	87
Figure 4.3	A source and receiver pair connected by the straight path and a curved path88
Figure 4.4	Ray paths in a Multi-Segment method. (a) Cases when path has one and two degrees of freedom. (b) Order of moving nodes in a path88
Figure 4.5	Number of connections per pixel for two selected whole-field methods89
Figure 4.6	Path connections from each node to the other nodes in a pixel. The number on top of each pixel shows the number of connections89
Figure 4.7	Number of connections in each pixel for a receiver90
Figure 4.8	A comparison between the calculated travel times by multi-segments method and the corresponding close form solution90
Figure 4.9	Travel time along different paths.....	91
Figure 4.10	Simulated model, high velocity anomaly at center91
Figure 4.11	Image quality versus the accuracy in travel time measurements and ray tracing92

Figure 4.12	Data file for one source and sixteen receivers placed in two parallel boreholes separated at 59.5 ^(m) distance.	93
Figure 4.13	Typical input velocity file. Assuming a homogeneous region divided into 66 pixels with same velocities equal to 1	94
Figure 4.14	Example of a section of a velocity output file	94
Figure 4.15	Example of the inversion performance output file	95
Figure 5.1	Helium filled balloons in air; different sizes and locations	112
Figure 5.2	Concrete monolith with controlled defects	113
Figure 5.3	Concrete block: (a) Simulated crack, (b) Concrete column.....	114
Figure 5.4	Kosciuzko bridge pier - Source and receiver locations and location of the cracks.....	115
Figure 5.5	Chute Hemmings dam - Source and receiver locations. All scales are in meters	116
Figure 5.6	Korean Demilitarized Zone (DMZ) - Source and receiver locations. Seven sets of 150 rays, total of 1050.....	117
Figure 6.1	The information density for three different shooting patterns. "." indicates source and "-" indicates receiver locations.....	133
Figure 6.2	Distribution of information content for small balloons. Assuming straight ray paths	134
Figure 6.3	Systematic and accidental errors for Balloon 1.....	135
Figure 6.4	Heterogeneity and anisotropy inspections for Balloon 1.....	136

Figure 6.5	Analysis of shadows for Balloon 1	137
Figure 6.6	Systematic and accidental errors for Balloon 2.....	138
Figure 6.7	Heterogeneity and anisotropy inspections for Balloon 2.....	139
Figure 6.8	Analysis of shadows for Balloon 2	140
Figure 6.9	Systematic and accidental errors for Balloon 3.....	141
Figure 6.10	Heterogeneity and Anisotropy inspections for Balloon 3	142
Figure 6.11	Analysis of shadows for Balloon 3	143
Figure 6.12	Distribution of information content for Balloon 4. Assuming straight ray paths	144
Figure 6.13	Systematic and accidental errors for Balloon 4.....	145
Figure 6.14	Heterogeneity and anisotropy inspections for Balloon 4.....	146
Figure 6.15	Analysis of shadows for Balloon 4	147
Figure 6.16	Distribution of information content for Concrete Crack (Side-to-Side shootings). Assuming straight ray paths	148
Figure 6.17	Systematic and accidental errors for Concrete Crack (Side-to-Side shootings)	149
Figure 6.18	Heterogeneity and anisotropy inspections for Concrete Crack (Side-to-Side shootings).	150
Figure 6.19	Analysis of shadows for Concrete Crack (Side-to-Side shootings)	151

Figure 6.20	Distribution of information content for Concrete Crack (top to left-Side shootings). Assuming straight ray paths.....	152
Figure 6.21	Systematic error and heterogeneity inspections for Concrete Crack (top to left-Side shootings).....	153
Figure 6.22	Analysis of shadows for Concrete Crack (top to left-Side shootings)	154
Figure 6.23	Distribution of information content for Concrete Crack (top to right-Side shootings). Assuming straight ray paths.....	155
Figure 6.24	Systematic error and Heterogeneity inspections for Concrete Crack (top to right-Side shootings).....	156
Figure 6.25	Analysis of shadows for Concrete Crack (top to right-Side shootings)	157
Figure 6.26	Distribution of information content for Concrete Column. Assuming straight ray paths	158
Figure 6.27	Systematic and accidental errors for Concrete Column.....	159
Figure 6.28	Heterogeneity and anisotropy inspections for Concrete Column.	160
Figure 6.29	Analysis of shadows for Concrete Column	161
Figure 6.30	Distribution of information content for Kosciuzko bridge pier Assuming straight ray paths.....	162
Figure 6.31	(a) Systematic and Accidental errors and (b) Heterogeneity inspections for Kosciuzko bridge pier	163

Figure 6.32	Analysis of shadows for Kosciuzko bridge pier (Top-to-Bottom shootings)	164
Figure 6.33	Analysis of shadows for Kosciuzko bridge pier (Side-to-Side shootings)	165
Figure 6.34	Distribution of information content for Chute Hemmings dam Assuming straight ray paths.....	166
Figure 6.35	(a) Systematic and accidental errors and (b) Heterogeneity inspections for Chute Hemmings dam	167
Figure 6.36	Heterogeneity and anisotropy inspections for Chute Hemmings dam	168
Figure 6.37	Analysis of shadows for Chute Hemmings dam	169
Figure 6.38	Distribution of information content for Korean DMZ. Assuming straight ray paths	170
Figure 6.39	Heterogeneity and anisotropy inspections for Korean Demilitarized Zone.....	171
Figure 6.40	Analysis of shadows for Korean Demilitarized Zone.....	172
Figure 7.1	(a) Singular values of a matrix with clearly identifiable cut-off point (b) Singular values of a matrix where cut-off point must be selected arbitrarily	190
Figure 7.2	Distribution of singular values for different case histories	191
Figure 7.3	Distribution of singular values for different regularization coefficients.....	192

Figure 7.4	Simulated cases: low and high velocity anomalies at center and off-center	193
Figure 7.5	Damping coefficient and image quality. Four simulated cases	193
Figure 7.6	Regularization coefficient and image quality. Four simulated cases	194
Figure 7.7	Straight and curved rays. The effect of regularization coefficient (resolvability).....	195
Figure 7.8	Inversion of laboratory data with regularization: Straight (left) and curved (right) rays. (a) Central, high velocity anomaly, 256 rays, $\lambda=10$ (refer to Figure 5-1d) (b) Off-center high velocity anomaly, 49 rays, $\lambda=2$ (refer to Figure 5-1a).....	196
Figure 7.9	Straight and curved rays. The effect of regularization coefficient (variability)	197
Figure 7.10	Optimization of regularization coefficient.....	198
Figure 7.11	Distribution of travel times in small balloons.....	199
Figure 7.12	Distribution of travel times in concrete crack	200
Figure 7.13	Maximum likelihood of small balloons (Gaussian distribution).....	201
Figure 7.14	Maximum likelihood of concrete crack (Gaussian distribution)	202
Figure 7.15	Gaussian (curve A) and exponential (curve B) distribution with zero mean and unit variance. The exponential distribution has the longer tail	203
Figure 7.16	Maximum likelihood of small balloons (exponential distribution) .	204

Figure 7.17 Inverted images for Balloon 3 with (a) optimal $\lambda=5$ and (b) with $\lambda=0.05$ (post peak)205

Figure 7.18 Maximum likelihood of concrete crack (exponential distribution) .206

Figure 7.19 Inverted images with optimal regularization coefficient, for (a) Balloon 1 (curved rays) and (b) Balloon 2 (straight rays) (thresholded, refer to Appendix F)207

Figure 7.20 Inverted images with optimal regularization coefficient for (a) Balloon 2 (curved rays) and (b) Balloon 3 (straight rays) (Thresholded, refer to Appendix F)208

Figure 7.21 Inverted images with optimal regularization coefficient for (a) Balloon 4 (curved rays) and (b) Side-to-side shootings data of concrete crack (straight rays).....209

Figure 7.22 Inverted images with optimal regularization coefficient, using straight rays, for concrete crack (a) Top to left-side shootings and (b) Top to right-side shootings.210

Figure 7.23 Inverted images with optimal regularization coefficient for concrete column, using (a) straight rays and (b) Curved rays (Thresholded, refer to Appendix F)211

Figure 7.24 Inverted images with optimal regularization coefficient, using straight rays, for (a) Kosciuzko bridge pier and (b) Chute Hemmings dam data212

Figure 7.25 Inverted images with optimal regularization coefficient for Korean Demilitarized Zone data (Thresholded, refer to Appendix F). Same results for both straight and curved rays.....213

LIST OF MATHGRAMS

Note: Several mathematical analyses are included in this report. In order to minimize disrupting the text, these analyses are extracted in math-sheets, herein called Mathgrams. Computations are performed with Mathcad software.

Mathgram 4.1	Computational demand (straight and curved rays).....	96
Mathgram 4.2	Computational demand for ray tracing methods	98
Mathgram 4.3	Sine-Arc two-Point method	102
Mathgram 7.1	DLSQ solution (HV-Center model). Random error is added to the data.....	214
Mathgram 7.2	DLSQ solution (HV-Center model). Systematic error is added to the data.....	216
Mathgram 7.3	Regularization solution (HV-Center model). Random error is added to the data.....	218
Mathgram 7.4	Regularization solution (HV-Center model). Systematic error is added to the data.....	220

NOTATIONS

m	Number of unknowns (pixels)
n	Number of rays (equations)
L	Coefficient matrix ($n \times m$)
L^T	Transpose of the coefficient matrix ($m \times n$)
V	Velocity
s	Vector of slownesses (1/velocity) ($m \times 1$)
s_0	Initial slowness
t, b	Vector of travel times ($n \times 1$)
R	Regularization matrix ($m \times m$)
I	Identity matrix
η	Damping coefficient in damped least square method
λ	Regularization coefficient
ω	Singular value
Ω	Diagonal matrix of singular values
k	Wave number
AAE	Average absolute error (%)
ASE	Average square error (%)
COV	Covariance

CHAPTER I

INTRODUCTION

Tomography (tomo: to cut or slice-*Greek*) is the inversion of measurements of multiple planes of a body. CE¹-tomography is the inversion of boundary measurements to determine the field of a physical parameter within a geoenvironment.

Although tomography was introduced early in this century, its applications in the geosciences and engineering only commenced in the early 1970's. Tomographic methods are widely applied in nuclear medicine (Cormak, 1973; Scudder, 1978), radio astronomy (Bracewell and Riddle, 1967), applied geophysics (Aki and Richards, 1980; Dines and Lytle, 1979; Lytle and Dines, 1980; Dyer and Wortington, 1988), earthquake seismology (Spencer and Gubbins, 1980), mining engineering (Paul, 1993), and civil engineering (Santamarina, 1994; Henrique, 1990) among other applied fields.

Possible tomographic applications in geosciences and engineering include: the detection of hazardous regions ahead of a mine face, assessing nuclear reactor and waste storage sites, mapping resources at a mine to detect deposits that pinch out but are suspected of reappearing elsewhere, determining the location and volume of oil present in possible secondary oil recovery fields, detecting fracture zones, assessing the field of stress, assessment of existing infrastructure, etc.

¹ CE stands for Civil Engineering

The purpose of this research was to assess the potential of tomographic imaging in a variety of Civil Engineering processes with emphasis on matrix-based inversion algorithms. While most prior civil engineering research in tomography has been based on simulated data, this research centers on case histories gathered under well-controlled, yet realistic field conditions.

1.1 Physical Issues

CE-tomographic imaging faces several difficulties related to its implementation in the field and to the mathematical/computational nature of the problem (Santamarina, 1994). A brief discussion follows, starting with physical restrictions.

1.1.1 Penetration vs. Resolution

Computerized Axial (Aided) Tomography Scanning (CAT Scan) has revolutionized medical X-ray imaging because of its ability to display the spatial distribution of X-ray attenuation over cross-sections of the body (Hounsfield, 1973). Tomographic reconstruction methods are applicable to imaging situations where the line integral of a parameter, such as X-ray attenuation or time delay, is available as the data is collected (Mersereau and Oppenheim, 1974; Scudder, 1978).

CE-tomography often requires sampling over large distances compared to medical applications. Therefore, low frequencies must be used to obtain adequate signal-to-noise levels over practical distances. This long wavelength

restriction limits the resolution of CE-tomographic images (resolution is in the same order of magnitude as wavelength λ).

1.1.2 Scanning and Geometry

Medical scans are reconstructed with a fixed data collection geometry. Conversely, CE-tomographic problems generally require a "new" scanning capability for each application. In a typical tomographic problem in the field, transducers are placed in boreholes (Figure 1-1), which may deviate from a straight line. Furthermore, the scanning geometry is quite restricted and the object can only be illuminated in a few preferential directions.

1.1.3 Testing Difficulties

This set of problems includes: source restrictions (directivity of different propagation modes, amplitude, repeatability), triggering errors (difficulties in stacking), noise (ambient, mechanical, electromagnetic, filtering and phase shift), source and receiver coupling to object, detection of true first arrivals, and accessibility to different faces of the object. The latter will reflect on the uneven distribution of information content, which is discussed later.

1.1.4 Wave Propagation Effects

Heterogeneity. Heterogeneity modifies spherical wave fronts, elongating them in the direction of higher velocity. When rays are drawn normal to wave fronts, ray bending is observed.

Anisotropy. Wave propagation in anisotropic media is complex: energy in shear waves splits, the ray direction is given by the direction of energy transport, the ray is not perpendicular to the wave front ("quasi" P or S waves), and the ray direction does not necessarily remain in the plane (Auld, 1973). Anisotropy alone does not lead to curved ray paths; however, anisotropy couples with vertical heterogeneity to deviate rays from the simplest straight-path condition.

Reflection and Refraction. At the interface between two materials with different impedance $I=\rho.v$ (ρ : material density; v : velocity), part of the energy is transmitted and part of the energy is reflected. Furthermore, mode conversion takes place: incident P-waves are reflected and refracted as P and S-waves, and the same occurs with the S-wave component normal to the interface. Generalized Snell's laws characterize the effect of interfaces.

1.2 Mathematical Issues

Data for seismic CE-tomographic imaging are line integrals of a physical parameter, along a specific path through the medium. For example, the travel time accumulated along a ray path between a source and a receiver can be expressed as the integral of slowness, and amplitude is the integral of attenuation. All examples given in this document use travel time observations that are imaged to determine a velocity distribution, but the method is completely general; any observation that can be defined as a line integral through the medium can be substituted throughout.

When seismic pulses are emitted in one well and detected in another well, the first arrival time of a ray i is the integral of $ds/V(x,z)$ from source to receiver, where ds is a differential length along the path and $V(x,z)$ is the seismic velocity field between the wells. There are two interrelated problems:

(1) *The forward problem* is the computation of first arrival times corresponding to a given velocity distribution. The forward problem presents no theoretical difficulty, yet there are computational restrictions and experimental difficulties (e.g. detection of first arrivals). One determination is made for each source-receiver pair. The problem is often treated in the two-dimensional case, i.e., seismic rays traveling within the plane of the wells.

(2) *The Inverse problem* is the determination of the field of seismic velocities from measured first arrival times. Ill-conditioning¹ and non-uniqueness of the solution are the major difficulties in the inverse problem. The problem is either under-determined, over-determined, or mixed-determined with no exact solution.

1.3 Organization of the Thesis

The goal of this research was to compute the tomographic inversion of travel time data in reference to civil engineering problems.

Chapter 2 presents a review of tomographic inversion methods. It includes matrix inversion methods, iterative methods, transform methods, and other methods (fuzzy logic, probability-based, and parameteric characterization of the unknown space).

Chapter 3 summarizes ray theory and ray tracing methods. This chapter starts with a description of ray theory and with the derivation of the Eikonal equation. Ray tracing methods are discussed (one-point methods, two-point methods, and whole field methods). A detailed description of each method is followed by a summary of advantages and short-comings.

¹ A problem is ill-conditioned, if the solution is sensitive to small changes in the data.

Chapter 4 describes tomographic software developments and design decision. Computational issues in inversion methods and a discussion of matrix inversion limitations are given to highlight the reasons for selecting matrix inversion methods. Implementation of ray bending, a comparative analysis of computational efficiency, and issues in non-linearity are discussed. Then, a detailed description of the development and current structure of the tomographic software running on sparse matrix methods is presented.

Chapter 5 describes a database of well documented case histories that was compiled for this study.

Chapter 6 centers on the development of data pre-processing strategies to identify possible errors and trends present in each data set. All case histories are inspected with the selected data pre-processing procedures.

Chapter 7 centers on the tomographic inversion of the case histories. Strategies for identifying regularization and damping coefficients for optimal solutions are investigated. A method based on statistical parameter estimation (maximum likelihood) is proposed and examined for selected case histories.

Chapter 8 presents a summary of main observations and salient conclusions of this research.

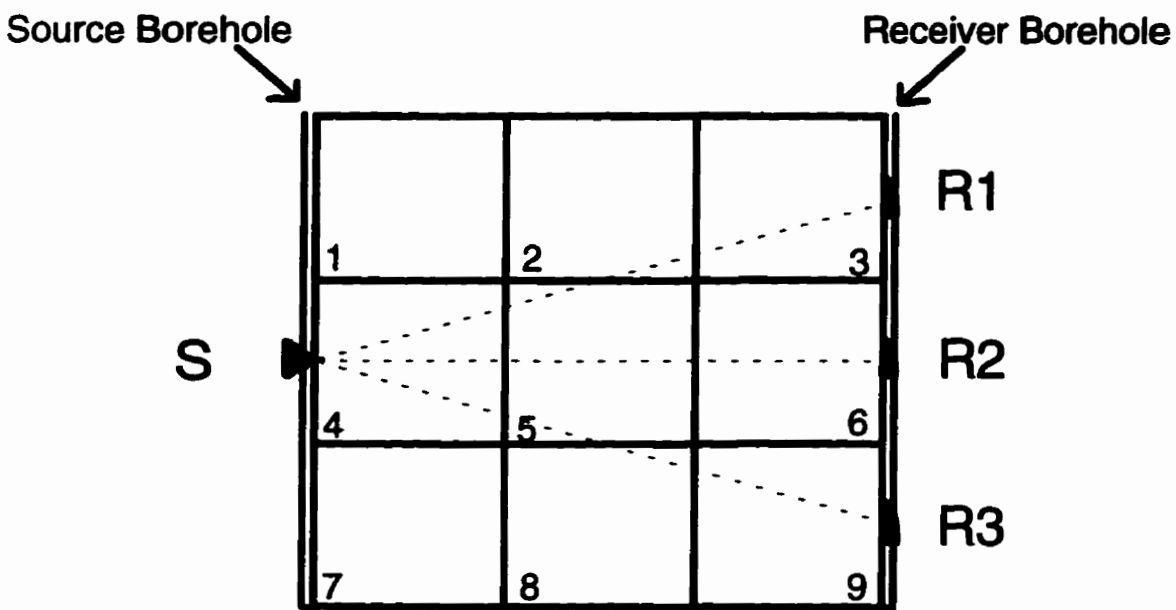


Figure 1-1: Definition of notation. The unknown region between source and receiver boreholes is divided into pixels.

CHAPTER II

INVERSION

2.1 The CE-Tomographic Problem

The following linear model is considered for the relationship between two vectorial quantities x and b in the classical tomographic problem:

$$L \cdot x = b \quad (2-1)$$

In velocity inversion, L is the matrix of segment lengths, x is the vector of slownesses, and b is the vector of measured travel times. The non-negative matrix L is adequately estimated by the forward ray tracing problem. However, the vector of travel times may include considerable systematic and accidental measurement errors ($t = b + \epsilon$). Then, the problem is to determine a vector s from the set of equations

$$L \cdot s = t \quad (2-2)$$

Methods that have been used to solve the inverse tomographic problem can be categorized as:

- *Matrix inversion methods*
- *Iterative methods*
- *Transform methods*

- *Other methods.*

A brief discussion of these approaches follows.

2.2 Matrix Inversion Methods

A linear system in matrix form (Equation 2-2) can be solved by matrix inversion methods. These methods are briefly formulated in Table 2-1 (Santamarina, 1994).

2.2.1 Least Squares Method

Usually, the set of Equations 2-2 is sparse, mixed-determined, and inconsistent.

This set of equations has no exact solution. Hence, a least squares solution \hat{s} can be selected such that

$$\|Ls-t\| \tag{2-3}$$

is minimal, where $\| \cdot \|$ denotes the Euclidean norm. The vector s is the least squares solution of Equation 2-2 if, and only if, $(Ls-t) \perp R(L)$, where $R(L)$ denotes the range of matrix L , i.e. the set of all vectors Ls . Rewriting $(Ls-t) \perp R(L)$ as $L^T(Ls-t)=0$, s is a least squares solution of (2-3) if and only if

$$L^T Ls=L^T t \tag{2-4a}$$

hence,

$$s=(L^T L)^{-1}L^T t \tag{2-4b}$$

Table 2-1: Matrix inversion methods (Santamarina, 1994).

Problem definition:

- Given: a space discretized in m -pixels, n -integral measurements obtained at boundaries $t[n,1]$, and the matrix $L[n,m]$ that characterizes how measurements scanned the space. The rank of L is $r \leq \min(m,n)$.
- Then: determine the distribution of the field parameter $s[m,1]$, such that $Ls=t$

Goal - Case	Objective Function	Inversion Equation
Even-determined: $r=m=n$	$L \cdot s = t$	$s = L^{-1} \cdot t$
Over-determined: $n > m = r$ least square solution	$\min\{E\}$ where $E = (t - L \cdot s_{est})^T (t - L \cdot s_{est})$	$s_{est} = (L^T \cdot L)^{-1} L^T \cdot t$
Under-determined: $r \leq n < m$ minimum distance solution	$\min\{D\}$ such that $L \cdot s - t = 0$ where $D = (s - s_0)^T (s - s_0)$ and s_0 is an initial estimate of s	$s_{est} = L^T (L \cdot L^T)^{-1} \cdot t$ or, $s_{est} = s_0 + L^T (L \cdot L^T)^{-1} \cdot (t - L s_0)$
Mixed-determined: damped least squares	$\min\{E + \eta \cdot D\}$ where η is a constant	$s_{est} = (L^T \cdot L + \eta^2 I)^{-1} L^T \cdot t$
Mixed-determined: singular value decomposition	$L = U \cdot \Omega \cdot V^T$ where U_i is eigenvector i of LL^T , V_i is eigenvector i of $L^T L$ and the diagonal of Ω are the square root of eigenvalues i (other entries=0)	$s_{est} = V \cdot \Omega^{-1} \cdot U^T \cdot t$
Noise in the data: regularization	$\min\{E + \lambda \cdot R \cdot s ^2\}$ where λ is a constant and R is a regularization matrix	$s_{est} = (L^T L + \lambda R^T R)^{-1} L^T t$

Note: Prediction error $E = (t - L \cdot s_{est})^T (t - L \cdot s_{est})$
 Solution length $D = s^T s$
 All solutions are of the form $s_{est} = M \cdot t$
 Forward simulation $t_{pred} = L \cdot s_{est}$
 Replacing $t_{pred} = L \cdot M \cdot t_{meas}$ and $s_{est} = M \cdot L \cdot s_{real}$
 Data resolution matrix $P_t = L \cdot M$ ideal $P_t = Identity$
 Model resolution matrix $P_s = M \cdot L$ ideal $P_s = Identity$

Comments:

The matrix L is called the data kernel
 If $r < m$ and $E=0$ the problem is "purely underdetermined"
 The narrower the band of P_s and P_t , the better the prediction
 All equations can be generalized for initial guess s_0 (see underdetermined case)

2.2.2 Minimum Norm Method

If the rank(L) is less than the number of unknowns, then there are an infinite number of vectors s that satisfy Equation 2-2. There is a unique vector in this set of solutions whose norm $(s-s_0)^T(s-s_0)$ is minimal and satisfies:

$$L.s-t = 0 \quad (2-5)$$

The solution is:

$$s = L^T(L.L^T)^{-1}t \quad (2-6a)$$

or

$$s = s_0 + L^T(L.L^T)^{-1}(t-L.s_0) \quad (2-6b)$$

where s_0 is an initial estimate of s . This is referred to as the minimum norm solution of Equation 2-2.

2.2.3 Damped Least Squares Method

An alternative solution may be to seek a balance between minimum norm and least squares error solutions by solving the following system of equations

$$\begin{bmatrix} L \\ \eta I \end{bmatrix} s = \begin{bmatrix} t \\ 0 \end{bmatrix} \quad (2-7)$$

This solution is known as the damped least squares solution, and may be expressed as

$$s = [L^T L + \eta^2 I]^{-1} L^T t \quad (2-8)$$

where η is a constant to be optimized. The damped least squares algorithm stabilizes the solution in cases where data contain noise.

2.2.4 Regularization and Data Errors

The measured vector of travel times t can be assumed to be equal to $b+\epsilon_t$ where b is the set of travel times, and ϵ_t is a vector of errors whose components average zero and have equal variance ω^2 . Then, the least squares solution \hat{s} of Equation 2-2 is the best estimate of the vector x in Equation 2-1, with minimum variance (The Gauss-Markov theorem, Silvey 1970). However, the variance can be very large for the least squares solution. In fact, the variance matrix $P(\Delta s \Delta s^T)$ in the full rank case equals

$$P[(L^T L)^{-1} L^T \epsilon_t \epsilon_t^T L (L^T L)^{-1}] = \omega^2 (L^T L)^{-1}, \quad (2-9)$$

where P denotes the probabilistic expectation, and Δs denotes the error vector. From Equation 2-9 we have

$$P[\|\Delta s\|^2] = \omega^2 \text{trace}[L^T L]^{-1} = \omega^2 \sum_j \frac{1}{\omega_j^2}. \quad (2-10)$$

Therefore, small singular values can generate large errors in the solution s (Sluis and Vorst, 1987). An efficient way to avoid this effect is regularization. It consists of adding information in the form of constraints in order to decrease the ill-conditioning of the problem. The goal is to find a kernel that captures some aspects of physics that can constrain the problem.

The implementation of regularization resembles the damped least squares method, where the identity matrix I is replaced by a smoothing matrix R to avoid the fluctuation behavior of the solution due to the presence of data errors. In this case, Equation 2-8 becomes

$$s = [L^T L + \lambda^2 R^T R]^{-1} L^T t \quad (2-11)$$

The matrix R can be formed by calculating the second spatial derivative of the image (Laplacian of s in two dimensions: the product of $R.s$ reflects the spatial variation of the image). The matrix R can also include filtering kernels, either to smooth images, to enhance contrast, or to highlight edges in preferential directions. Figure 2-1 shows some sample kernels. These kernels are moving windows placed on the original image to create the new filtered image. Mathematically speaking, regularization is a convolution of the inverted image with a kernel (Santamarina, 1994). Physically, these kernels tend to decrease the degree of fluctuation in pixel values by chopping-off the high frequencies. For instance, the first kernel which applies general smoothing tends to evaluate the value of a pixel by averaging the values of that pixel and its eight neighbors. The highest weighting is given to the main pixel at the center of the window. The advantage of this smoothing is to avoid sudden changes in the image. However, it blurs the sharp edges of an image.

In cases where edge detection of interest, other kernels should be used. Another alternative for detecting edges is using the Walsh transform (Golubov, *et. al.*, 1991). Unlike the Fourier series which is a decomposition of functions into sinusoidal waves, the Walsh functions are rectangular waves. Therefore, the Walsh functions try to detect the edges rather than smoothing the peripheries of an image.

2.2.5 Singular Value Decomposition (SVD)

Any $n \times m$ matrix L can be written as an orthogonal $n \times n$ matrix U , an orthogonal $m \times m$ matrix V , and a $n \times m$ diagonal matrix Ω with diagonal elements $\omega_1 \geq \omega_2 \geq \omega_3 \geq \dots \geq \omega_m \geq 0$ such that

$$L=U\Omega V^T \tag{2-12}$$

This is the singular value decomposition of matrix L (Michelena, 1993). The entries ω_j are the singular values of L , and the columns of U and V are the left and the right singular vectors of L , respectively. The columns of the matrix U are the eigenvectors of LL^T and the corresponding eigenvalues are ω_j^2 . Similarly, ω_j^2 are eigenvalues for L^TL and its eigenvectors are the columns in matrix V .

A geometrical interpretation of this method relates the linear mapping between orthonormal bases in source and image spaces (given the right and left singular vectors, respectively), where the mapping is represented by the diagonal matrix (Sluis and Vorst, 1987). Singular value decomposition facilitates the characterization of the level of information in the system and the "conditioning" of the problem. In addition, diagonal matrices are computationally efficient.

2.3 Iterative Methods

Data storage and computation time requirements in CE-tomography stimulate the implementation of iterative methods. The best known algorithms in this group are (Gordon, 1974): Algebraic Reconstruction Technique (ART), and Simultaneous Iterative Reconstruction Technique (SIRT).

The following procedure describes the ART algorithm:

For ray i .

- 1- Trace ray,
- 2- Calculate the lengths of ray segments in each pixel traced by ray i from source to receiver,
- 3- Compute the residual for the ray: (measured minus calculated time),
- 4- Adjust the slowness of each touched pixel to cancel the time residual,

$$s_i^{q+1} = s_i^q + \frac{\text{sgn}(l_i) \cdot |l_i|^p \cdot \Delta t_i^q}{\sum_k |l_k|^{p+1}} \quad p=1/(w-1) \quad (2-13)$$

in which $\text{sgn}(\)$ is the sign function and s_i^q denotes slowness of the i th pixel in the q th iteration. The choice of $w=2$ (minimal energy corrections) leads to Kaczmarz's method which is a typical least squares solution of this equation.

- 5- Repeat steps 1 to 4 for each ray until the total time residual for each ray becomes less than a previously defined acceptable value.

This method converges to a solution if the problem is even-determined (number of independent equations and unknowns is equal). Errors in the data or in the tracing model may cause fluctuation in pixel values in the vicinity of the optimal solution.

The SIRT method is an averaging form of ART, designed to improve convergence. Corrections for all rays are computed prior to updating the approximation for s . SIRT converges slower than ART, but has advantages with regard to stability (McMechan, 1987).

The procedure to solve the inversion problem by SIRT follows:

- 1- Trace ray,
- 2- Calculate the lengths of the ray segments in each of the pixels that the ray passes through, from source to receiver,
- 3- Compute the time residual for the ray (observed time minus calculated time) using the current slowness distribution, and save the values,
- 4- Repeat steps 1 to 3 for all rays,
- 5- Adjust the slowness in each pixel taking into consideration all corrections,
- 6- Repeat steps 1 to 5 until the time residual becomes less than an acceptable value that was previously defined.

Step 5 involves the averaging of all slowness values or other weighting schemes (Dines and Lytle, 1979). The general expression is (Sluis and Vorst, 1987):

$$s_i^{q+1} = s_i^q + \left(\frac{w}{U_m} \right) \sum \left(\frac{d_i \cdot t_j^q}{Q_j} \right) \quad 0 < w < 2 \quad (2-14a)$$

$$U_m = \sum |d_m|^v, \quad Q_j = \sum |d_{ij}|^{2-v} \quad 0 \leq v \leq 2 \quad (2-14b)$$

The algorithm by Dines and Lytle (1979) is obtained for $v=0$ and $w=1$.

An image represented by (s_1, s_2, \dots, s_n) , can be considered as a single point in an n -dimensional space (Krylov subspace). In this space, each of the equations represents a hyper-plane. Therefore, if a unique solution to these equations exists, the intersection of these hyperplanes is a single point, which is the desired solution.

Other examples of this type of method are MART which is a multiplication form of ART:

$$s_j^{q+1} = \left(\frac{\Delta t_i^q}{\sum l_{ij}} \right)^{n_{ij}} s_j^q \quad (2-15)$$

and WART which is a weighted form of ART, where the weighting is based on the length of the rays (Peterson *et al.*, 1985).

2.4 Transform Methods

Fourier transform methods are commonly used in medical X-ray tomography,

where a full range of radiation angles can be imposed. The object can be "illuminated" by:

- Parallel beam projections (Figure 2-2)
- Fan beam projections
 - a- Equi-distance projections (Figure 2-3)
 - b- Equi-angular projections (Figure 2-4)
 - c- Equi-distance and equi-angular projections (Figure 2-5)

Modifications are required to apply parallel beam projections and fan beam projections to geophysical applications within cross-hole and vertical seismic profiling.

2.4.1 High Frequency Illumination - Fourier Slice Theorem

The Fourier Slice Theorem states that a slice of the two-dimensional Fourier transform of an object is equal to the one-dimensional Fourier transform of the corresponding parallel beam projection of the object (Figure 2-6). The mathematical verification of this theorem follows (Kak and Slaney 1988).

Recall the Fourier transform of a function, $f(t)$ as $F(\omega)$:

$$F(\omega) = \int_{-\infty}^{\infty} f(t)e^{-i2\pi\omega t} dt \quad (2-16)$$

Likewise, the two-dimensional Fourier transform of a function in a two-dimensional space, $f(x,y)$, is $F(u,v)$:

$$F(u, v) = \int_{-\infty}^{\infty} \int_{-\infty}^{\infty} f(x, y) e^{-j2\pi(ux+vy)} dx dy \quad (2-17)$$

Therefore, the Fourier transform of the object along the line $v=0$ is

$$F(u, 0) = \int_{-\infty}^{\infty} \int_{-\infty}^{\infty} f(x, y) e^{-j2\pi ux} dx dy \quad (2-18)$$

In this integral, the exponential term is not a function of y ; thus, the integral can be separated by the transitivity rule:

$$F(u, 0) = \int_{-\infty}^{\infty} \left[\int_{-\infty}^{\infty} f(x, y) dy \right] e^{-j2\pi ux} dx \quad (2-19)$$

The term in brackets is equal to the parallel projection of $f(x, y)$ along the y axis (or $\theta=0$)

$$P_q(t) = \int_{-\infty}^{\infty} f(x, y) dy \quad (2-20)$$

The function $P_\theta(t)$ is known as the Radon transform of the function $f(x, y)$. Substituting $P_\theta(t)$ in Equation (2-19),

$$F(u, 0) = \int_{-\infty}^{\infty} P_q(t) e^{-j2\pi ux} dx \quad (2-21)$$

This equation, which resembles Equation (2-16), is the simplest form of the Fourier Slice Theorem and shows that a one-dimensional projection of a function in the space domain can be defined by its two-dimensional Fourier transform in Fourier space. Thus, multiple projections in the time domain, defined as $P(t)$, can

be used to form $F(u,v)$ in the Fourier space. A complete picture of the object requires projections for different angles θ .

Algorithm with interpolation in the frequency domain. The following steps are involved in tomographic inversion based on the Fourier Slice Theorem:

- Determine projections, $P_\theta(t)$. These are either travel time or amplitude "shadows". Each shadow is defined on a t -axis which is at an angle θ with respect to the x -axis.
- Compute the one-dimensional Fourier transform of each projection, $S_\theta(\omega)$.
- Assemble the 2-dimensional frequency domain function of the space, $F(u,v)$, by placing each $S_\theta(\omega)$ along a radial line from the origin ($u=0, v=0$).
- Interpolate the values of each $S_\theta(\omega)$ in the polar coordinate system (θ, ω) , onto the Cartesian grid (u,v) .
- Compute the 2-D inverse Fourier transform of $F(u,v)$ to determine the space function $f(x,y)$.

Interpolation in the space domain: Filtered Back-Projection Algorithm. There are two sources of error in the above algorithm: one is in transferring values in polar coordinates (θ, ω) onto Cartesian coordinates (u,v) in the frequency domain. The second one is the fan-effect of polar measurements $S_\theta(\omega)$ away from the origin.

Several observations are highlighted (Kak and Slaney, 1988). First, projections in the Fourier space $S_\theta(\omega)$ are nearly independent, as they only share the origin ($u=0, v=0$), which is the DC component. Second, the Fourier transform of the space $F(u,v)$ is obtained by a summation of transformed projections $S_\theta(\omega)$; thus, given the linearity of the Fourier transform, the x,y space can be constructed as a summation of inverted $S_\theta(\omega)$. Third, the fanning difficulty can be corrected by multiplying transformed projection $S_\theta(\omega)$ by a pie-shaped wedge, i.e., a linearly increasing high pass filter. This filtering process cancels the common DC

component, hence, filtered transformed projections $FS_{\theta}(\omega)$ are totally independent. Therefore, one of the main advantages of this algorithm is the ability to start the reconstruction procedure as soon as the first projection has been obtained, which increases time efficiency and decreases memory requirements.

The filtered back-projection algorithm is summarized in the following steps:

- Determine projections, $P_{\theta}(t)$
- Compute the one-dimensional Fourier transform of each projection, $S_{\theta}(\omega)$
- Multiply each $S_{\theta}(\omega)$ by the width of the wedge at that frequency, or by its distance to the origin. For example, if there are N equally spaced projections in 180° , the wedge at frequency ω has width $2\pi\omega/N$.
- Invert filtered projections $FS_{\theta}(\omega)$ to obtain filtered projections $FP_{\theta}(t)$ in the space domain.
- "Smear" the inverted filtered projections $FP_{\theta}(t)$ onto the x,y space, along the ray paths, interpolating among cells in the x,y grid.
- Add the contribution of all filtered back-projections onto the cells in the x,y space.

2.4.2 Diffraction: Fourier Diffraction Theorem

The wavelength of some frequency components may approach the size of typical structures within the body. In this case, diffraction will play an important role in reconstructing the image. The filtered back-projection algorithm was based on the Fourier slice theorem and assumed that energy travels in straight ray paths. This assumption is not true when diffraction phenomena prevail; in this case, the flow of energy is described by the wave equation. The 2-dimensional wave equation is:

$$\frac{\partial^2 u(\vec{r})}{\partial x^2} + \frac{\partial^2 u(\vec{r})}{\partial y^2} - \frac{1}{v^2} \frac{\partial^2 u(\vec{r})}{\partial t^2} = 0 \quad (2-22)$$

where the wavefield $u(r,t)$ represents the particle motion in a seismic wave or the electromagnetic field amplitude at location r and time t . The field $u(r,t)$ can be decomposed into multiple frequency components. The wave equation can be re-written for one component, $u(r)$, for a temporal frequency ω (Kak and Slaney 1988):

$$\frac{\partial^2 u(\vec{r})}{\partial x^2} + \frac{\partial^2 u(\vec{r})}{\partial y^2} + k^2 u(\vec{r}) = 0 \quad (2-23)$$

where the wavenumber $k=2\pi\omega/v$ is constant in homogeneous media. A solution to this equation is

$$u(\vec{r}) = e^{i\vec{k}\cdot\vec{r}} \quad (2-24)$$

where the vector $k=(k_x, k_y)$ and $|k|^2=k_x^2+k_y^2$ is the 2-dimensional propagation vector and $u(r)$ represents a 2-dimensional plane wave of spatial frequency k . This form of $u(r)$ can represent any 2-dimensional function as a weighted sum of plane waves. This fact can be verified by substituting Equation 2-24 into Equation 2-23 (Kak and Slaney 1988). The presence of anomalies in the medium invalidates the homogeneity assumption.

Born Approximation. The total wavefield, $u(r)$, can be considered as a sum of an incident field, $u_o(r)$ which is a solution of Equation 2-23, and a scattered field, $u_s(r)$, as $u(r)=u_o(r)+u_s(r)$.

The wave equation for the scattered component $u_s(r)$ can be obtained by substituting the total field in Equation 2-23,

$$\frac{\partial^2 u_s(\vec{r})}{\partial x^2} + \frac{\partial^2 u_s(\vec{r})}{\partial y^2} + k_0^2 u_s(\vec{r}) = -u(\vec{r})\alpha(\vec{r}) \quad (2-25)$$

where $\alpha(r)$ is the object field

$$\alpha(\vec{r}) = k^2 [n^2(\vec{r}) - 1] \quad (2-26)$$

and n is the refractive index. Equation 2-25 is the scalar Helmholtz equation. It can not be solved for $u_s(r)$ directly, but a solution can be written in terms of Green's function (Witten *et al.*, 1993; Kak and Slaney, 1988). The Green's function represents the solution of the wave equation for a single delta function.

$$\frac{\partial^2 g(\vec{r}-\vec{r}')}{\partial x^2} + \frac{\partial^2 g(\vec{r}-\vec{r}')}{\partial y^2} + k_0^2 g(\vec{r}-\vec{r}') = -\delta(\vec{r}-\vec{r}') \quad (2-27)$$

Therefore, a solution in terms of Green's function assumes the total scattered field as a summation of point scatterers, which is a valid assumption based on Huygens' principle:

$$u_s(\vec{r}) = \int g(\vec{r}-\vec{r}')\alpha(\vec{r}')u(\vec{r}')d\vec{r}' \quad (2-28)$$

This convolution equation for the scattered field is in terms of the total field, i.e., the scattered field u_s is a function of the incident field u_o and the scattered field itself. The Born approximation assumes that the scattered field is much smaller than the incident field, $u_s \ll u_o$. Then, Equation 2-28 is re-written as a first approximation:

$$\left[u_s(\vec{r}) \right]_{1st} = u_B(\vec{r}) = \int g(\vec{r}-\vec{r}')\alpha(\vec{r}')u_o(\vec{r}')d\vec{r}' \quad (2-29)$$

Knowing the first estimate of the scattered field, u_B , the total field can be better approximated as $u = u_o + u_B$ and replaced back into equation 2-28. The new estimate of the scattered field is Born's second approximation.

Rytov Approximation. The Rytov approximation is derived by considering the total field as an exponential of a complex phase $\varphi(r)$,

$$u(\vec{r}) = e^{\varphi(\vec{r})} \quad (2-30)$$

where the total complex phase φ is taken as the sum of the incident φ_o and scattered phase φ_s

$$\varphi = \varphi_o + \varphi_s \quad (2-31)$$

The three phases are complex quantities, and functions of \vec{r} . The solution of the wave equation, expressed as an integral equation, is (Kak and Slaney, 1988)

$$u_o \varphi_s = \int_{V'} g(\vec{r} - \vec{r}') u_o \left[(\nabla \varphi_s)^2 + o(\vec{r}') \right] d\vec{r}' \quad (2-32)$$

where the complex phase of the scattered field is a function of itself. The Rytov approximation considers:

$$(\nabla \varphi_s)^2 + o(\vec{r}) \cong o(\vec{r}) \quad (2-33)$$

Then, the first Rytov approximation to Equation 2-31 becomes

$$u_o \varphi_s = \int_{V'} g(\vec{r} - \vec{r}') u_o o(\vec{r}') d\vec{r}' \quad (2-34)$$

Therefore,

$$\varphi_s(\vec{r}) = \frac{1}{u_o(\vec{r})} \int_{V'} g(\vec{r}-\vec{r}') u_o(r') d\vec{r}' \quad (2-35)$$

and, recalling Equation 2-29

$$\varphi_s(\vec{r}) = \frac{u_B(\vec{r})}{u_o(\vec{r})} \quad (2-36)$$

Projections in Frequency Domain=Circular Arcs. If a single plane wave is considered for the incident field, Equation 2-29 can be rewritten as (Kak and Slaney, 1988)

$$u_B(\vec{r}) = \frac{j}{4\pi} \int \alpha(\vec{r}') u_o(\vec{r}') \int_{-\infty}^{\infty} \frac{1}{\beta} e^{j[\alpha(x-x')+\beta(y-y')]} d\alpha d\vec{r}' \quad (2-37)$$

where the plane wave is shown decomposed as (this is a crucial step in the derivation),

$$\frac{1}{\pi} \int_{-\infty}^{\infty} \frac{1}{\beta} e^{j[\alpha(x-x')+\beta(y-y')]} d\alpha \quad (2-38)$$

For an array of receivers located along $y=y_o$, Equation 2-37 becomes

$$u_B(x, y = y_o) = \frac{j}{4\pi} \int \frac{\alpha(\vec{r}')}{\beta} e^{j[\alpha(x-x')+\beta(y_o-y')]} e^{jk_o y'} d\vec{r}' \int_{-\infty}^{\infty} d\alpha \quad (2-39)$$

The first integral is the two-dimensional Fourier transform of the object function $o(r)$. The Fourier transform of the scattered field $u_B(x, y_o)$ is $U_B(\alpha, y_o)$,

$$U_B(\alpha, y_o) = \frac{j}{2\sqrt{k^2 - \alpha^2}} e^{j\sqrt{k^2 - \alpha^2} y_o} O(\alpha, \sqrt{k^2 - \alpha^2} - k) \quad (2-40)$$

where $O(\alpha, f(k))$ is the Fourier transform of the object function $o(r)$. In this derivation, the following property of Fourier integrals was used

$$\int_{-\infty}^{\infty} e^{i(\omega-\alpha)x} dx = 2\pi\delta(\omega - \alpha) \quad (2-41)$$

Equation 2-40 relates the two-dimensional Fourier transform of the object $O(k)$ to the one-dimensional Fourier transform of the scattered field at the receiver line. U_B in the Fourier domain (k_x - k_y space) is a set of points on a semicircular arc which has a radius equal to k . The range of changes in point positions is from $-k$ to k .

In summary, the Fourier diffraction theorem is based on the wave equation, and states that *the Fourier transform of the scattered field of a projection is equal to the Fourier transform of the object over a semicircular arc* (Figure 2-7). Note that the high frequency limit of the Fourier diffraction theorem is the Fourier slice theorem.

Inversion Procedure. Inversion of different fields can also be done by implementing interpolation in the frequency domain (Kak and Slaney, 1988) or in the space-domain ("back propagation" Devaney, 1984). However, unlike the Fourier Slice Theorem, frequency domain interpolation appears more efficient. The following steps are involved in tomographic inversion based on the Fourier Diffraction Theorem for a set of data gathered at a specific illuminating angle, α :

- Determine projections, $P_\alpha(t)$.
- Compute the one-dimensional Fourier transform of each projection, $O_\alpha(\omega)$.
- Compute the 2-dimensional Fourier transform of the wave field, $U(k_x, k_y)$, along the receiver line, $y=y_0$, based on Equation 2-39.

- Interpolate $U(k_x, k_y)$ along semicircular arcs up to the end points $\sqrt{2}k_0$, in a Cartesian grid.
- Compute the 2-D inverse Fourier transform of the wavefield $U(k_x, k_y)$ in order to determine the object wavefield in space domain $o(x, y)$.

2.5 Other Methods

2.5.1 Fuzzy Logic (Backprojection and min-max)

Projections capture the "shadows" of anomalies. Backprojection and superposition of these shadows on the space of the problem helps define position, size, and type (high or low velocity) of anomalies. It can be shown that if superposition is implemented with min-max operators, the procedure corresponds to fuzzy-logic-based constraining of the anomaly (Santamarina, 1991).

2.5.2 Probability-Based

This group of methods is based on the distribution of data and model parameters. Gaussian and Poisson distributions are frequently selected, obtaining explicit expressions for the estimated model parameters (see Menke, 1989; Shepp and Vardi, 1982). The maximum likelihood and the maximum entropy solutions are two well-studied methods in this category.

2.5.3 Parametric Characterization of the Unknown Space

If the number of independent observations is limited, pixel-based solutions offer

either limited resolution or a high degree of under-determination. An alternative approach is to represent the medium by a limited number of parameters (e.g., background velocity, anomaly location, size and velocity). These parameters are then inverted by sequential forward simulation and minimization of the residual of measurements (Santamarina, 1994; Santamarina and Reed, 1994).

2.6 Summary and Conclusions

Several methods have been used to solve the inverse tomographic problem; they can be categorized as: (i) matrix inversion methods, (ii) iterative methods, (iii) transform methods, and (iv) other methods.

Iterative methods are not stable in ill-conditioned problems. Transform methods are restricted to straight ray projections (space transformations could be invoked to generalize the solution to heterogeneous, anisotropic media). Matrix methods are versatile and computationally efficient. However, efficient storage and computation are required.

Small singular values can generate large errors in the solution. Regularization adds information in the form of constraints in order to decrease the ill-conditioning of the problem. Hybrid solutions can be attempted to enhance the resolvability of inverted images (e.g., fuzzy logic pre-processing followed by regularization).

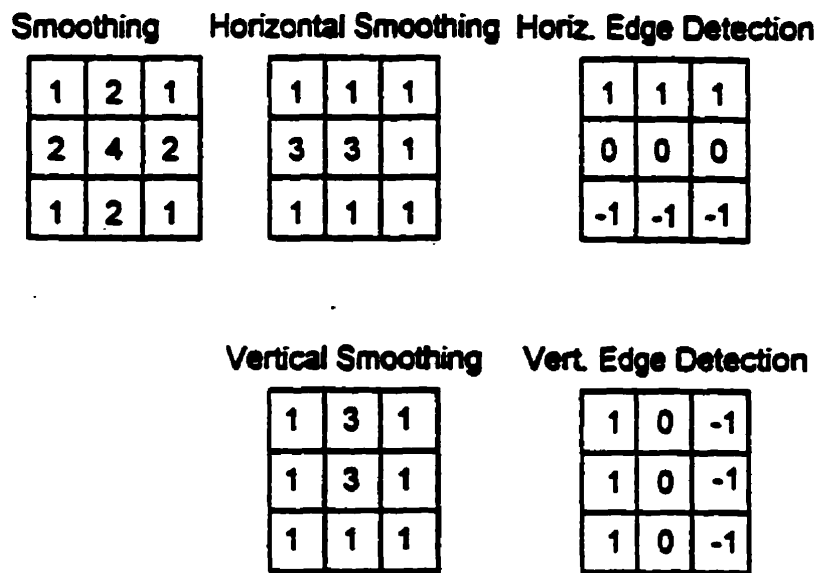


Figure 2-1: Filtering kernels for different types of regularization smoothing (Santamarina, 1994).

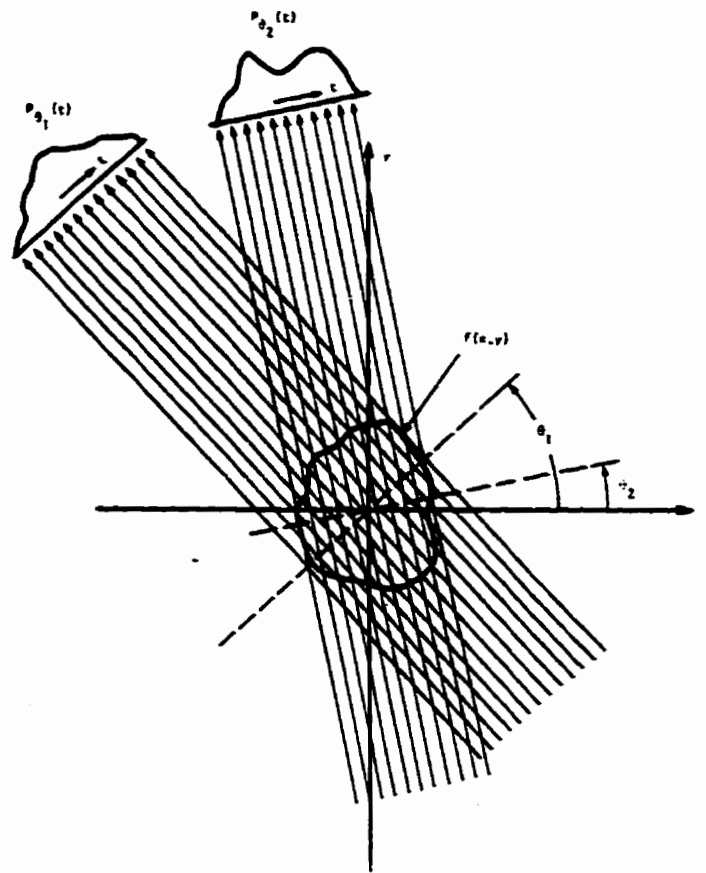


Figure 2-2: Parallel beam projections are taken by measuring a set of parallel rays for a number of different angles (Kak and Slaney, 1988).

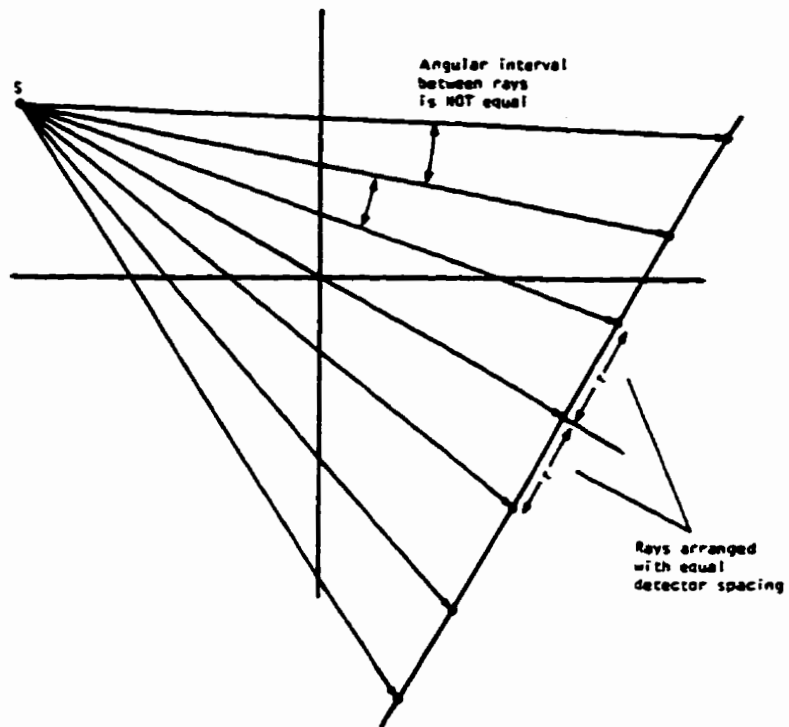


Figure 2-3: Equi-distance fan beam projections (Kak and Slaney, 1988).

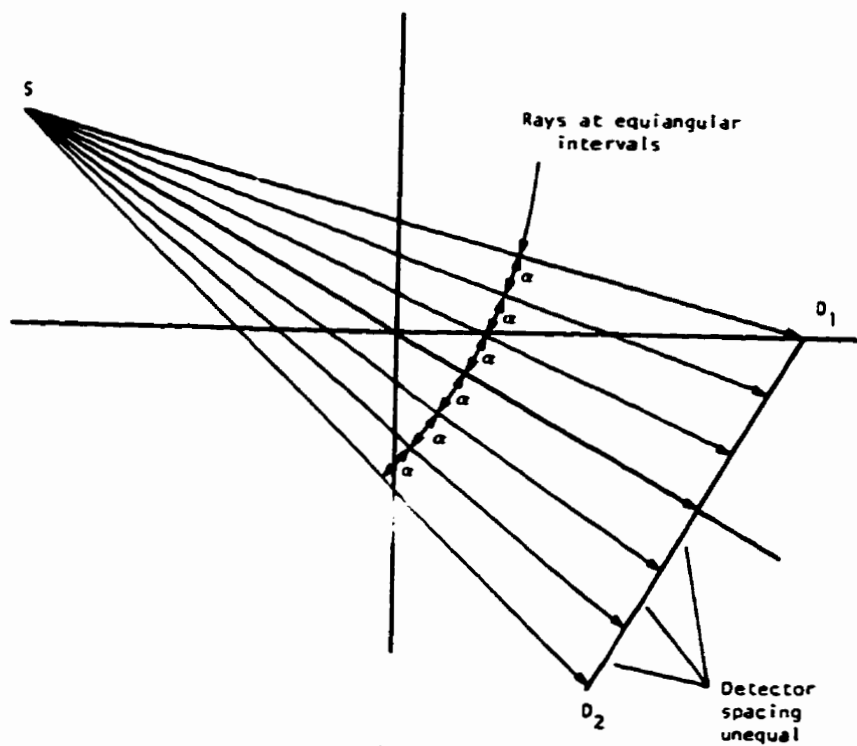


Figure 2-4: Equi angular fan beam projections (Kak and Slaney, 1988).

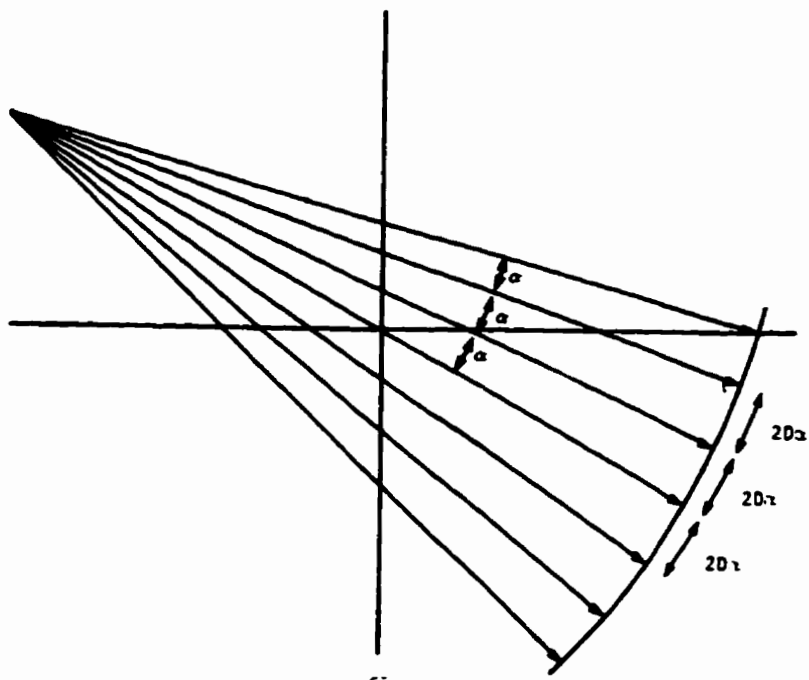


Figure 2-5: Equi-distance and equi-angular fan beam projections (Kak and Slaney, 1988).

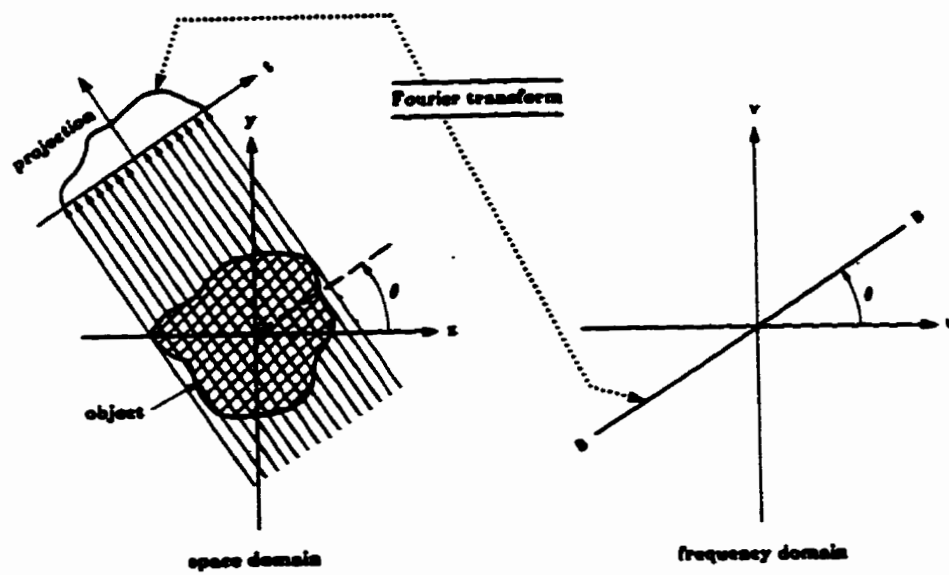


Figure 2-6: The Fourier slice theorem relates the Fourier transform of a projection to the Fourier transform of the object along radial line (Pan and Kak, 1983).

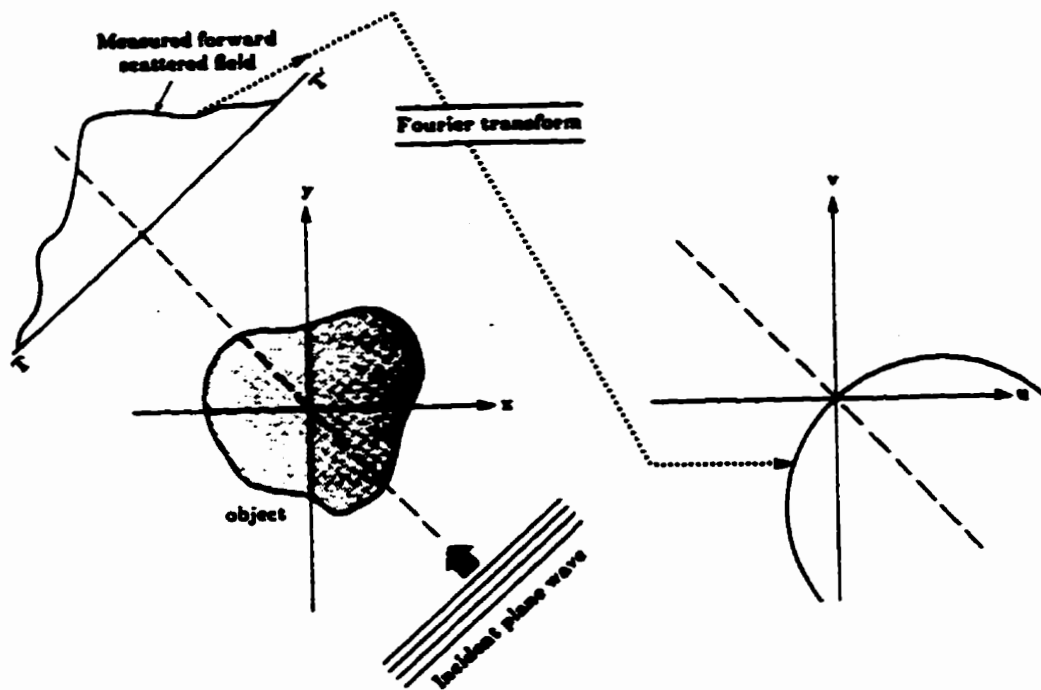


Figure 2-7: The Fourier diffraction theorem relates the Fourier transform of a diffracted projection to the Fourier transform of the object along a semicircular arc (Pan and Kak, 1983).

CHAPTER III

RAY THEORY AND RAY TRACING

3.1 Introduction

The analysis of wave propagation is often simplified to exercises with straight lines connecting sources and receivers. In this case, the matrix L is fixed and the inversion problem is linear. However, geoenvironments of interest are not homogeneous and isotropic. If the velocity contrast in the medium is more than 15 to 20 percent, rays bend toward higher velocity regions (Dines and Lytle, 1979). In this case, entries in the matrix L depend on a prior estimate of the velocity field, the inversion problem becomes non-linear, and iterative solutions are used to solve the tomographic inversion.

In general, it is assumed that "picked travel times" correspond to paths of shortest travel path (Fermat's principle). Ray tracing is implemented to determine shortest travel paths. This chapter presents a comprehensive review of solutions that have been proposed to solve the forward, ray tracing problem. Advantages and limitations are highlighted.

3.2 Ray Theory-Eikonal Equation

The wave surface or wave front is the locus of points which have the same

phase of motion at a given instant of time. Rays are normal to wave surfaces and give the direction of energy propagation in the medium. A "normal mode" is a preferred frequency of the system. Therefore, a solution based on normal modes involves the summation of contributions from the various preferred frequencies of vibration of the system.

There are many ways to solve the wave equation, meeting boundary and initial conditions. One solution is to transform the wave equation into the Eikonal equation and to solve it in terms of wave surfaces and rays, i.e., group velocity. Another solution is a development through specific boundary conditions and solutions in terms of normal modes, i.e., phase velocity. In some instances, the physical conditions of the problem lead to the simpler solution in terms of rays; in others, the solution in terms of normal modes is more satisfactory (Officer, 1974).

Three fundamental concepts in wave mechanics are frequently invoked in ray tracing:

- *Fermat's principle* states that the ray path between two points is such that travel time is minimum, i.e. the travel time between two points is stationary.
- *Snell's law* states that the change in the product of the refraction index and a direction cosine along the ray path is equal to the space rate of variation of the refraction index with respect to the appropriate coordinate $n=n(x,y,z)$. Snell's law satisfies Fermat's principle.
- *Huygens' principle* states that the disturbance at time $t=t_0+dt$ can be obtained from each point on the wave surface at time $t=t_0$, acting as a secondary source.

The term *head wave* is often encountered in the ray tracing literature. It refers to a refracted wave front that arrives before the direct wave (Figure 3-1). Thus, these arrivals are picked in first-arrival procedures. Another frequently

encountered term is *shadow zones*. Shadows can be observed in refraction surveys as a result of unique layering and velocity conditions (Figure 3-2); in this case, the shadow zone is relatively devoid of first arrivals (head waves). Shadows also take place in transmission surveys behind anomalies with high impedance mismatch with respect to the background medium, as shown in Figure 3-3.

3.2.1 Eikonal Equation: Derivation, Importance and Limitations

The three-dimensional wave equation for an isotropic medium is:

$$\frac{\partial^2 \zeta}{\partial x^2} + \frac{\partial^2 \zeta}{\partial y^2} + \frac{\partial^2 \zeta}{\partial z^2} = \frac{1}{c^2} \frac{\partial^2 \zeta}{\partial t^2} \quad (3-1)$$

where ζ is the displacement of an element in rectangular coordinates (x,y,z) at time t, and c is the velocity of the wave. A general solution for Equation 3-1 is a simple harmonic solution, with a varying amplitude in space

$$\zeta = A(x, y, z) e^{i\omega(u(x,y,z)/c_0 - t)} \quad (3-2)$$

where u is the wave front position. The condition that relates amplitude A and u is obtained by substituting Equation 3-2 into the wave equation (Equation 3-1) Equating imaginary and real parts, respectively (Officer, 1974),

$$2 \left(\frac{\partial u}{\partial x} \frac{\partial A}{\partial x} + \frac{\partial u}{\partial y} \frac{\partial A}{\partial y} + \frac{\partial u}{\partial z} \frac{\partial A}{\partial z} \right) + A \left(\frac{\partial^2 u}{\partial x^2} + \frac{\partial^2 u}{\partial y^2} + \frac{\partial^2 u}{\partial z^2} \right) = 0 \quad (3-3)$$

and

$$\frac{\partial^2 A}{\partial x^2} + \frac{\partial^2 A}{\partial y^2} + \frac{\partial^2 A}{\partial z^2} - A \frac{\omega^2}{c_0^2} \left[\left(\frac{\partial u}{\partial x} \right)^2 + \left(\frac{\partial u}{\partial y} \right)^2 + \left(\frac{\partial u}{\partial z} \right)^2 \right] = -\frac{\omega^2}{c^2} A \quad (3-4)$$

Equation 3-4 can be reordered as:

$$\left(\frac{\partial u}{\partial x}\right)^2 + \left(\frac{\partial u}{\partial y}\right)^2 + \left(\frac{\partial u}{\partial z}\right)^2 - n^2 - \frac{\lambda_0^2}{4\pi^2} \left[\frac{1}{A} \left(\frac{\partial^2 A}{\partial x^2} + \frac{\partial^2 A}{\partial y^2} + \frac{\partial^2 A}{\partial z^2} \right) \right] = 0 \quad (3-5)$$

where λ_0 is the wavelength of the wave with reference velocity c_0 . If the last term in Equation 3-5 is assumed to be equal to zero, then

$$\left(\frac{\partial u}{\partial x}\right)^2 + \left(\frac{\partial u}{\partial y}\right)^2 + \left(\frac{\partial u}{\partial z}\right)^2 = \frac{c_0^2}{c^2} = n^2 \quad (3-6)$$

where n is the refractive index and c_0 is the wave velocity in a reference medium. Equation 3-6 is the Eikonal equation. This time-independent equation can be applied in the solution of cases where c is a function of the space coordinates (heterogeneous media).

Let us focus on Equation 3-5 and review the conditions that lead to the Eikonal equation. It is assumed that the second term in Equation 3-5 is equal to zero. In general, the expression in parentheses is not zero. Hence, this assumption is valid only if $\lambda_0=0$, that is, in the high frequency limit. However, the order of magnitude of λ_0 is defined by the physical conditions of the problem. Therefore, the Eikonal equation is a good approximation to the wave equation if the curvature of the wave front is small over a wavelength, but it is not a good approximation to the wave equation in regions with rapid changes in velocity over the dimensions of the wavelength (Officer, 1974). In other words, the Eikonal equation is a solution of the wave equation if the rate of change of parameters is small with respect to the parameters themselves.

The Eikonal equation leads directly to the concept of rays. Rays are the normals to the wave fronts with direction of propagation (Lee and Stewart, 1981):

$$\left(-\frac{1}{\partial u / \partial x}\right) dx = \left(-\frac{1}{\partial u / \partial y}\right) dy = \left(-\frac{1}{\partial u / \partial z}\right) dz \quad (3-7)$$

where the denominators are the direction numbers of the normal. The relation between direction cosines and direction numbers yields

$$\frac{dx}{dL} = k \left(\frac{\partial u}{\partial x} \right) \quad \frac{dy}{dL} = k \left(\frac{\partial u}{\partial y} \right) \quad \frac{dz}{dL} = k \left(\frac{\partial u}{\partial z} \right) \quad (3-8)$$

where k is a constant and dL is an element of the ray path. Squaring and adding the three Equations 3-8, and recalling Equation 3-6,

$$\left(\frac{dx}{dL} \right)^2 + \left(\frac{dy}{dL} \right)^2 + \left(\frac{dz}{dL} \right)^2 = k^2 \left[\left(\frac{\partial u}{\partial x} \right)^2 + \left(\frac{\partial u}{\partial y} \right)^2 + \left(\frac{\partial u}{\partial z} \right)^2 \right] = k^2 n^2 \quad (3-9)$$

The sum of the three terms on the left is equal to 1.0 because they are direction cosines in three dimensions. Then, $k=1/n$ and Equations 3-8 become

$$n \left(\frac{dx}{dL} \right) = \frac{\partial u}{\partial x} \quad n \left(\frac{dy}{dL} \right) = \frac{\partial u}{\partial y} \quad n \left(\frac{dz}{dL} \right) = \frac{\partial u}{\partial z} \quad (3-10)$$

Taking a derivative along the ray d/dL for each of these equations results in (only shown for the first equation),

$$\frac{d}{dL} \left(n \frac{dx}{dL} \right) = \frac{d}{dL} \left(\frac{\partial u}{\partial x} \right) = \frac{\partial}{\partial x} \left(\frac{\partial u}{\partial x} \frac{dx}{dL} + \frac{\partial u}{\partial y} \frac{dy}{dL} + \frac{\partial u}{\partial z} \frac{dz}{dL} \right) \quad (3-11)$$

The three Equations 3-10 can be multiplied by the term in parentheses in each case, and replaced into the last term of Equation 3-11. Considering the definition of direction cosines, the right-hand side of Equation 3-11 reduces to $\partial(n)/\partial x$. Repeating the same procedure for the other two Equations in 3-10,

$$\frac{d}{dL} \left(n \frac{dx}{dL} \right) = \frac{\partial n}{\partial x} \quad \frac{d}{dL} \left(n \frac{dy}{dL} \right) = \frac{\partial n}{\partial y} \quad \frac{d}{dL} \left(n \frac{dz}{dL} \right) = \frac{\partial n}{\partial z} \quad (3-12)$$

These are three members of the ray equation in which the index of refraction n characterizes the medium. They may be considered as a generalized form of

Snell's law. Therefore, these equations could be used to trace rays in three dimensional heterogeneous media (Lee and Stewart, 1981). The general form of Equations 3-12 is:

$$\frac{d}{dL} \left(n \frac{dr}{dL} \right) = \nabla n \quad (3-13)$$

The ray solution is a complete solution to any particular propagation problem within the validity of the approximation of the Eikonal equation to the wave equation. In other words, a solution based on the ray assumption first carries the approximation of the Eikonal equation, and second, it assumes that energy propagates in a narrow bundle of rays.

Since ray theory is based on the Eikonal equation approximation, spatial frequencies corresponding to scales smaller than the first Fresnel zone width would not be accurately recovered by the ray assumption (Williamson and Worthington, 1993). Hence, ray theory can not be employed to compute travel times in cases where the diffraction phenomenon takes place. This phenomenon can be explained by Huygens' principle and the concept of Fresnel zone. The Fresnel zone is that portion of a reflecting interface that produces in-phase reflected waves at a detecting point, i.e., constructive interference (Figure 3-4). Therefore, a large region is responsible for the reflected energy rather than just a point on the reflector (ray theory assumption-Sheriff, 1978). Figure 3-5 shows that as the body becomes smaller than the Fresnel zone, it becomes in effect a point reflector, and it is nearly indistinguishable from a diffractor.

Ray Assumption. The interaction of waves with inclusions depends primarily on the size of the inclusion D with respect to the wave length λ . The ray assumption applies when $D \gg \lambda$. More specifically, ray tomography is applicable when the scale length of the anomaly is at least the radius of the first Fresnel zone: if the average ray length is n wavelengths, the size of the inclusion must be at least ξ .

$\lambda \cdot (n)^{0.5}$, where ξ varies between 0.5 and 1 (Santamarina, 1994). The "straight ray" assumption dominated the development of engineering tomography during the 80's, as an extension of X-ray tomographic imaging in medical applications. From optics, the straight ray approximation applies if the travel length $L \gg \lambda/2\pi$, if the wavelength is significantly smaller than the size of the anomaly, and if velocity changes are less than 20% to 30%.

Diffraction. When the size of inclusions is within the same order of magnitude as the wavelength, the ray approximation does not hold, and propagation must be considered from the point of view of the wave front and scattered energy. Diffraction degrades the quality of tomograms when the linear ray assumption is made: low velocity inclusions are imaged smaller than real size (high velocity anomalies are imaged larger). Low velocity anomalies are difficult to detect when the plane of receivers is located about twice the diameter of the inclusion away from it.

Fresnel's ellipse. The position of scatterers that affect wave arrival at the source is related to the wave length λ . Indeed, waves scattered from diffractors within an ellipse, so that the travel distance is the straight distance d plus $\lambda/4$ or $\lambda/2$, will arrive in phase with the direct wave traveling the straight path d . This observation is relevant in selecting ray-tracing algorithms (often a "thick ray" assumption is used), and in selecting source and receiver configuration: transducers too close together do not necessarily add information content.

3.3 Ray Tracing Methods

Ray tracing is a two-point boundary value problem: the end points are specified (the source and receiver positions), and the propagation path and time must be

determined. Ray theory is used in the development of some ray tracing algorithms. However, there are more general solutions. In all cases, ray tracing fulfills Fermat's principle. Ray tracing techniques are categorized as: *One-point methods*, *Two-point methods*, and *Whole field methods*.

3.3.1 One-Point Methods

These methods are also known as initial value methods or shooting methods. In this case, the two-point boundary value problem is approached by iteratively solving an initial value problem with one fixed end point, and subsequently varying the initial ray trajectory or take-off angle. Therefore, the main purpose of these methods is integrating the initial value formulation of the problem and employing a procedure to find the starting direction which yields the desired ray path. Figure 3-6 shows a schematic view of this type of methods. Primary ray tracing assumes "point velocities" and interpolates values, rather than selecting rigid pixels boundaries.

There are two important steps in one-point methods: first, the initial guess of the take-off angle, and second, the algorithm which traces the ray from the initial point to the end point.

The equations for the initial value problem can be defined in a simple form if the ray path is specified parametrically in terms of position vector $r(t)$ and a slowness vector $s(t)$ where the parameter t is the cumulative travel time. The slowness vector $s(t)$ is defined in the direction tangent to the ray and as the inverse of the local seismic wave velocity in that direction, v (Chernov, 1960; Eliseevnin, 1965). This definition leads to

$$\frac{d\vec{r}}{dt} = v^2 \vec{s} \quad (\text{Note: } \vec{v} \cdot \vec{s} = 1 \text{ unit vector}) \quad (3-14)$$

The rate of change of slowness along the ray is

$$\frac{d\vec{s}}{dt} = -\frac{\nabla v}{v} \quad (3-15)$$

In three-dimensional space, these equations represent a system of six first order differential equations which must be integrated numerically to find the ray path. However, because of the relation between slowness and velocity, one equation is redundant and it may be eliminated (Julian and Gubbins, 1977). Appendix A gives computationally convenient forms of these equations in Cartesian coordinates; redundancy has been eliminated by expressing s in terms of two angles giving its direction (Gheshlaghi, 1992). The spherical form of these equations can be found in Julian and Gubbins (1977).

The system of first order differential equations may be solved with standard numerical integration techniques. Sambridge and Kennett (1990) solved these equations with a fourth-order Runge-Kutta algorithm. Their method also employed the paraxial boundary value ray tracing of Cerveny, *et. al.* (1984) which may be applied to ray tracing in laterally varying layered media. Julian and Gubbins (1977) employed a step-size extrapolation method. Lytle and Dines (1980) started from Snell's law and derived a refractive index equation in two dimensions rather than the ray equation. In their approach, the differential equation describing ray paths can be obtained by considering that

$$\frac{\sin(\alpha + \Delta\alpha)}{\sin\alpha} = \frac{v + \Delta v}{v} \quad (3-16)$$

In the limit, this equation leads to the differential form of Snell's law:

$$\text{Cos}\alpha \cdot d\alpha = (\text{Sin}\alpha)(dv / v) \quad (3-17)$$

If Equation 3-17 is written in terms of coordinates (x,y) and the ray tangent angle θ , the refractive index equation can be derived as follows (see Lytle and Dines, 1980)

$$\frac{d\theta}{dL} = \frac{1}{n} \left[\frac{\partial n}{\partial y} \text{Cos}\theta - \frac{\partial n}{\partial x} \text{Sin}\theta \right] \quad (3-18)$$

where n is the refractive index and dL is the arc length of the ray path. They used the Runge-Kutta algorithm to determine the ray path based on a given initial angle (The algorithm is summarized in Appendix B).

The determination of the starting direction which causes the ray to pass through the desired end point involves finding solutions to two nonlinear simultaneous equations specified implicitly in terms of the differential Equations 3-14 and 3-15:

$$x(i_0, \varphi) = X \quad \text{and} \quad y(i_0, \varphi) = Y \quad (3-19)$$

where the x and y are the calculated coordinates of the end of the ray with starting shooting angle i_0 and starting azimuth φ , and X and Y are the desired end coordinates of the ray, i.e., the coordinates of the receiver.

Several methods are employed to solve these equations. Newton-Raphson's method and an extension of the "false position" method are the common approaches. Since the above equations are generally nonlinear, both methods must be applied iteratively.

The improved estimate of (i_0, φ) is obtained by solving the system of linear equations

$$\begin{bmatrix} \frac{\partial x}{\partial i_0} & \frac{\partial x}{\partial \varphi} \\ \frac{\partial y}{\partial i_0} & \frac{\partial y}{\partial \varphi} \end{bmatrix} \begin{bmatrix} i_0^{n-1} & -i_0^n \\ \varphi^{n-1} & -\varphi^n \end{bmatrix} = \begin{bmatrix} X & -x(i_0^n, \varphi^n) \\ Y & -y(i_0^n, \varphi^n) \end{bmatrix} \quad (3-20)$$

where the superscripts indicate the value of the corresponding parameter in each iteration. The calculation of the partial derivatives consumes a lot of time. As with the ray path system, two additional systems of ordinary differential equations of the same order should be solved (Julian and Gubbins, 1977).

The method of "false position" employed by Julian and Gubbins (1977) calculates only the ray path at each iteration. However, it converges more slowly (Julian and Gubbins, 1977): an improved estimate of (i_0, φ) is obtained at each stage of the iteration. This improved estimate is calculated by approximating the functions $x(i_0, \varphi)$ and $y(i_0, \varphi)$ by planes passing through the values calculated from three previous estimates. These planes take on the values X and Y , respectively along two straight lines. The desired improved estimate can be obtained from the intersection of these two straight lines. A compact form for the desired equations is

$$\begin{vmatrix} i_0 - i_0^1 & i_0 - i_0^2 & i_0 - i_0^3 \\ x^1 - X & x^2 - X & x^3 - X \\ y^1 - Y & y^2 - Y & y^3 - Y \end{vmatrix} = 0 \quad (3-21)$$

and similarly for φ

$$\begin{vmatrix} \varphi - \varphi^1 & \varphi - \varphi^2 & \varphi - \varphi^3 \\ x^1 - X & x^2 - X & x^3 - X \\ y^1 - Y & y^2 - Y & y^3 - Y \end{vmatrix} = 0 \quad (3-22)$$

where the superscripts indicate the three previous estimates. This method is more efficient than Newton-Raphson's method (Julian and Gubbins, 1977).

Advantages of One-Point Methods.

- One-point methods are suitable to perform 3-D ray tracing in which receivers are distributed along some line profile, e.g. line, curved, piece-wise, etc. (Nolet, 1987).
- These methods can be employed where source location is initially unknown, e.g. earthquake location.
- One-point methods are easy to apply and need less computer memory storage than two-point methods (Iyer and Hirahara, 1993).

Limitations of One-Point Methods.

- Do not find diffracted ray paths (Moser, 1991).
- Do not always converge to a solution (Asakawa and Kawanaka, 1993).
- Are not able to handle head waves (Asakawa and Kawanaka, 1993).
- Can not find ray paths in shadow zones (Moser, 1991).

3.3.2 Two-Point Methods

Two-point methods are also known as bending methods. These methods start with specific initial and end points, and choose the ray path which satisfies Fermat's principle.

Bending Method

In this method, an initial ray path is assumed and then perturbed while keeping end points fixed (Figure 3-7). The procedure is repeated until an acceptable stable minimum time is found. Generally, the first guess is the straight path. Um and Thurber (1987) applied this method to a variety of laterally heterogeneous velocity models. They suggested a three-point perturbation scheme and

considered two approaches for perturbation (Figure 3-8 and 3-9). One approach is that points in a new path are sought starting from one end-point. The other approach is that new points are sought simultaneously starting from both end-points. They finally adopted the second approach. Travel time is computed as a summation. Um and Thurber (1987) defined the rate of perturbation R (Figure 3-10). The direction of offset n is based on the curvature direction of a minimum time ray path. Their derivation of the ray equation is:

$$-\frac{d^2r}{dL^2} = \frac{\left[(\nabla v) - \left(\frac{dv}{dL} \right) \left(\frac{dr}{dL} \right) \right]}{v} \quad (3-23)$$

where r is the position vector along the ray path. The second term on the right hand side of this equation is the component of the velocity gradient parallel to the ray path. Therefore, this equation states that the component of the velocity gradient normal to the ray vector is normal to the curvature of the ray path. If one considers the local ray direction as the direction of the line that connects two contiguous end points, as in Figure 3-8, the component of the velocity gradient normal to that direction gives the curvature direction. Thus, the offset direction for the point x'_k , which satisfies Equation 3-23, may be defined as:

$$n' = (\nabla v) - \frac{[(\nabla v) \cdot (x_{k+1} - x_{k-1})](x_{k+1} - x_{k-1})}{|x_{k+1} - x_{k-1}|^2} \quad (3-24)$$

where the second term is the component of the velocity gradient parallel to the ray direction. The unit vector direction is obtained as $n = n'/|n'|$.

Santamarina and Cesare (1995) proposed another perturbation procedure for ray tracing in vertically heterogeneous and anisotropic media (Figure 3-10). In this method, the straight segment between contiguous nodes is split in half and the new node is displaced in the normal direction until time is minimized. The process is repeated recursively.

Advantages of Bending Methods

- Always converge to a solution.
- Diffracted rays and rays which pass through shadow zones can be found.

Limitations of Bending Methods

- There is no certainty as to whether the path corresponds to the absolute minimum travel time or to a local minimum (Thurber and Ellsworth, 1980).
- There may be more than one solution for a source and receiver pair.
- These methods can not be applied to problems where the location of one end point is known while the location of the other point must be determined, e.g. earthquake location.

Sine-Arcs and Simplex Optimization

The method proposed by Prothero *et al.* (1988) starts by specifying the velocity at nodal points. Then, interpolation is used to estimate velocity at an arbitrary location:

$$\begin{aligned} V = & (X_{i+1} - X)(Y_{j+1} - Y)(Z_{k+1} - Z)V_{i,j,k} + (X - X_i)(Y_{j+1} - Y)(Z_{k+1} - Z)V_{i+1,j,k} \\ & + (X_{i+1} - X)(Y - Y_j)(Z_{k+1} - Z)V_{i,j+1,k} + (X - X_i)(Y - Y_j)(Z_{k+1} - Z)V_{i+1,j+1,k} \\ & + (X_{i+1} - X)(Y_{j+1} - Y)(Z - Z_k)V_{i,j,k+1} + (X - X_i)(Y_{j+1} - Y)(Z - Z_k)V_{i+1,j,k+1} \\ & + (X_{i+1} - X)(Y - Y_j)(Z - Z_k)V_{i,j+1,k+1} + (X - X_i)(Y - Y_j)(Z - Z_k)V_{i+1,j+1,k+1} \end{aligned} \quad (3-25)$$

where the i , j , and k indices are used for surrounding points and X , Y , and Z characterize the location of the point of interest.

The starting ray path is found by searching the minimum travel time along circular arcs connecting the source and the receiver. If an inappropriate arc is chosen, convergence to local travel time minima may occur. The selected

starting ray is perturbed until the minimum travel time is obtained. Prothero *et al.* (1988) distorted the selected circular path by adding sine waves, systematically varying their amplitudes to minimize travel time. The distortion is expressed as

$$\begin{aligned} dx(n,i) &= A_x(n) \cdot \text{Sin}(n \cdot \pi \cdot d \cdot i / L) \\ dy(n,i) &= A_y(n) \cdot \text{Sin}(n \cdot \pi \cdot d \cdot i / L) \end{aligned} \quad (3-26)$$

where n is the harmonic number, $dx(n,i)$ and $dy(n,i)$ are the translation of the i th point on the path due to n th order sine wave, $A_x(n)$ and $A_y(n)$ are the vertical and horizontal amplitudes of the n th order sine wave, d is the spacing between points on the path, i is the index of the i th point, and L is the arc length of the circular path.

The amplitude of each perturbing sine arc is optimized with the Simplex optimization algorithm. The Simplex method is used for the minimization of a function of n variables. The procedure consists of comparing the values of the function at $(n+1)$ vertices of a general polygon or "simplex", followed by the replacement of the vertex with the highest value by another point (Nelder and Mead, 1965). The simplex in the two-dimensional space is a triangle, and it is a tetrahedron in the three-dimensional space.

A schematic of the "Simplex" search is shown in Figure 3-11. B, O, and W are three arbitrary points in the two-dimensional space of $A_x(n)$ and $A_y(n)$. To reach the lowest value of the travel time function the Simplex, i.e. triangle, should be moved downhill. Find the vertex with the highest travel time (worst: W) and the one with shortest time (best: B). Reject W and substitute it with another point. Point R is obtained as a reflection of W. If the travel time corresponding to $A_x(n)$ and $A_y(n)$ at R, $t(R)$ is lower than $t(O)$ and $t(B)$, increase the distance twice (E). If $t(B) \leq t(R) \leq t(W)$, R is selected. If $t(R) > t(W)$, then a contraction occurs. If the contraction (C) produces a better value than W, C is selected; otherwise, a shrinkage occurs and all vertexes, except the best one, move directly toward B

by half of the original distance from it (points S in Figure 3-11). Figure 3-12 shows the contours for travel time values in A_x - A_y space. The minimum value of the travel time is located at the center of these contours. The points marked W, O, and B are the three initial guesses. The procedure is repeated for each harmonic.

Advantages of the Sine-Arc + Simplex Optimization

- This method is fast, and it always converges (Prothero *et al.*, 1988).
- Diffracted rays and rays that pass through shadow zones can also be found by this method.

Limitations of the Sine-Arc + Simplex Optimization

- It is assumed that the medium is continuous and has a unique minimum (Nelder and Mead 1965). In real cases, the search may converge to a local minimum.

Polygonal Path Method

This method was proposed by Stöckli (1984) for transversely isotropic media. It assumes that wave surfaces are polygonal surfaces (Recall that wave surfaces are ellipsoidal in transversely isotropic materials). Therefore, if z is the axis of symmetry (Figure 3-13),

$$F(x,z) = \left(\left| \frac{x}{a} \right|^p + \left| \frac{y}{b} \right|^p \right)^{\frac{1}{p}} \tag{3-27}$$

Then, the true wave surface can be approximated as,

$$G(x,y,z) = F\{(x^2 + y^2 + z^2)^{1/2}, z\} = 1 \tag{3-28}$$

The more general case, where z is not the axis of symmetry, can be obtained by an orthogonal change of axes. Optimization involves finding the value of p in Equation 3-27 that satisfies Fermat's principle for each ray path.

Advantages of the Polygonal Path Method

- A simple iteration gives the best value of p .
- This method is useful for ray tracing in layered media.

Limitations of the Polygonal Path Method

- This method can not solve the ray tracing problem in media with high velocity contrast where the wave surface changes rapidly.

3.3.3 Whole-Field Methods

Whole field methods compute local travel times between nodes in the whole space of interest before ray paths are identified for each source-receiver pair. These methods are also known as network methods (Moser, 1994).

Finite Difference Method

Vidale (1988 in 2D and 1990 in 3D) proposed a wave front tracing technique based on a finite-difference approximation of the Eikonal equation. Matsuoka and Ezaka (1990) proposed a finite-difference solution based on the reciprocity principle (see method by Asakawa and Kawanaka, 1993). More recently, a systematic application of Huygens' principle within a finite-difference approximation was proposed by Podvin and Lecomte (1991).

Vidale's method creates a mesh of points (Figure 3-14). Assume that the travel time at point A is t_0 . Travel times at the four points B_i adjacent to A are determined as follows:

$$t_i = \frac{d}{2}(s_{B_i} + s_A) + t_0 \quad (3-29)$$

where d is the mesh spacing, s_A is the slowness at point A, and s_{B_i} is the slowness at the grid point B_i . The travel time at C1 is determined using the Eikonal equation and the assumption of a plane wave front:

$$\left(\frac{\partial t}{\partial x}\right)^2 + \left(\frac{\partial t}{\partial z}\right)^2 = s(x,z)^2 \quad (3-30)$$

In finite differences, the terms in Equation 3-30 can be approximated as follows (see Figure 3-14):

$$\frac{\partial t}{\partial x} = \frac{1}{2d}(t_0 + t_2 - t_1 - t_3) \quad (3-31a)$$

and

$$\frac{\partial t}{\partial z} = \frac{1}{2d}(t_0 + t_1 - t_2 - t_3) \quad (3-31b)$$

Substituting Equation 3-31a and Equation 3-31b into Equation 3-30 leads to:

$$t_3 = t_0 + \sqrt{2(d.s)^2 - (t_2 - t_1)^2} \quad (3-32)$$

Similar equations for travel times can be computed for spherical wave fronts. Assume that the travel time to the center of curvature of the wave front is t_s . Then travel times to A, B1, B2, and C are (see Figure 3-14)

$$t_0 = t_s + s\sqrt{x_s^2 + z_s^2} \quad (3-33)$$

$$t_1 = t_s + s\sqrt{(x_s + d)^2 + z_s^2} \quad (3-34)$$

$$t_2 = t_s + s\sqrt{x_s^2 + (z_s + d)^2} \quad (3-35)$$

$$t_3 = t_s + s\sqrt{(x_s + d)^2 + (z_s + d)^2} \quad (3-36)$$

Once all travel times through the media are calculated, the steepest gradient in the travel time data is used to identify the shortest travel time paths for each source and receiver pair.

Advantages of the Finite Difference Method

- This method allows for the subsequent assignment of ray paths and arrival amplitudes, reducing the computation time significantly by eliminating the trial and error process of ray shooting (Asakawa and Kawanaka, 1993; Iyer and Hirahara 1993).
- Algorithms are simple and robust, solutions are generally acceptable for various velocity fields (Geoltarine and Brac, 1993).
- These algorithms can be used in conjunction with Kirchhoff depth migration.

Limitations of the Finite Difference Method

- Finite difference methods present difficulties when applied to models with sharp velocity contrasts.
- The ray path consists of line segments connecting grid points between cells of different velocities (no refraction). This problem is overcome by Ishii, Rokugawa and Suzuki (1988) by placing nodes on cell boundaries (Asakawa and Kawanaka, 1993).

Multiple Segment, Network Methods

These methods are also known as grid methods. In Moser's method, the area of interest is divided into a grid of pixels (Moser, 1991). Each point on the grid is

connected to all other near neighboring points (Figure 3-15). The travel time between two connected nodes is defined as their Euclidean distance multiplied by the average slowness of the two nodes. The velocity in a pixel is assumed constant. Travel times for all ray segments are computed in the forward stage. Minimum time rays between source-receiver pairs are selected in the backward stage. The search for optimal ray paths within the network is based on search algorithms in graph theory (see Nilsson, 1980). Moser (1991) implemented breadth-first search. The tree starts with the source $t=0$, and it is expanded following network nodes and their links.

The method by Asakawa and Kawanaka (1993) is also a network technique but in this case, the space is searched for each shot (Figures 3-16 and 3-17). The method attempts to find optimal crossing points on all boundaries so that travel time is minimized. Consider a ray path crossing the segment AB on a certain cell boundary and reaching point D on the opposite side of the boundary. Assume that we want to calculate travel time t_D at point D. Travel times t_A at A and t_B at B are known. Then, the travel time t_C is linearly interpolated:

$$t_C = t_A \frac{d-r}{d} + t_B \frac{r}{d} \quad (3-37)$$

Finally, the time at D is:

$$t_D = t_C + s\sqrt{l_x^2 + (l_y + r)^2} \quad (3-38)$$

where $l_x = x_2 - x_1$, $l_y = y_2 - y_1$, and s is the pixel slowness. Combining Equations 3-37 and 3-38

$$t_D = t_A \frac{d-r}{d} + t_B \frac{r}{d} + s\sqrt{l_x^2 + (l_y + r)^2} \quad (3-39)$$

If Equation 3-39 is differentiated with respect to r , and equated to zero, the value of r for minimum t_D is obtained:

$$r = \frac{\Delta T l_x}{\sqrt{S^2 d^2 - \Delta T^2}} - l_y \quad (3-40)$$

and replacing back in Equation 3-39:

$$t_b = t_a + \Delta t \frac{l_y}{d} + \frac{l_x}{d} \sqrt{S^2 d^2 - \Delta t^2} \quad (3-41)$$

The condition for the correct ray path to cross the segment AB and reach the point D is:

$$s \cdot d \cdot \cos \alpha \leq \Delta t \leq s \cdot d \cdot \cos \beta \quad (3-42)$$

or

$$S^2 d^2 \frac{l_x^2}{l_x^2 + l_y^2} \leq (\Delta T)^2 \leq S^2 d^2 \frac{(l_y + d)^2}{l_x^2 + (l_y + d)^2} \quad (3-43)$$

The forward algorithm starts from the selected shot point and advances the network column-by-column, accumulating travel time (see Figure 3-16). The lowest travel time is assigned at nodes. At the end of the forward process, minimum "source times" have been assigned to nodes along vertical cell boundaries. The backward algorithm starts at each receiver and moves back towards the source. At a given node on a vertical boundary, the "ray time" can be computed as the addition of "source time" and "receiver time". The crossing point is optimized to minimize the ray time, as described above. This method resembles heuristic graph search strategies (Nilsson, 1980).

The method proposed by Sassa *et al.* (1989) is a shot-based network method similar to the forward algorithm by Asakawa and Kawanaka (1993). The authors view it as a Huygens' based approach (Figures 3-18). The backward algorithm in Asakawa and Kawanaka (1993) is replaced by a second forward scan of the network, whereby crossing points are optimized (Figures 3-19),

Advantages of Multiple Segment Network Methods

- These methods successfully compute diffracted ray paths and paths in shadow zones.
- All source-receiver pairs are preprocessed at once (forward process common to all rays).
- These methods avoid the numerical instabilities in spaces where velocity changes abruptly.

Limitation of Multiple Segment Network Methods

- They require large computer memory.
- The computation time is significant, yet linearly dependent on the number of nodes (at least in Moser's method). Computational efficiency increases for large problems, such as 3D surveys.
- In Moser's method, the angle of refraction does not change continuously with the angle of incidence, and the ray path may refract between cells of equal velocity.

3.4 Summary and Conclusions

Ray theory is a complete solution to any particular propagation problem within the validity of the approximation of the Eikonal equation to the wave equation. In other words, a solution based on the ray assumption first carries the approximation of the Eikonal equation and second, it assumes that energy propagates in a narrow bundle of rays. Therefore, ray tracing methods based on ray theory (one point methods) can not predict travel times in shadow zones and diffracted regions. Other ray tracing methods can successfully overcome these problems, give a solution for shadow zones, and estimate diffracted travel times.

Closed-form solutions are possible for simple velocity fields.

One-point methods are efficient and have low memory demands, yet, they have all the restrictions inherent in ray theory. Furthermore, they may never converge.

Two-point methods are flexible and efficient, require low memory storage, and can solve travel times in shadow zones and diffracted ray paths. However, they may not be able to find the global minimum.

Whole-field methods can identify global minimum travel times, including shadow and diffracted zones. While the solution is computer demanding, all rays from a given shot are solved at once.

A summary of ray tracing methods is given in Table 3-1.

Table 3-1: Ray tracing methods.

Method	Procedure	Abilities	Short comings
One-Point Methods	<ol style="list-style-type: none"> 1. Initial guess of the take-off angle. 2. Trace rays from source to receiver. 	<ul style="list-style-type: none"> • Suitable for 3D ray tracing. • Useful for cases with Unknown source location. • Easy to apply. • Limited computer memory. 	<ul style="list-style-type: none"> • Not for diffracted rays or ray paths in shadow zones. • Not always converge. • Unable to handle head waves.
Two-Point Methods	<ol style="list-style-type: none"> 1. Assuming an initial ray path. 2. Perturb the path to minimize travel time. 	<ul style="list-style-type: none"> • Always converge to a solution. • Diffracted rays and rays in shadow zones can be found. 	<ul style="list-style-type: none"> • Solution may converge to local minima. • Demand more computer memory than one-point methods.
Whole-Field Methods	<ol style="list-style-type: none"> 1. Compute travel time for different segments. 2. Find the best path by graph search. 	<ul style="list-style-type: none"> • Compute diffracted ray paths and paths in shadows. • Avoid the numerical instabilities in spaces where velocity changes abruptly. 	<ul style="list-style-type: none"> • Significant computation time and memory demand. • Angle of refraction may not change continuously with angle of incidence.

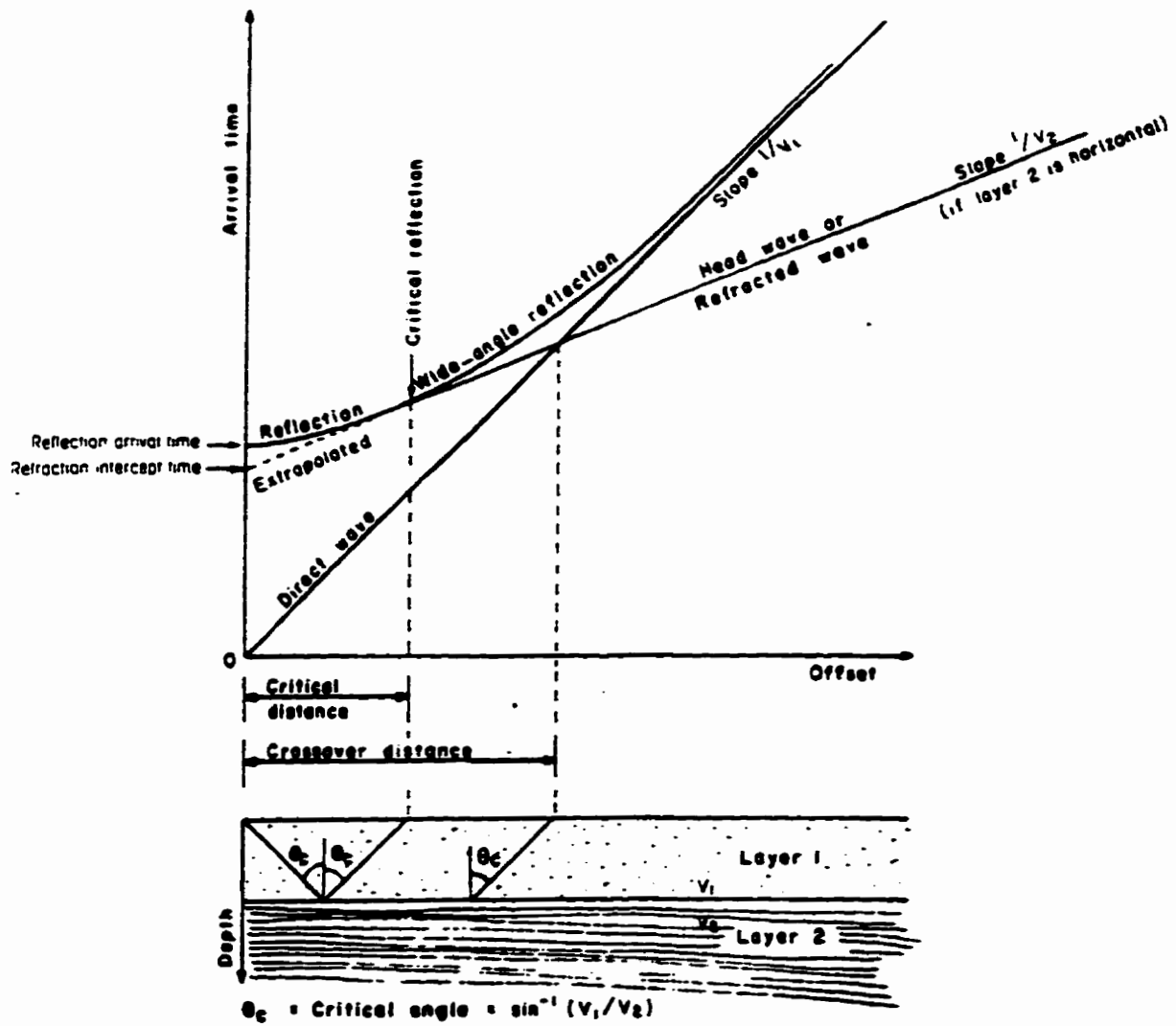


Figure 3-1: Head waves from a horizontal refractor (layer 2). Head waves begin at the critical distance and overtake the direct waves at the crossover distance (Sheriff, 1989).

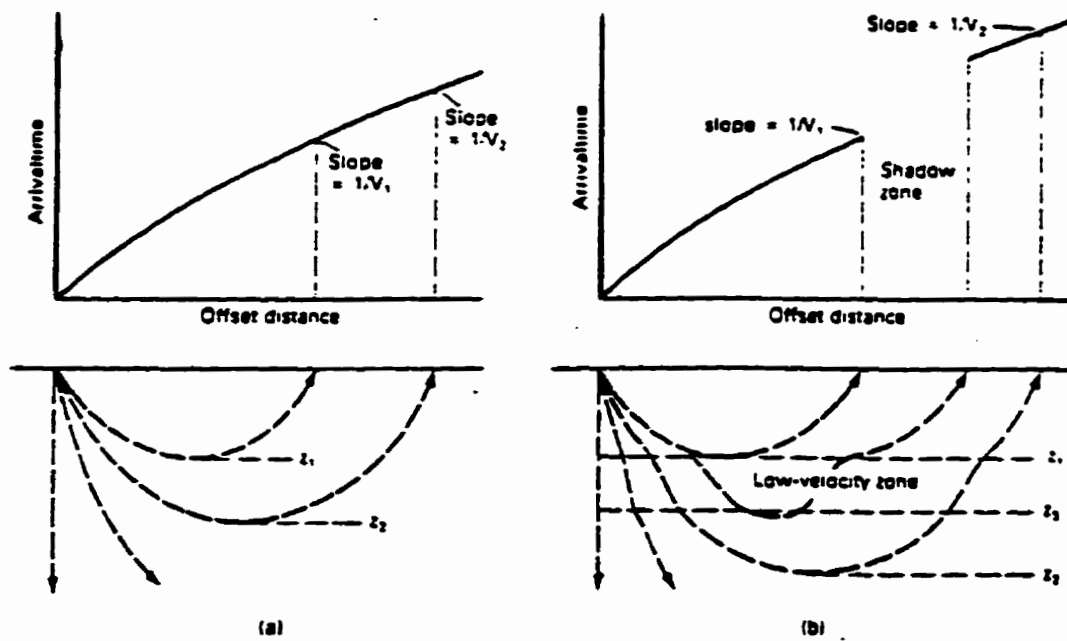


Figure 3-2: Arrival time-distance curves for diving waves. Starting angles= 0° , 10° , 20° , and 30° ; velocity gradient is (a) continuous velocity gradient; (b) velocity gradient interrupted by a low-velocity zone from z_1, z_3 resulting in a shadow zone (Sheriff, 1989).

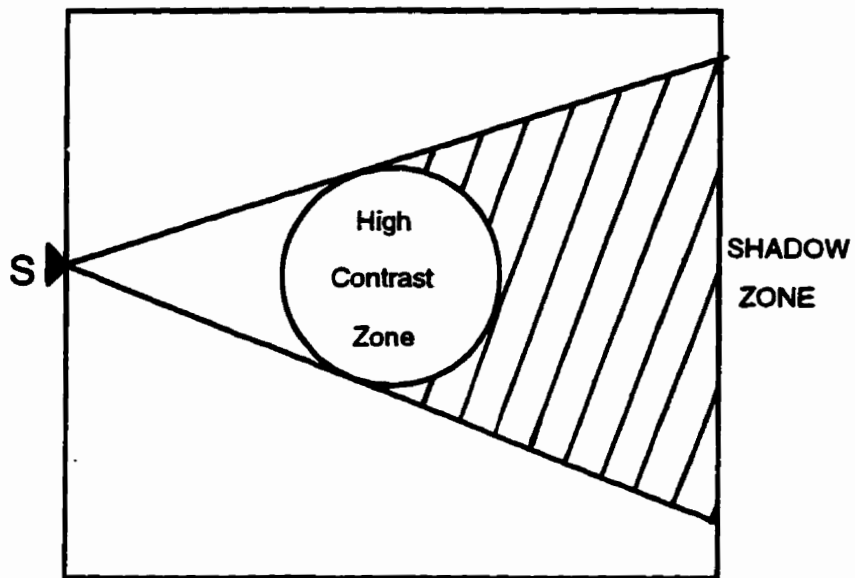


Figure 3-3: Shadow zone in the presence of a high impedance region.

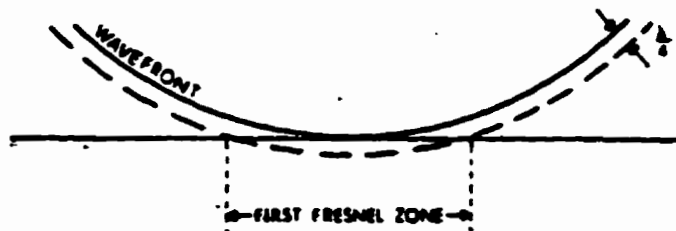


Figure 3-4: The first Fresnel zone: Interaction between a wave front and the interface between two media (Sheriff, 1978).

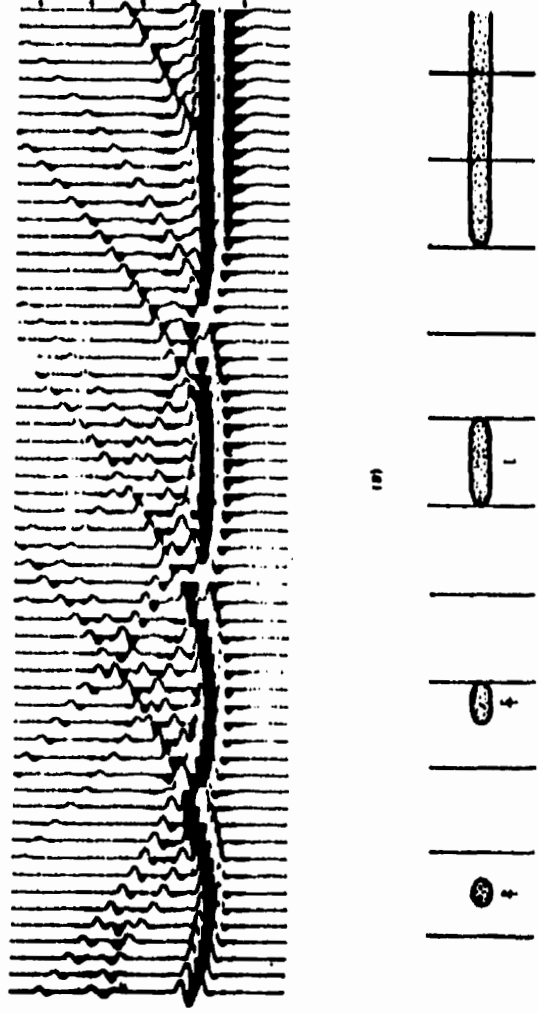


Figure 3-5: Fresnel zone and different size bodies (Sheriff, 1978).

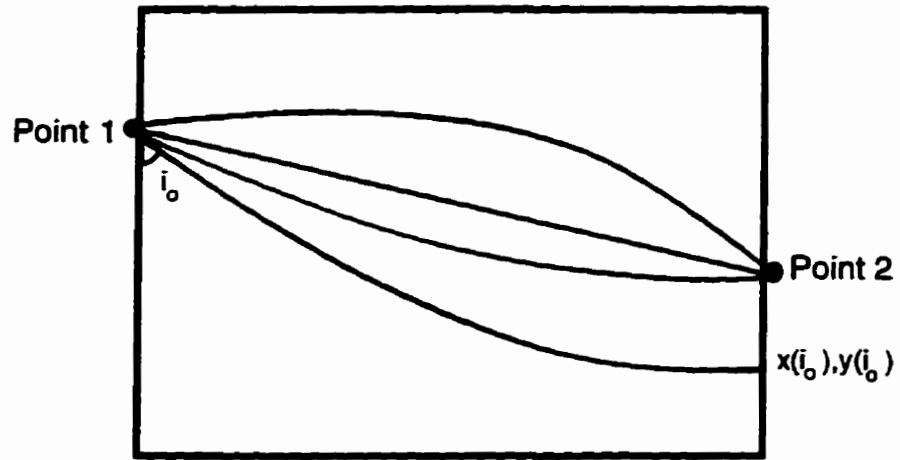


Figure 3-6: One point method in two dimensions - A schematic representation.

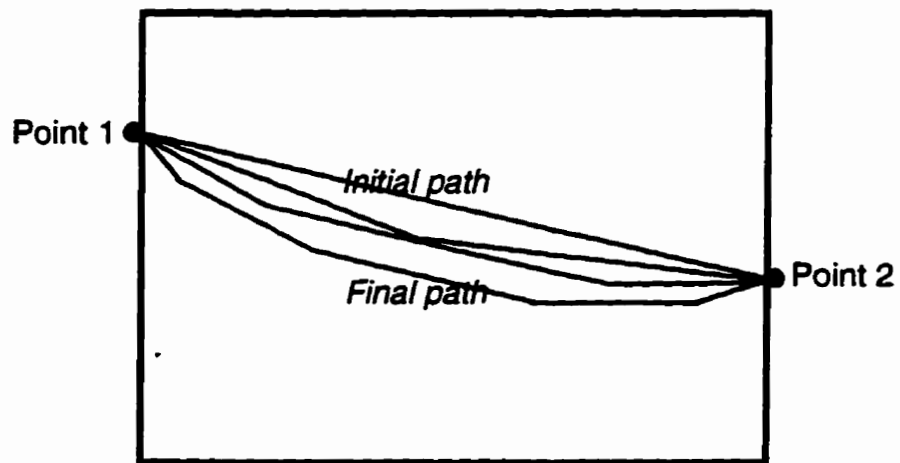


Figure 3-7: An example of perturbing rays in bending methods.

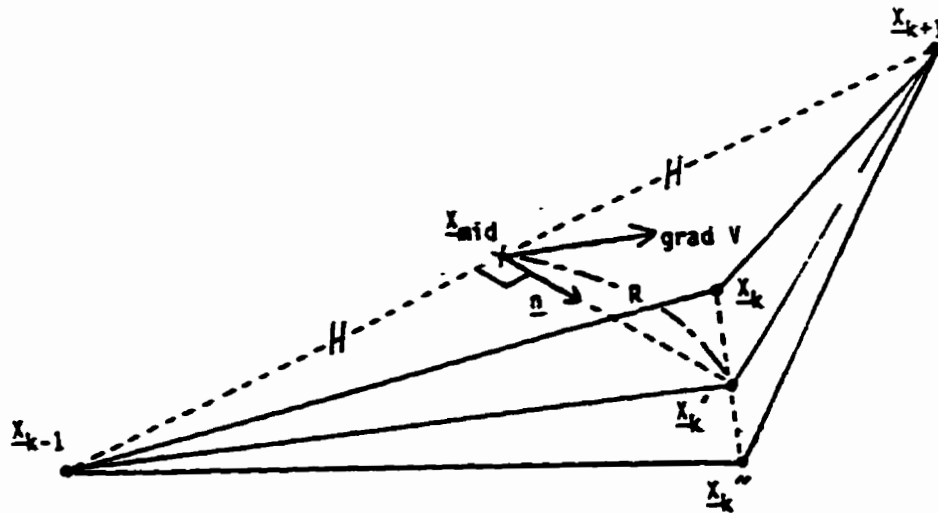


Figure 3-8: Three-point perturbation scheme in three dimensions. (Um and Thurber, 1987).

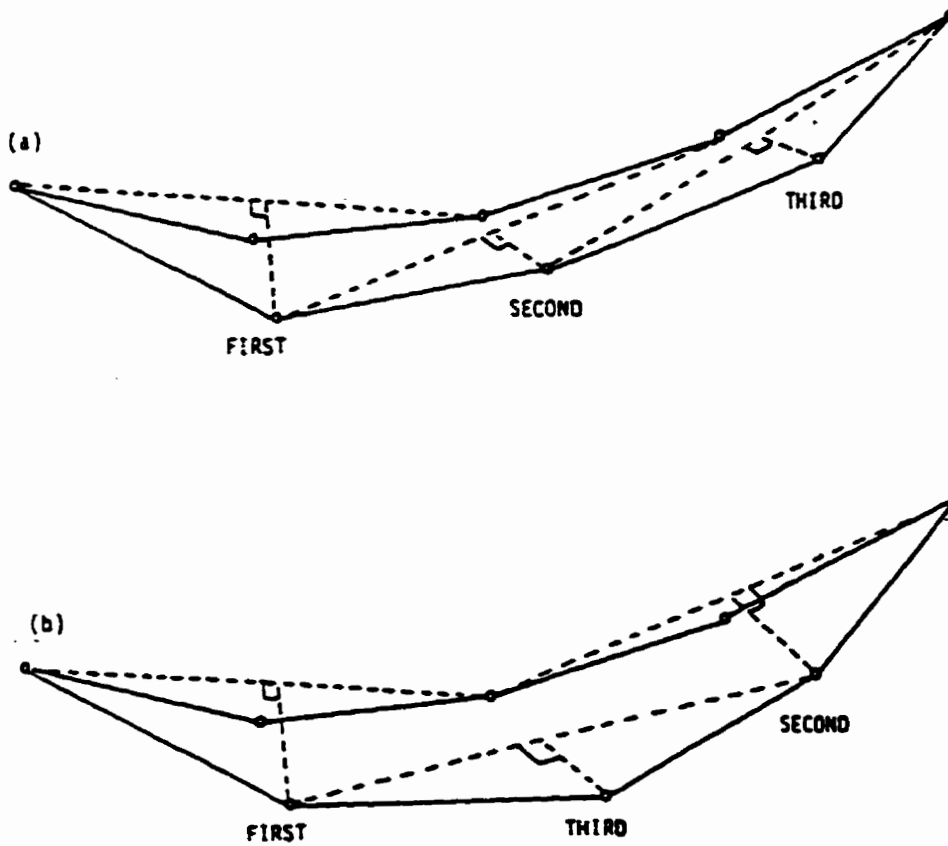


Figure 3-9: Two approaches to perturb ray paths (Um and Thurber, 1987).

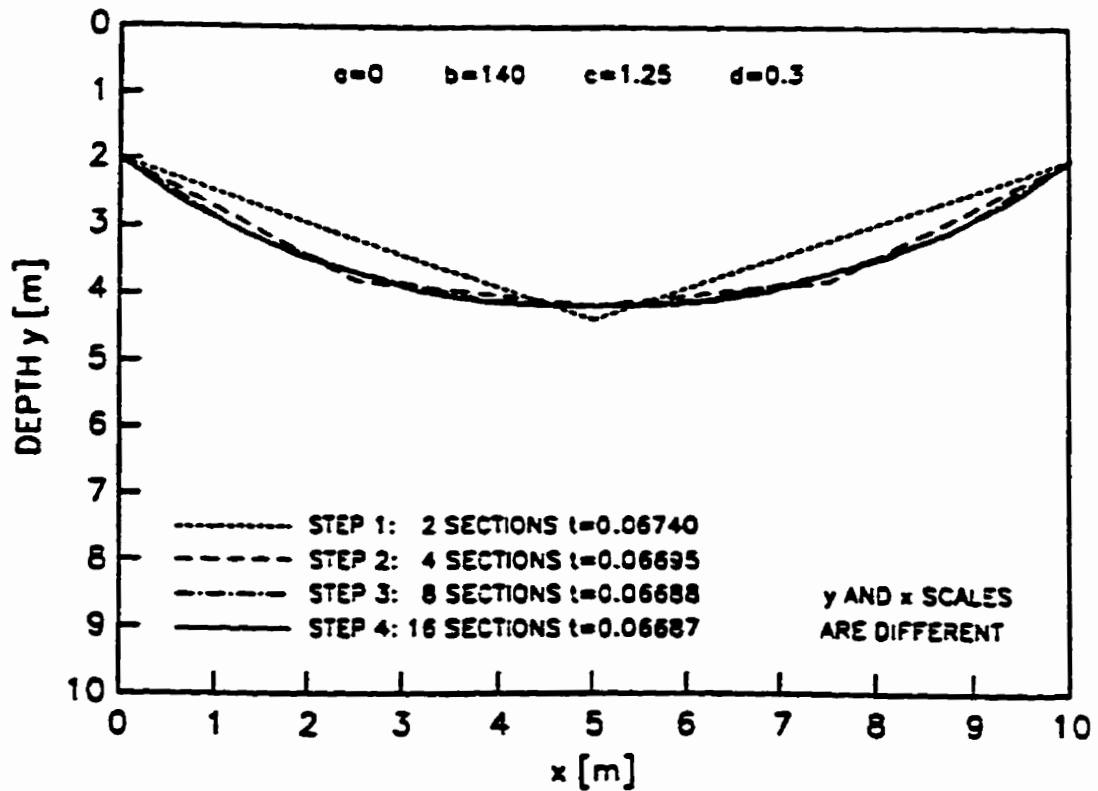


Figure 3-10: Perturbing the ray path by mid-point method (Santamarina and Cesare, 1994).

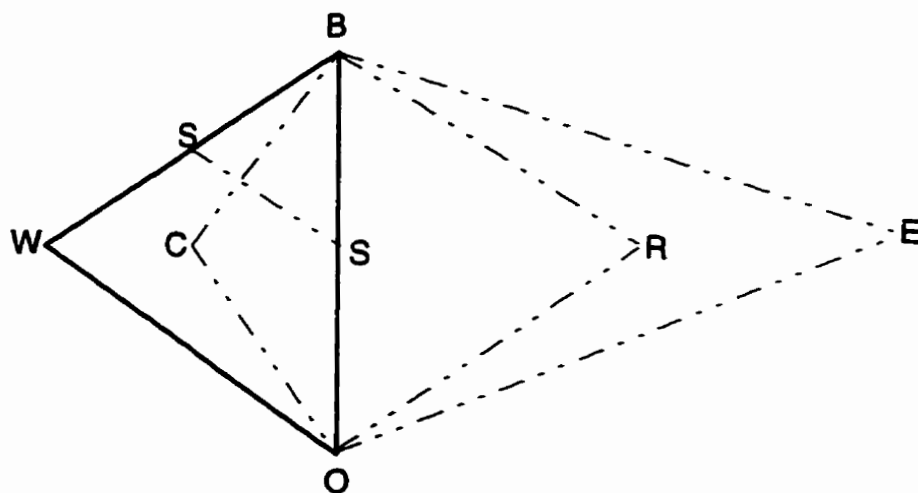


Figure 3-11: Two-dimensional simplex BWO illustrating the four mechanisms of movement: reflection (R), expansion (E), contraction (C), and shrinkage (S).

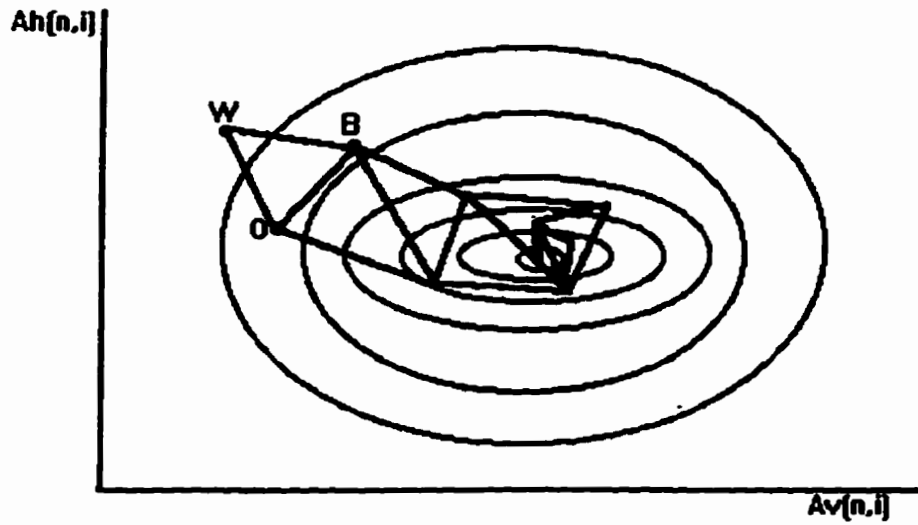


Figure 3-12: An example of the Simplex moving on the response surface contour plot.

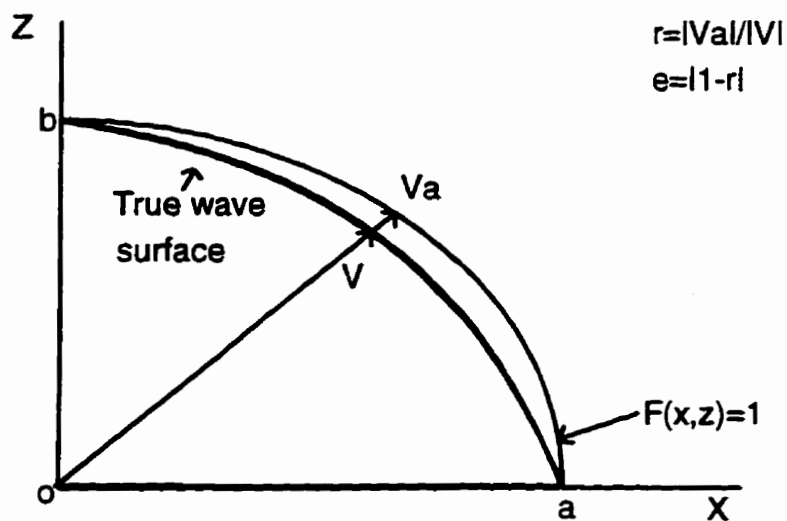


Figure 3-13: True wave surface and approximating wave surface F. For each direction of the ray; e is taken as indicative of goodness of fit (Stöckli, 1984).

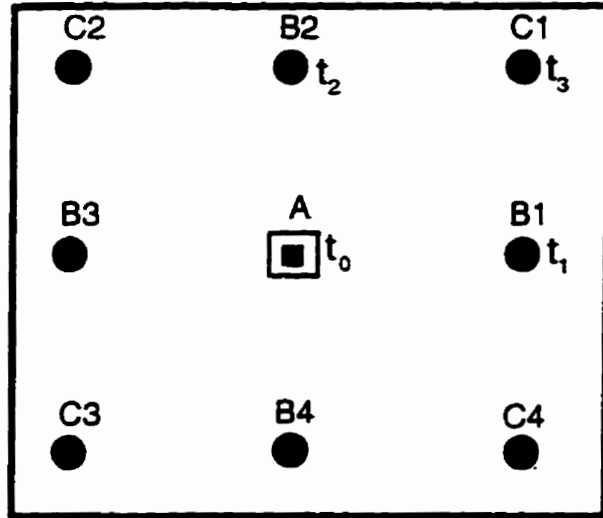


Figure 3-14: The source grid point A and the eight points in the ring surrounding point A (Vidale, 1988).

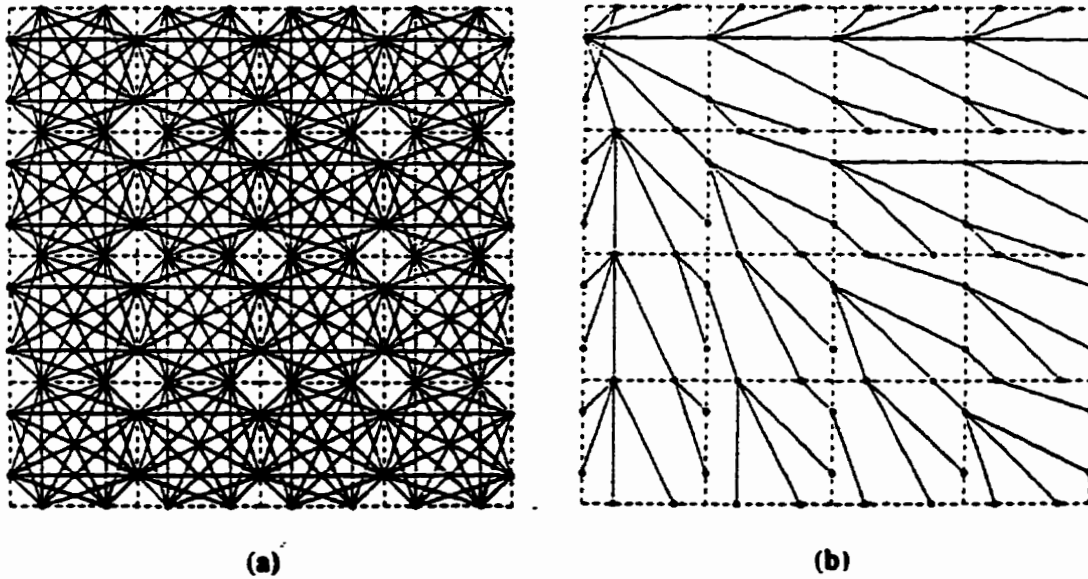


Figure 3-15: Cell organization of a network, (a) Dashed lines: cell boundaries. Black circles: nodes. Solid lines: connections. (b) Shortest path from one node to other nodes in a homogeneous model (Moser, 1991).

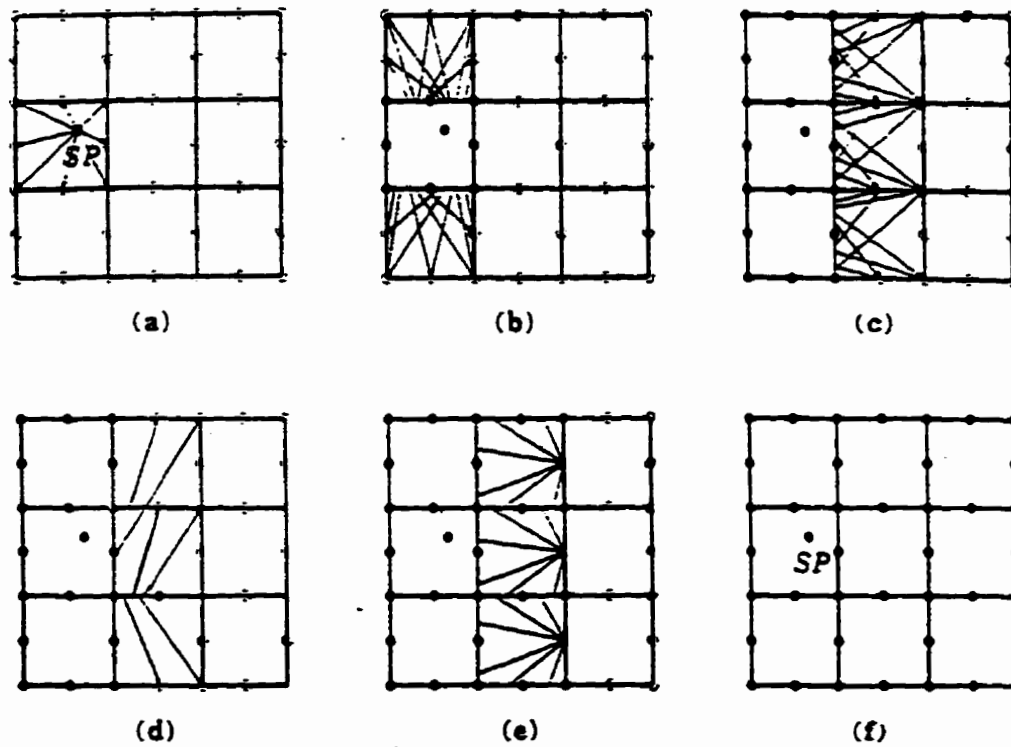


Figure 3-16: Forward process in the LTI method (Asakawa and Kawanaka, 1993).

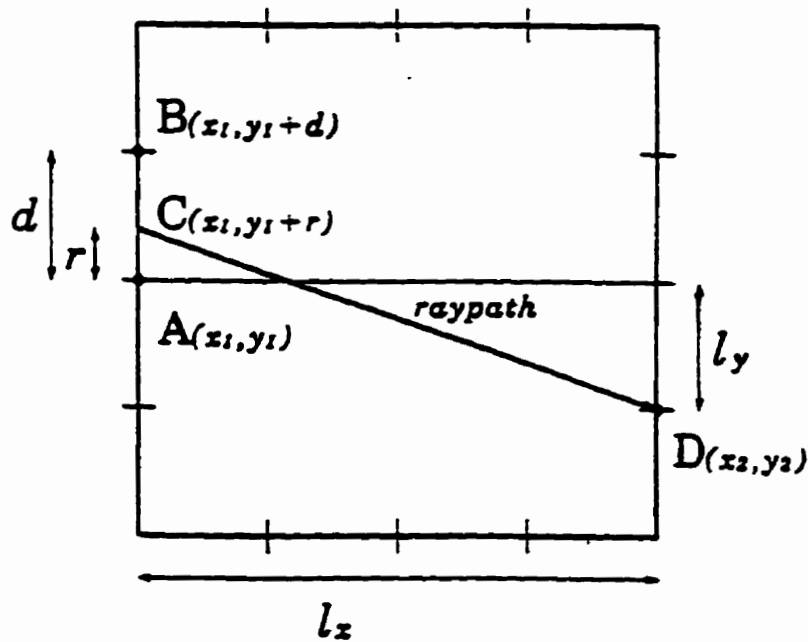


Figure 3-17: A ray path crosses segment AB at point C and reaches point D in a cell (Asakawa and Kawanaka, 1993).

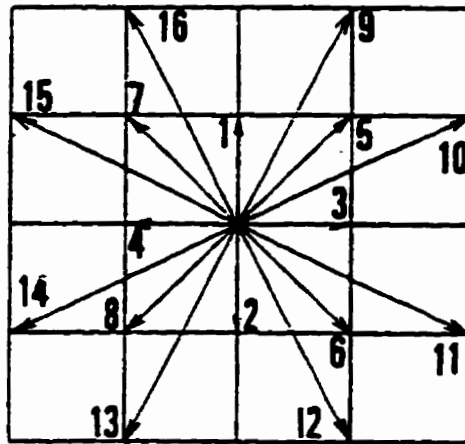


Figure 3-18: Rays from a seismic Huygens' source toward sixteen grid points (Sassa, 1989).

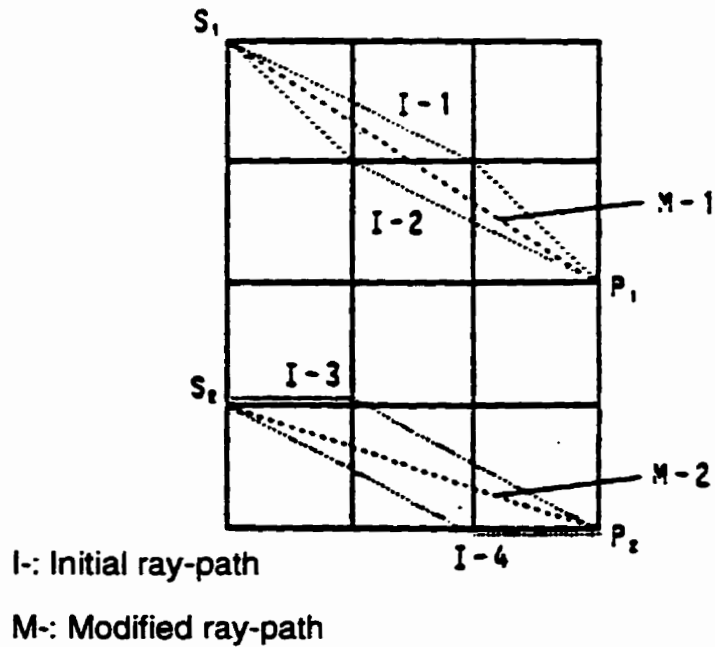


Figure 3-19: Example of initial and modified ray paths in Sassa's method (Sassa, 1989).

CHAPTER IV

SOFTWARE FOR CE-TOMOGRAPHIC STUDIES (DESIGN DECISIONS)

4.1 Introduction

A program for tomographic inversion was written as part of this study. The selected tomographic inversion methods are based on matrix analysis methods (Chapter 2). Ray bending and straight ray algorithms are included (refer to Chapter 3). The program is in structured form to facilitate future additions and modifications. This chapter starts with an overview of numerical issues involved in inversion and ray tracing algorithms. Design decisions are highlighted.

4.2 Numerical Issues in Inversion Algorithms

The inverse tomographic problem can be solved with several methods categorized as: (i) Iterative methods (ii) Transform methods, (iii) Matrix inversion methods, and (iv) other methods. The methods were reviewed in Chapter 2.

Iterative methods are not always stable in ill-conditioned problems. Transform methods are restricted to straight ray projections (space transformations could be invoked to generalize the solution to heterogeneous, anisotropic media). Matrix methods are versatile, computationally efficient, and robust. However, efficient storage and computation are required. Hybrid solutions can be

attempted to enhance the resolvability of inverted images (e.g., fuzzy logic pre-processing followed by regularization).

The coefficient matrix (L) is sparse. Storage and computation time can be decreased more than one order of magnitude when adequate computational techniques are used. In a dense $n \times n$ matrix, the order of computation complexity is $O(n^3)$ and $O(n^2)$ for storage. The application of direct methods with sparse matrix techniques requires $O(n^2)$ and $O(n^{-1.4})$, respectively (Golub & Van Loan, 1983). However, efficient iterative algorithms combined with sparse matrix techniques can reduce the order of computational complexity to $O(n^{1.3})$ and storage requirements to $O(n)$.

Consider a space discretized into equal numbers of columns and rows and tested in a cross-hole; the resulting matrix L contains $\approx 1.5\sqrt{n}$ non-zero elements in each row of n entries, e.g. if there are $n=20 \times 20$ pixels, the length of each row is 400 and only about 30 entries are non-zero. Adequate data structures can be very effective to avoid storage problems (see also Tallin and Santamarina, 1989).

4.3 Computational and Physical Issues in Ray Tracing

If ray bending takes place, ray paths depend on inverted pixel velocities, thus the tomographic problem becomes non-linear. If it is appropriate to consider propagation in terms of rays, ray bending can be taken into consideration in iterative algorithms and matrix methods. In this non-linear problem, ray paths depend on the velocity field. Thus, the matrix of travel lengths L_{ij} is not constant and must be recalculated with a digital ray-tracing algorithm as the field of velocity evolves during successive iterations or inversions. Ray tracing

algorithms assume Fermat's shortest time criterion (Santamarina and Gheshlaghi, 1995).

This section presents an attempt to compare the computational efficiency of ray tracing methods. It also provides some evidence of the accuracy needed in ray tracing to solve the inversion problem, within the context of other errors in CE-tomography.

4.3.1 Assumptions and Fundamental Cases

The computational time demand for ray tracing methods is based on the number of segmental travel time calculations. Discretize the medium into pixels (Figure 4-1) and assume that:

- The medium is divided into n rows and n columns. Therefore, the number of pixels is n^2 .
- Full cross-hole tomographic measurements are conducted: all rays are shot from a source to all receivers on the opposite side.
- Sources and receivers are located at the mid-height of pixels along vertical boundaries.
- Rays can cross from one pixel to its vertical or horizontal neighbor, but not directly to its diagonal neighbor.

Case 1: Straight Rays

Based on these assumptions, the total number of travel time calculations can be computed for the simplest case where straight rays are assumed. This is the lowest bound to all methods.

Table 4-1: Computation of total number of travel times, assuming straight rays.

Vertical Step	Number of rays	No. of seg. per ray	Tot. No. of segments
0 $\Delta y^{[i]}$	n	n	n^2
1 Δy	$2(n-1)$	$(n+1)$	$2(n^2-1^2)$
2 Δy	$2(n-2)$	$(n+2)$	$2(n^2-2^2)$
.	.	.	.
.	.	.	.
.	.	.	.
$(n-1) \Delta y^{[ii]}$	$2[n-(n-1)]$	$[n+(n-1)]$	$2[n^2-(n-1)^2]$
Total Number of Segmental Travel Times = $n^2[1+2(n-1)]-2[1^2+2^2+\dots+(n-1)^2]$			
[i] Horizontal ray, [ii] Most diagonal ray			

In Table 4-1, Δy is of one-pixel height. Mathgram 4-1 (case 1) shows a plot of the number of segmental travel time computations for the straight ray assumption (nttcs) as a function of n . Note that the trend can be approximated by n^3 function. The least squares fit results in the following approximate equation

$$\text{nttcs} \approx 1.33 n^3.$$

If the number of pixels is very large, the computation of accurate travel lengths loses relevance to the solution, and the Pythagorean computation can be reduced to "touched=1" and "not-touched=0". Such a method was proposed by Dines and Lytle (1979). A related optimized method can be found in Tallin and Santamarina (1992).

Case 2: Curved Rays

Assume that curved rays are concave and that they extend between the upper-most and lower-most positions of the source and receiver (Figure 4-2, rays #2

and #3). Apparently, such rays have the same number of segments and intersections as the corresponding straight rays (Figure 4-2, ray #1). However, the number of segments in horizontal rays is sensitive to the curvature of the ray (compare ray paths in Figure 4-2 versus the corresponding ray paths in Figure 4-3). This is true even when the ray is similar to path #3 in Figure 4-2, but when the curvature of the ray exceeds the new position of either source or receiver (e.g. path #4 in Figure 4-2 and curved path in Figure 4-3), two more segments are added to each ray for each additional row difference.

Assume that the number of segments is increased only in horizontal rays deflecting one pixel out of their positions. Then, each horizontal ray will have $(n+2)$ segments. All together, horizontal rays will involve $n(n+2)$ segmental travel time computations rather than n^2 . Thus, the total number of segmental travel time computations is increased by $2n$. Given that the process is of order n^3 , this additional number of computations can be disregarded (Mathgram 4-1, case 2).

One-Point Methods. The method introduced by Lytle and Dines (1980) is selected for analysis. In this method, the computation of a fourth-order Runge-Kutta method is based on the number of selected points during the ray tracing procedure (primary ray tracing assumes "point velocities" and interpolates values, rather than selecting rigid pixels boundaries). If a n step ray is assumed, to have a parameter comparable with other methods, the fourth-order Runge-Kutta method will require $4xn$ calculation for each ray to be traced (four evaluations are needed at each step, Forsythe *et al.*, 1977). Suppose that for each pair of source and receiver, the ray path is defined for m shooting angles. Then, the number of calculations needed for only primary ray tracing by this method is in the order of $4xmxn^3$ (see Mathgram 4-2). Final pixel values must still be computed (similar demand as curved rays). In addition, overhead calculations are required for determining shooting angles. This overhead

computation demand can not be defined by a specific number, and it can differ from one algorithm to another.

Some tricks may be implemented to decrease the amount of computation. For example, ray paths from a given source are computed for different shooting angles only once. Optimization for each receiver is based on interpolation between these primary paths.

In this case, there are: m primary paths (i.e., m shooting angles) and n interpolated paths (i.e., one for each receiver). Then, the problem for the n sources has the following level of computational demand: $n \times (m \text{ primary paths}) + 1.32n^3$ ntcs (as in curved rays) + additional overhead. The optimization overhead is proportional to the number of rays n^2 .

Two-Point Methods. In the Sine-Arc two-point method (Mathgram 4-3), the number of computations will be a factor (A) times the number of calculations needed for curved rays (Mathgram 4-1, Case 2). This factor is the number of Sine-Arc amplitudes which may be considered for each ray. Thus, the process remains n^3 . The optimization overhead is proportional to the number of rays, n^2 .

In the multiple segment two-point method by Santamarina and Cesare (1995), the number of segmental travel time calculations depends on the number of segments, degrees of freedom, and the sweeping area. In this case, every row in the range of sweeping outside the source and receiver position demands two more travel time calculations. Each node moved to minimize the travel time requires the re-evaluation of all segments on both sides of the node. Table 4-2 gives an estimate of the number of calculations for this method (refer to Figure 4-4): The overhead demand is proportional to the number of nodes times n^2 .

Table 4-2: An estimate of the number of calculations in multiple segmentation two-point method.

Nodes	No. of travel time calculations
0	$1.3xn^3$
1	$1.3x6n^3$
3	$1.3x15n^3$
7	$1.3x25n^3$

All two-point methods can be optimized by computing all rays from a given source simultaneously. In this case, the search space is reduced for each ray as it becomes constrained by its neighbors (two rays from a source never meet). Savings are proportional to n^3 (plus overhead) shifting curves parallel down toward the straight ray solution.

Whole-Field Methods. Two types of node patterns for whole-field methods are shown in Figure 4-5a&b. Both patterns have $\beta=24$ possible segments. In "case a", there are no connections along pixel boundaries. However in "case b", neighboring nodes can be connected.

The main point in this type of method is that if all cells are of equal geometry, lengths are computed for only one cell during the forward process:

$$\text{Total number of travel time calculations} = \beta n^2$$

but in reality, only β computations are necessary to obtain lengths

In the backward process, we assume that the time required for "if-statements" in these methods is similar to the computation time required for other arithmetic operations (multiplication, division, and exponentiation). In addition, the following assumptions for graph search algorithms are made: (1) do not check backward

at connections; (2) expand nodes on right vertical wall first, then those on horizontal boundaries (Figure 4-6); and (3) the search advances by columns.

Based on these assumptions, the number of connections in the pixels that contain the source (or receiver) is six. For the other pixels on that column the number of connections is twelve, and for the pixels in all other columns is twenty four (Figure 4-7). Therefore, the number of computations for a single source or receiver is

$$n \text{ rays: } [(nx12)-6]+(n-1)xn24=24n^2-12n-6$$

and for the total (n) sources and receivers is

$$n^2 \text{ rays: } nx\{[(nx12)-6]+(n-1)xn24\}=24n^3-12n^2-6n$$

Case 3 in Mathgram 4-2 shows the total number of computations vs. n for whole field methods.

4.3.2 Other Comments

- The density of overhead computations varies among methods and it may be a decisive factor (e.g. computation time required for determining shooting angles in one-point method).
- Two rays from a source never cross. Hence, one-point methods and two-point methods can be readily optimized by searching all rays from a given source at once. The reduction in computational demand is proportional to n^3 , shifting curves parallel towards the straight-ray case.

4.3.3 Accuracy in Travel-Time Measurements and Ray Tracing

Amplitudes of first arrivals may be smaller than the amplitudes of later arrivals

(This case has been often observed in our laboratory). If diffracted waves have noticeable amplitude, they can influence travel time observations, whereby late arriving diffracted waves can be chosen as first arrivals. Moser (1994) suggested that such problems can be solved by constrained shortest time paths, and showed that the effect is not as severe as indicated by Geoltarine and Brac (1993). He also argued that the mechanism that causes later arrivals to have larger amplitudes than first arrivals could be compensated by the wave-front healing effect so that amplitudes of first arrivals may not be as systematically smaller as predicted by Geoltarine and Brac (1993).

Figure 4-8 compares computed travel times by the multi-segment method and the closed-form solution for a vertically heterogeneous and anisotropic medium (Santamarina and Cesare, 1995). The accuracy is striking, at least for this simple case of continuous velocity fields.

Significant deviations in ray path can often imply only minor differences in travel time, e.g., compare the time along a straight path between two points with respect to the time along a bi-linear path (Figure 4-9). Thus, one must question the accuracy needed in ray tracing algorithms, not for time prediction, but for the computation of pixel travel lengths in L . In order to study this effect, a central high velocity anomaly simulated case was considered (Figure 4-10). The test method follows: (1) the vector of travel times t_{opt} and the matrix of lengths L_{opt} are determined for optimal travel paths (wide scanning with small step), (2) alternative paths are selected by restricting the scanning step in the ray tracing algorithm and corresponding times are computed, L' and t' , (3) the image is inverted in each case and the velocity vector is obtained for the optimal case and other cases, V_{opt} and V' , and (4) the error in path, time, and velocity are computed.

Two error norms were used, the sum of absolute values (Equation 4-1) and the sum of squared values, producing similar trends.

$$AAE\% = \frac{\sum_{p \text{ pixels}} |V_i^{\text{real}} - V_i^{\text{inv}}|}{m} \frac{1}{V_{\text{ave}}} * 100 \quad (4-1)$$

Figure 4-11a shows that the average absolute error AAE in pixel travel time computed with rays of different curvature is related to the AAE in travel length per pixel. However, only a 1% error in time relates to an average 4-pixel widths difference in travel length per pixel (400%); given that the average travel length per pixel is 20 pixel widths, the percent average error is 4/20=20%. Figures 4-11b&c show that the error in pixel velocities can be justified as a result of error in measurement or error in ray paths, i.e., ray model.

It can be concluded that while more accurate travel paths can improve the inverted image, the demand on accurate ray paths must not exceed measurement accuracy on travel times, which is usually about 1%.

4.4 WATOM-I: General Approach

The main structure of the Waterloo Tomographic software (WATOM-I) is based on matrix inversion solutions, using sparse matrix algorithms. Straight rays and Sine-Arc are two ray tracing possibilities in version-I.

4.4.1 Ray Tracing

Encoded ray tracing algorithms allow either straight rays or two-point Sine-Arc rays. The Sine-Arc ray path deviates from the straight ray path of length L as

prescribed by a Sine-Arc with wavelength $2L$. The parameter being optimized is the amplitude of the sine that renders the minimum integral time. The Sine-Arc method is fast, precise for a wide range of problems, and it enforces some smoothness to the solution. The region scanned during the search for minimum time ranges from five pixels above to five pixels below the straight path that connects the source to the receiver. The scanning step is " $0.2 \times (\text{pixel height})$ ". Shorter time paths outside this region would be greatly attenuated and would be probably overlooked while picking first arrivals (Geoltarine and Brac, 1993; Laboratory observations in the Wave-Geomeia Laboratory, University of Waterloo). Only one parameter is optimized for the full ray.

4.4.2 Matrix Inversion

Direct matrix inversion techniques are usually not employed because of data storage and computation time requirements. However, L-matrices are highly sparse: the number of non-zero elements is about the number of pixels across the discretized space. The sparsity of matrices involved in tomographic problems enables us to employ efficient storage and solvers. If iterative methods are employed, acceleration can be used to increase the rate of convergence.

Data Structures. The *ia-ja* data structure for a $n \times m$ matrix with N non-zero entries needs:

- A single subscript array (length n), which is used to store all non-zero elements of the coefficient matrix.
- An index array (length $n+1$) to store the location of the starting point of each row.
- An index array (length n) to store the column location of each non-zero element of matrix L .

Given the following sparse matrix L,

$$\begin{bmatrix} 5 & 0 & 0 & 1 & 3 \\ 9 & 8 & 0 & 0 & 1 \\ 0 & 0 & 6 & 2 & 0 \\ 0 & 7 & 7 & 5 & 0 \\ 0 & 0 & 8 & 4 & 4 \end{bmatrix} \quad (4-2)$$

the arrays in the *ia-ja* representation are:

- **a** = (5 1 3 9 8 1 6 2 7 7 5 8 4 4)
- **ia** = (1 4 7 9 12 15)
- **ja** = (1 4 5 1 2 5 3 4 2 3 4 3 4 5).

A row-index data structure is also employed in the WATOM-I program and differs from the *ia-ja* data structure. Elements in the row-index data structure are:

- An array of length $n+1$ which includes non-zero elements in matrix L.
- An index array of length $n+1$ which contains the locations of non-zero and diagonal elements.

For the previous example, these two arrays are:

- **sa**=(5 8 6 5 4 x 1 3 9 1 2 7 7 8 4)
- **ija**=(7 9 11 12 14 16 4 5 1 5 4 2 3 3 4).

where x is an arbitrary number.

Link-lists can also be used as a data structure. The main advantage of link-lists as compared to the *ia-ja* and row-index data structures is the ability to insert a value by modifying just a single row. This advantage results from storing pointers which show the location of the next value in the main array (which is used to store non-zero values). The location of the first value can be shown by a header variable, and there is a terminator which gives the location of the last value.

Inversion: Conjugate Gradient. If the coefficient matrix is symmetric and positive-definite, then, the conjugate gradient method is a very efficient inversion method.

Regularization and damped least squares methods are implemented in WATOM-I. Since matrices $L^T L$, $R^T R$, and I are square, symmetric, and positive-definite, the conjugate gradient method is used (Note that regularization and damped least squares methods produce coefficient matrices with different structures).

4.4.3 WATOM-I: Structure

WATOM-I runs in a workstation. The dimensions of arrays are not strictly restricted in the workstation environment. However, they are clearly subjected to size limitations in DOS-based systems. Two parameters are pre-defined in WATOM-I to control convergence: (i) **Maxiter** fixes the maximum number of iterations, and (ii) **Contol** sets the convergence tolerance or maximum tolerable error.

Schematic flowcharts of steps in L and R matrix entries computation are given in Appendix C. A global flowchart gives the WATOM-I algorithm (Appendix C).

Input-Output

Input parameters are encoded in an arbitrarily named file (name must not exceed twelve characters including the three letters for file name extension). This text file is prepared in advance using spread sheet programs or text editors. The format of the input file is (an example of the data file is given in Figure 4-12):

- **First and second lines: header lines for comments and descriptions, file specification, and other necessary information. There is no restriction on the format of these two lines. The total length of each line should be less than 72 characters.**
- **Parallel lines of data in eight columns, separated by one or more spaces. The first column is a line number, or ray number. The next seven columns include source coordinates (Xs, Ys, Zs), receiver coordinates (Xr, Yr, Zr) and travel time for source-receiver pair. Note that the source and the receiver coordinates are given in three dimensions even though this version of the program assumes a two-dimensional inversion plane (X-Z). Therefore, the "Y" dimension or second coordinate should be zero in all cases.**
- **Sources and receivers may be located anywhere in the region.**

All other required information is interactively requested. A typical input dialog follows:

1. **"Input No. of rays and pixels .. =====>:"**
"No. of rays" is the number of lines of data in the data file. "No of pixels" is the number of discrete elements in the selected mesh (number of unknowns).
2. **"Input No. of rows and columns ... =====>:"**
"No of rows" is the number of pixels in the vertical direction of the selected mesh. "No of columns" is the number of pixels in the horizontal direction of the selected mesh.
3. **"Width and Height of the region .. =====>:"**
These are the dimensions of the region to be inverted (in the same units of length). The inverted velocity is in units of these lengths over the unit of input travel times.

4. "(R)egularization or (D)LSQR ... =====>:"

The inversion problem can be solved by regularization or damped least squares. Characters R/r or D/d allow the user to select between these two options.

Depending on the answer to the previous question, one of the following questions will be asked (5a or 5b).

5a. "Input Regularization coefficient value =====>:"

The smoothness of the inverted image is proportional to this parameter. The "best value" depends on the amount of noise in the given data. Thus, this parameter is a variable to be parametrically studied by the user.

5b. "Input DLSQR coefficient value =====>:"

This is the coefficient to the identity matrix for the damped least squares solution and balances least squares and solution norm. It is case specific. Thus, this parameter is a variable to be parametrically studied by the user.

6. "Name of input data file =====>:"

The structure of this ASCII file was previously described.

7. "(S)traight rays or (C)urved rays =====>:"

Straight ray tracing (choose "S" or "s"), or curved ray tracing ("C" or "c") can be selected. Curved rays use the Sine-Arc method.

8. "Name of the initial velocity file ... =====>:"

If "curved rays" is selected, a velocity field should be input. This velocity field can be the inverted image from the last inversion (obtained with the same set of travel times), or a velocity pattern based on prior information about the region. This is an ASCII file. Arbitrary or computed pixel values for this file

can be given in a sequence of numbers in (a) row(s) or in a column. One or more spaces or a comma should be used to separate two successive numbers. A typical file is given in Figure 4-13.

If "straight paths" are assumed, the average velocity of the field should be input. This value is used as an initial condition by WATOM-I. Therefore, not only the rate of convergence but also the inverted image can be improved by a proper input of average velocity.

A typical output of pixel velocities is presented in Figure 4-14. This output can be imaged by specialized display softwares, as a contour map, pixel map, etc. A second output file (Figure 4-15) gives: No. of iterations (before fulfilling an specific RMS value criterion), RMS value in each iteration, and final maximum error (gives the closeness to the given data).

Appendix D includes the Waterloo Tomographic software (WATOM-I).

4.5 Summary and Conclusions

The coefficient matrix (L) is large and sparse. In a dense $n \times n$ matrix, the order of computation complexity is $O(n^3)$ and $O(n^2)$ for storage. However, efficient iterative algorithms combined with sparse matrix techniques can reduce the order of computational complexity to $O(n^{1.3})$ and storage requirement to $O(n)$.

Travel time is relatively insensitive to variations in ray path. Often, most computational efforts in ray tracing are spent in optimizing travel times to the point that the estimated time error becomes significantly lower than measurement errors. However, optimization alters ray paths and the length that

rays traverse different cells. This affects tomographic reconstruction. The significance of this effect was evaluated with simulated data to facilitate comparison. It was shown that while more accurate travel paths can improve the inverted image, the accuracy in ray paths does not need to exceed measurement accuracy on travel times, which is usually about 1% (at best).

A program for tomographic inversion was written as part of this study. The selected tomographic inversion methods are based on matrix analyses. Damped Least Squares and Regularization solutions have been encoded. Straight rays and optimal Sine-Arc algorithms were implemented for ray tracing in the case of linear and non-linear problems.

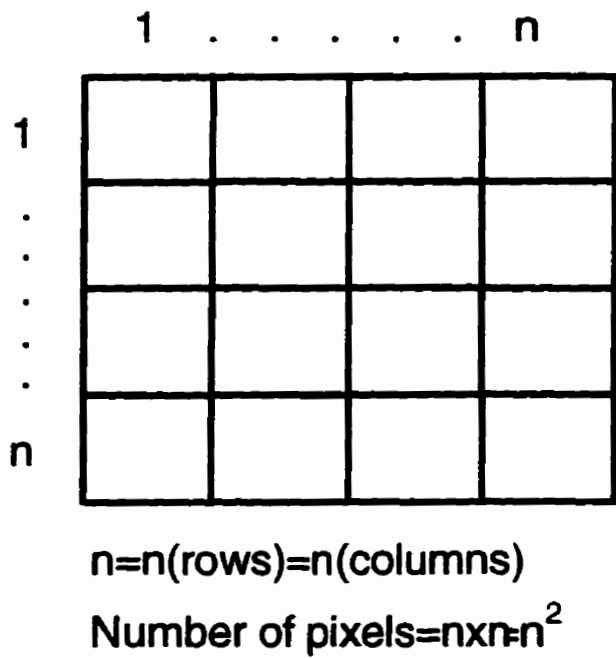


Figure 4-1: A region divided by 4x4 pixels.

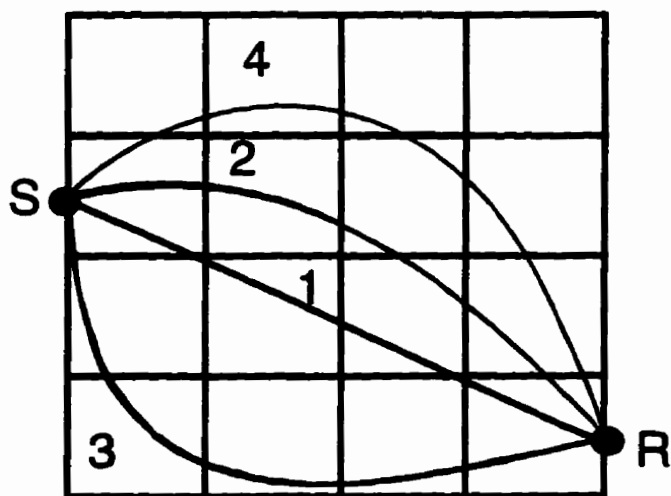


Figure 4-2: A source and receiver pair connected by different paths.

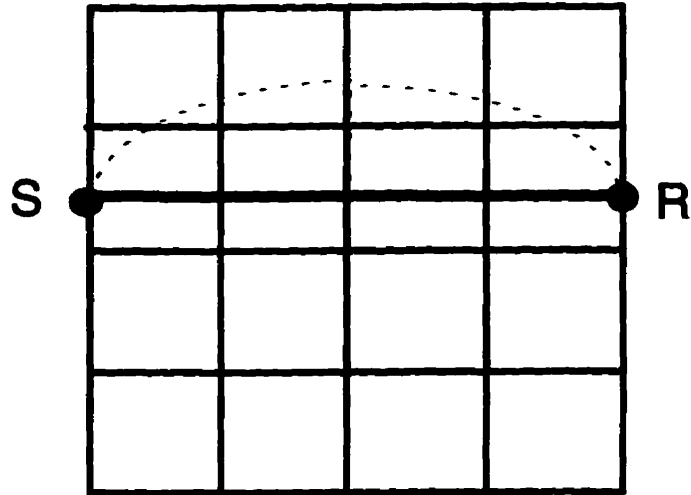


Figure 4-3: A source and receiver pair connected by the straight path and a curved path.

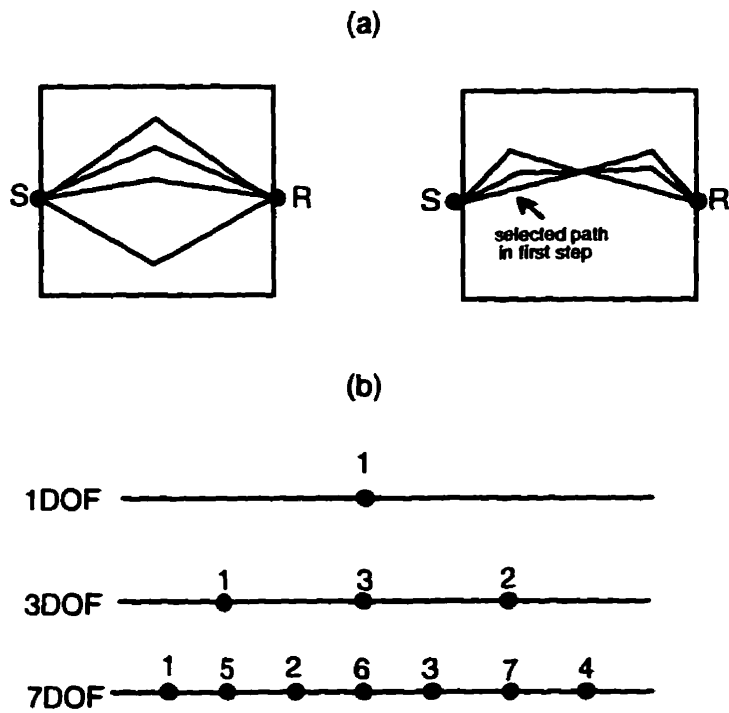


Figure 4-4: Ray paths in a Multi-Segment method. (a) Cases when path has one and two degrees of freedom. (b) Order of moving nodes in a path.

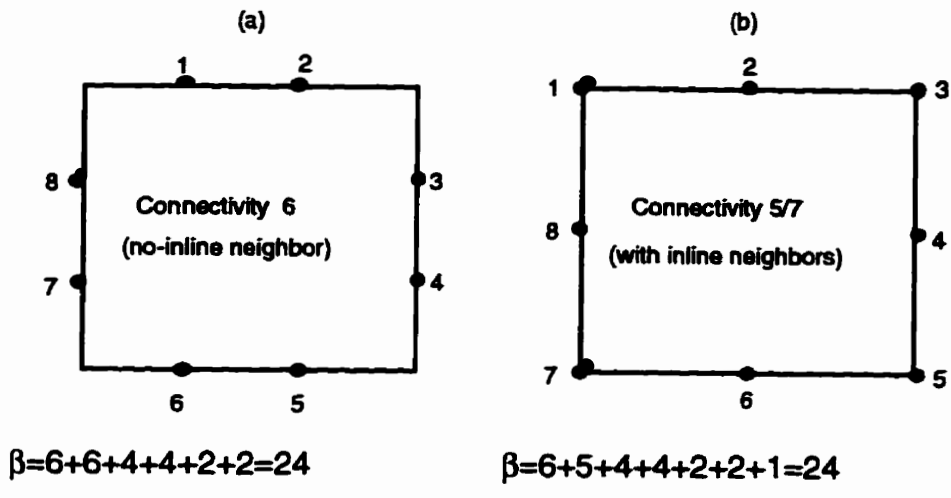


Figure 4-5: Number of connections per pixel for two selected whole-field methods.

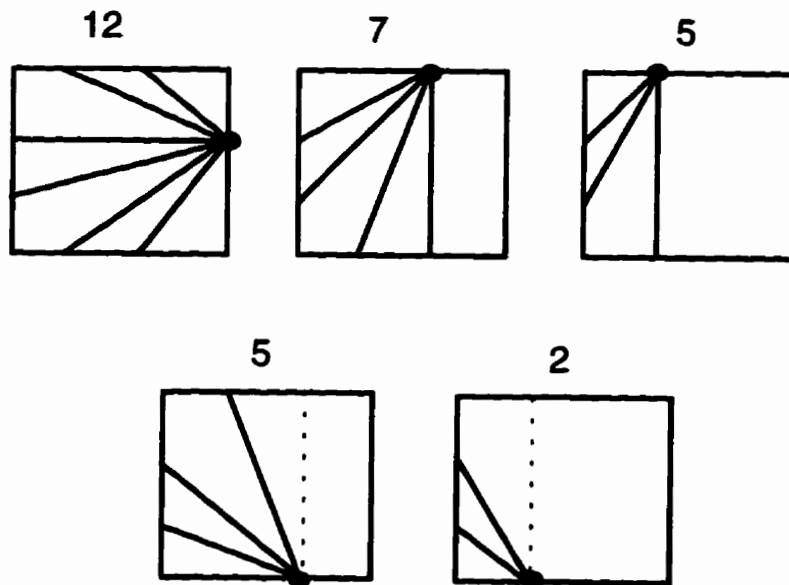


Figure 4-6: Path connections from each node to the other nodes in a pixel. The number on top of each pixel shows the number of connections.

24	24	24	12
24	24	24	12
24	24	24	6
24	24	24	12

● R

Figure 4-7: Number of connections in each pixel for a receiver.

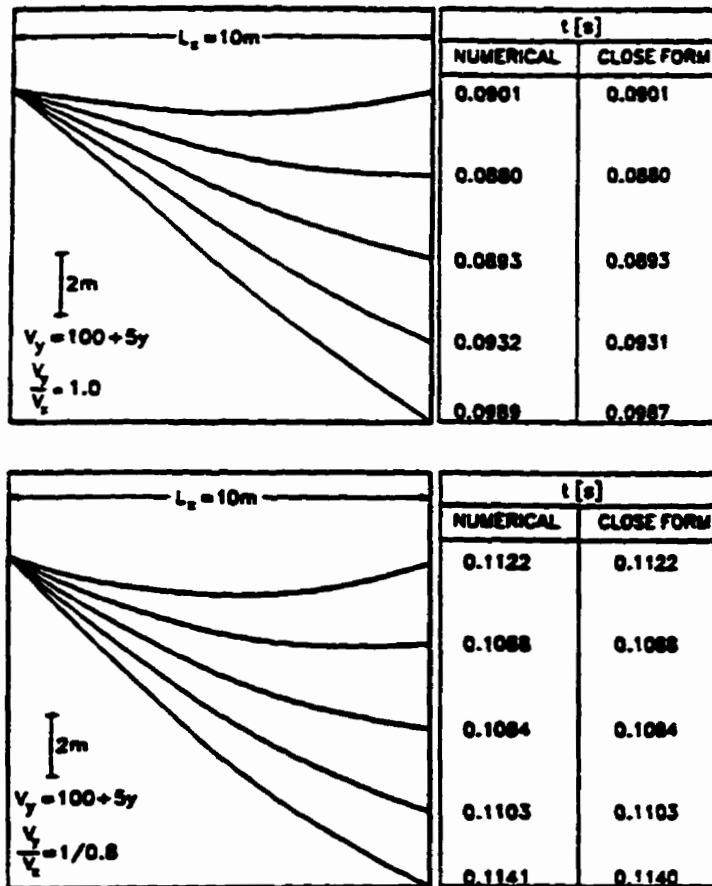


Figure 4-8: A comparison between the calculated travel times by multi-segments method and the corresponding close form solution (Santamarina and Cesare, 1994).

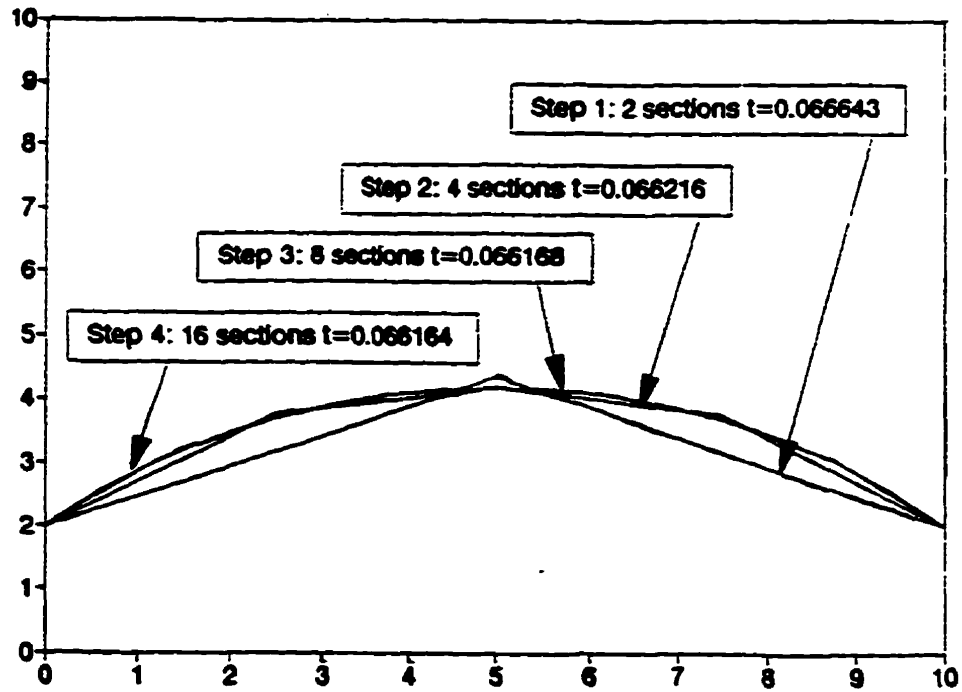


Figure 4-9: Travel time along different paths (Santamarina and Cesare 1992).

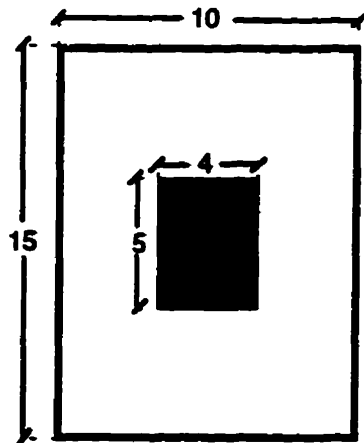
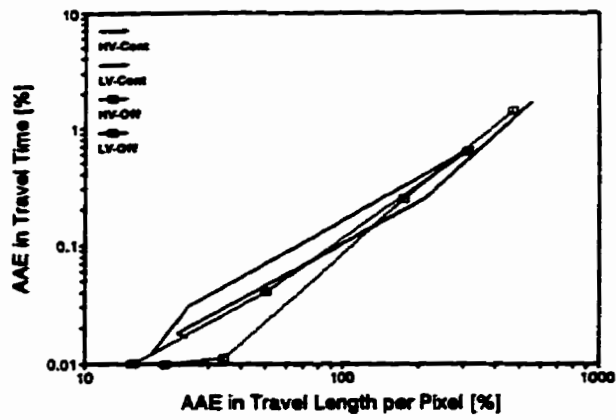
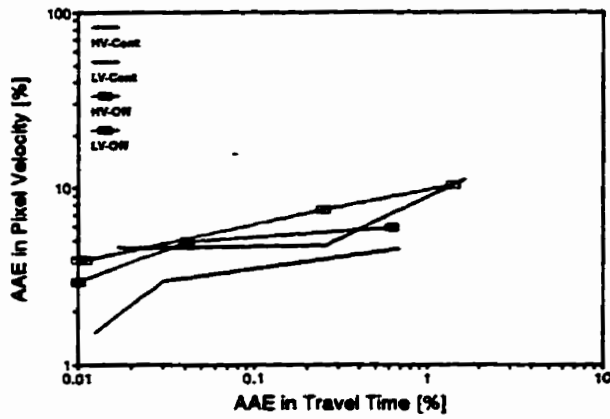


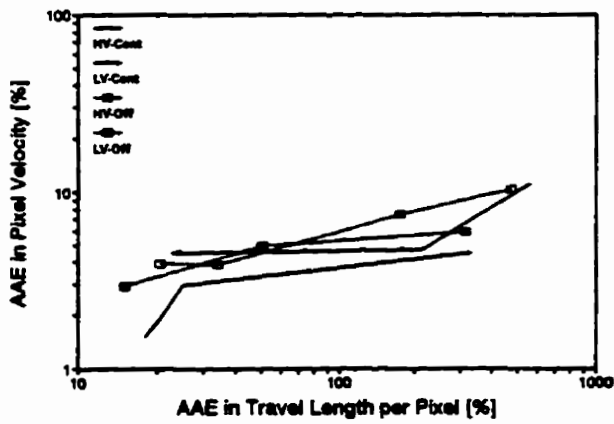
Figure 4-10: Simulated model, high velocity anomaly at center.



(a)



(b)



(c)

Figure 4-11: Image quality versus the accuracy in travel time measure and ray tracing.

Balloon data. Units in ft, ms.

#/256	Source (x,y,z)			Receiver (x,y,z)			Travel time
0	0.0	0.0	5.2501	59.50	0.0	5.2500	4.41
1	0.0	0.0	5.2501	59.50	0.0	8.5000	4.43
2	0.0	0.0	5.2501	59.50	0.0	11.750	4.44
3	0.0	0.0	5.2501	59.50	0.0	15.000	4.48
4	0.0	0.0	5.2501	59.50	0.0	18.250	4.52
5	0.0	0.0	5.2501	59.50	0.0	21.500	4.58
6	0.0	0.0	5.2501	59.50	0.0	24.750	4.63
7	0.0	0.0	5.2501	59.50	0.0	28.000	4.66
8	0.0	0.0	5.2501	59.50	0.0	31.250	4.71
9	0.0	0.0	5.2501	59.50	0.0	34.500	4.76
10	0.0	0.0	5.2501	59.50	0.0	37.750	4.85
11	0.0	0.0	5.2501	59.50	0.0	41.000	4.92
12	0.0	0.0	5.2501	59.50	0.0	44.250	5.05
13	0.0	0.0	5.2501	59.50	0.0	47.500	5.15
14	0.0	0.0	5.2501	59.50	0.0	50.750	5.32
15	0.0	0.0	5.2501	59.50	0.0	54.000	5.44

Figure 4-12: Data file for one source and sixteen receivers placed in two parallel boreholes separated at 59.5 (m) distance.

1.,1.,1.,1.,1.,1.,1.,1.,1.,1.
1.,1.,1.,1.,1.,1.,1.,1.,1.,1.
1.,1.,1.,1.,1.,1.,1.,1.,1.,1.
1.,1.,1.,1.,1.,1.,1.,1.,1.,1.
1.,1.,1.,1.,1.,1.,1.,1.,1.,1.
1.,1.,1.,1.,1.,1.,1.,1.,1.,1.
1.,1.,1.,1.,1.,1.

Figure 4-13: Typical input velocity file. Assuming a homogeneous region divided into 66 pixels with same velocities equal to 1..

v(1)= 3.44
v(2)= 3.32
v(3)= 3.43
v(4)= 3.55
v(5)= 3.54
v(6)= 3.53
v(7)= 3.55
v(8)= 3.42
v(9)= 3.43

Figure 4-14: Example of a section of a velocity output file.

iter = 1 rms = 0.573254324408763851E-12
iter = 2 rms = 0.797918658182052098E-25
iter = 3 rms = 0.901146719950356492E-39
iter = 4 rms = 0.558238485838429981E-52
iter = 5 rms = 0.376780910927233054E-65
iter = 6 rms = 0.248253025017300200E-78
iter = 7 rms = 0.190678642189774752E-91
iter = 8 rms = 0.230596113047614409E-104
iter = 9 rms = 0.142712113588909162E-117
iter = 10 rms = 0.304794942904023085E-130
iter = 11 rms = 0.202263862556677051E-143
iter = 12 rms = 0.429720579581301554E-156
max error = 1.65598720952372580

Figure 4-15: Example of the inversion performance output file.

Mathgram 4-1: Computational demand (straight and curved rays)

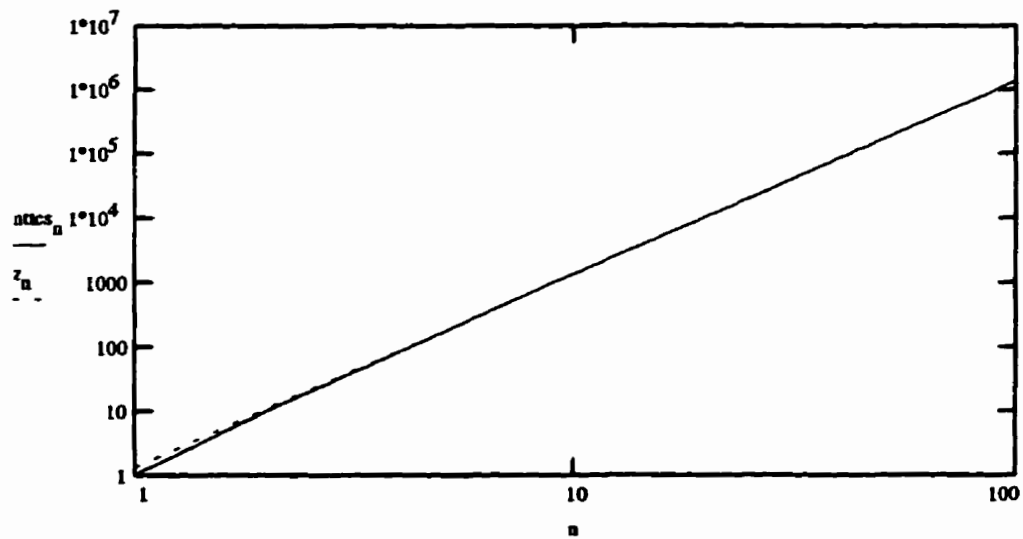
Case 1: Straight Rays

$N := 100$

$n := 1..N$

$$ntcs_n := n^2 \cdot (1 + 2 \cdot (n - 1)) - 2 \cdot \sum_{i=1}^{n-1} i^2 \qquad ntcs_1 := 1$$

approximation: $z_n := 1.33 \cdot n^3$

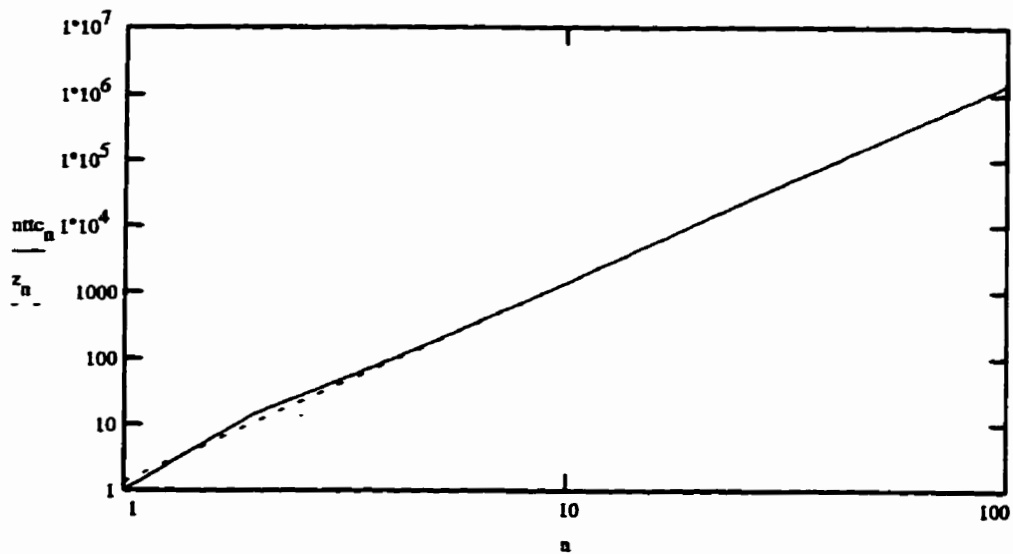


Computational demand for straight ray assumption (medium divided into $n \times n$ pixels with n sources and n receivers).

Case 2: Curved rays (one pixel curvature on horizontal rays)

$$ntc_n := n^2 \cdot (1 + 2 \cdot (n - 1)) - 2 \cdot \sum_{i=1}^{n-1} i^2 + 2 \cdot n \quad ntc_1 := 1$$

approximation: $z_n := 1.33 \cdot n^3$



Computational demand for curved ray assumption (medium divided into $n \times n$ pixels with n sources and n receivers).

Mathgram 4-2: Computational demand for ray tracing methods

Parameters:

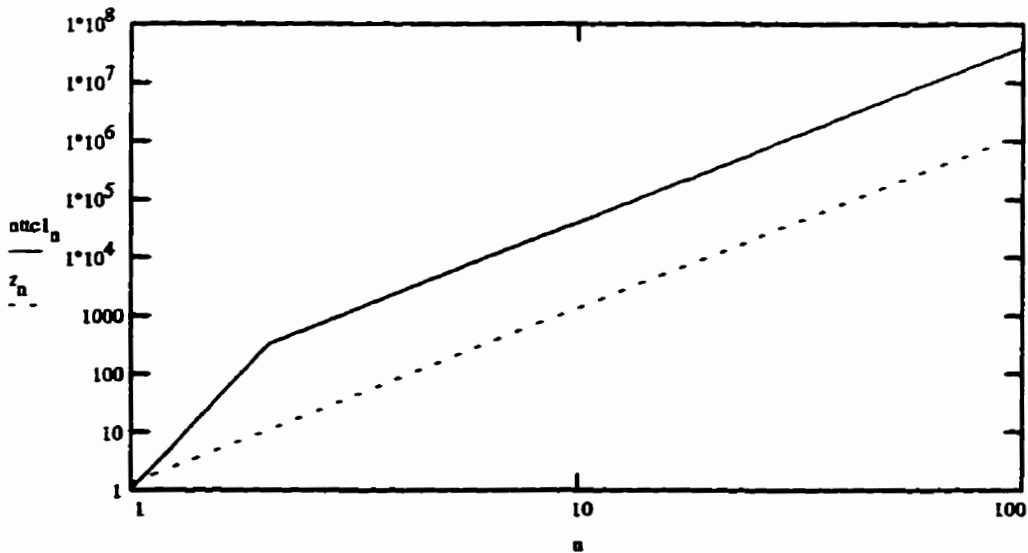
$N := 100$ $n := 1..N$

Approximation: $z_n := 1.33 \cdot n^3$

Case 1: One-Point Methods

Number of trial shots: $m := 10$

$nttc1_n := 4 \cdot m \cdot n^3$ $nttc1_1 := 1$



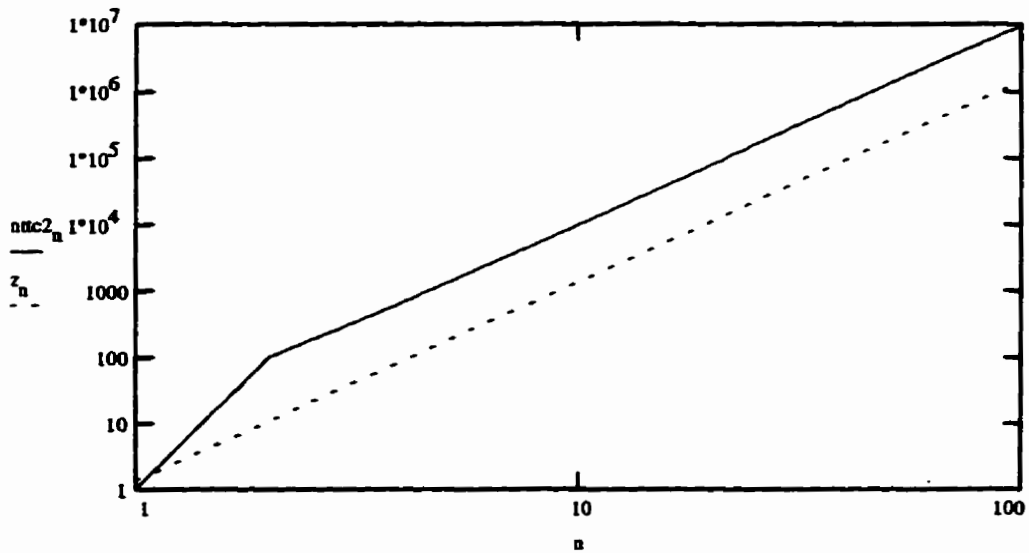
Approximate computational demand for typical One-Point method (medium divided into $n \times n$ pixels with n sources and n receivers).

Case 2a: Two-Point methods (Sine-Arc method)

number of searched paths: $A := 7$

$$nttc2_n := A \cdot \left[n^2 \cdot (1 + 2 \cdot (n - 1)) - 2 \cdot \sum_{i=1}^{n-1} i^2 + 2 \cdot n \right] \quad nttc2_1 := 1$$

approximation: $z_n := 1.33 \cdot n^3$



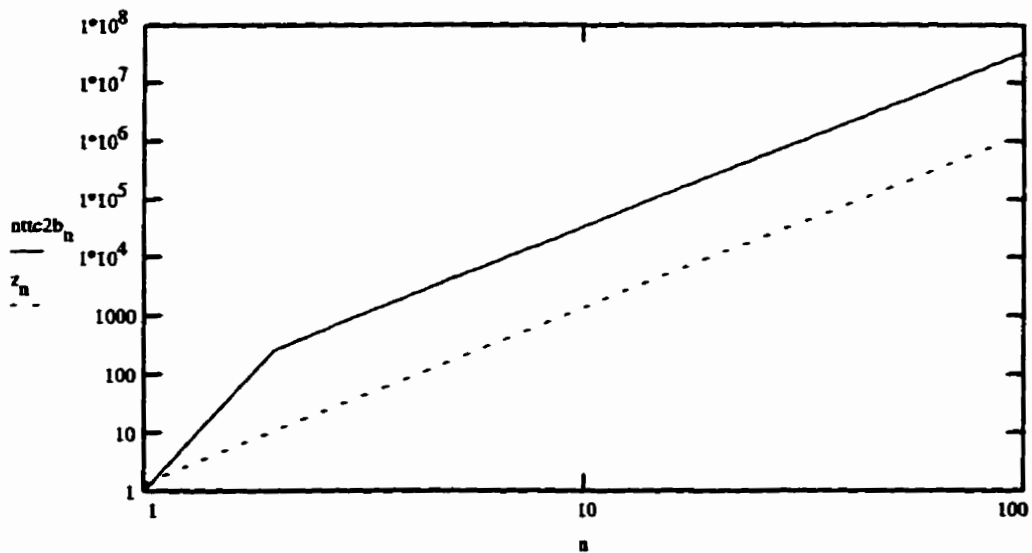
Approximate computational demand for Sine-Arc Two-Point ray tracing method (medium divided into $n \times n$ pixels with n sources and n receivers).

Case 2b: Two-Point methods (Multi-segments method)

number of searched paths: $A := 25$

$$nttc2b_n := A \cdot \left[n^2 \cdot (1 + 2 \cdot (n - 1)) - 2 \cdot \sum_{i=1}^{n-1} i^2 \right] \quad nttc2b_1 := 1$$

approximation: $z_n := 1.33 \cdot n^3$



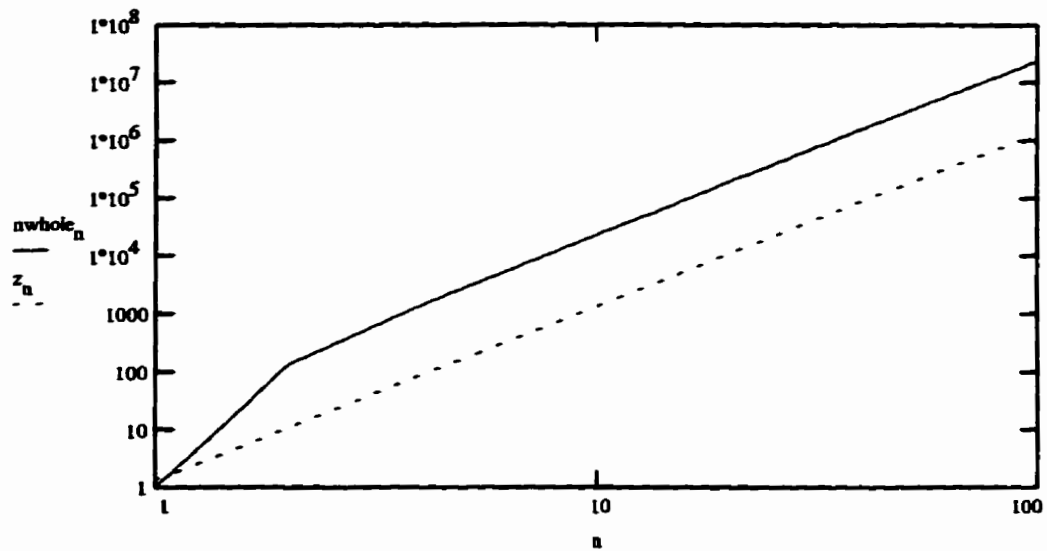
Approximate computational demand for Multi-segment Two-Point method for seven degrees of freedom (medium divided into $n \times n$ pixels with n sources and n receivers).

Case 3: Whole field methods

$$n_{\text{whole}_n} := n \cdot (24 \cdot n^2 - 12 \cdot n - 6)$$

$$n_{\text{whole}_1} := 1$$

approximation: $z_n := 1.33 \cdot n^3$



Approximate computational demand for Whole-Field methods (medium divided into $n \times n$ pixels with n sources and n receivers).

Mathgram 4-3: Sine-Arc Two-Point Method

Parameters:

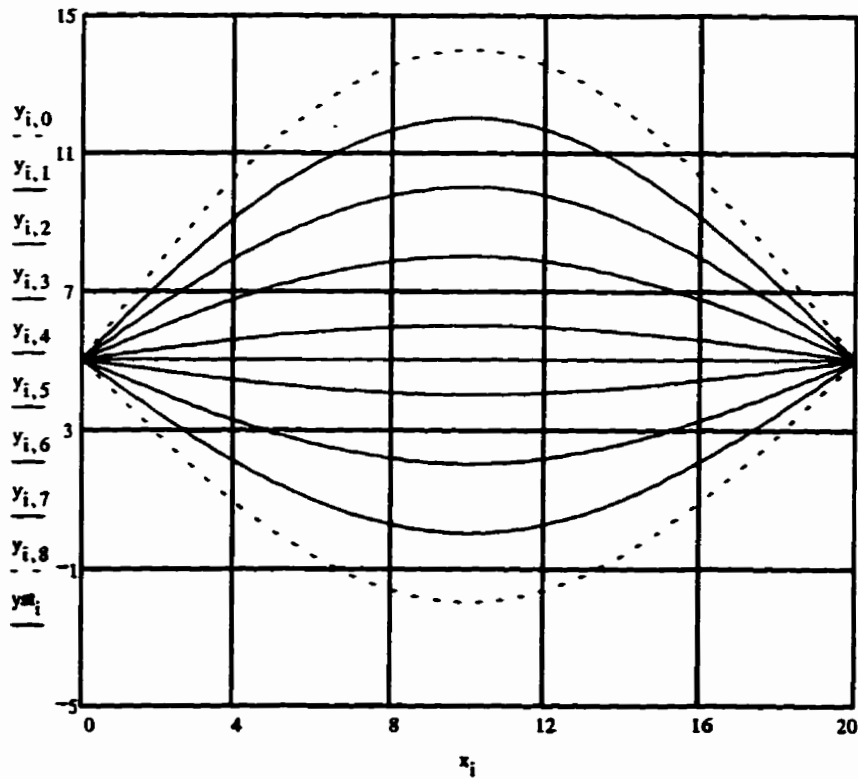
$$L := 20 \quad i := 0..100 \quad j := 0..8$$

$$x_i := \frac{i \cdot L}{100} \quad A_j := (j - 4) \cdot 2 + 1.$$

Case 1:

$$y_s := 5 \quad y_r := 5$$

$$y_{i,j} := y_s + x_i \frac{y_r - y_s}{x_{100} - x_1} + \left[A_j \cdot \sin \left[\frac{\pi \cdot (x_i)}{L} \right] \right] \quad y_{st_i} := y_s + x_i \frac{y_r - y_s}{x_{100} - x_1}$$

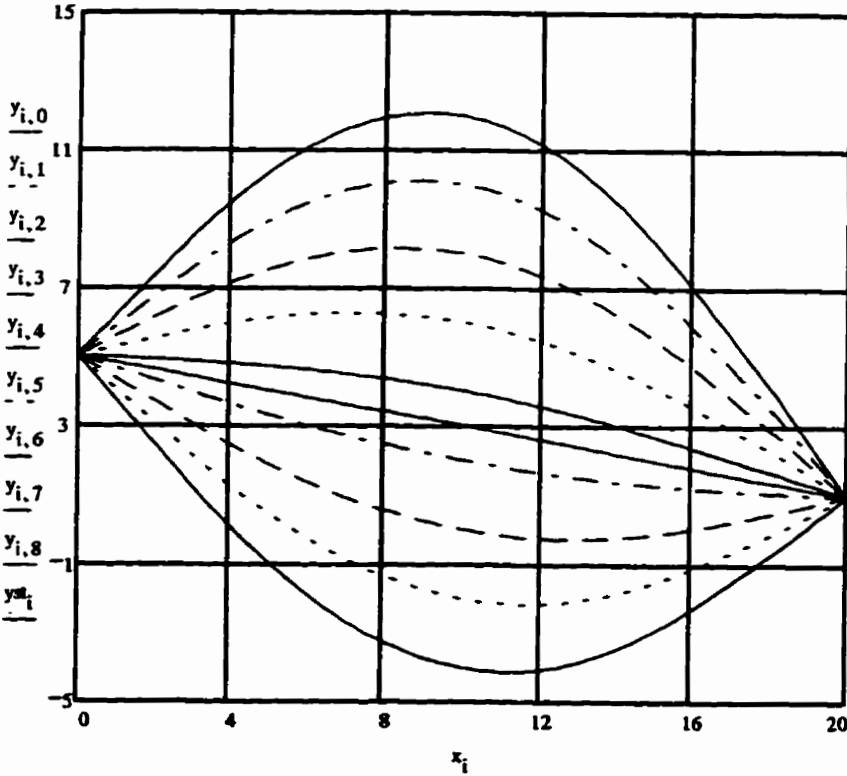


Sin-Arc paths for the case when source and receiver are at the same level.

Case 2:

Source and Receiver locations: $y_s := 5$ $y_r := 1$

$$y_{i,j} := y_s + x_i \frac{y_r - y_s}{x_{100} - x_1} + \left[A_j \cdot \sin \left[\frac{\pi \cdot (x_i)}{L} \right] \right]$$
$$y_{s,i} := y_s + x_i \frac{y_r - y_s}{x_{100} - x_1}$$



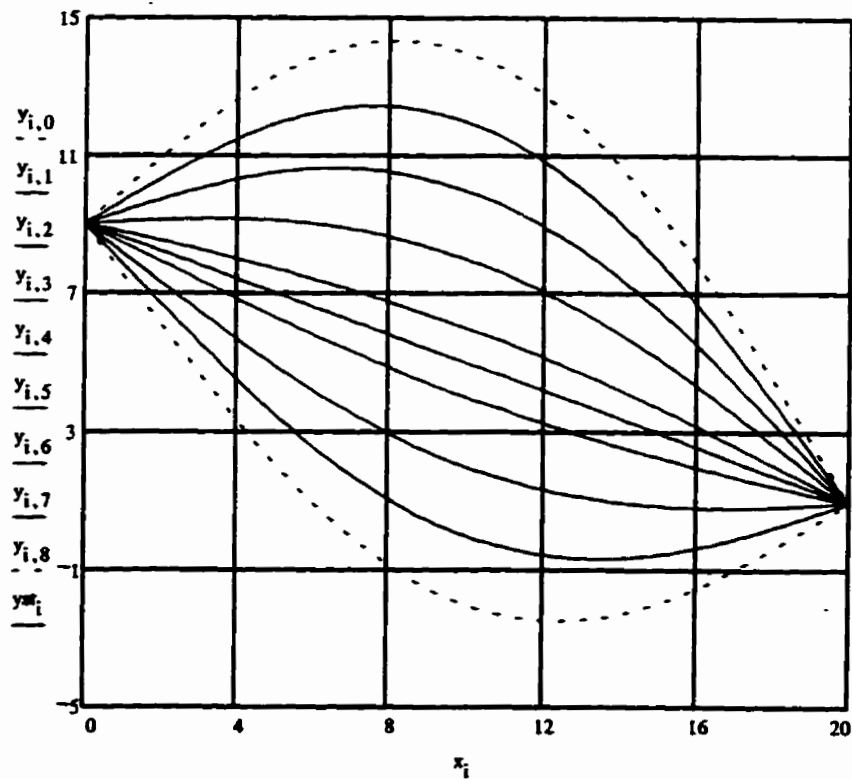
Sin-Arc paths for the case when source and receiver locations are at one-row different elevation.

Case 3:

Source and Receiver locations: $y_s := 9$ $y_r := 1$

$$y_{i,j} := y_s + x_i \frac{y_r - y_s}{x_{100} - x_1} + \left[A_j \cdot \sin \left[\frac{\pi \cdot (x_i)}{L} \right] \right]$$

$$y_{st_i} := y_s + x_i \frac{y_r - y_s}{x_{100} - x_1}$$



Sin-Arc paths for the case when source and receiver locations are at a two-row different elevation.

CHAPTER V

DATA BASE OF CASE HISTORIES

5.1 Introduction

Prior experience with simulated data has shown that the quality of inversion is unrealistically good when compared to inversions with real data. In part, this reflects the compatibility of forward simulation algorithms with hypotheses made in the inversion stage. A central goal of this study was to assess the potential of inversion methods with real data, for which a database of well documented case histories was compiled. This chapter presents these cases.

5.2 Case Histories

A database of case histories was compiled. The main characteristics of these cases are summarized in Table 5-1. A detailed description of each case is presented in the text. All corresponding input files to be used with WATOM-I are printed in Appendix E.

5.2.1 High Velocity Circular Anomaly - Acoustic Waves

The purpose of these tests was to permit visualization of the anomaly and to operate with simple wave propagation physics (only P-waves are possible in air).

Table 5-1: Case Histories.

Case history	Description	Characteristic	Purposes
<p>Balloon (<u>Four Cases</u>)</p>	<p>High Velocity Circular Anomaly Left-Side Off-Centered Top-Side Off-Centered and Centered</p>	<p>Acoustic waves</p>	<p>Visualization of anomaly Simplicity (only P-waves)</p>
<p>Concrete Block (<u>Two Cases</u>)</p>	<p>Simulated Crack Side-to-Side shooting Top to Left-Side shooting Top to right-Side shooting Concrete Column</p>	<p>Well controlled features</p>	<p>Tomographic imaging of well defined defects (Crack and Column)</p>
<p>Kosciuzko Bridge</p>	<p>Shooting from top and one side to bottom and the other side</p>	<p>Very noisy data</p>	<p>Assess the condition of a massive, large size concrete pier</p>
<p>Chute Hemmings Dam</p>	<p>Shooting from downstream face of the dam to upstream face</p>	<p>Asymmetric structure</p>	<p>Picture the internal condition of a pillar and state of shotcrete</p>
<p>Korean DMZ</p>	<p>Seven sets of parallel shootings</p>	<p>Heterogeneous, anisotropic background</p>	<p>Assess the location of a tunnel</p>

Data acquisition: Real data were obtained in the laboratory using a 1.5mX1.5m frame to represent the plane under study. Air was the homogeneous medium, $V=355\text{m/s}$ (Santamarina, *et. al.* , 1991). Figure 5-1 shows a schematic diagram of the test configuration for the following four cases.

Balloon 1: A 0.23m diameter circular high velocity inclusion was simulated with a balloon filled with helium ($V=921\text{m/s}$). The balloon was located on the left-side, off-centered within the frame (Figure 5-1a). Signals were detected at 7 equally spaced receivers (capacitor microphones) that were installed on one side of the frame representing the receivers borehole. The source (miniature hammer-and-plate) was activated at 7 equally spaced locations along the opposite side to generate cross-hole data. A PC-based digital storage oscilloscope was triggered with the source.

Balloon 2: A 0.23m diameter circular high velocity inclusion was simulated with a balloon filled with helium ($V=921\text{m/s}$). The balloon was located on the top-side, off-centered within the frame (Figure 5-1b). The source-receiver configuration was the same as for Balloon 1.

Balloon 3: A 0.23m diameter circular high velocity inclusion was simulated with a balloon filled with helium ($V=921\text{m/s}$). The balloon was located on the center of the frame (Figure 5-1c). The source-receiver configuration was the same as for Balloon 1.

Balloon 4: A 0.46m diameter circular high velocity inclusion was simulated with a balloon filled with helium and placed at the center of the instrumented frame (Figure 5-1d). In this case, 16 equally spaced receivers (capacitor microphones) were installed on one side of the frame to represent a borehole. The source (miniature hammer-and-plate) was activated at 16 equally spaced locations

along the opposite side to generate cross-hole data. The PC-based digital storage oscilloscope was triggered with the source.

5.2.2 Concrete Block - Well Controlled Features

The purpose of these tests was to assess tomographic images in concrete with well defined internal features (Gheshlaghi, *et. al*, 1995).

Data Acquisition: The medium was a concrete monolith (1.2x1.2x6.1m) containing a variety of model defects (Figure 5-2). Defects were pre-constructed and placed in the form prior to casting. The monolith was allowed to cure for three months prior to testing. The data were collected in a laboratory by Ontario Hydro. A Soniscope was used for data collection (central frequency: 50 Khz). Two cases are discussed.

Simulated Crack: An open crack was simulated with a slot that was cut in the concrete monolith using a diamond wire saw, 3 months after casting. The slot was 12mm wide and extended across the width of the block at an inclination of 26°. Readings were taken from the top to both vertical faces (11x10 rays for each side) and across the monolith (10x10 rays), giving a total of 320 travel time readings. Figure 5-3a shows details of this case.

Concrete Slab: A Sonotube (0.46 m diameter by approximately 2 m high) was placed vertically in the monolith form and loosely filled with crushed limestone (nominally 20 mm size) to a height of 0.91 m. As the concrete was poured into the monolith form, the Sonotube was raised to leave a column of aggregate supported by the fresh concrete. The stone was selected to be the same as the coarse aggregate in the monolith concrete. Readings were taken at 23 locations

from 23 shootings on the opposite side giving a total of 529 travel time readings (Figure 5-3b).

5.2.3 Kosciuzko Bridge - Very Noisy Environment

The purpose of this tomographic study was to assess the condition of a massive, large concrete pier.

Data Acquisition: The pier dimensions were 5.52m x 5.52m. Two sides of the pier were instrumented with 14 receivers (piezo-pads) each (28 total). The same number of sources (hand sledge hammer) were activated on the other two sides of the pier (Figure 5-4). A longitudinal closed crack was visible and possibly extended from one side to the other side of the pier (Santamarina, C., Tallin, A., Wakim, T., 1991). High traffic and vibration levels made data acquisition difficult.

5.2.4 Chute Hemmings Dam - Asymmetric Structure

The objective was to give a picture of the internal condition of the pillar and some information on the mechanical characteristics of shotcrete.

Data Acquisition: The medium was the pillar of a concrete dam (Figure 5-5). Acoustic waves were generated by explosives (boosters) at 15 locations, triggering them with low electrical voltage. A set of fifteen accelerometers of constant sensitivity in the frequency-band 1-15 KHz was located on the downstream face of the dam. Sixty-one traces (out of 225 traces) were rejected because the received energy was not sufficiently high to enable travel time determination (Rhazi, J., 1995).

5.2.5 Korean DMZ - Heterogeneous, Anisotropic Background

The purpose of this tomographic study was to assess the location of a tunnel in a heterogeneous and anisotropic medium (Figure 5-6).

Data Acquisition: The tunnel was located 81 m below the surface. It was approximately 2.7m wide and 2.2m high. The source was an electric arc discharge device with a frequency range of 1.4-1.7 KHz. The receivers were hydrophones with appropriate amplification and frequency filtering.

Seven cross-hole data sets were collected by simultaneously lowering both source and receiver in parallel vertical holes, 15.2m apart. Measurements were repeated every 0.2 meter. One hundred and fifty travel times were measured in each set. In the first data set, source and receiver were positioned at the same elevation.

The elevation differences between source and receiver, for the next six sets, were 3.90m=(S90-R86.1), 8.90m=(S92-R83.1), 14.90m=(S95-R80.1), -4.10m=(S86.-R90.1), -8.90m=(S84-R93.1), -15.1m=(S81-R96.1), respectively. The minus sign indicates that source elevation is lower than receiver elevation (Rechtien *et al.*, 1995).

5.3 Summary

The quality of inversions using simulated data is unrealistically good when compared to inversions with real data. In part, this reflects the compatibility of forward simulation algorithms with hypotheses made in the inversion stage. A central goal of this study was to assess the potential of inversion methods with

real data, for which a database of well documented case histories was compiled. The database consists of five case data sets of histories (eleven cases) including both laboratories and field cases.

The four balloon cases permit physical visualization of the anomaly and allow a corroboration of results. This case is based on simple wave propagation physics (only P-waves are possible in air).

The three cases in the concrete specimen with defects permit studying tomographic imaging in a real civil engineering material with controlled defects.

The Kosciuzko bridge pier data involves a massive, large concrete pier. The data were collected in a very noisy environment.

The Chute Hemmings dam data permits the study of a massive structure with poor illumination angles.

The tomographic data from the Korean Demilitarized Zone involved a low velocity anomaly (tunnel) in a heterogeneous and anisotropic medium. The difficulties of inverting these data are assessed in the following chapter.

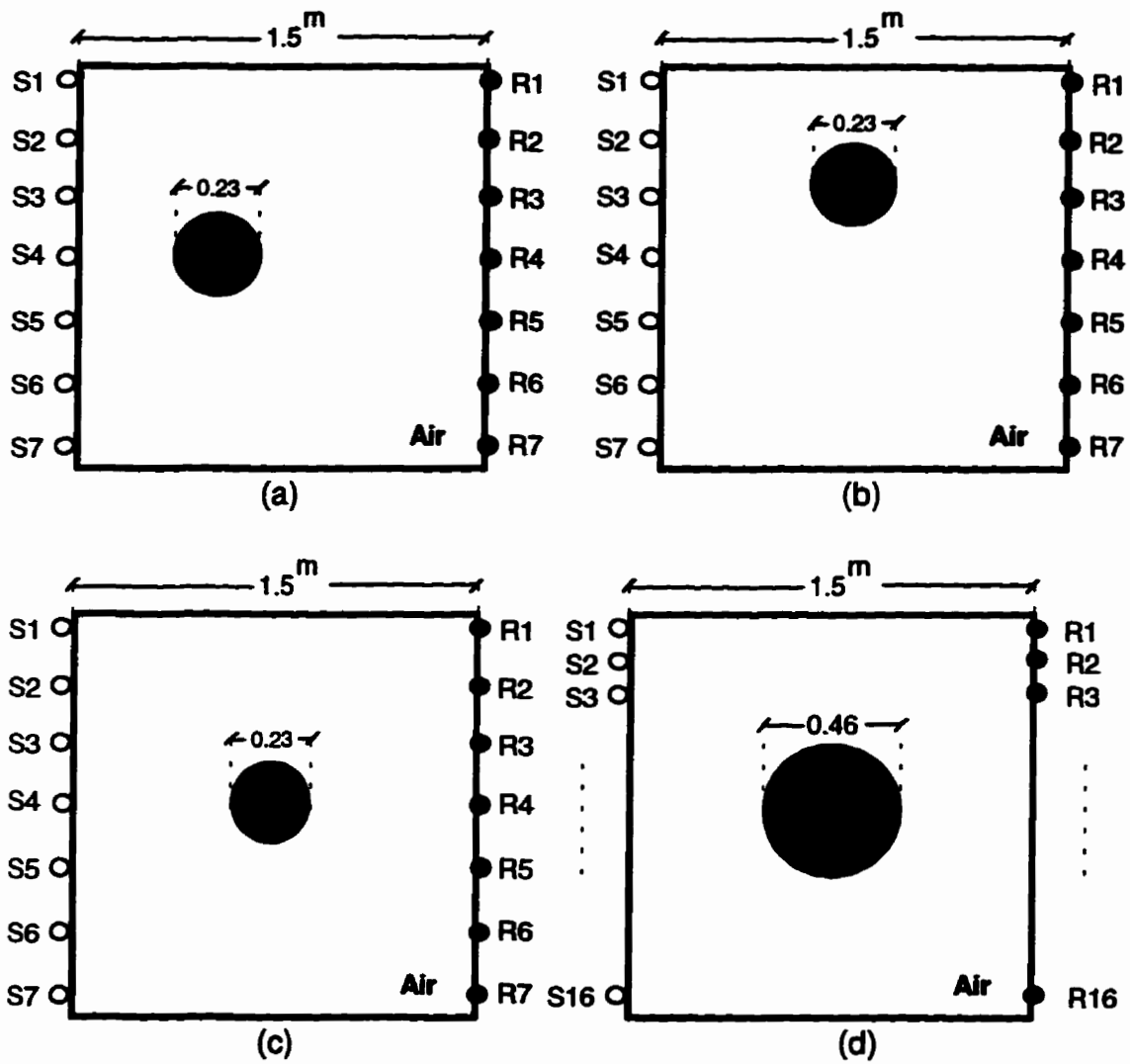


Figure 5-1: Helium filled balloons in air; different sizes and locations.

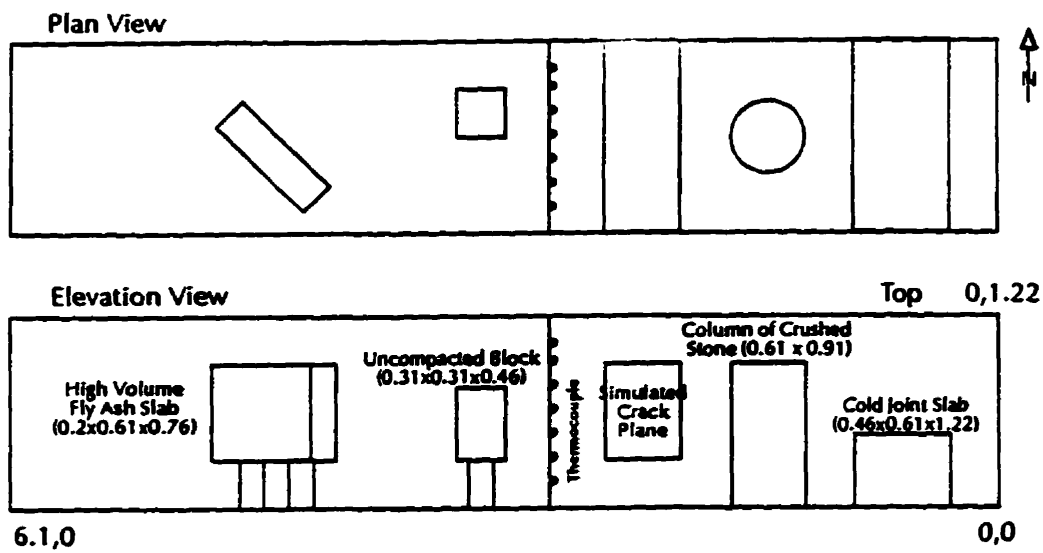
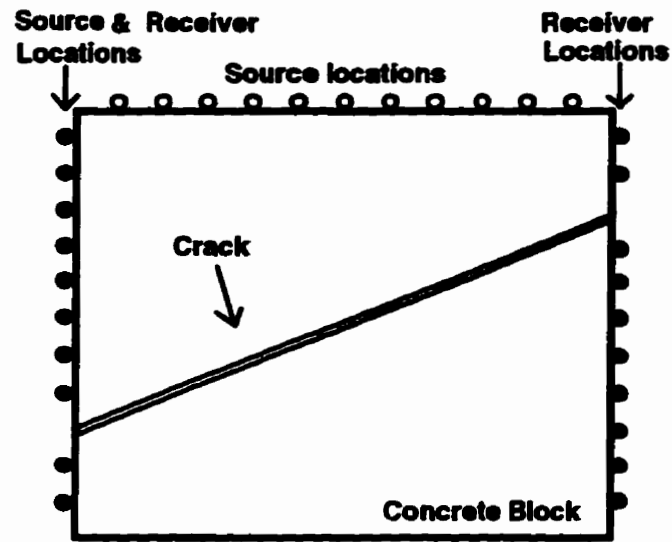
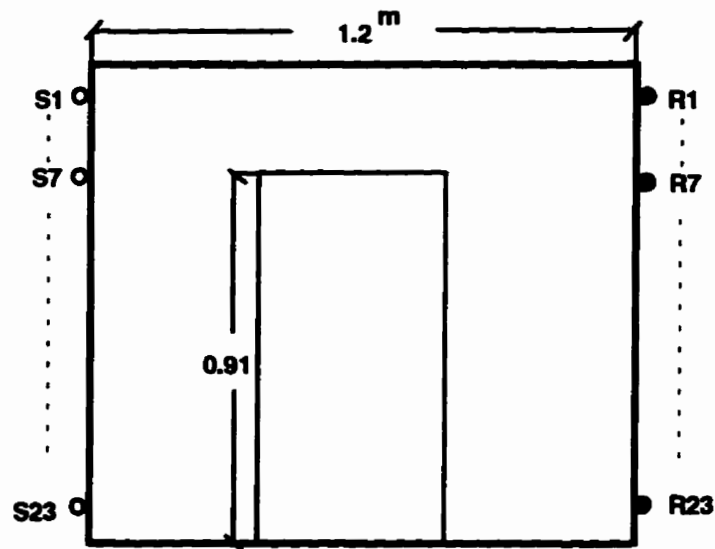


Figure 5-2: Concrete monolith with controlled defects.



(a)



(b)

Figure 5-3: Concrete block: (a) Simulated crack, (b) Concrete column.

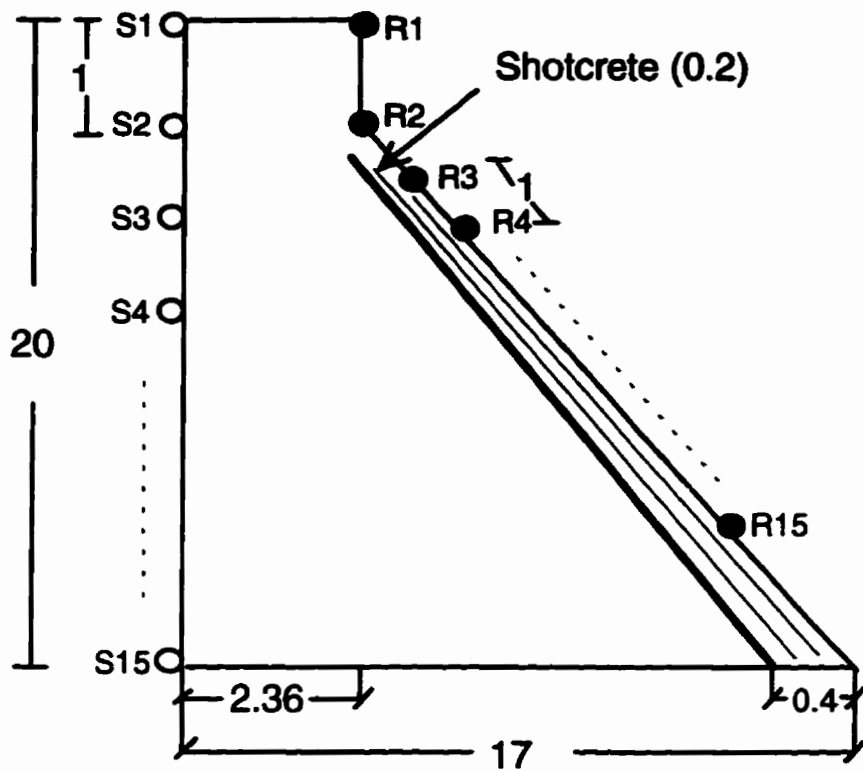


Figure 5-5: Chute Hemmings dam - source and receiver locations. All scales are in meters.

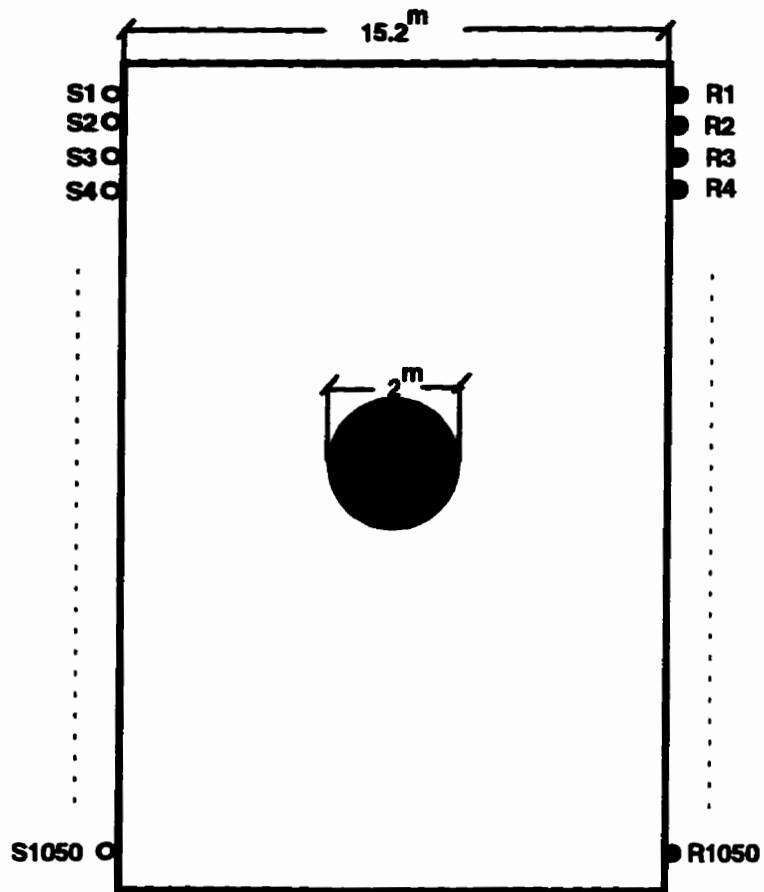


Figure 5-6: Korean Demilitarized Zone (DMZ) - source and receiver locations. Seven sets of 150 rays, total of 1050.

CHAPTER VI

DATA PRE-PROCESSING STRATEGIES

6.1 Purpose

In an inversion process with simulated data, the inverted image can simply be tested with the simulated model. However, the inversion of real data usually faces problems of nonuniqueness due to mixed-determination, uneven distribution of information, and the presence of noise (Morozov, 1993).

Additional information can be added in the form of constraints to avoid unrealistic solutions. For instance, knowing the geological formation of the rock at a given site can be helpful to avoid unrealistic values for the rock properties. However, this additional information has its own uncertainties.

Another option to provide foresight into the problem is to preprocess the data. The following strategies could be employed in a pre-processing study: quantification of systematic and accidental errors, source coupling, global information content (SVD), distribution of information content, synograms, plots of average velocity and residuals. Emphasis will be placed on the distribution of information content, detection of errors, anisotropy, gradual changes, and anomalies (SVD is addressed in Chapter VII).

6.2 Distribution of Information Content

Gathering data in CE-tomographic testing is almost always restricted to some limited illumination angles. Hence, the distribution of information is not even throughout the medium. For example, the number of rays crossing a pixel is different for each pixel. This means that there is more information in some regions of the medium than in others. It is possible that no information would be available from some parts. Therefore, knowing the distribution of information can be helpful in designing adequate source and receiver configurations to assess the optimal even distribution of information.

The simplest characterization of information content is to compute the total travel length for all rays that traverse a pixel. If the tomographic problem is cast in matrix form, the length of the columns of the matrix L provide this information for each pixel. Figure 6-1 shows the information density for three different shooting patterns. If the final image is correlated with the corresponding image of information, the analyst is well advised to skeptically review the inversion.

6.3 Systematic and Accidental Errors

The presence of accidental and systematic errors can be investigated with travel length vs. travel time plots. The boundary condition is zero travel time for zero length of rays. Therefore, the regression of (t_i, l_i) should go through the origin. The ordinate crossing of the regression line marks the average systematic error (e.g., trigger delay) data. This analysis is weakened when all rays are of about the same length (e.g. pure cross-hole case).

Single off-line data carry accidental errors. These errors are usually due to reading errors or missing true first arrivals etc. Accidental errors can be

identified by plotting the projections corresponding to a source or to a receiver, herein called shadows.

Accidental Gaussian errors are canceled out in least squares solutions. This is not the case for systematic errors. The best alternative is to identify them and remove them. Otherwise, the measurements are equivalent to $(t_i + \Delta t)$ and the solution becomes

$$s = \left[(L)_{\text{pseudo}}^{-1} t \right] + \left[(L)_{\text{pseudo}}^{-1} \Delta t \right] \quad (6-1)$$

where $(L^{-1})_{\text{pseudo}}$ is the pseudo-inverse obtained with any of the methods described before.

The analysis of systematic and accidental errors is a helpful tool in determining the order of magnitude of damping and regularization coefficients. Furthermore, systematic errors can be corrected.

6.4 Analysis of Shadows

The analysis of projections, or “shadows”, might be the best way to pre-assess the position and size of inclusions in the medium and the presence of accidental errors. This study can be conducted in different ways. Fan ray paths and parallel ray paths are two possibilities. In the case of fan ray paths, average velocities are computed for each source and receiver pair assuming a straight ray path, and then plotted against receiver locations.

6.5 Heterogeneity and Anisotropy

The polar and spatial distributions of velocity in a medium can be used to

evaluate heterogeneity and anisotropy. Only estimated average velocities can be computed before inversion:

$$(V_i)_{ave} = \frac{(L_i)_{estimate}}{t_i} \quad (6-2)$$

The straight ray assumption is employed as a first approximation to L_i .

The plot of average velocities versus average depth of the shot can highlight the presence of anomalies as well as any global trend such as vertical heterogeneity.

The degree of anisotropy can be inspected by plotting average velocities vs. the inclination of rays in either polar or Cartesian plot.

This pre-processor can be used to evaluate a proper initial guess for the velocity of the background. For instance, in the case of a vertically heterogeneous medium, velocity can be defined as a function of depth ($V=a+bZ$). This study can also be employed to estimate an initial value for thresholding.

6.6 Case Histories and Pre-Processing

6.6.1 Balloon 1

Assuming straight ray paths, the distribution of information for this case is given in Figure 6-2. The figure shows a high concentration of information in the center of the medium. The first and last rows of pixels have the lowest information content. This plot can be used to design the configuration of sources and receivers before the test is implemented and decrease the mixed-determination of the problem.

The systematic triggering error can be evaluated from Figure 6-3a. The linear regression analysis shows an 0.15ms average systematic error in the data. Off-line data indicates the presence of an anomaly and the effect of accidental errors (Figure 6-3b). This well-behaved data indicate that the optimum regularization coefficient should be selected in a low range .

For the purpose of heterogeneity inspection, Figure 6-4a shows changes in average velocity versus depth. An average depth for each pair of source and receivers is computed as:

$$\bar{Z}_{ave} = \frac{Z_{source} + Z_{receiver}}{2} \quad (6-3)$$

While most paths show an average velocity of 13.8 (in/ms), some rays in depths 20-40 (inches) indicate higher velocity, about 14.5 (in/ms). This suggests the presence of a high velocity region at mid-depth. The value of the high velocity region helps to select a proper threshold during post-processing for image enhancement to differentiate between the anomaly and the background in the image.

The plot to inspect for anisotropy is shown in Figure 6-4b. The analysis of a single fan is biased by the presence of the anomaly. However, when all the shots are plotted at once there is no conclusive trend to suggest an anisotropic background, which is indeed the case for air.

Figure 6-5 shows the analysis of individual projections or shadows for this case. For sources 1 and 2, the presence of an inclusion can not be seen until the last rays. The presence of the inclusion has affected the average velocity for that part of the medium scanned with rays shot from sources 3, 4, and 5. The effect of the inclusion on the average velocity is almost diminished for the source 6 and 7. The inclusion has affected the rays emitted from source 4 more than sources 3 and 5. Therefore, the inclusion should be located in front of source 4.

The average velocities for the rays emitted from sources 1 and 2 only increased for the last two rays. For sources 6 and 7 average velocities decreased for the last 3 rays. Therefore, it can be deduced that the size of the inclusion is about one receiver interval or $9\text{in}(=0.23\text{m})$.

The presence of accidental error can be noted in many cases, e.g., note the fluctuation in the shadow of the first source (Figure 6-5a).

6.6.2 Balloon 2

The pre-processing of the data for Balloon 2 followed a similar procedure outlined for Balloon 1. Figures 6-6 to 6-8 show the results. The distribution of information content for this case history is the same as for the Balloon 1 case (Figure 6-2). A proper setup configuration for sources and receivers can be the same as for Balloon 1. Due to high degree of systematic and accidental errors (Figures 6-6a & b) a higher degree of smoothing should be expected for this case, compared to Balloon 1.

Data preprocessing shows a homogenous isotropic background with a high velocity anomaly in the upper part above the center (Figure 6-7). The value of average velocity for anomaly can be used as an initial guess for thresholding.

Figure 6-8 shows the analysis of shadows for this case. The location of the inclusion has affected the rays shooting from sources 1, 2, and 3 more than the other rays emitted from the other sources. The rays emitted from the last three sources have not been affected by the inclusion presence, except for the first two receivers. The location of the inclusion can be inspected from source 3 shootings where a symmetric trend for the first 4 rays with a peak at ray 3 can be seen. Therefore, the inclusion should be located in front of source 3.

The first two rays emitted from source 1 are not affected by the inclusion and for sources 6 and 7 the average velocities for the last 4 rays are decreased. Thus, the size of the inclusion should be about one receiver interval or 9in(=0.23m).

6.6.3 Balloon 3

The distribution of information content for Balloon 3 is similar to that for Balloon 1 (Figure 6-2). The pre-processing of the data for this case history followed a similar procedure, outlined for Balloon 1. Figures 6-9 and 6-10 show the results. Data preprocessing shows a homogenous isotropic background with a high velocity anomaly in the center.

The optimal configuration for source and receiver locations can be evaluated from the distribution of information content (Figure 6-2). The plots for systematic and accidental errors indicate low accidental errors for this case history (Figure 6-9). This well-behaved data suggest a low value for the optimum regularization coefficient.

Figure 6-10a shows a high velocity region in the center of the medium (depths 25 to 35 inches). The presence of the anomaly can hardly be deduced from Figure 6-10b. Since the anomaly is in a location where most of the rays pass through, the average velocity of the anomaly has been averaged with the background velocity. Therefore, a proper threshold to differentiate between the anomaly and the background in the image can hardly be selected.

Figure 6-11 shows the analysis of shadows for this case. The inclusion has affected rays shooting from sources 3 and 4. The symmetry, in average velocities, of rays emitted from source 4, and the symmetry for rays emitted from sources 2 and 6, suggest the location of the inclusion in the center of the region.

6.6.4 Balloon 4

The information content for this case history is given in Figure 6-12. A high concentration of information in the center and a low concentration in the first and last row are the main characteristics of this case history.

The plots of travel time vs. travel length for this case are given in Figure 6-13a&b, respectively. An apparently high average systematic error of 0.676ms is calculated by linear regression of the whole data set (Figure 6-13a). However, this is biased by the higher effect of the high velocity anomaly on the shorter rays (Figure 6-13b). The low level of accidental errors suggests a low value for the optimal regularization coefficient.

Figure 6-14a shows that the central location of the anomaly affects all long rays at depth 20-45 (inches). This plot can be used to select a proper threshold and to differentiate between the anomaly and the background in the inverted image. Anisotropy inspection in Figure 6-14b indicates an isotropic background.

Figure 6-15 shows the analysis of shadows for this case. The presence and location of an inclusion can be deduced from these plots. Accidental errors can also be noted.

6.6.5 Crack in Concrete (Side-to-Side Shootings)

The information content of this case history is given in Figure 6-16. The low information contents which are apparent in the two dark pixels in third and seventh row are due to the absence of sources or receivers in those regions.

The plots of travel times vs. travel lengths for this case are given in Figure 6-17a&b. It is clear that there are two fundamentally different ray paths. The same average velocities would be calculated if the velocity for data in the upper set would be computed with a shorter length ($l-\Delta l$). An average systematic error of 0.003ms is calculated for the lower set, using a regression process (Figure 6-17a). This plot could also be interpreted as a very systematic difference between 2 sets of measurements, such as different equipment, different operators, etc. Once such a plot is available, the analyst must identify the physical or experimental cause before processing.

For those rays which do not cross the crack (lower set) the average velocity is about 4.65km/s (Figure 6-18). It appears that the real ray paths are out of plane. The extra distance Δl can be computed from these data assuming a homogeneous medium with $V=4.64\text{km/s}$: $\Delta l=1.2\text{m}$. For comparison, the width of crack is 12mm.

Figure 6-19 shows the plots of the average velocities vs. receiver locations and inclination: the dual trend is the most indicative of spatially related bias. Projections follow similar trends for all sources, except for sources number 9 and 10. The high velocities correspond to paths which do not cross the crack. A sudden drop in velocities appears for rays crossing the crack. However, the computed average velocity increases as the distance from source-to-receiver increases. Indeed, the wave front travels around the open crack and out of the plane of the transducers. Thus, shorter straight paths are affected more by the three-dimensional deviation.

6.6.6 Crack in Concrete (Top-to-Left Side Shootings)

Figure 6-20 shows the information content for this case history. The highest

information content is in the central source area. Low information comes from the crack area and only the last part of the crack is crossed by a few rays.

The plots of systematic and accidental error for this case are given in Figure 6-21a. A low average systematic error of -0.006ms is calculated with a regression analysis (Figure 6-21a). Figure 6-21b shows that with a straight path assumption an average velocity of 4.6km/s can be calculated for those parts of the medium traversed by rays which do not cross the crack. Those few rays crossing the crack show lower average velocity (3.65km/s to 4.2km/s).

The plots of average velocity vs. receiver locations, i.e. shadows, are given in Figure 6-22. The average velocity remains 4.6km/s until the rays cross the crack (rays from all sources to receivers 9 and 10). This shows a homogenous medium for the left part of the block from receiver 1 to 8. A low velocity anomaly should be expected for the lower part.

6.6.7 Crack in Concrete (Top-to-Right Side Shootings)

Figure 6-23 shows the information content of this case history. The information content for the right part of the block is almost even. However, the highest information content is in the central receiver area. No information content can be found in the left side.

The plots of systematic and accidental errors for this case are given in Figure 6-24a. A low average systematic error of 0.03ms is calculated with regression analysis (Figure 6-24a).

Figure 6-24b shows that with a straight path assumption an average velocity of 4.6km/s is calculated for those rays which do not cross the crack (rays

connecting first and second receivers to all sources). Those rays crossing the crack have lower average velocities of 2.5km/s to 4.0km/s. As the ray paths increase, the effect of out-of-plane rays decreases, and the average velocity approaches the value in the uncracked concrete.

The analysis of shadows is given in Figure 6-25. The plots shows that the data from the first two receivers are not affected by the crack.

6.6.8 Column of Aggregate

The information content of the column of aggregate is given in Figure 6-26. Due to the symmetry of the medium and the source-receiver pattern, the central pixel carries the highest information content. This study helps design the setup configuration of sources and receivers to decrease the mixed-determination of the problem.

A systematic error of -2.16ms was computed with regression analysis (Figure 6-27a). A number of accidental errors in the data are revealed in Figure 6-27b.

The heterogeneity analysis (Figure 6-28a) shows that the medium should consist of two different parts. The main part has an average velocity of about 4.4km/s, which is the average of the concrete and aggregate velocities. The velocity of the other part is higher and about 4.6km/s, which is the velocity of concrete. The presence of aggregate can be noted from depth 0.3m where the average velocity starts to decrease. The velocity values of these two regions can be used in determining the proper thresholds for post-processing of the final image.

Figure 6-29 shows the analysis of shadows for this case history. A reasonable drop in average velocities of the rays from source 7 to receivers 7 to 13 shows

the location of the top part of the aggregate column. The drop indicates that the rays have traveled in the shortest time path (Fermat's principle) and have started to bend toward the high velocity concrete, rather than traveling in a straight path through the aggregate column. The rays then travel in straight paths from receiver 13 to 23. Therefore, the average velocity have dropped from 4.6km/s (good concrete) to 4.4km/s, which is an average velocity for the concrete and aggregate column. The ray bending effect can be found for the rays connecting sources 8 and 9 to receivers 7 to 13. Note the presence of clearly noisy data points. These should be identified and removed or "regularized" before inversion.

6.6.9 Kosciuzko Bridge Pier

The distribution of information content for this case history is given in Figure 6-30. The information content distribution on the two main diagonals is asymmetric due to sources and receivers configurations. The configuration appears well-designed.

A high number of accidental errors occur in the upper triangular part of the plot, affecting primarily short rays (Figure 6-31a). Also, an average systematic error of 0.51ms is calculated with regression analysis. The level of errors indicates that the optimum regularization coefficient should be very high.

Figure 6-31b shows a very homogeneous medium with average velocity of 170 in/ms. Therefore, a constant initial velocity should be selected for all pixels. A reasonable guess is the evaluated average velocity.

Two sets of shadow analysis are given in Figures 6-32 and 6-33 for the top to bottom and side to side shootings, respectively. A highly homogeneous medium is revealed based on the top to bottom shootings (Figure 6-32). The crack presence can not be seen in the top to bottom shootings since all the rays have to cross the crack, and therefore an average velocity of 170in/ms is calculated in all shadows. However, in the side to side data (Figure 6-33), a low average velocity for rays connecting sources 16 to 21 to receiver 19 and receiver 22 can be seen. This is due to the presence of a crack across the pier in that region.

6.6.10 Chute Hemmings Dam

The distribution of information content is given in Figure 6-34. A high concentration of information in the center and left upper part of the medium and a lack of data in the lower part (foundation) are the main characteristics of this plot. The configuration of sources and receivers is very poor in this case history.

Figure 6-35a shows high accidental errors in this data. Therefore, the optimum regularization coefficient should be selected in a very high range.

A homogeneous medium with an average velocity of about 4.1km/s can be seen in Figures 6-35b and 6-36a. Figure 6-36b shows a very isotropic medium. Therefore, a constant initial velocity should be selected for all pixels. A reasonable guess is the evaluated average velocity.

The analysis of shadows for this case history indicates a high degree of error in the data (Figure 6-37). The average velocity trend for sources 4, 5, 6, 7, 8 and 9 may reflect the higher velocity of massive-densified concrete in the center of the dam, as compared to the peripheries.

6.6.11 Korean Demilitarized Zone

The information content for this case history shows a smooth coverage of rays in the region of interest in the center of the figure (Figure 5-42). However, due to lack of information in the upper and lower part of the medium, it is possible that some ghosts appear in the inverted image of those regions.

Figure 6-39a shows that the velocity increases with depth, and Figure 6-39b shows a global anisotropic variation of velocity. Thus, the background medium is vertically heterogeneous and anisotropic. Hence, the initial velocity should be defined as a function which reflects the background characteristics (e.g. $V=a+bZ$).

The analysis of shadows in this case history is based on parallel ray projection rather than fan rays as for previous case histories (Figure 6-40). A similar drop in the average velocities at a depth of about 160m suggests the possibility of a low velocity zone at that depth.

6.7 Discussion and Conclusions

The main problem in inversion is non-uniqueness. To avoid some of the unrealistic solutions, the solution could be constrained. However, how are constraints selected?

In this chapter, it was shown that data pre-processing can be employed to preview the characteristics of the medium (anisotropy, heterogeneity, and presence of anomalies), to check the quality of the data (errors), and to identify possible biases such as the distribution of information content.

The polar and spatial distributions of velocity in a medium can be used to evaluate heterogeneity and anisotropy. However, only estimated average velocities can be computed before the inversion process.

The presence of accidental and systematic errors can be investigated with travel length vs. travel time plots. This analysis is weakened when all rays are of about the same length.

The distribution of information can be helpful in designing adequate transducer configurations and in improving the inversion strategy.

The analysis of projections, or "shadows", might be the best way to pre-assess the position and size of inclusions in the medium. Fan ray paths and parallel ray paths are two possibilities.

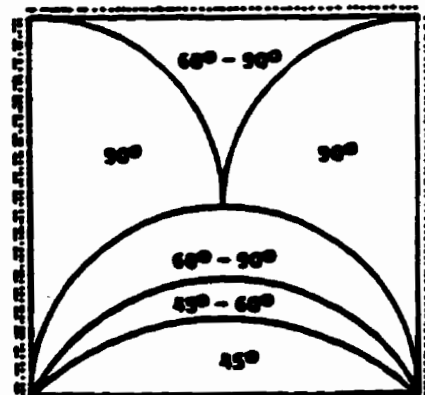
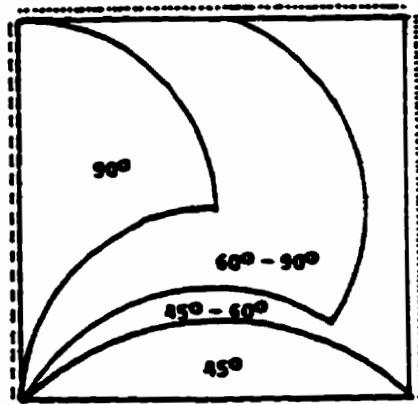
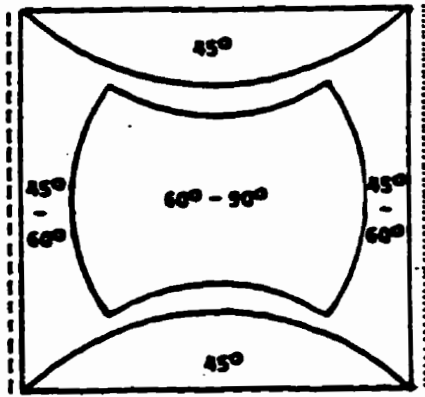


Figure 6-1: The information density for three different shooting patterns. “.” indicates source and “-” indicates receiver locations.

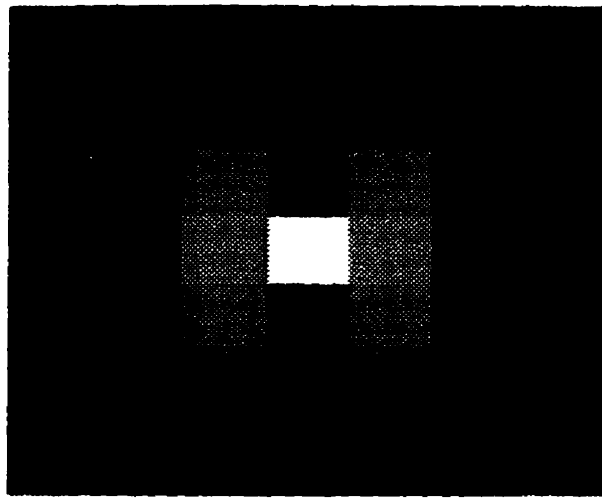
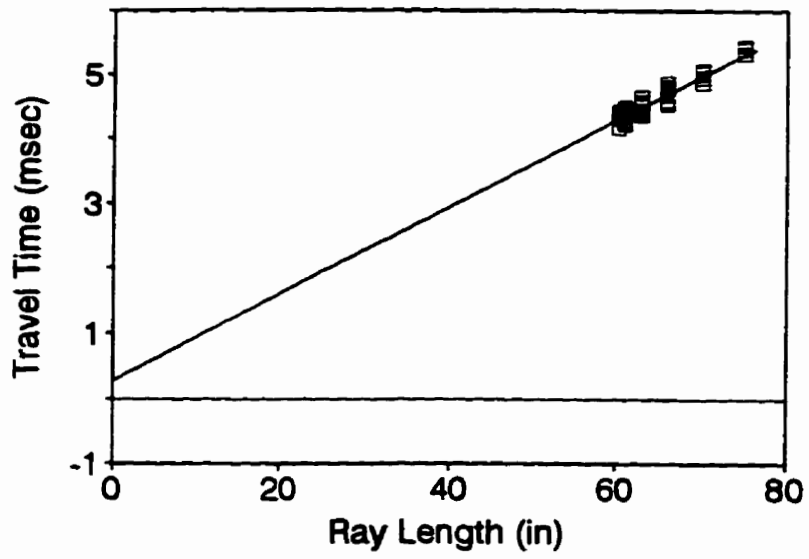
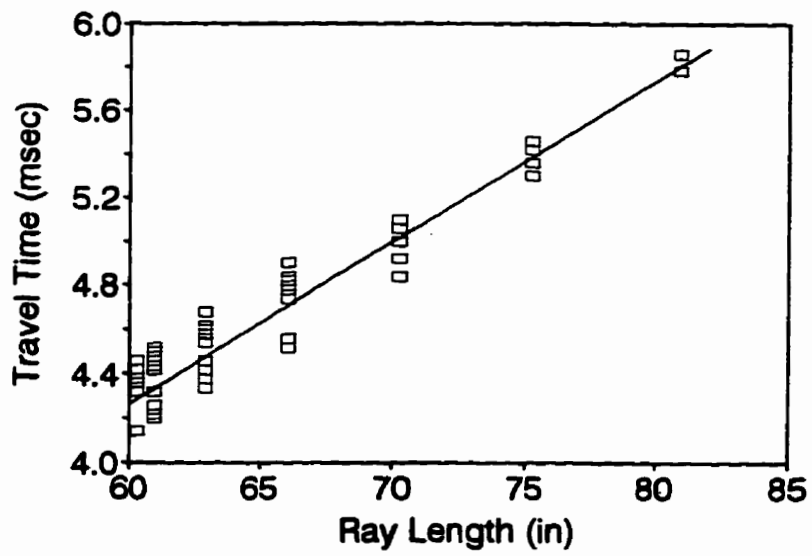


Figure 6-2: Distribution of information content for small balloons. Assuming straight ray paths.

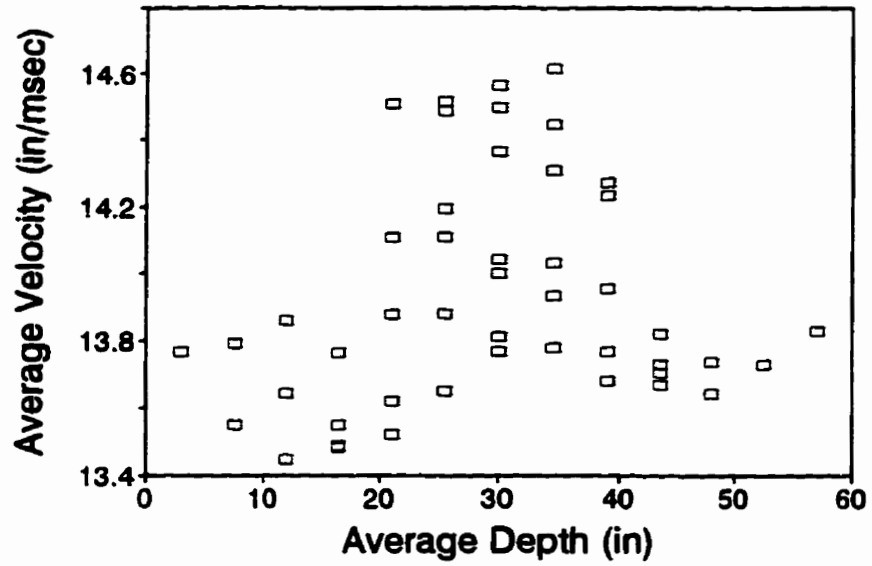


(a)

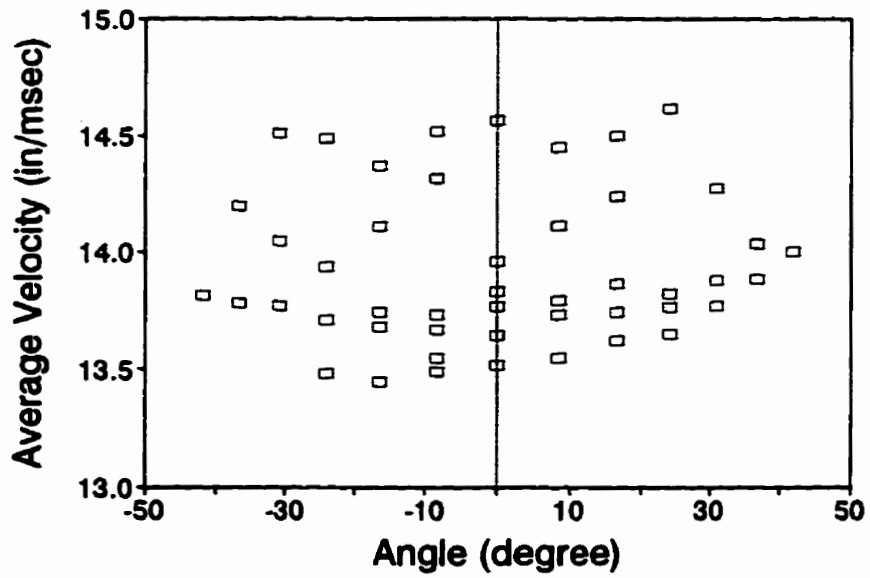


(b)

Figure 6-3: Systematic and accidental errors for Balloon 1.

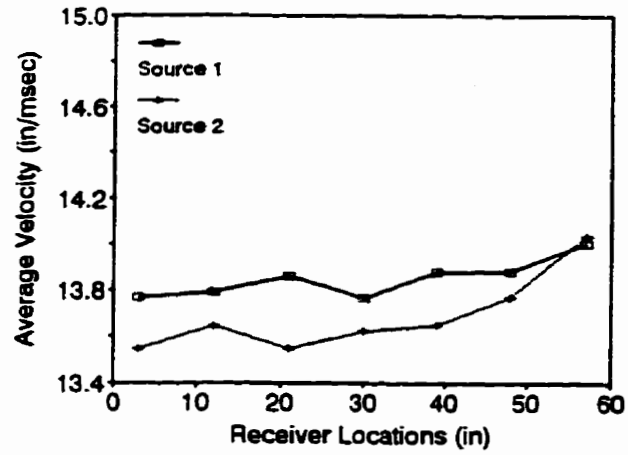


(a)

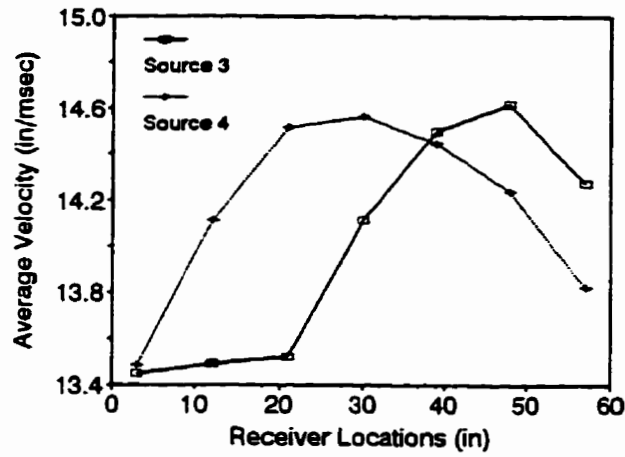


(b)

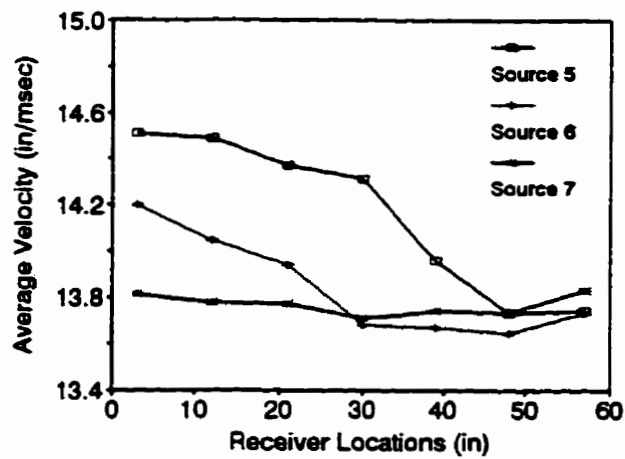
Figure 6-4: Heterogeneity and anisotropy inspections for Balloon 1.



(a)

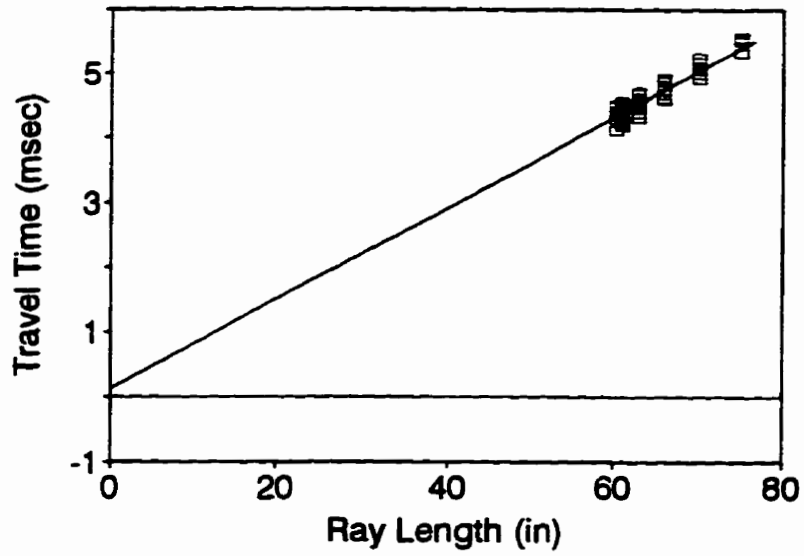


(b)

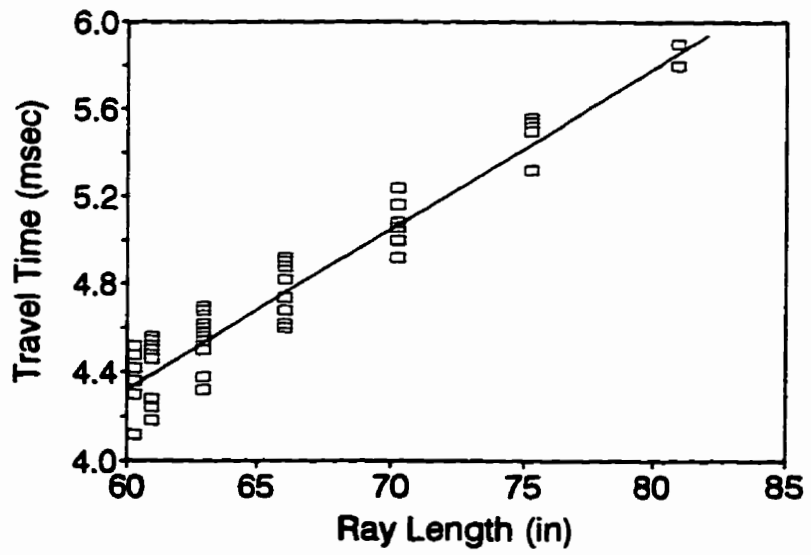


(c)

Figure 6-5: Analysis of shadows for Balloon 1.

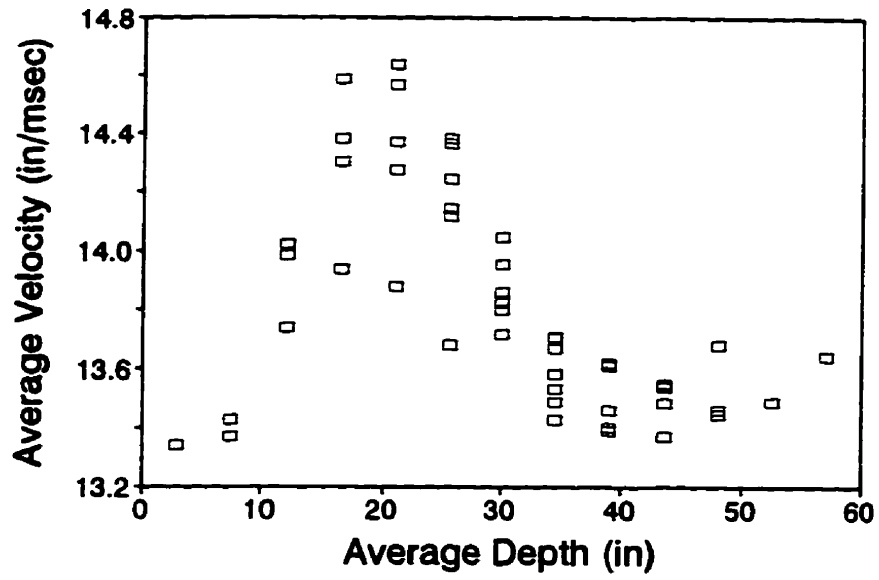


(a)

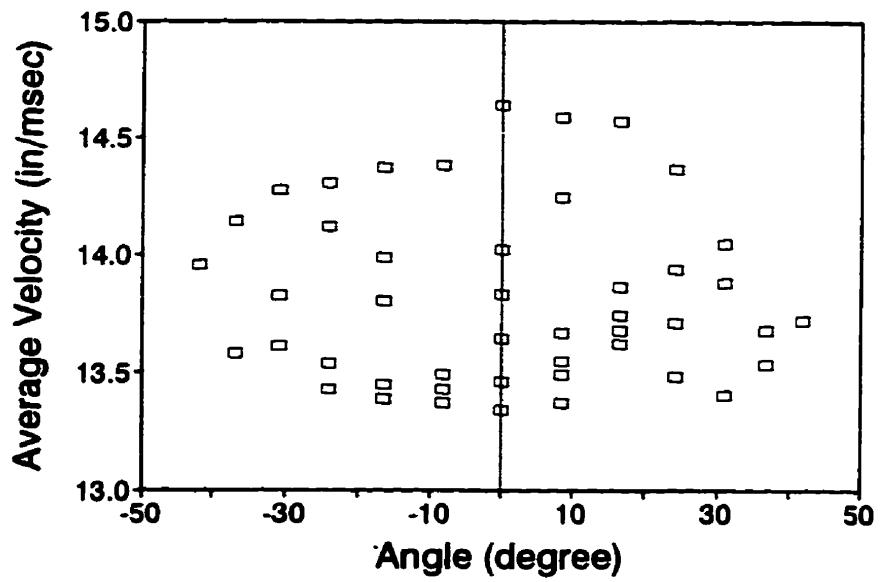


(b)

Figure 6-6: Systematic and accidental errors for Balloon 2.

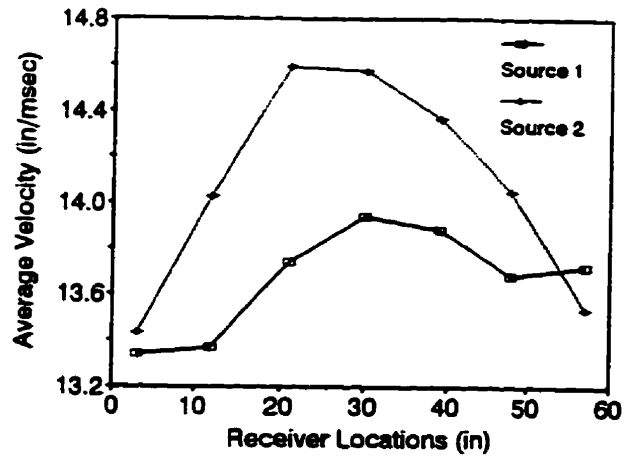


(a)

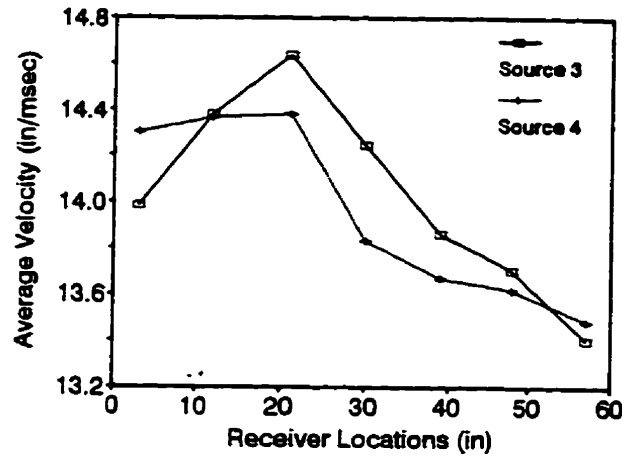


(b)

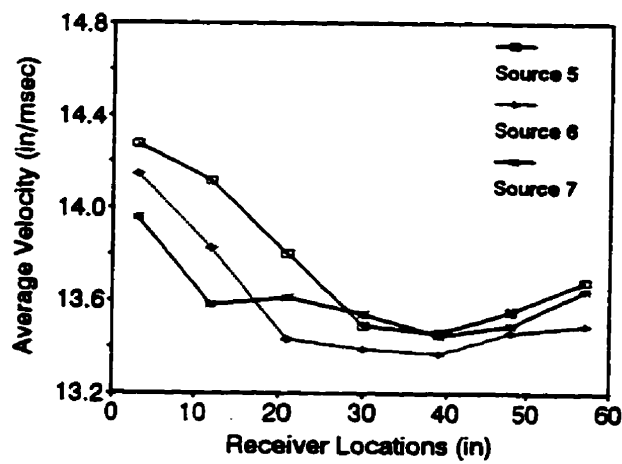
Figure 6-7: Heterogeneity and anisotropy inspections for Balloon 2.



(a)

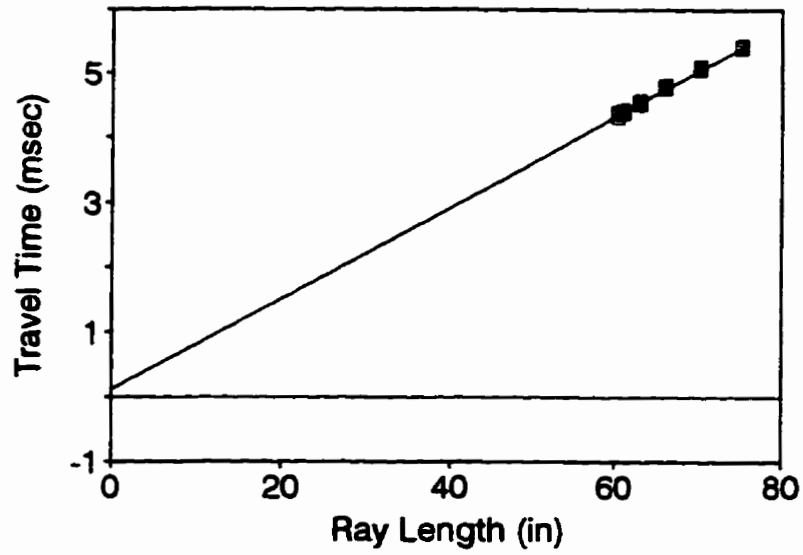


(b)

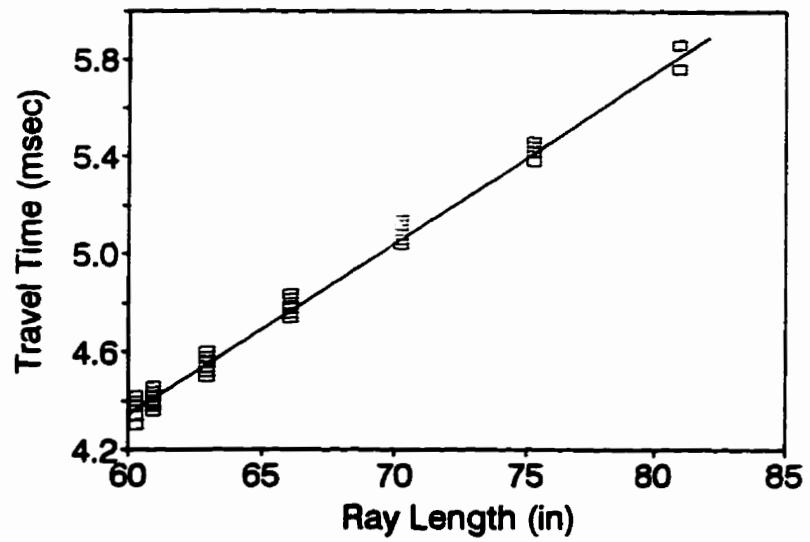


(c)

Figure 6-8: Analysis of shadows for Balloon 2.

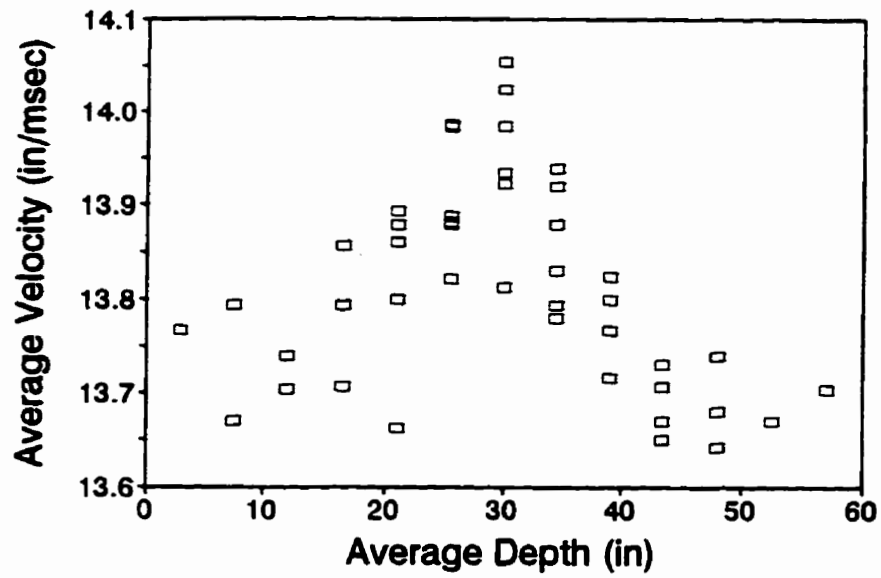


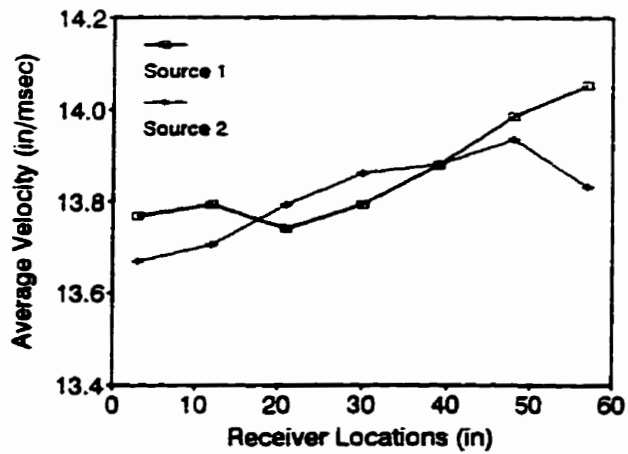
(a)



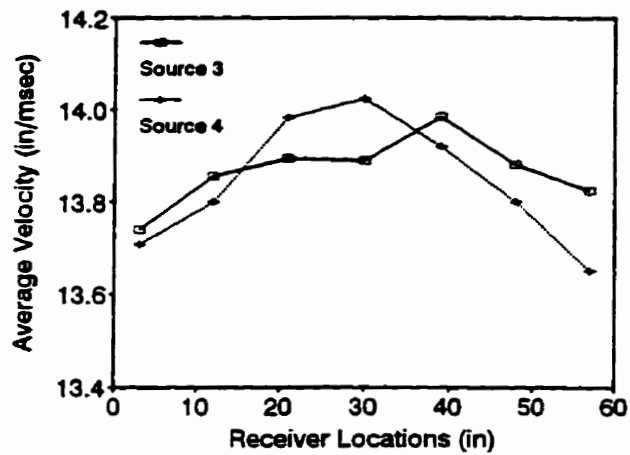
(b)

Figure 6-9: Systematic and accidental errors for Balloon 3.

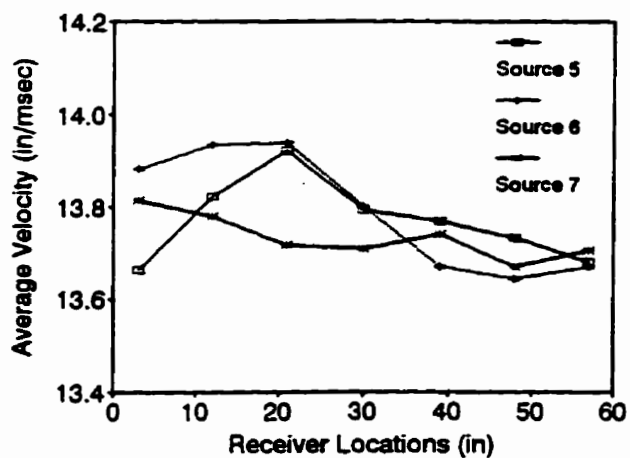




(a)



(b)



(c)

Figure 6-11: Analysis of shadows for Balloon 3.

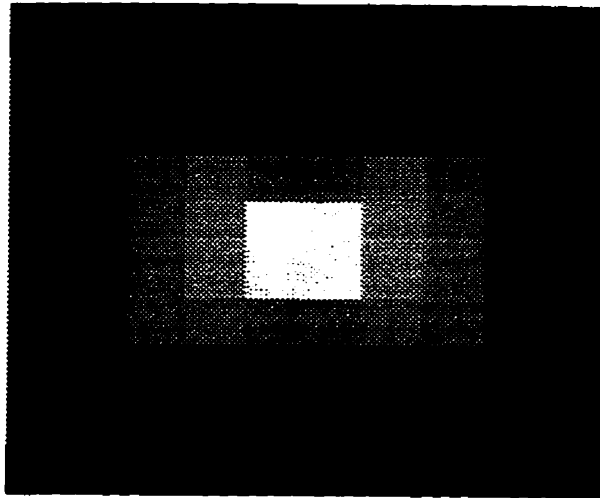
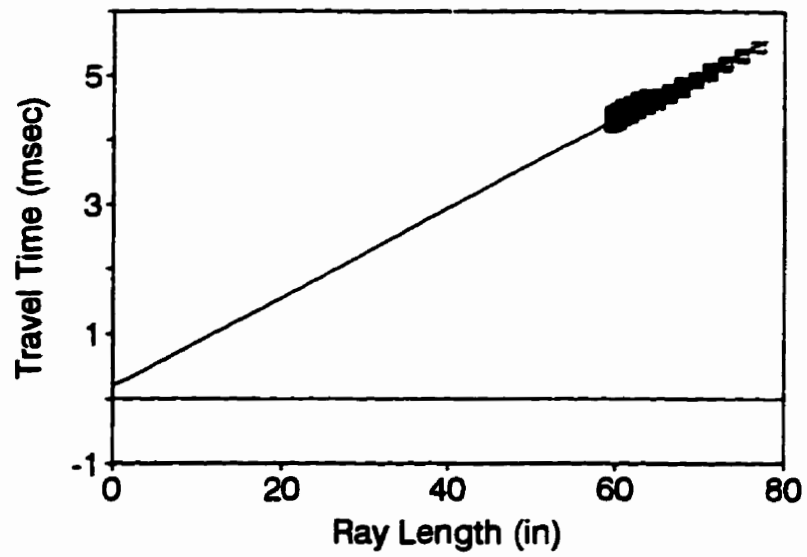
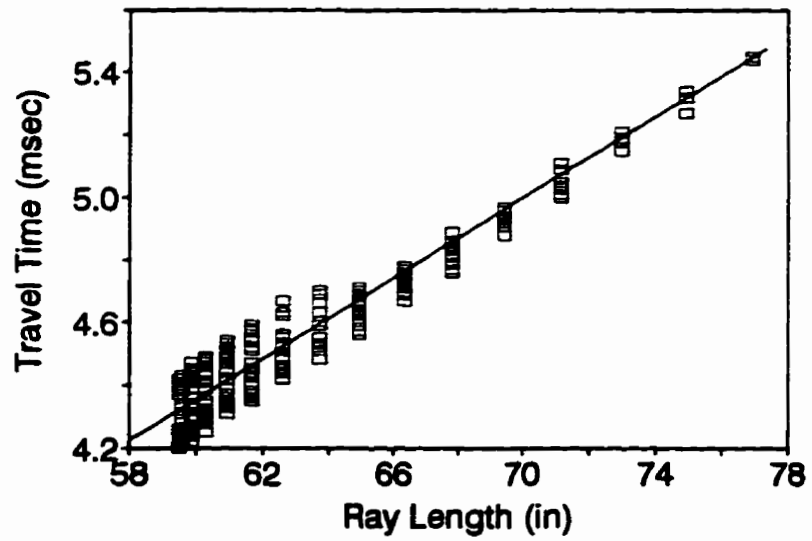


Figure 6-12: Distribution of information content for balloon 4. Assuming straight ray paths.

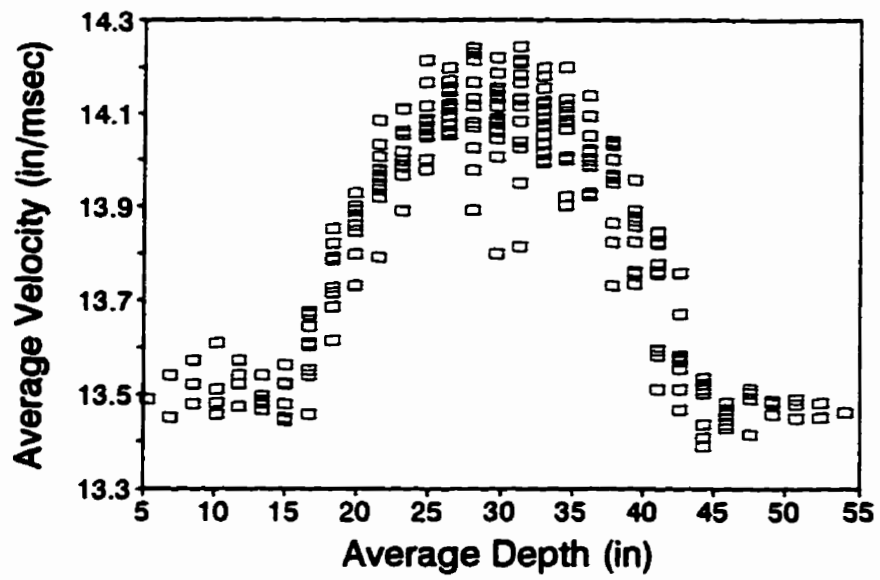


(a)

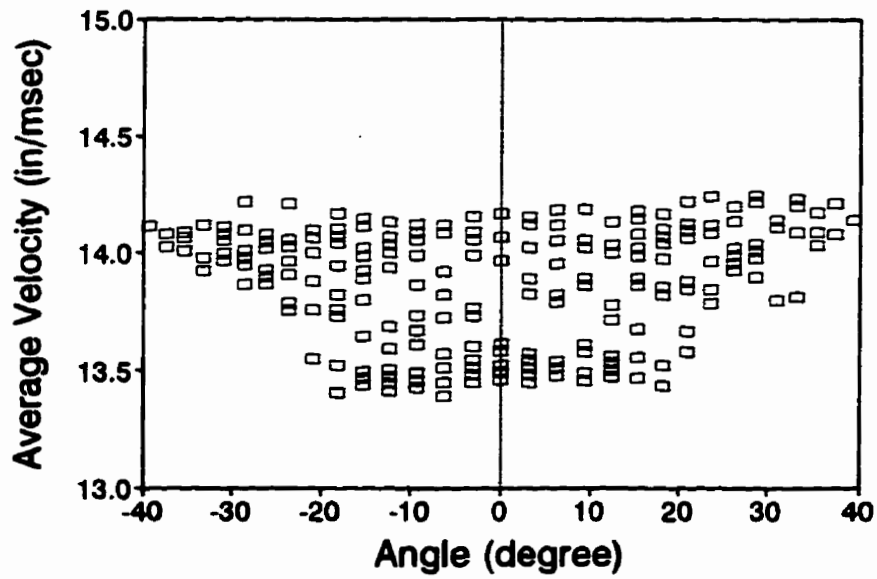


(b)

Figure 6-13: Systematic and accidental errors for Balloon 4.



(a)



(b)

Figure 6-14: Heterogeneity and anisotropy inspections for Balloon 4.

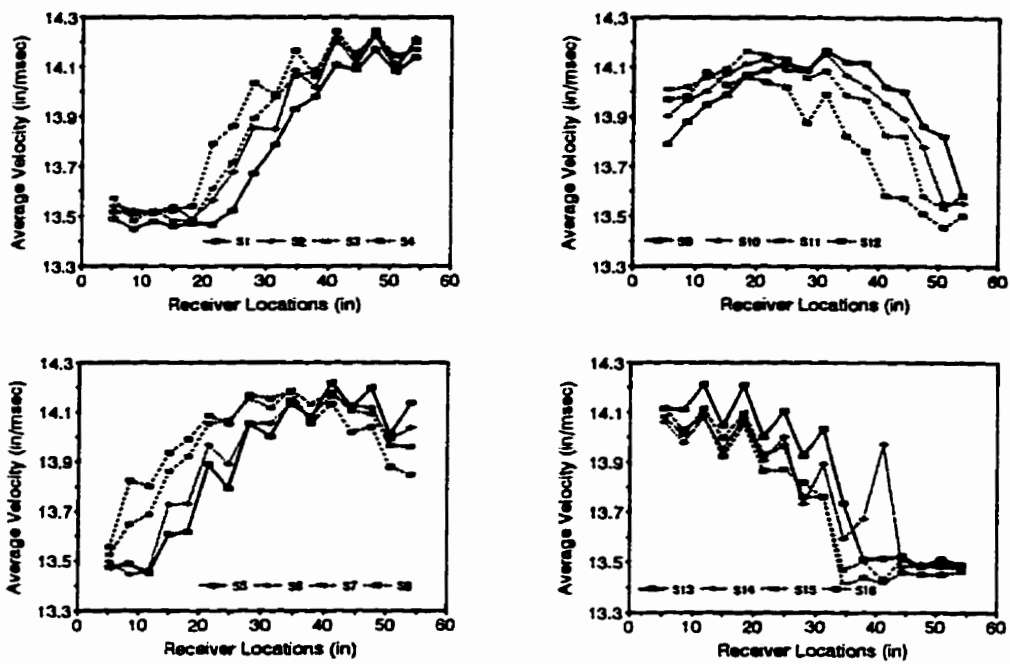


Figure 6-15: Analysis of shadows for Balloon 4.

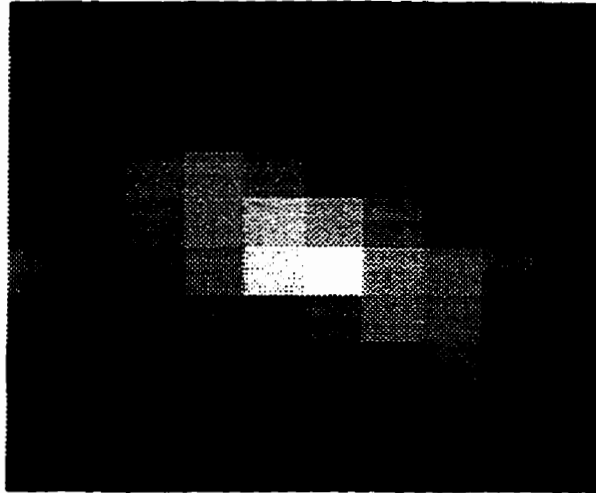
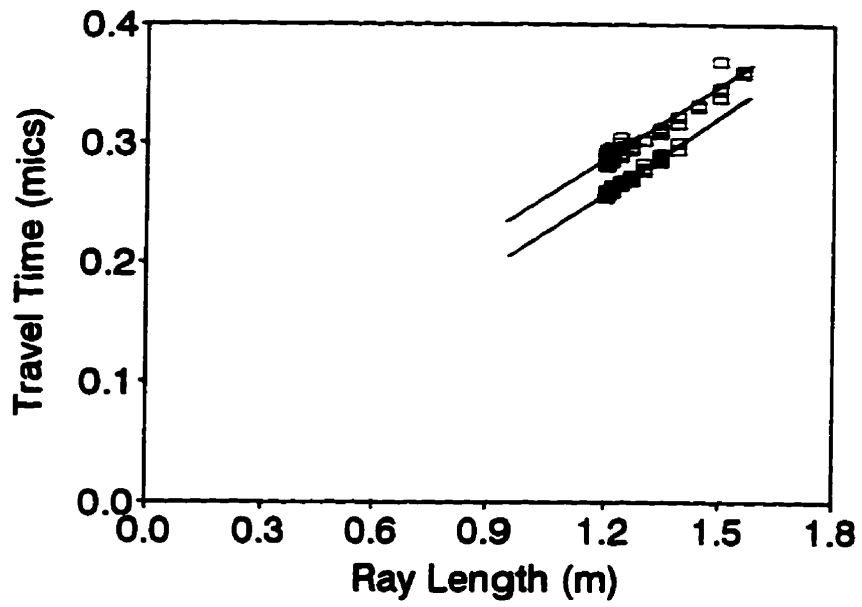
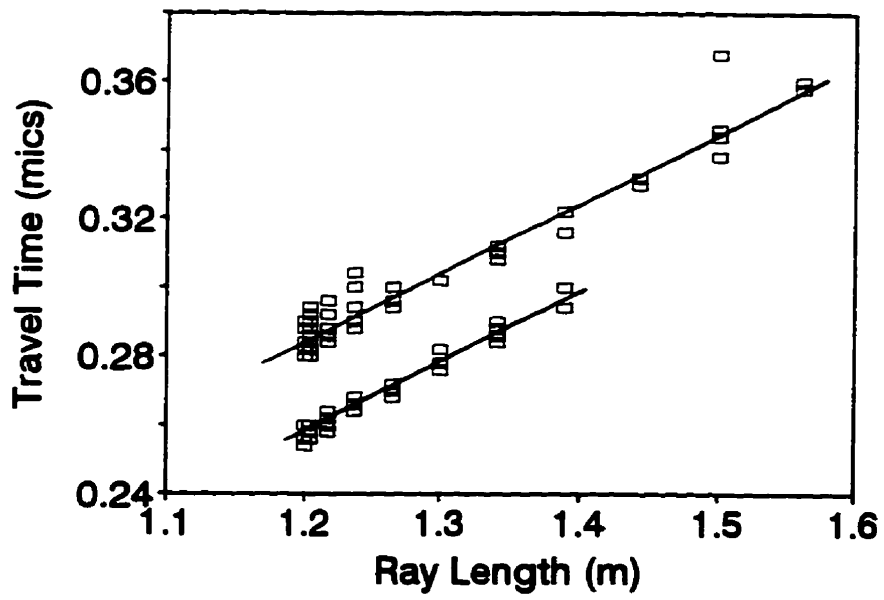


Figure 6-16: Distribution of information content for Concrete Crack (Side-to-Side shootings). Assuming straight ray paths.

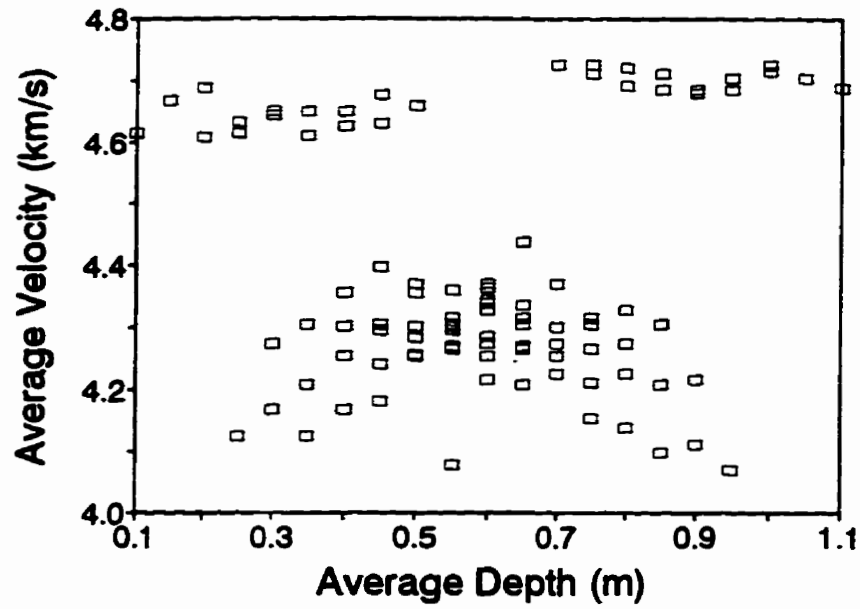


(a)

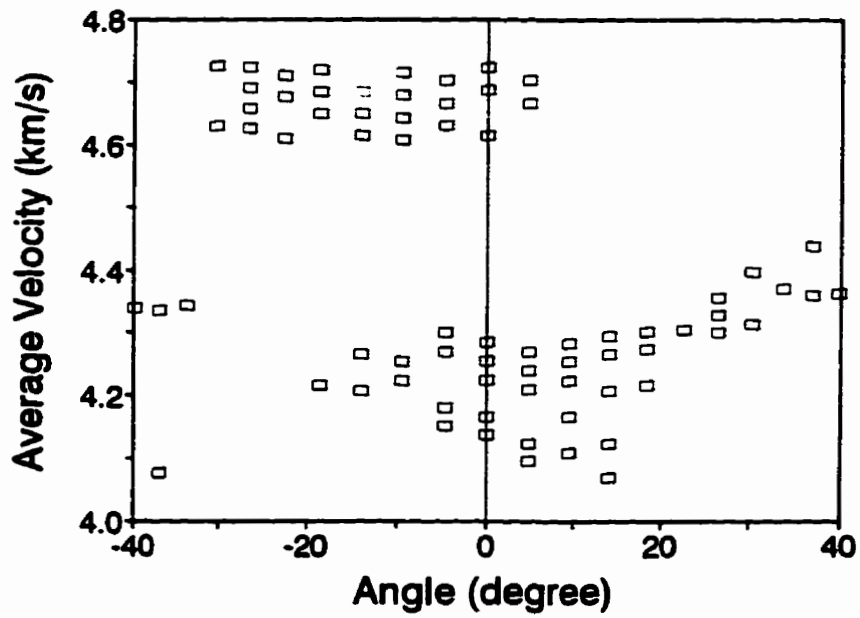


(b)

Figure 6-17: Systematic and accidental errors in Concrete Crack (Side-to-Side shootings).



(a)



(b)

Figure 6-18: Heterogeneity and anisotropy inspections for Concrete Crack (Side-to-Side shootings).

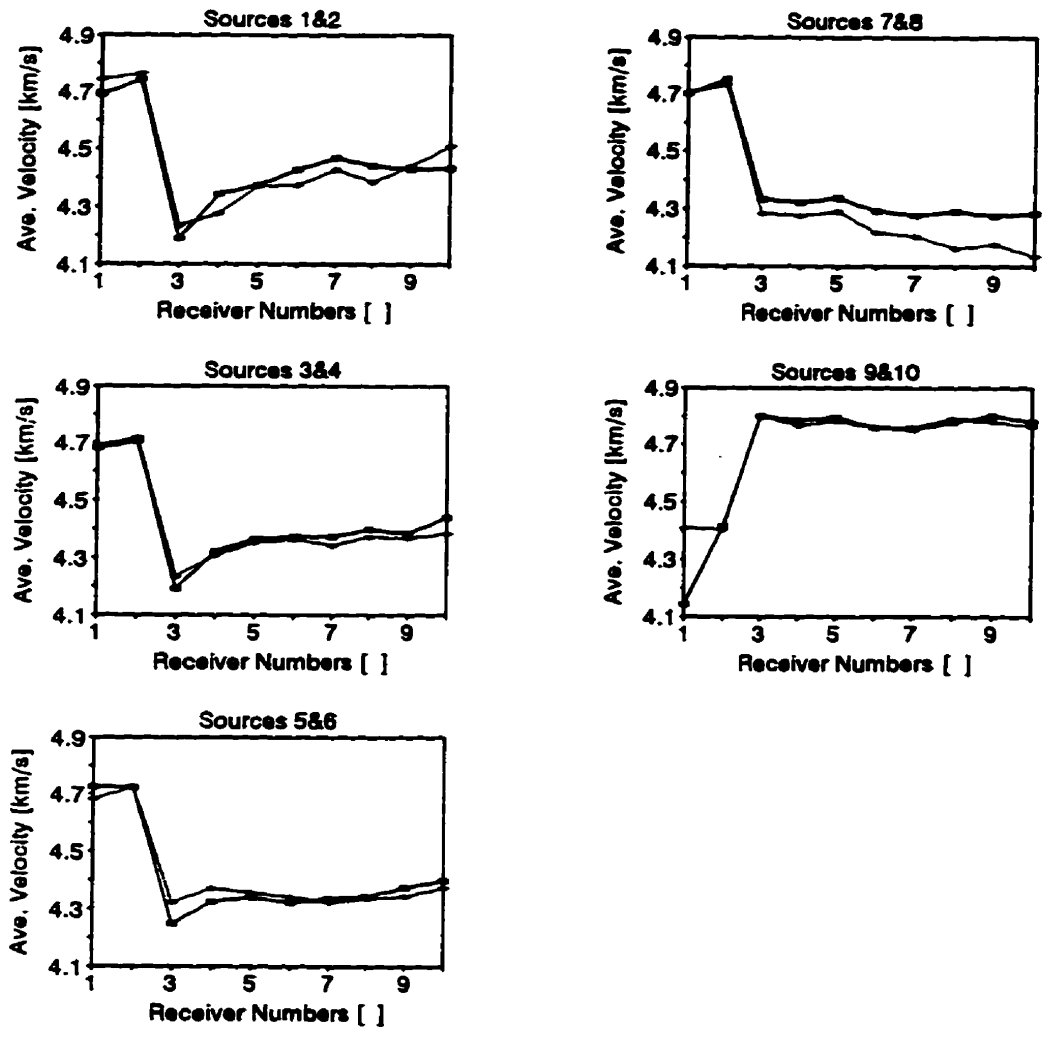


Figure 6-19: Analysis of shadows for Concrete Crack (Side-to-Side shootings).

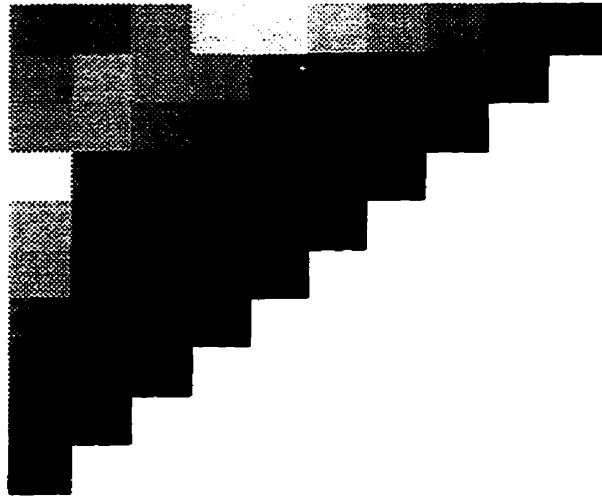
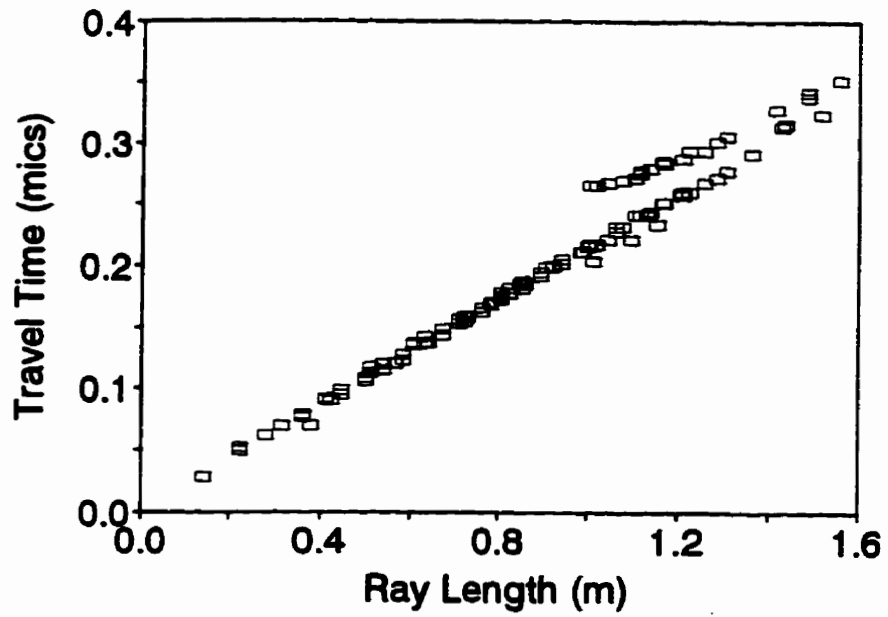
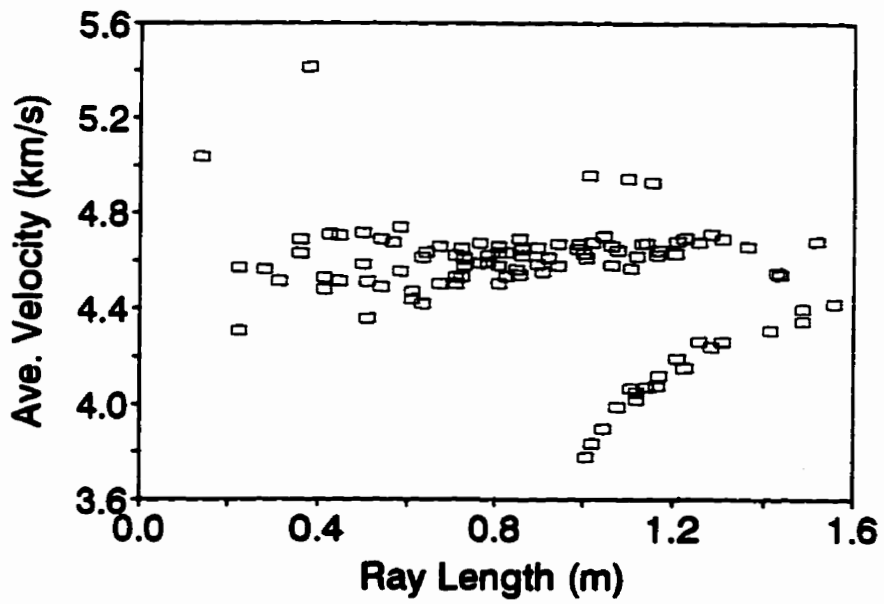


Figure 6-20: Distribution of information content for Concrete Crack (top to left-side shootings). Assuming straight ray paths.



(a)



(b)

Figure 6-21: Systematic error and heterogeneity inspections for Concrete Crack (Top to Left-Side shootings).

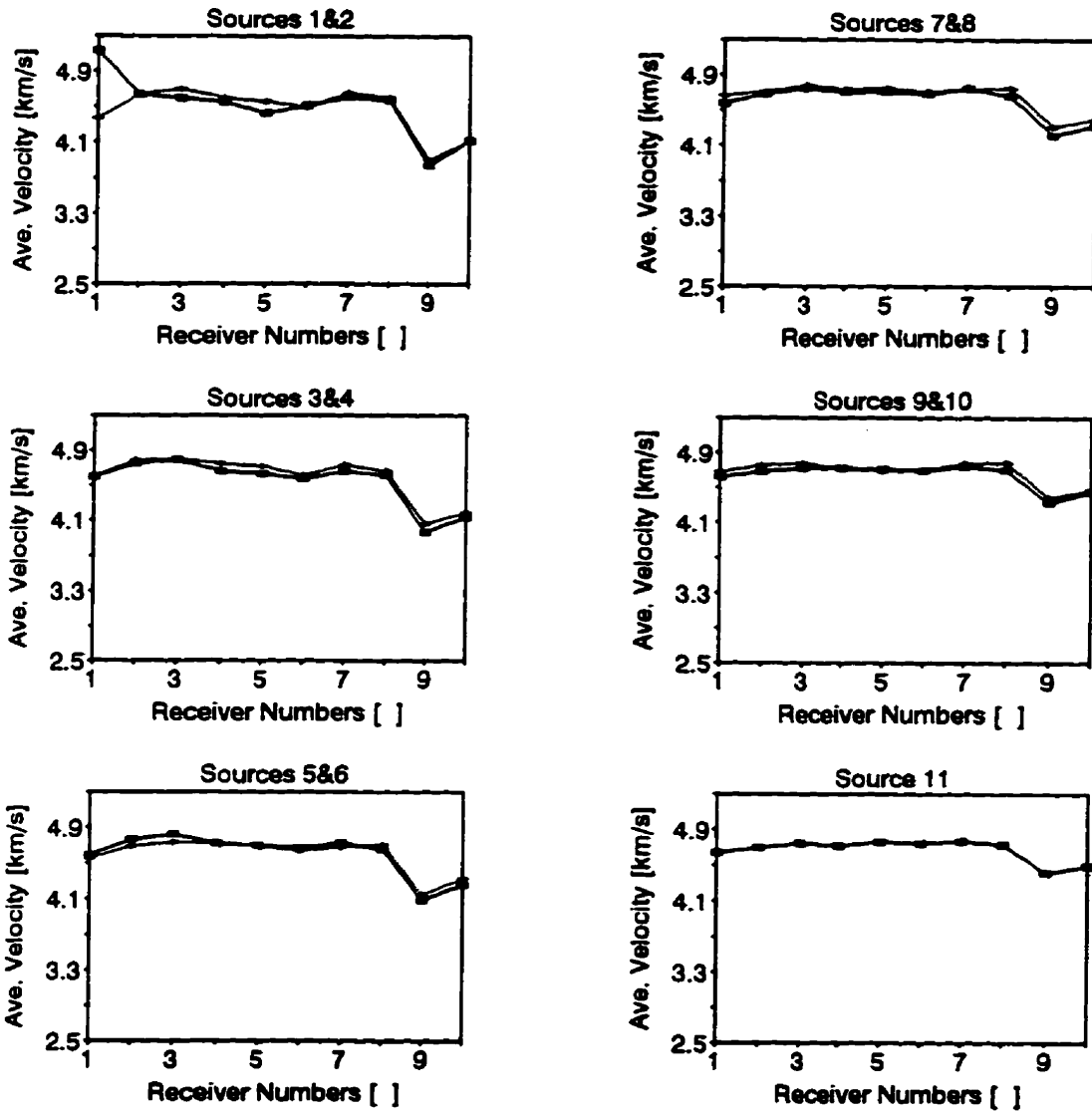


Figure 6-22: Analysis of shadows for Concrete Crack (Top to Left-Side shootings).

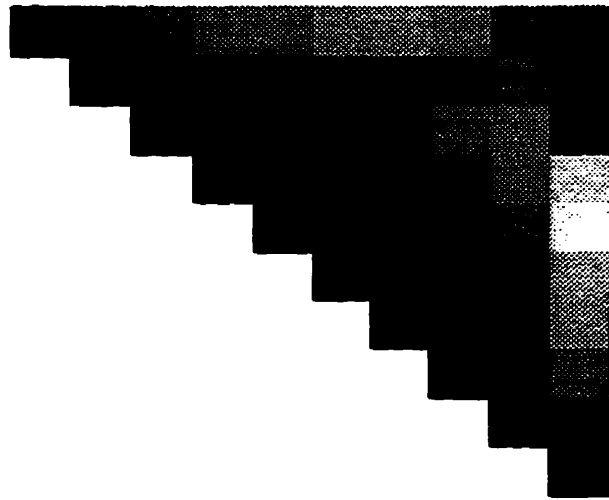
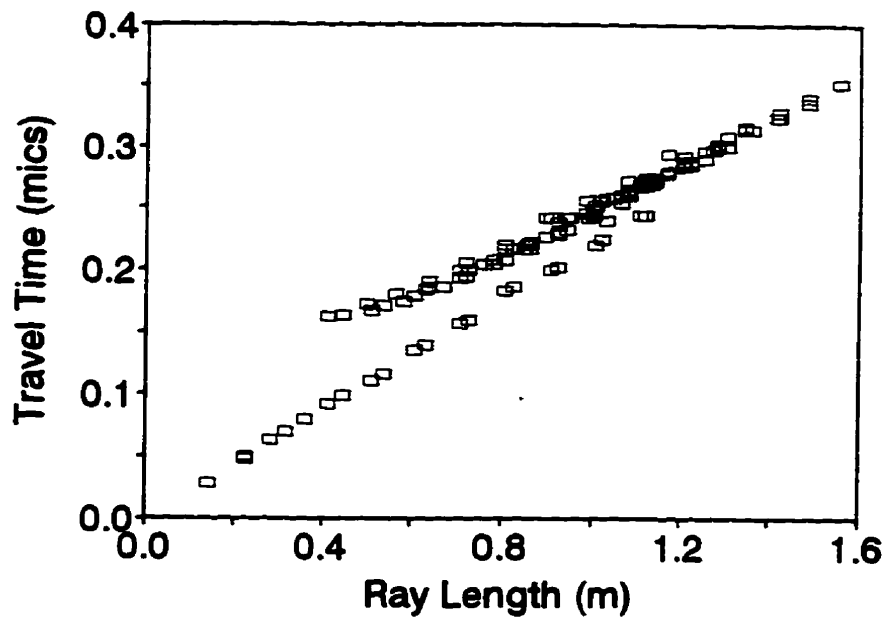
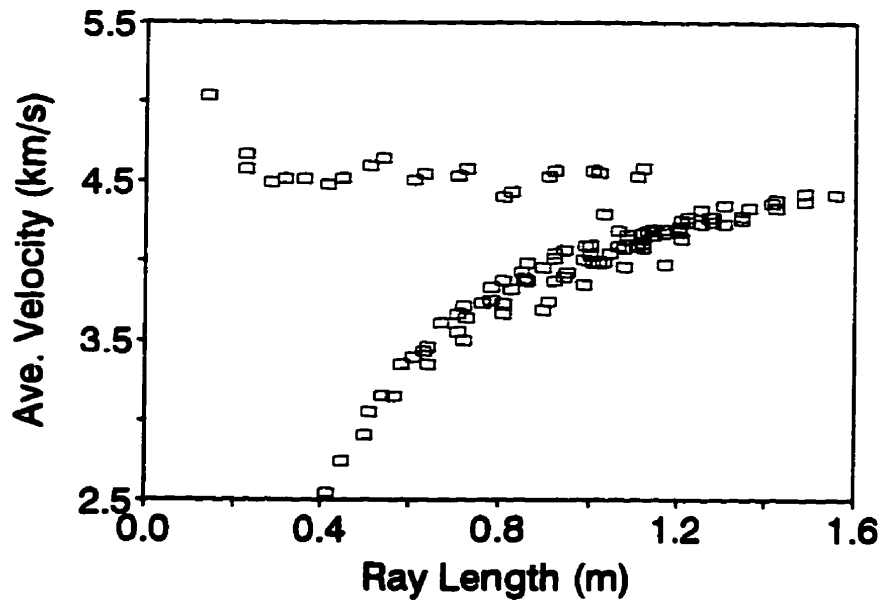


Figure 6-23: Distribution of information content for Concrete Crack (top to right-side shootings). Assuming straight ray paths.



(a)



(b)

Figure 6-24: Systematic error and heterogeneity inspections for Concrete Crack (Top to Right-Side shootings).

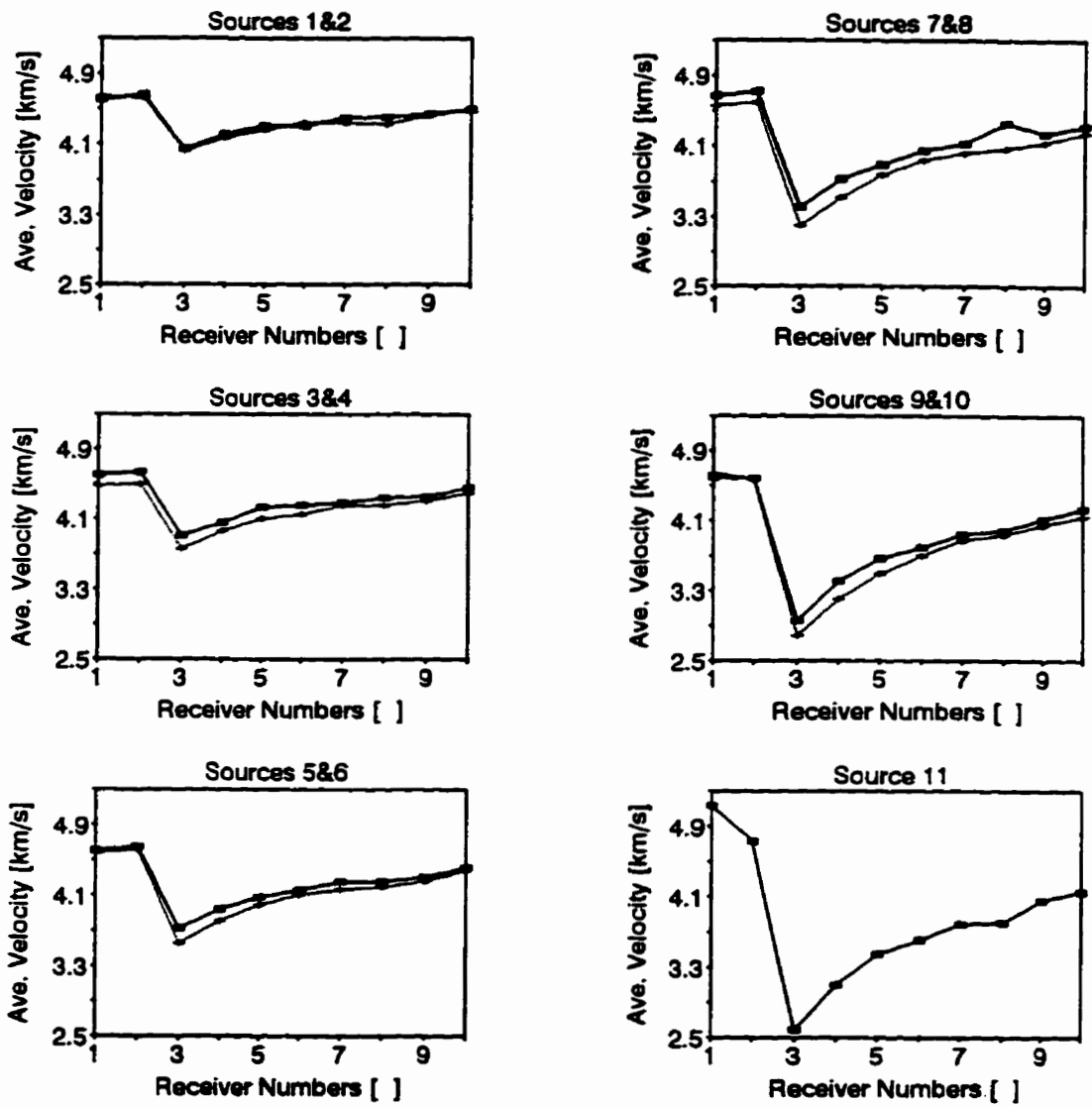


Figure 6-25: Analysis of shadows for Concrete Crack (Top to Right-Side shootings).

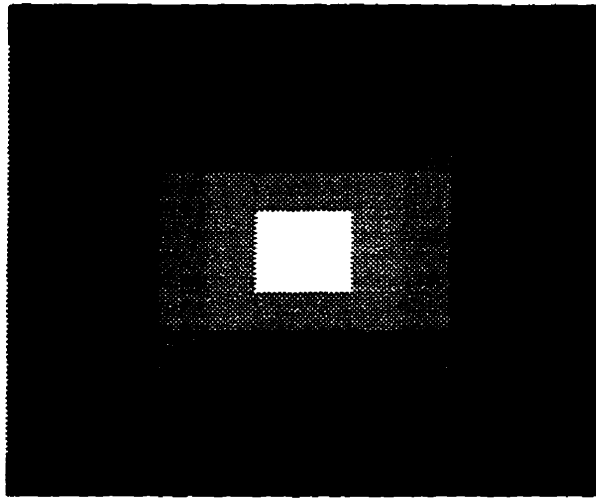
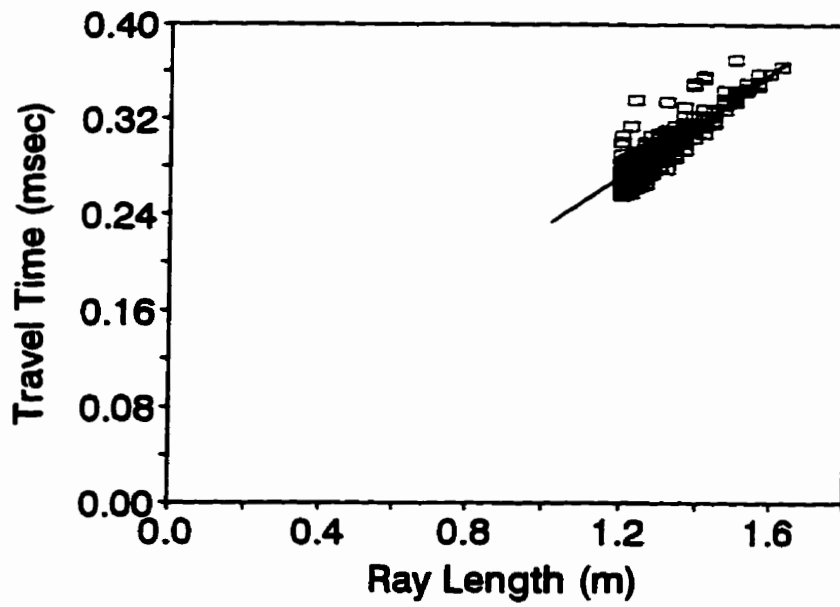
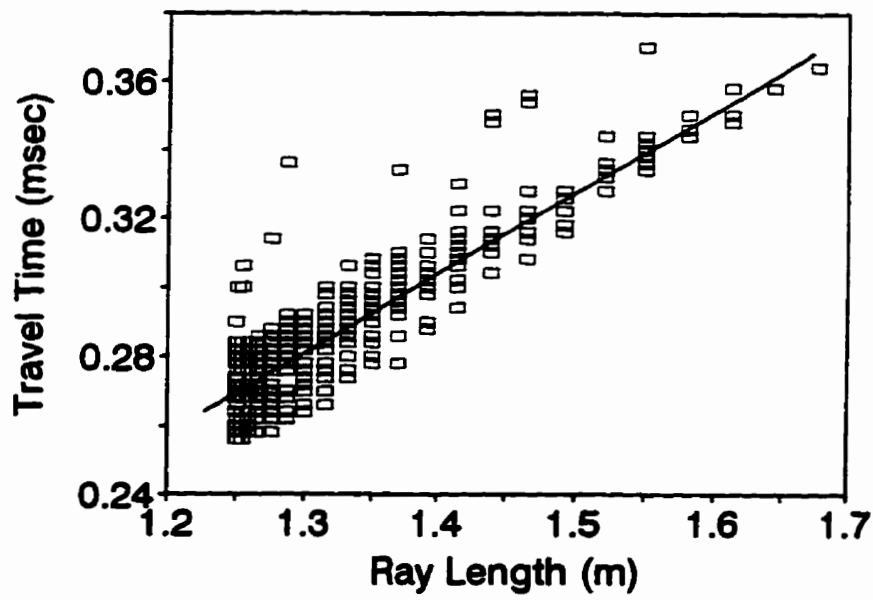


Figure 6-26: Distribution of information content for Concrete Column. Assuming straight ray paths.

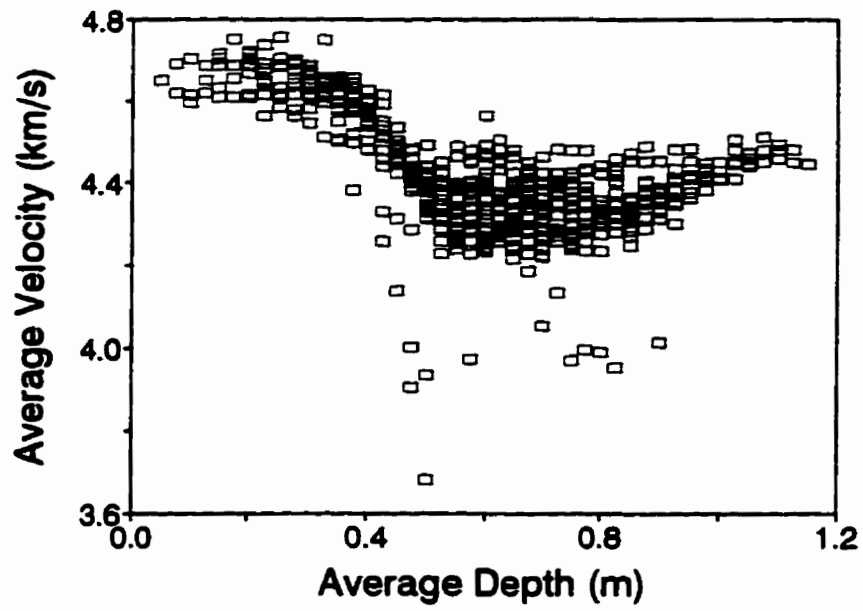


(a)

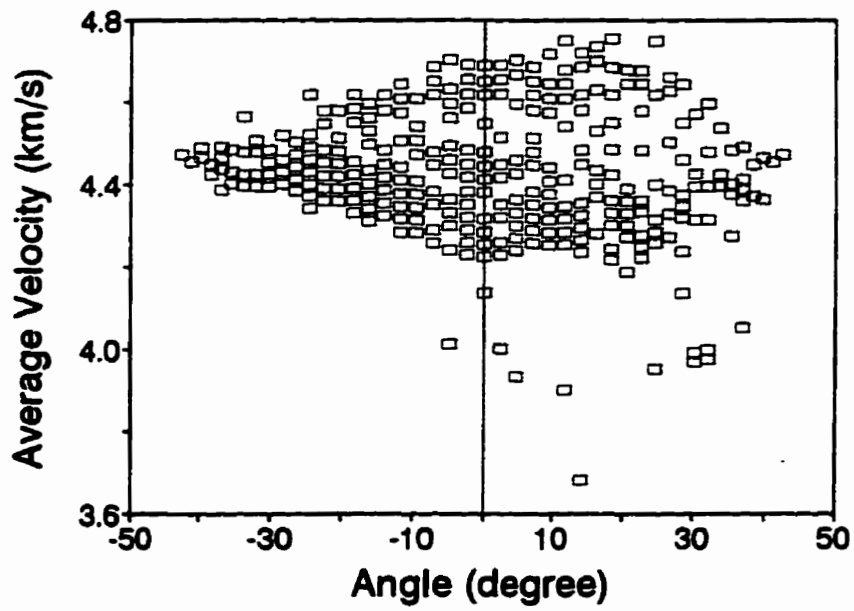


(b)

Figure 6-27: Systematic and accidental errors for Concrete Column.



(a)



(b)

Figure 6-28: Heterogeneity and anisotropy inspections for Concrete Column.

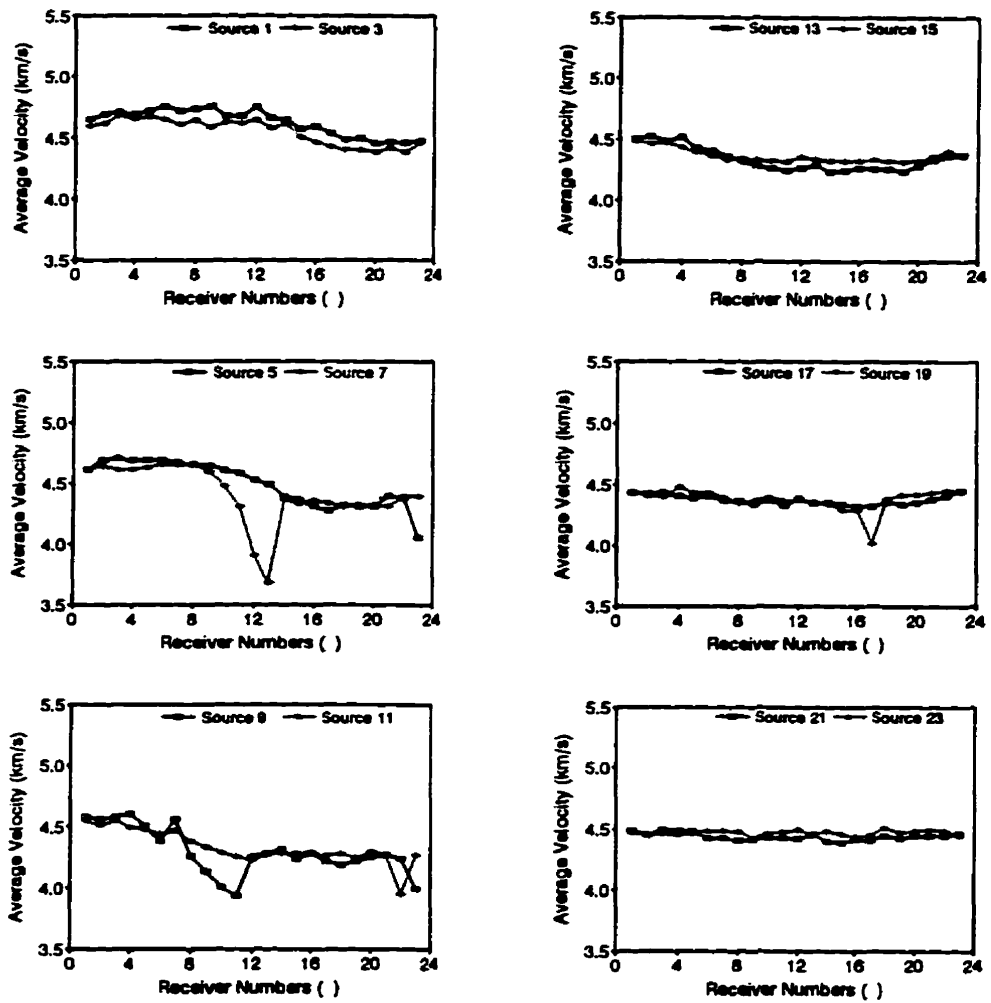
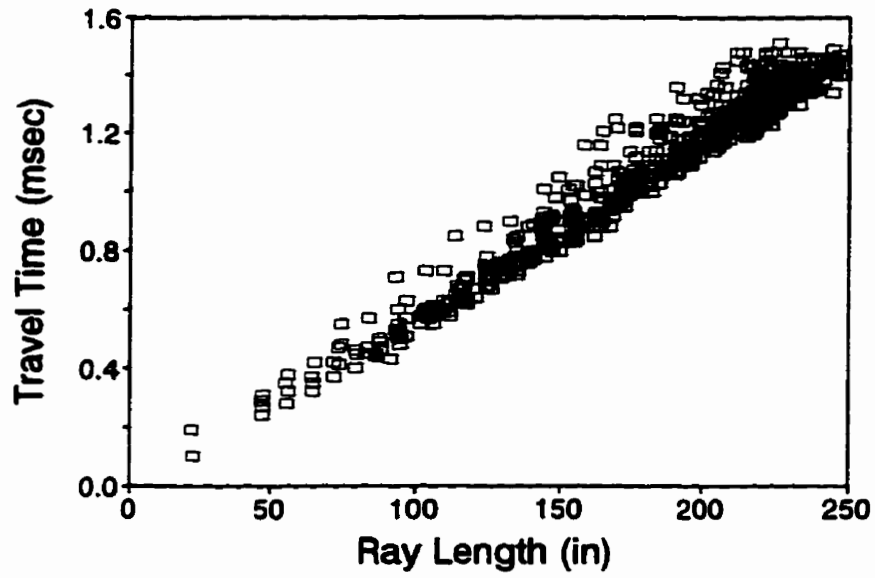


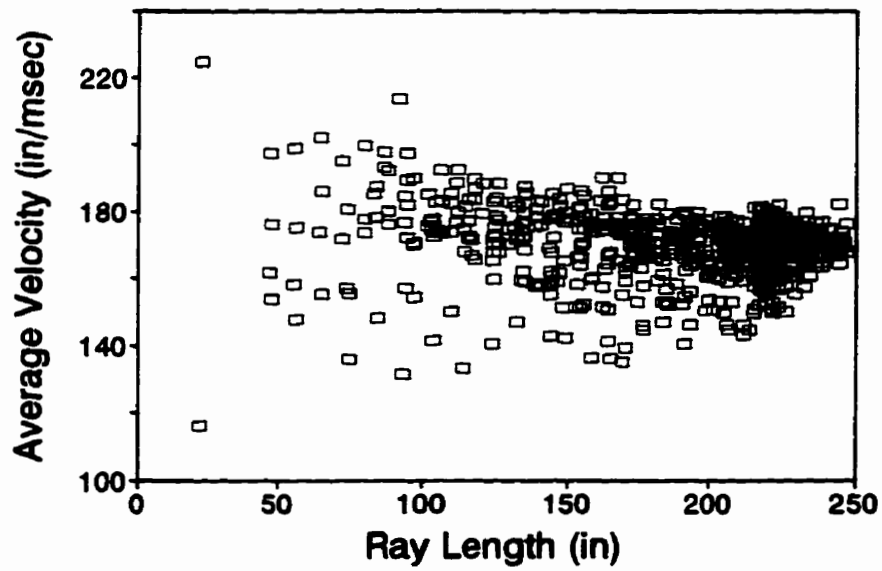
Figure 6-29: Analysis of shadows for Concrete Column.



**Figure 6-30: Distribution of information content for Kosciuzko bridge pier.
Assuming straight ray paths.**



(a)



(b)

Figure 6-31: (a) Systematic and accidental errors and (b) Heterogeneity inspections for Kosciuzko bridge pier.

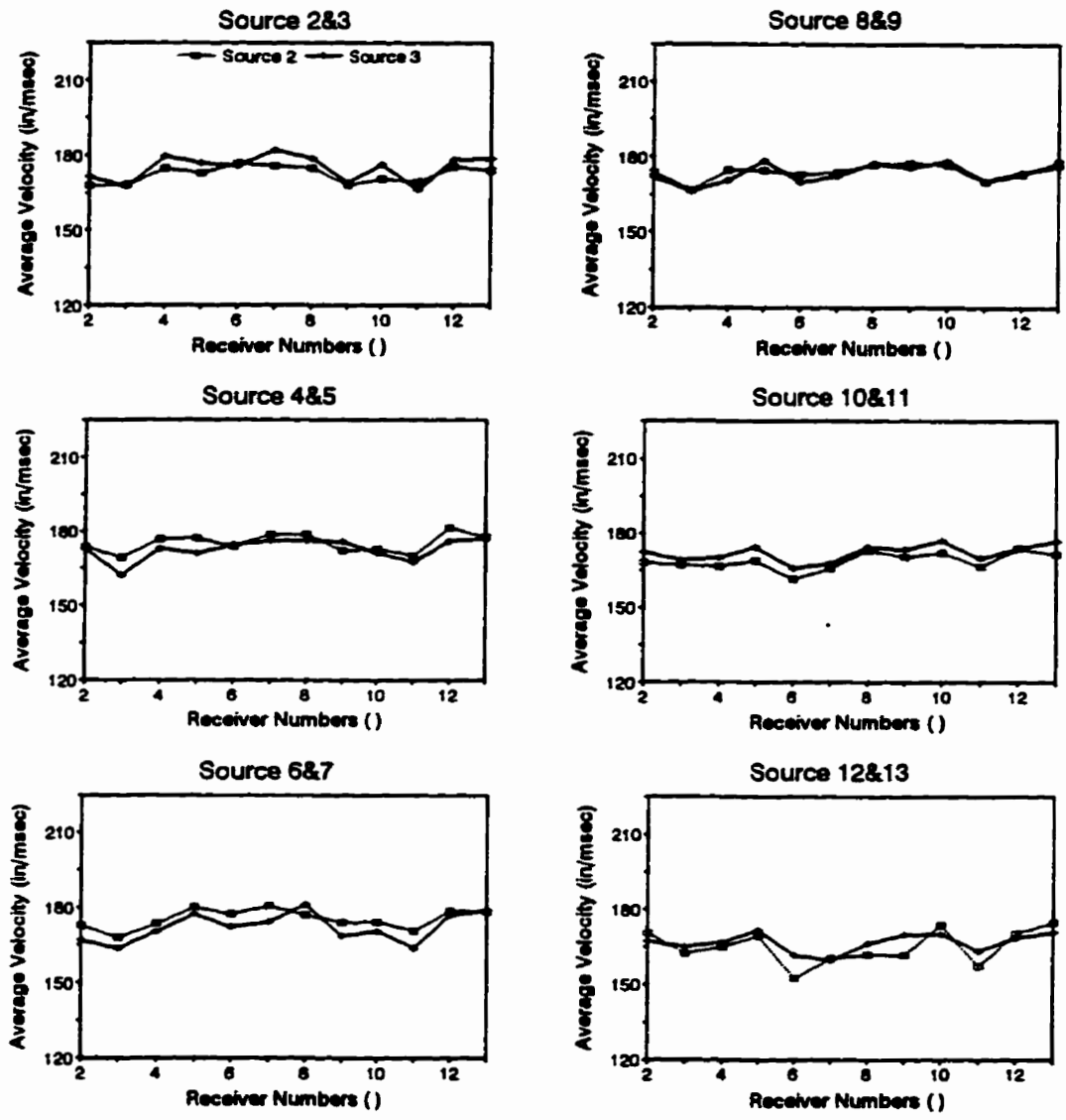


Figure 6-32: Analysis of shadows for Kosciuzko bridge pier (Top-to-Bottom shootings).

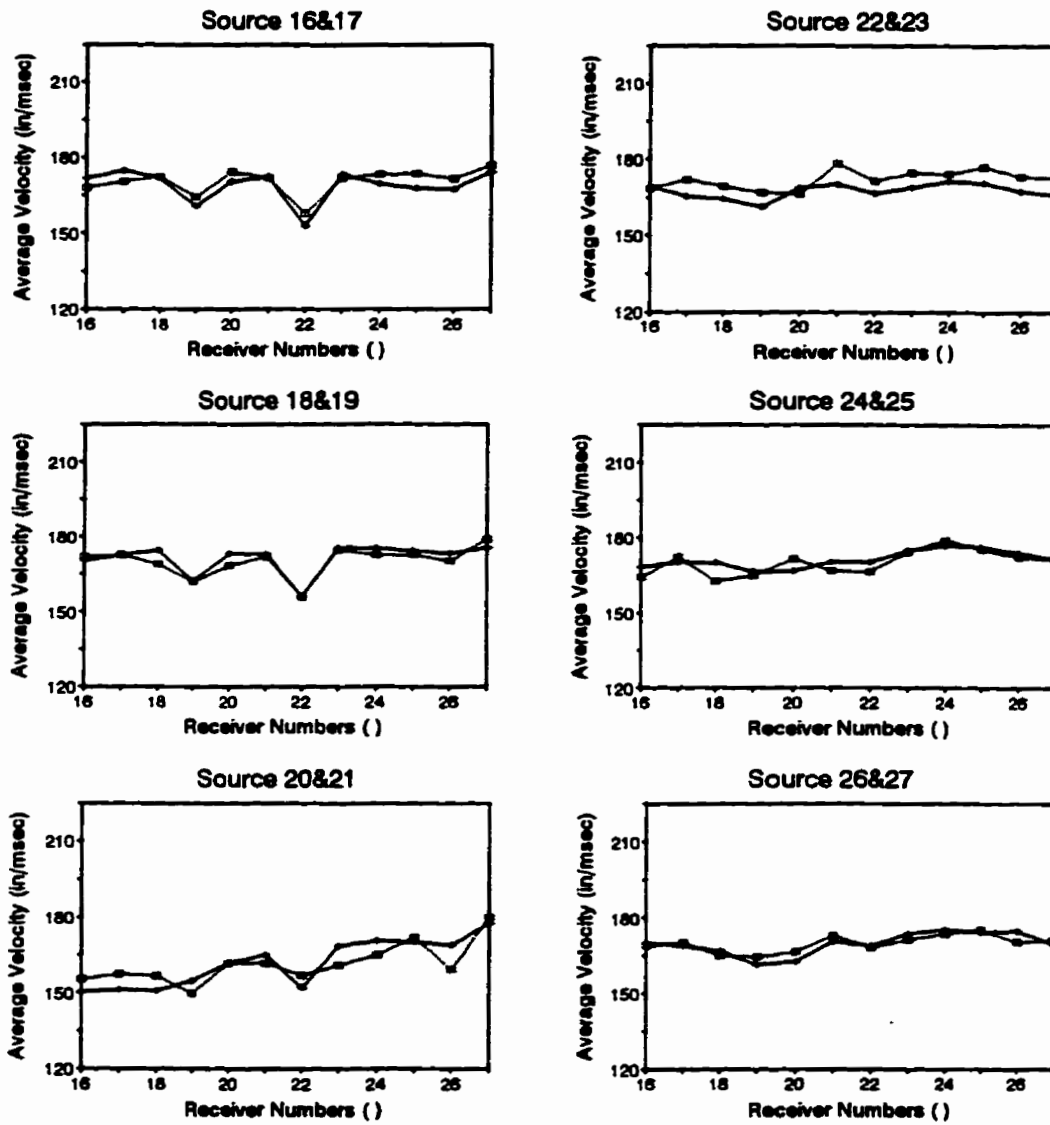


Figure 6-33: Analysis of shadows for Kosciuzko bridge pier (Side-to-Side shootings).

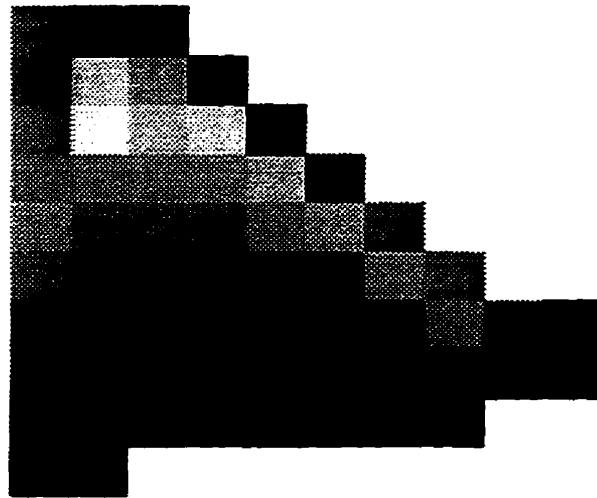
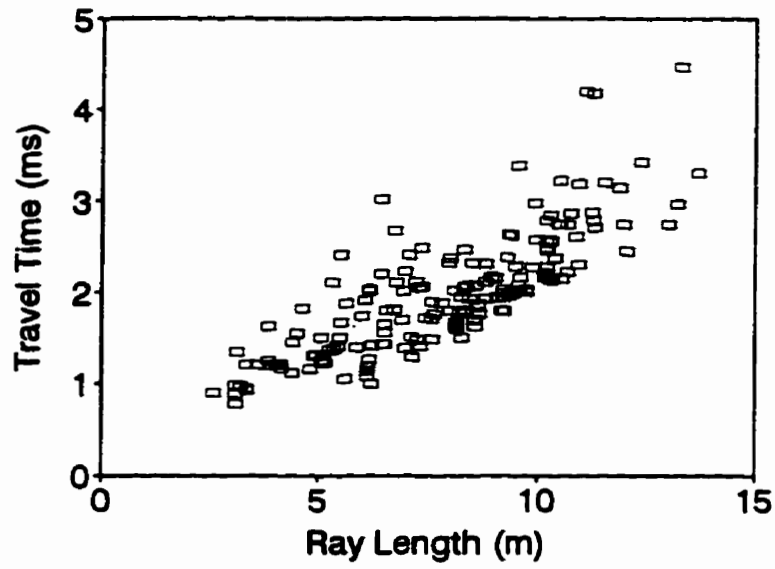
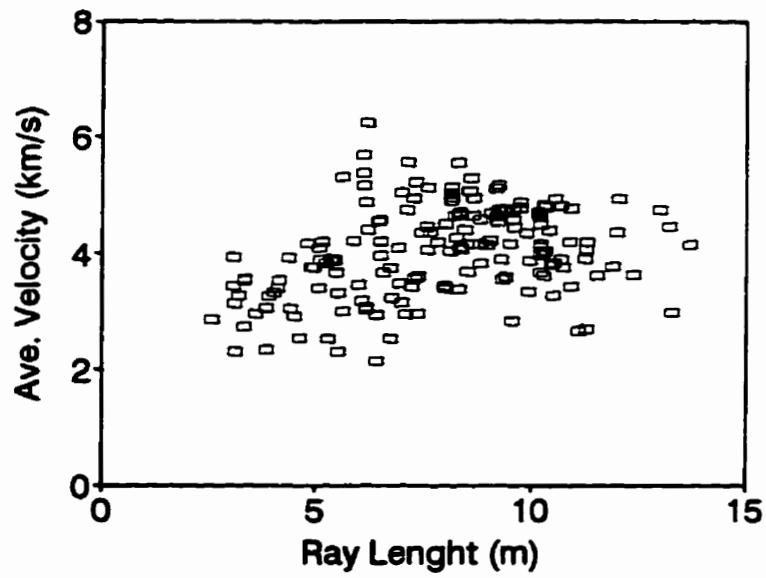


Figure 6-34: Distribution of information content for Chute Hemmings dam. Assuming straight ray paths.

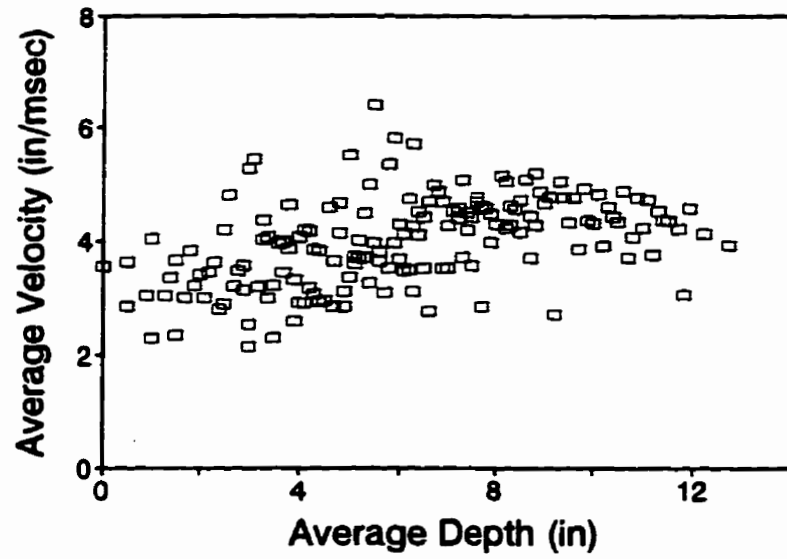


(a)

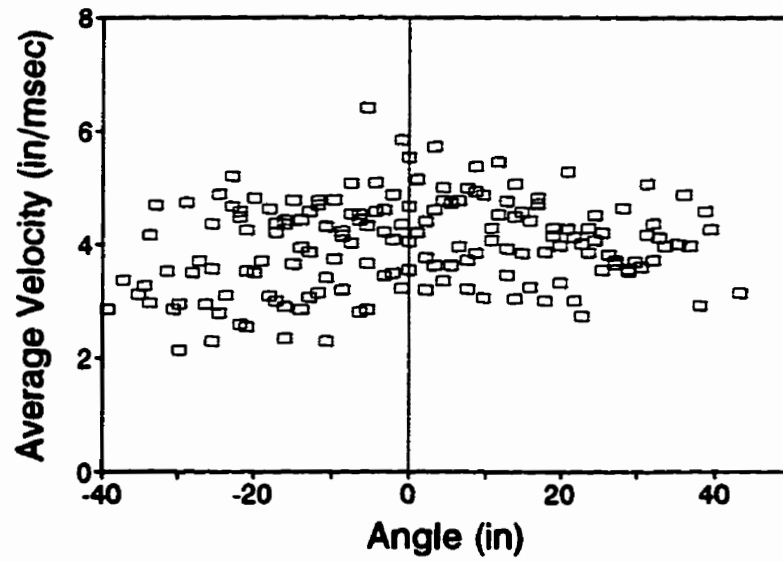


(b)

Figure 6-35: (a) Systematic and accidental errors and (b) Heterogeneity inspections for Chute Hemmings dam.



(a)



(b)

Figure 6-36: Heterogeneity and anisotropy inspections for Chute Hemmings dam.

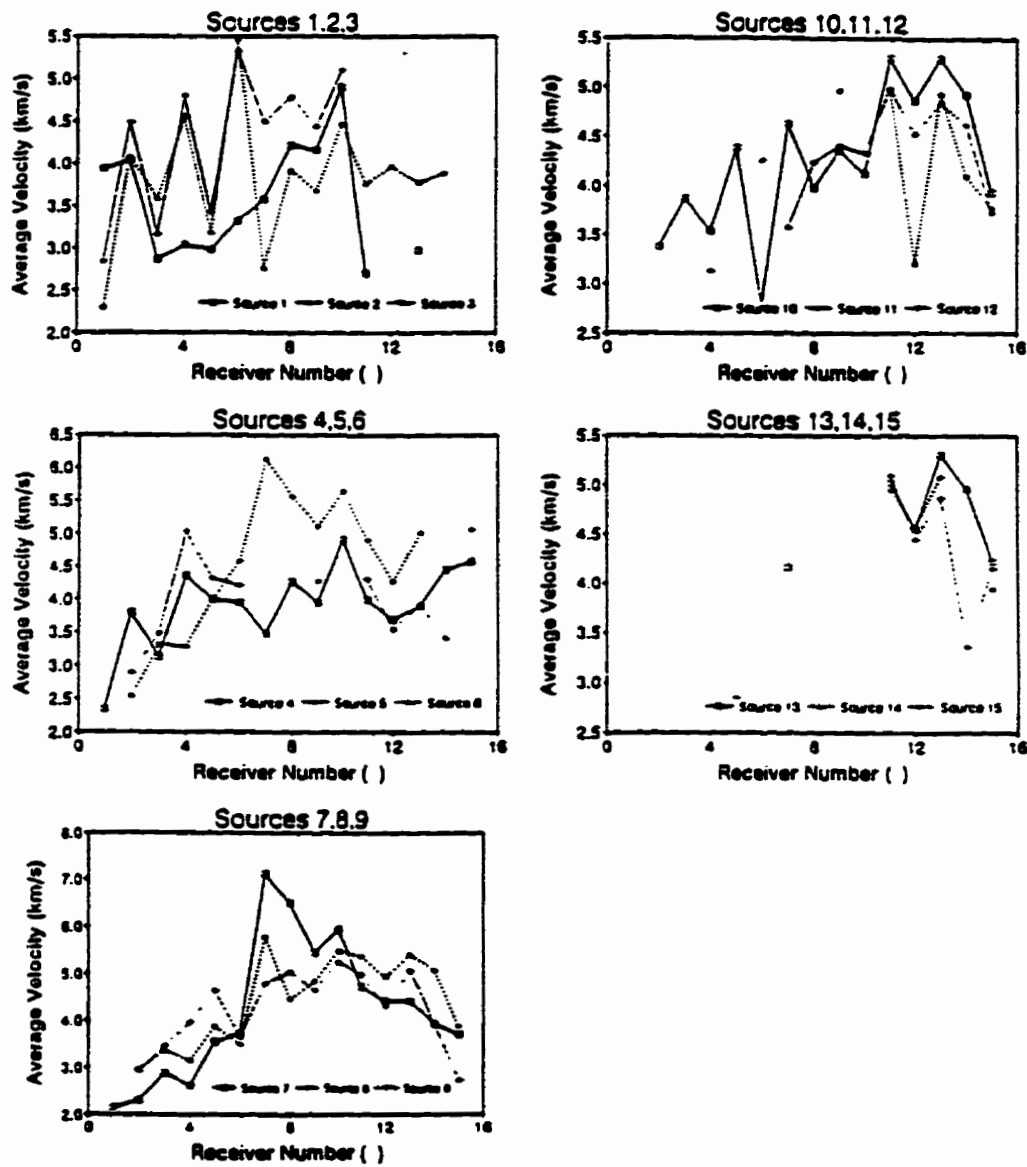


Figure 6-37: Analysis of shadows for Chute Hemmings dam.

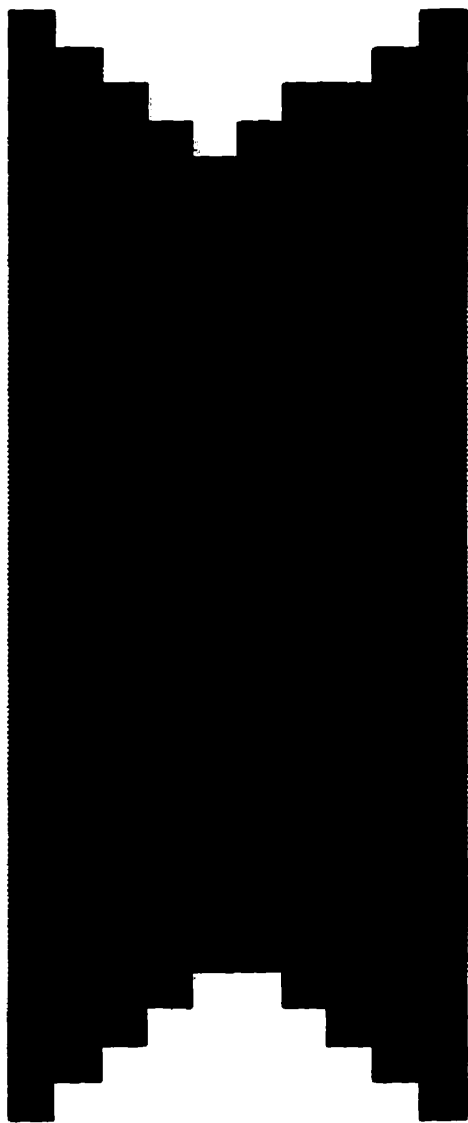
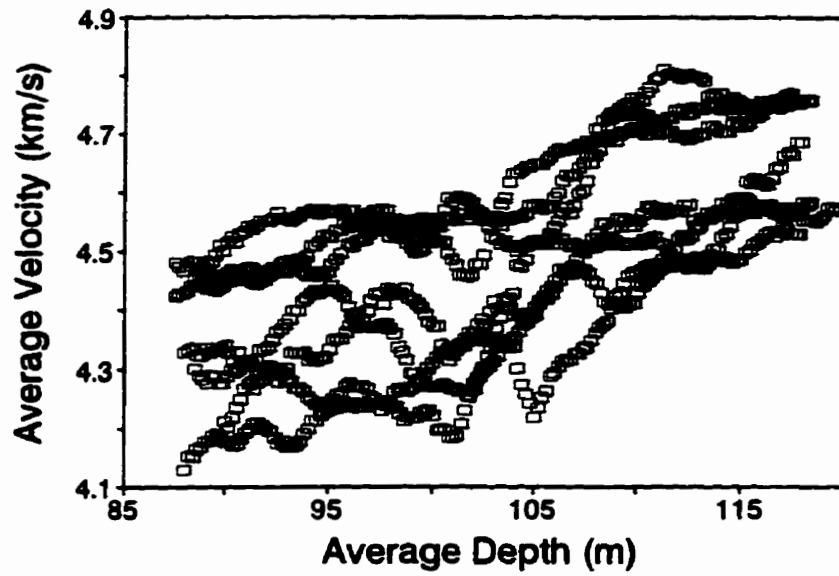
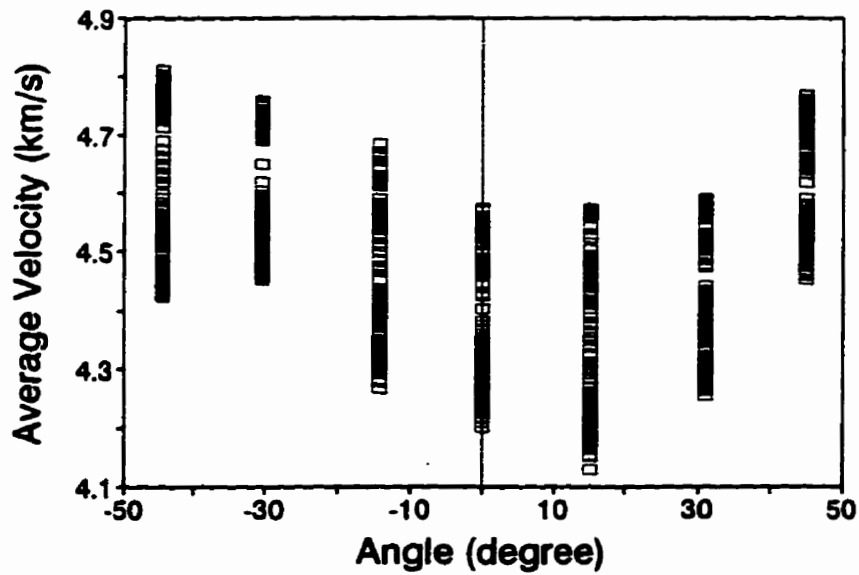


Figure 6-38: Distribution of information content for Korean DMZ. Assuming straight ray paths.



(a)



(b)

Figure 6-39: Heterogeneity and anisotropy inspections for Korean Demilitarized Zone.

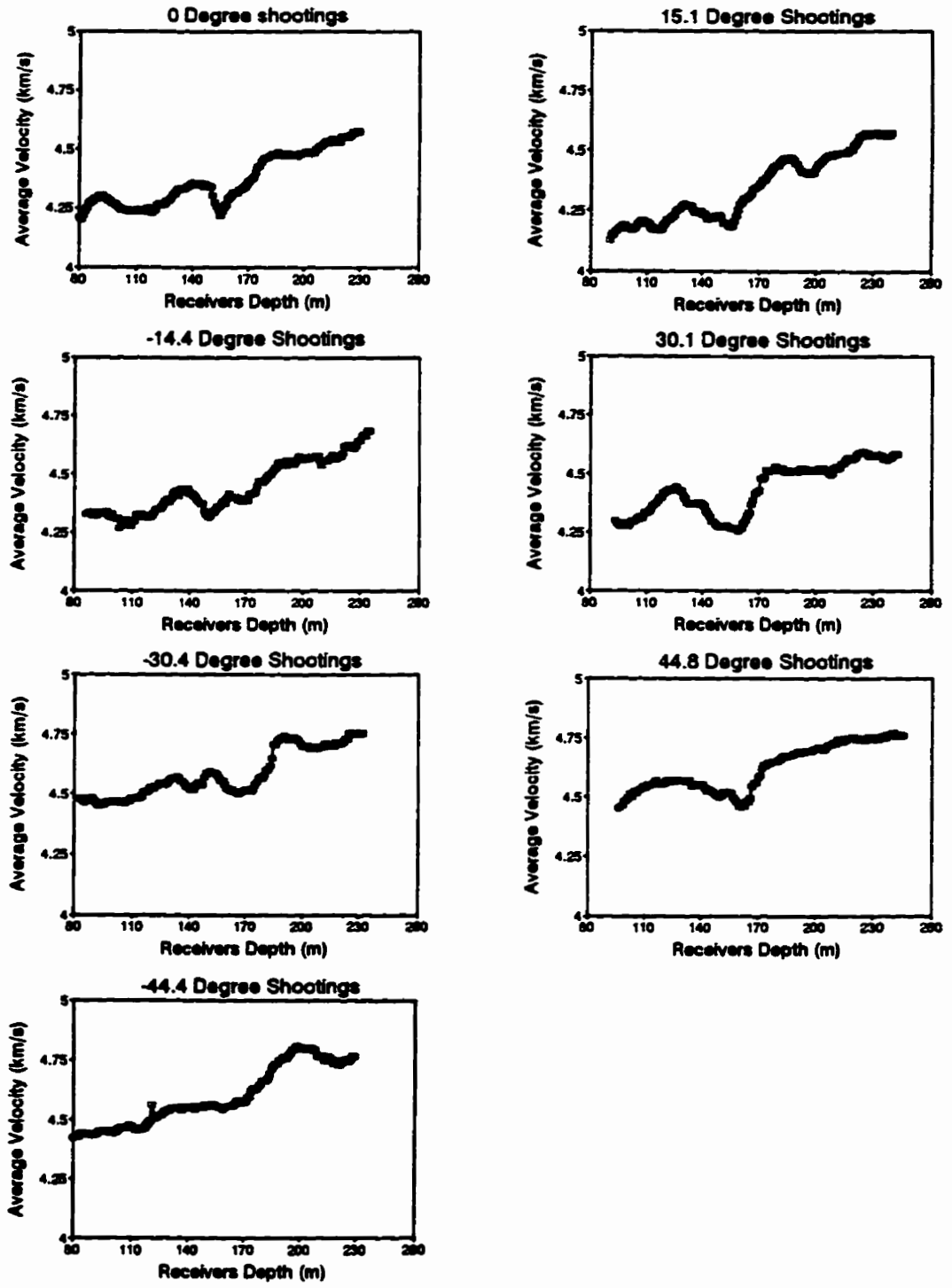


Figure 6-40: Analysis of shadows for Korean Demilitarized Zone.

CHAPTER VII

INVERSION OF CASE HISTORIES - OPTIMAL INVERSION STRATEGIES -

7.1 Introduction

Tomographic problems are usually mixed-determined, in which some linear combinations of the image parameters are over-determined and some are under-determined. Under-determination (or mixed-determination) and noise in the data make tomographic inversion problems ill-conditioned.

If the problem is under-determined, then the data contains information about only some parts of the image and no information is provided about the other parts, which is called the null space. In other words, the null space is not illuminated by the data (refer to distribution of information content for case histories in Chapter 5). Any choice of the image parameters can satisfy the data in the null space. The size of the null space is crucial, since it determines the degree of ill-conditioning of the problem and thus the number of mesh elements in the inversion process.

A priori information can be added to decrease the size of the null space, i.e., to specify those image parameters (unknowns) that reside in the null space. The DLSQ solution is a combination of the least squares and the minimum length solutions (refer to Chapter 2)

$$s = [L^T L + \eta^2 I]^{-1} L^T t \quad (7-1)$$

The method overcomes the singularity of the coefficient matrix. The “best solution” is obtained for a certain damping coefficient, which is case dependent.

In the case of a mixed-determined problem and noisy data, the regularization method is applied by adding information in the form of constraints (refer to Chapter 2),

$$s = [L^T L + \lambda^2 R^T R]^{-1} L^T t \quad (7-2)$$

Regularization can be performed in different ways. For example, if the solution must be smooth, the regularization matrix R is the second derivative operator. The “optimal regularization coefficient” that gives the best solution is not known in advance. Therefore, the optimal damping and regularization coefficients should be determined when the inverse problem is to benefit from DLSQ and regularization solutions. This chapter begins with a view of possible imaging errors. Then, procedures are investigated to determine optimal damping and regularization coefficients.

7.2 Null Space and Singular Values (Global Information)

Spectral decomposition or Singular Value Decomposition (SVD) is one of the possibilities to identify the size of the null space. As discussed in chapter II, any $n \times m$ matrix can be written as the product of three matrices:

$$L = U \Omega V^T \quad (7-3)$$

Matrix Ω is a diagonal matrix whose entries are called the singular values (ω_i^2). The number of non-zero singular values indicates the rank of the matrix, or the number of independent equations in the data space. On the other hand, the

number of zero singular values determines the size of null space. The problem is to assess how close should a singular value be to zero before it stops contributing to the solution.

The matrix U is an $n \times n$ matrix and its vectors are eigenvectors of LL^T and span the data space. The eigenvalues of LL^T are ω_i^2 . The matrix V is an $m \times m$ matrix and its vectors are eigenvectors of $L^T L$ and span the image parameter space. The eigenvalues of $L^T L$ are ω_i^2 .

One way to determine the size of the null space is to plot the sizes of the singular values against their index numbers (Figure 7-1). This is the spectrum of the data kernel. As shown in the figures, the selection of the cut-off point may be fuzzy. If small singular values are considered, the solution variance will be very large since it is proportional to $1/\omega_i^2$ (refer to Equation 2-10). On the other hand, excluding small singular values results in degraded image resolution.

Plots of the sizes of the singular values against their index number for three case histories are shown in Figure 7-2. It can be seen that the global information content can be much less than expected from the number of rays.

Figure 7-3 shows the effect of adding *a priori* information, using regularization, on the size of the null space of Balloon 1 data (Figure 5-1a) . The number of zeros decreases with an increase in regularization coefficient.

7.3 Damped Least Squares Solution - Optimal η

Simulated cases (Figure 7-4) were investigated to determine the optimal damping coefficient η . Straight paths were used, therefore, the matrix L is the same in all cases. Results are evaluated in terms of the average absolute error

(AAE) in pixel velocity between the input (real) image and the inverted output (inverted) image (normalized with respect to the average pixel velocity).

$$AAE\% = \frac{\sum_{pixels} |v_i^{real} - v_i^{inv}|}{m} * \frac{1}{V_{ave}} * 100 \quad (7-4)$$

Results for the four simulated cases in Figure 7-4 are presented in Figure 7-5. It can be seen that the quality of the image worsens with either lack or excessive damping, and that optimal damping is not unique but depends on the velocity field.

7.4 Regularization Solution - Optimal λ

The previous cases were investigated to determine the optimal regularization coefficient λ . Straight paths were used in all cases. Figure 7-6 shows the results in terms of average absolute error in pixel velocity. It can be seen that the optimal regularization coefficient for each case is different and depends on the velocity field.

7.5 Damped Least Squares vs. Regularization - Noisy Data

Simulated data obtained with straight-rays for the high velocity central anomaly (Figure 7-4a) were made “noisy”, first by adding random noise $t_i = t_i + md(1)$, and second, by adding a proportional systematic error $t_i = t_i + 0.5$ where 0.5 is about 5% of t_{ave} . The noisy data set was inverted using damped least squares and regularization.

Damping and regularization coefficients η and λ were gradually changed until optimal images were obtained. Mathgrams 7-1 to 7-4 show the optimal solutions for each case.

Results indicate that regularization, in comparison to DLSQ, is an effective alternative to lessen the problem of noise (systematic and random cases) in mixed-determined problems. Furthermore, it is seen that both methods give better solutions in the case of presence of systematic noise (error) rather than random noise (error) presence.

7.6 Regularization - Straight and Bent Rays

The high velocity helium balloon in Figure 5-1d was inverted with different values of the regularization coefficient λ , using straight rays. The resulting pixel values were used to re-trace rays for a second iteration with bent rays. The second inversion for each set was repeated with the same regularization coefficient used in the corresponding first iteration.

The average square error ASE in pixel velocity between inverted images and the known real pixel velocities are plotted versus the regularization coefficient λ in Figure 7-7, where

$$ASE\% = \sqrt{\frac{\sum_{\text{pixels}} (v_i^{\text{real}} - v_i^{\text{inv}})^2}{m}} * \frac{1}{V_{\text{ave}}} * 100 \quad (7-5)$$

The increase in regularization diminishes the effect of high pixel variability and the squared error ASE. However, excessive regularization flattens pixel values within the anomaly, increasing the deviation of the image from the true condition. Curved rays magnify the effect of variability at low λ ; however, they lead to better

images for all values of λ above a threshold of smoothness. This plot highlights the underlying trade-off between resolution and variance. A similar study was conducted with a smaller high velocity anomaly placed off-center left (Figure 5-1a). The result was identical to the one shown in Figures 7-7. Tomograms for these two cases are shown in Figure 7-8. It is important to highlight that these data could not be successfully inverted with standard ART and SIRT algorithms.

7.7 Optimal λ in Real Situations (Unknown Solution)

The optimal coefficient of regularization is case dependent, and must be determined by comparing data and image/model parameters. Several guidelines have been proposed (Morozov, 1993; Hansen 1992). The same study conducted in Figure 7.7 was analyzed, but recognizing that in real situations the “true image” is “unknown”; thus, inversion-based results must be used. The coefficient of variation for pixel values in each image is plotted in Figure 7-9. The coefficient of variation (COV) is the ratio of the standard deviation and the mean of pixel values. The figure shows three regions: high variability for low λ , very low variability for high λ (the velocity field becomes uniform for excessive smoothing), and an intermediate region with acceptable inversions for a relatively wide range in regularization coefficient λ .

Inversions with curved rays lead to higher variability because they tend to preserve the contrast in the region. However, the trend of COV vs. λ is very similar in both cases. Thus, optimal regularization coefficients can be selected with straight rays.

Criteria were evaluated for the side-to-side shootings case in concrete crack data. Results are presented in Figure 7-10. Figure 7-10a shows the change in

the coefficient of variation of pixel slowness with the coefficient of regularization. This definition of COV(s) is based on the whole set of pixel slownesses, and tends to promote global smoothness. An alternative approach is to define local measures of variability. The difference in slowness between a pixel and its local average is

$$\Delta s_i = \frac{1}{8}(s_u + s_d + s_l + s_r + 4s_i) - s_i \quad \text{or} \quad \underline{\Delta s} = \frac{1}{8} \underline{R} \cdot \underline{s} \quad (7-6)$$

The plot of $\|\Delta s\|$ with the coefficient of regularization shows a similar trend as observed in Figure 7-10a. On the other hand, over-smoothness increases the residual $\|Ls-t\|$. Following Hansen (1992), Figure 7-10b shows L-shape curve of norm of the local error $\|R_s\|$ vs. the residual $\|Ls-t\|$ for different regularization coefficients.

The coefficient of regularization can be selected to correspond to the value where these measures of image/solution adequacy change, e.g., the maximum curvature of the L-shape curve (Hansen and O'leary, 1993). Images reconstructed with regularization coefficients close to the break in these curves were visually analyzed ($0.001 < \lambda < 0.01$). The optimal image was generated with regularization coefficient $\lambda=0.005$. The value of λ at the break in $\|R_s\|$ -vs.- $\|Ls-t\|$ curves leads to under-smoothed images.

7.8 Statistical Parameter Estimation - Maximum Likelihood

The statistical parameter estimation techniques incorporate several methods that use certain measurements of a system and estimate other parameters associated with the system. Parameter estimators use knowledge of the system and sample data. In a tomographic inversion, these methods can be employed to estimate the image values using gathered data. The maximum likelihood

method is one such technique that can be employed to estimate the required system parameters.

The maximum likelihood method asserts that the optimum values of the system parameters maximize the probability that the observed data are in fact observed. Therefore, if the data have a certain statistical distribution, then the best system parameters are those which give the maximum probability for that distribution. For instance, if the data are Gaussian, their distribution can be characterized in terms of a variance and a mean. In this case, the system parameters can be found by selecting different variance and mean values until maximum probability is obtained.

In the case of using DLSQ or regularization, the unknown parameter is optimal damping or regularization coefficient for a certain image. While the previously mentioned methods used slowness to determine optimal coefficient, the ML method can be employed to determine the optimal coefficient based on assuming a certain distribution for travel times (data). In this case, the optimal coefficient is the one which gives the maximum value of the joint distribution of the observed data (t_{obs}) and computed data ($t_{comp}=L_{comp} \cdot S_{inv}$), during a forward process using the inverted image values. In fact, the joint distribution gives the correlation between these two data sets.

To assess the distribution of a tomographic data set, the histograms of travel times are evaluated. The number of appearances are computed for each of 10 ranges between the highest and the lowest measured travel times. Figures 7-11 and 7-12 show the plots for case histories discussed in Chapter V.

A common characteristic of all side-to-side data is a peak value at the beginning followed by a slight decrease at the end. The data distribution is different for the top to side data (ref. to crack data in Figure 7-11b&c).

Assuming Gaussian distributions for the observed data t_{obs} and computed data t_{comp} in the linear inverse problem $Ls=t$, their joint distribution can be characterized as:

$$P(t) = [\text{cov}(t_{obs}, t_{comp})]^{-1/2} (2\pi)^{-n/2} \exp\left[-\frac{1}{2}(t-Ls)^T [\text{cov}(t_{obs}, t_{comp})]^{-1}(t-Ls)\right] \quad (7-7)$$

where n is the number of data (rays) (Menke, 1984).

The results for the small balloon (Balloons 1 to 3) data (Figure 5-1a, b, and c) are presented in Figure 7-13. The plots show a flat area followed by a sudden decrease in the probability values as the regularization factors are increased. The optimal regularization factor can be evaluated at the intersection point of the two best lines passing through the data points in these two areas. The results show under-smoothed images similar to the L-shape method.

The results for the concrete crack data (Figure 7-14) are the same as the previous cases; except for the side-to-side data, the two lines are hardly distinguishable (Figure 7-14a).

The exponential distribution is an alternative to the Gaussian distribution. The exponential distribution has a longer tail and sharper peak than the Gaussian distribution (Figure 7-15). Assuming exponential distributions for the observed and computed data in the linear inverse problem $Ls=t$, their joint distribution can be characterized as:

$$P(t) = [\text{cov}(t_{obs}, t_{comp})]^{-n/2} (2)^{-n/2} \exp\left[-(2)^{1/2} [\text{cov}(t_{obs}, t_{comp})]^{-1} |t-Ls|\right] \quad (7-8)$$

where n is the number of data (rays) (Menke, 1984).

The results for the small balloon data (ref. to Figure 5-1a,b,and c) give the

exact optimal regularization coefficient (λ) as a peak for all three cases (Figure 7-16). However, a higher peak (post peak=0.05) is apparent in Figure 7-16c (Balloon 3, center balloon). Figure 7-17 gives the inverted images for Balloon 3 case with optimal $\lambda=5$ and $\lambda=0.05$ (post peak). It can be realized that the inverted image with $\lambda=0.05$ is under-smoothed. Therefore, for the purpose of programming, the safe way to evaluate optimal regularization coefficients is to start with large regularization values. The optimal value is the first available peak.

Figure 7-18 shows the plots for crack data. The optimal value for top-to-side data is correctly evaluated (Figure 7-18b&c). However, the optimal value for side-to-side crack data (Figure 7-18a) is underestimated.

It is appropriate to inquire why the exponential distribution gives more accurate results than the Gaussian distribution. In fact, the exponential distribution has the same relationship to the L_1 norm as the Gaussian distribution has to the L_2 norm. If the data are very accurate, then the fact that one prediction falls far from its observed value is important. A L_2 norm is employed, since it weights the larger errors preferentially. On the other hand, if the data are expected to scatter widely about the trend, then no significance can be placed upon a few large prediction errors. A L_1 norm is used, since it gives more equal weight to errors of different size. A long-tailed distribution, like pure tomographic data (Ref. to Figures 7-11 to 7-12a), implies many scattered data points, and therefore an exponential distribution is more appropriate.

7.9 Tomographic Inversion of Case Histories - Procedure

Using the exponential distribution assumption for travel time data, the maximum

likelihood value of the joint distribution of measured and computed travel times for all case histories was obtained. All the case histories were inverted with the evaluated optimal regularization coefficients with this method.

7.9.1 Balloon 1

Figure 7-8b shows the results of inverting this case history assuming straight (left) and bent rays (right). The output velocity of the first iteration (straight rays) was used as the initial velocity for the ray tracer to compute the matrix L (bent rays). The heterogeneity and anisotropy inspections (Figure 6-4) and the analysis of shadows (Figure 6-5) for this case history indicate a two phase medium. Therefore, a threshold value equal to the evaluated average velocity in the region of the anomaly (14.5 in/ms) was selected to differentiate between the anomaly and the background. The threshold value was gradually increased until only one anomaly clearly remained in the inverted image. Figure 7-19a shows the exact location of the high velocity helium balloon in the medium. The initial and the enhanced images for this case history are given in the corresponding mathgram in Appendix F.

7.9.2 Balloon 2

This case history was examined with both straight and bent rays. The output velocity of the first iteration (straight rays) was used as the velocity field for the ray tracer (bent rays). Figures 6-7 and 6-8, which represent heterogeneity and anisotropy inspections and analysis of shadows for this case history, indicate a two phase medium. Therefore, a threshold value equal to the evaluated average velocity for the region of the anomaly (14.5 in/ms) was selected to differentiate between the anomaly and the background in the inverted image. The threshold value was gradually increased until only one anomaly clearly remained in the

image. Figure 7-19b shows the inverted image with straight rays; the highest value in the medium appeared in a pixel adjacent to the real location of the balloon. Using curved rays, the exact location of the high velocity helium balloon was evaluated in the inverted image (Figure 7-20a). Note that a higher velocity is computed for the balloon in the inverted image with ray tracing compared to the one with straight rays. The initial and the enhanced images for this case history, for both straight and bent rays, are given in the corresponding mathgrams in Appendix F.

7.9.3 Balloon 3

Because of the similarity in geometry between this case history and balloon 4, this case was only examined with straight rays. The inverted image is given in Figure 7-20b. Figures 6-10a and 6-11, which represent heterogeneity inspection and analysis of shadows for this case history, indicate a two phase medium. Therefore, a threshold value equal to the evaluated average velocity for the region of the anomaly (14.0 in/ms) was selected. The threshold value was gradually increased until only one anomaly remained in the inverted image. Figure 7-20b shows the enhanced inverted image for this case history. The initial and the enhanced images for this case history are given in the corresponding mathgram in Appendix F.

7.9.4 Balloon 4

The results of inverting this case history assuming straight (left) and bent rays (right) are given in Figure 7-8a. Inverted images show the effect of the distribution of information content with two low velocity regions which appear on the top and bottom of the high velocity balloon in both images. The output velocity of the first iteration (straight rays), was used to retrace rays (bent rays). The heterogeneity and anisotropy inspections (Figure 6-14) and the analysis of

shadows (Figure 6-15) indicate a two phase medium for this case history. Therefore, a threshold value equal to the evaluated average velocity for the region of the anomaly (14.15 in/ms) was selected to differentiate between the anomaly and the background. The threshold value was gradually increased (up to 15.2) until only one anomaly appeared in the inverted image. Figure 7-21a shows the exact location of the high velocity helium balloon in the medium. Appendix F presents the corresponding mathgram of the initial and the enhanced images for this case history.

7.9.5 Crack in Concrete (Side-to-Side shootings)

Due to the out-of-plane nature of this problem (Chapter 6), this case history was inverted only with straight ray paths. The information from pre-processors indicates that this is a two phase medium consisting of a high velocity concrete and a low velocity region due to presence of the crack. Therefore, a threshold value based on the average velocity of the concrete (4.8 km/s) was selected to differentiate between the background concrete and the region of the crack in the inverted image. In this case history, as opposed to the last four cases, the anomaly is a low velocity zone. Therefore, the selected threshold was based on applying a limitation on the maximum velocity. The threshold value was increased up to 6 (km/s). However, the enhancement in the image was minute. The enhanced inverted image is given in Figure 7-21b. The crack can be traced in this figure. Appendix F presents the initial and enhanced inverted images for this case history in the corresponding mathgram.

7.9.6 Crack in Concrete (Top to Left-Side shootings)

Only half of the medium was illuminated due to the geometry of the source and receiver locations in this case history. The rays traveled out of the plane of the

tomogram. Therefore, this case history was inverted only with straight ray paths. The information from pre-processors indicate that this is a two phase medium consisting of a high velocity concrete and a low velocity region. However, due to the presence of pixels with zero values, the image could not be enhanced with a thresholding criterion. The inverted image is given in Figure 7-22a. The effect of the crack can be seen in the eighth pixel of the first column and its neighbor pixels. Appendix F presents the mathgram of the inverted image for this case history.

7.9.7 Crack in Concrete (Top to Right-Side shootings)

Due to the configuration of source and receiver locations, only half of the medium was illuminated in this case history. The out-of-plane problem for this case history exists as it was for the last two cases. Therefore, straight ray paths were used during the inversion process. The information from pre-processors indicate that this is a two phase medium consisting of a high velocity concrete and a low velocity crack. However, due to the presence of pixels with zero values, the image could not be enhanced with a thresholding criterion. Figure 7-22b shows the inverted image for this case history. That part of the crack which was illuminated can be traced in this figure. Appendix F presents the mathgram for this case history.

7.9.8 Column of Aggregate

This case history was studied with both straight and bent rays. Figures 7-23a and 7-23b show the enhanced inverted images. The information from pre-processors indicate that this is a two phase medium consisting of the high velocity concrete and the low velocity region, due to the presence of the aggregate column. Therefore, a threshold value based on the evaluated average

velocity for the concrete (4.65 km/s) was selected to differentiate between the background concrete and the column of aggregate region in the inverted image. In this case history the anomaly is a low velocity zone. Therefore, the selected threshold was based on limiting the maximum velocity in the corresponding mathgram. Using curved rays, the size and location of the aggregate column can be seen clearly in the enhanced inverted image. The initial and enhanced images with straight and bent rays, for this case history, are given in the Appendix F.

7.9.9 Kosciuzko Bridge Pier

The analysis of this case history with pre-processors indicates a very homogeneous medium. Hence, straight rays were used during the inversion process and no thresholding was applied. Due to the high degree of homogeneity in the region, thresholding was used. Figure 7-24a shows the inverted image for this case history. A high velocity in the center of the pier and an extended crack from the left to the right side are apparent in this figure. These two features can also be seen in the inverted image with contour mapping in the corresponding mathgram file in Appendix F.

7.9.10 Chute Hemmings Dam

The pre-processor analyses for this case history indicate a homogeneous-isotropic medium. Hence, no thresholding was applied and straight rays were used during the inversion process. The inverted image for this case history is given in Figure 7-24b. The figure shows a very homogeneous medium in all parts except for the shotcrete parts. Note the effect of high velocity in the shotcrete region on increasing velocity of the adjacent pixels. The effect decreases for more distant pixels. The corresponding mathgram file is given in Appendix F.

7.9.11 Korean Demilitarized Zone

This case history was studied with both straight and bent rays. The inverted images for both cases were identical. The pre-processor analyses for this case history show a vertically heterogeneous and anisotropic medium. However, due to the presence of the two very low information content regions at the top and bottom of the tomogram, a high and a low threshold values were selected. The enhanced inverted image is given in Figure 7-25. The location of the tunnel can clearly be seen in the middle of the image. However, the heterogeneity of the medium is diminished in this process. The initial and the enhanced inverted images for this case history are given in the corresponding mathgram in Appendix F.

7.10 Summary and Conclusions

Tomographic problems are usually mixed-determined. Under-determination (or mixed-determination) and noise in the data make the tomographic inversion problems ill-conditioned.

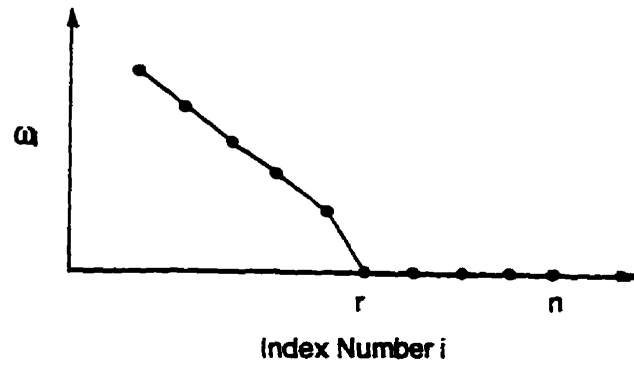
Adding *a priori* information is one way to decrease the size of the null space. *A priori* information in the form of constraints helps to specify those image parameters (unknowns) that reside in the null space. Constraints can be readily implemented in damped least squares (DLSQ) and regularization solutions.

The quality of the image worsens with either lack of or excessive damping or regularization coefficients. The optimal coefficient is not unique, but depends on the velocity field, the reality of the data, and other problem parameters.

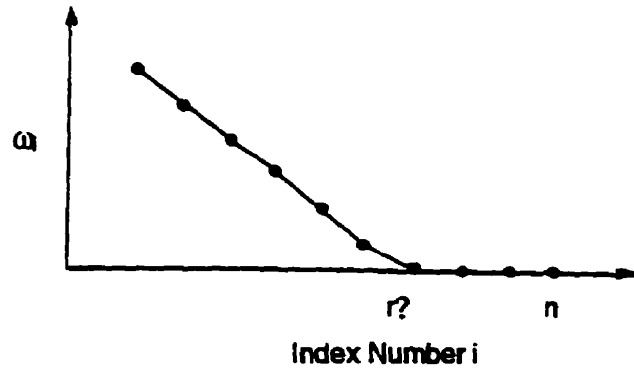
One way to determine the size of the null space is to plot the sizes of the singular values against their index numbers. This is the spectrum of the data kernel and highlights the true amount of global information, which is often much less than the number of measurements.

Criteria were evaluated to determine the optimal coefficient. The coefficient of variation (COV), based on the whole set of pixel slownesses, tends to promote global smoothness. An alternative approach is to define local measures of variability.

The maximum likelihood method asserts that the optimum values of the system parameters maximize the probability that the observed data are in fact observed. Assuming a Gaussian distribution for the travel time data, the optimal regularization coefficient can be obtained from a cumulative number of appearances of the data vs. travel time data plot. However, the results show under-smoothed images similar to the previous methods. Another option is to assume an exponential distribution for the travel times data. The results obtained for the optimal regularization coefficient lead to certain peak values which give the optimal regularization coefficients in the different case histories. The exponential distribution has the same relationship to the L_1 norm as the Gaussian distribution has to the L_2 norm. A high-order norm should be employed for short-tailed data. The tomographic data, and especially side-to-side shootings, appear to have a long-tail distribution.

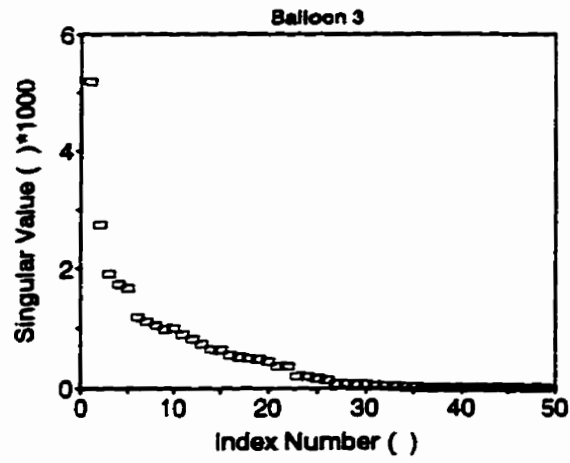


(a)

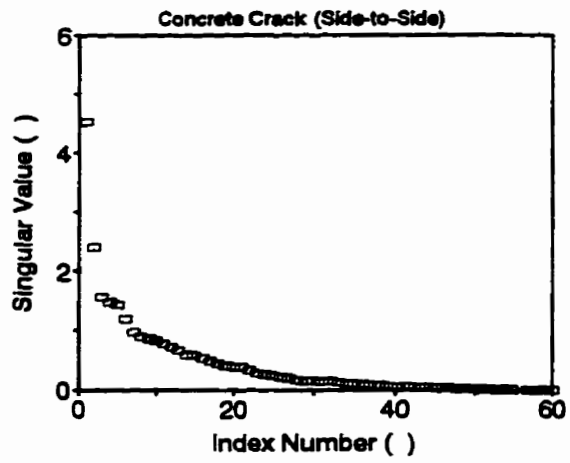


(b)

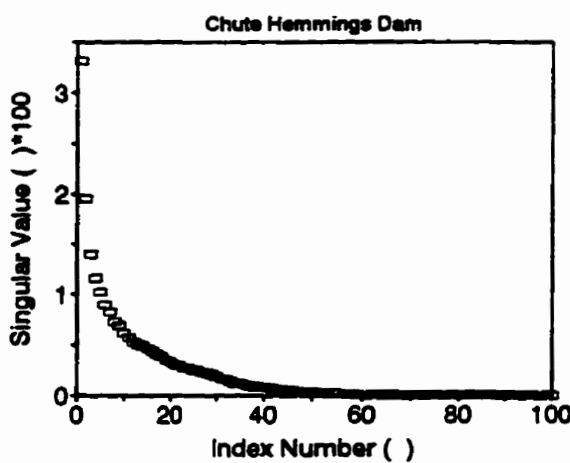
Figure 7-1: (a) Singular values of a matrix with clearly identifiable cut-off point
 (b) Singular values of a matrix where cut-off point must be selected arbitrarily.



(a)

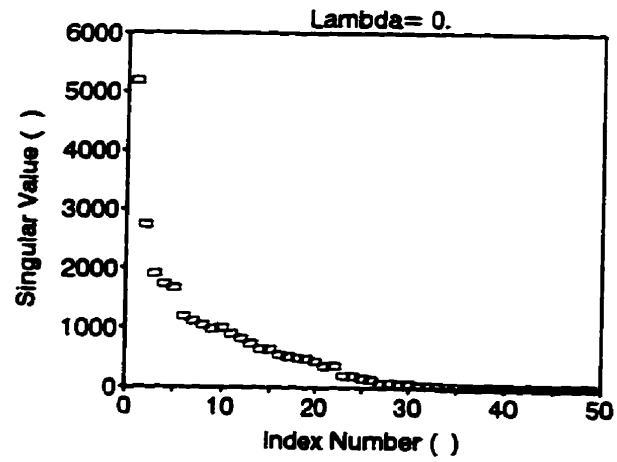


(b)

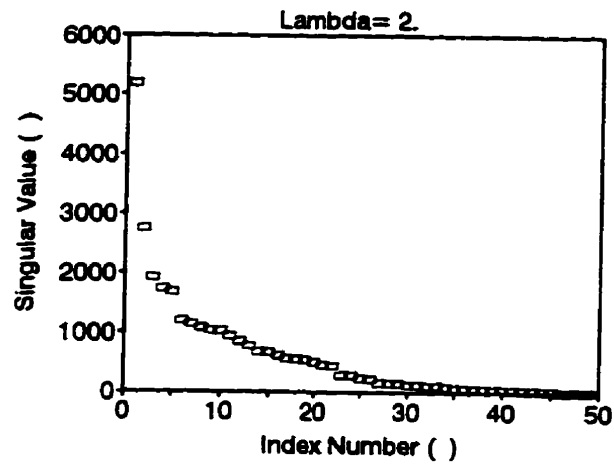


(c)

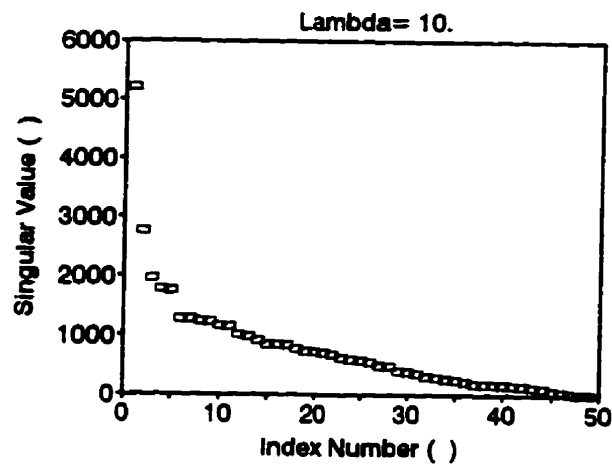
Figure 7-2: Distribution of singular values for different case histories.



(a)



(b)



(c)

Figure 7-3: Distribution of singular values for different regularization coefficients.

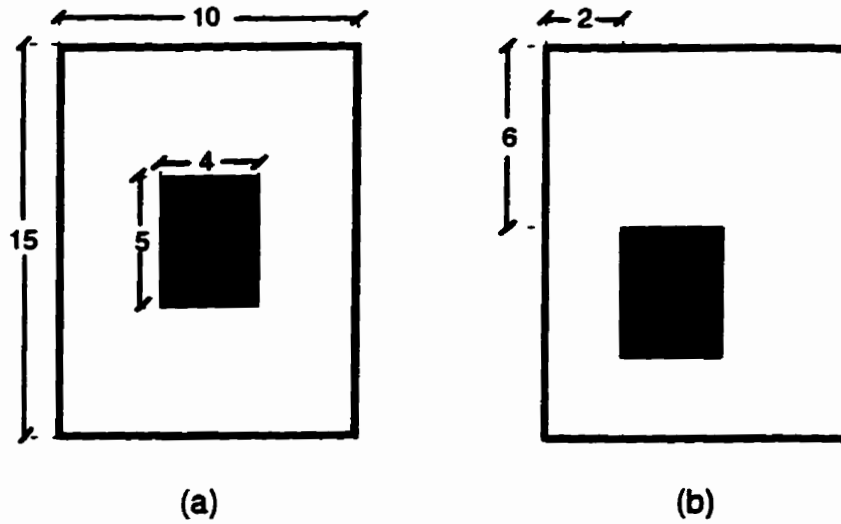


Figure 7-4: Simulated cases: low and high velocity anomalies at center and off-center.

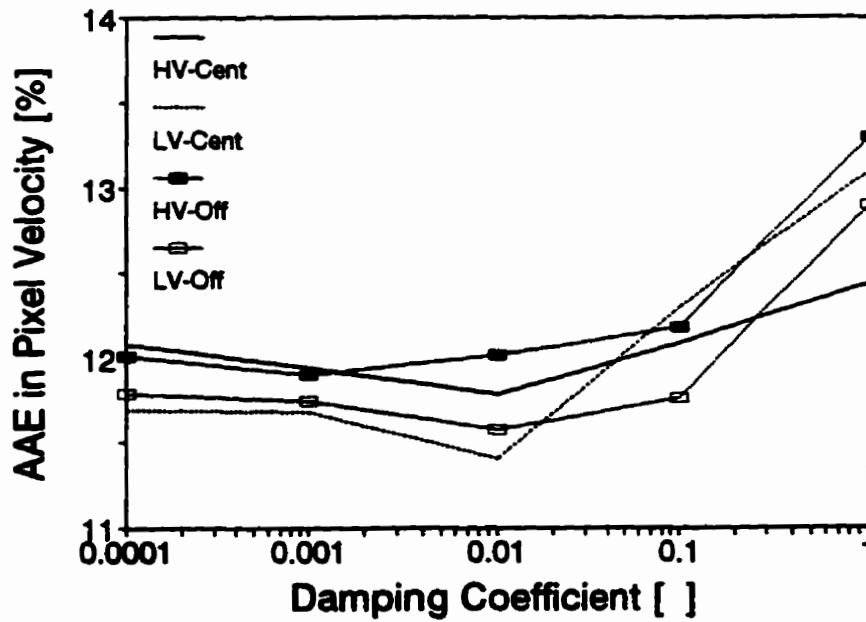


Figure 7-5: Damping coefficient and image quality. Four simulated cases.

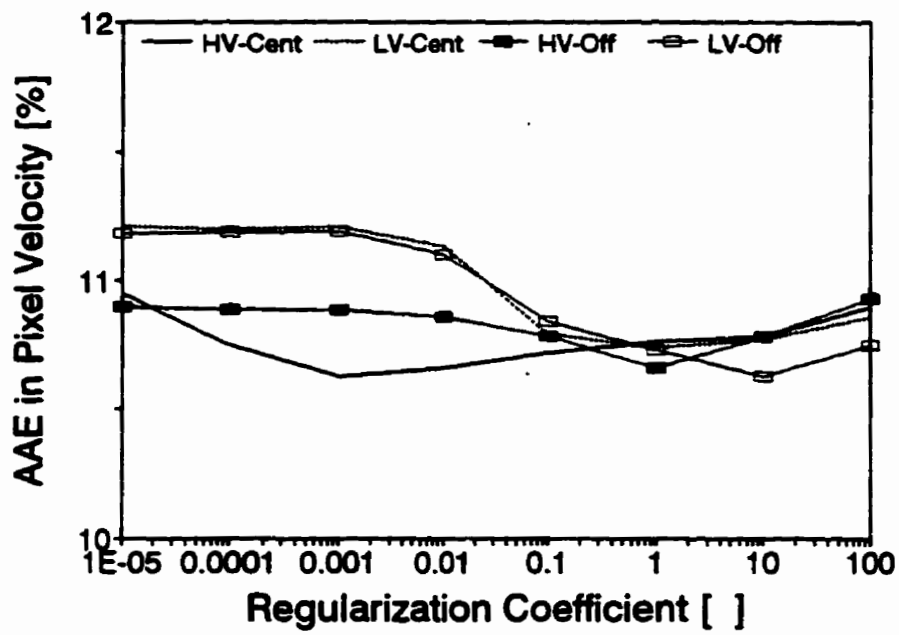


Figure 7-6: Regularization coefficient and image quality. Four simulated cases.

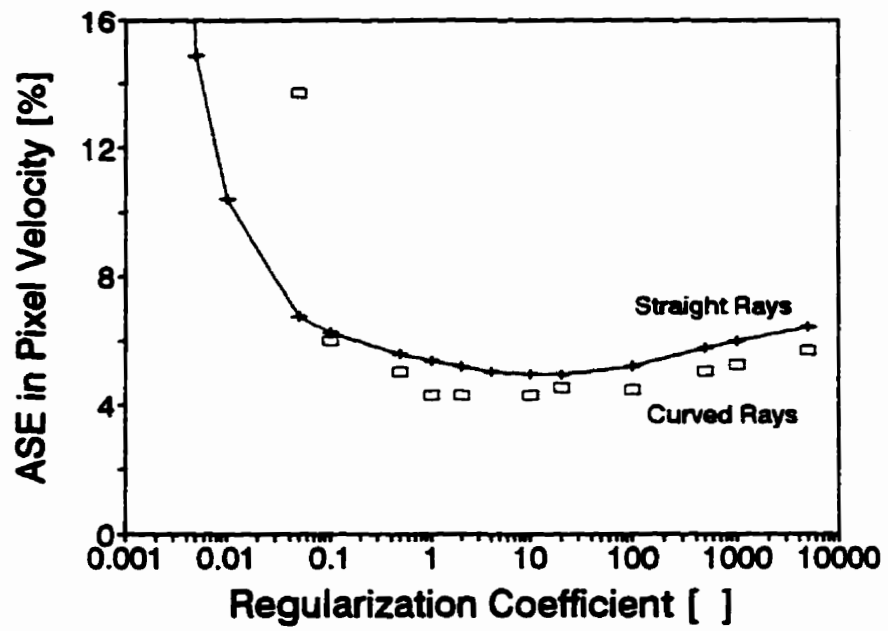
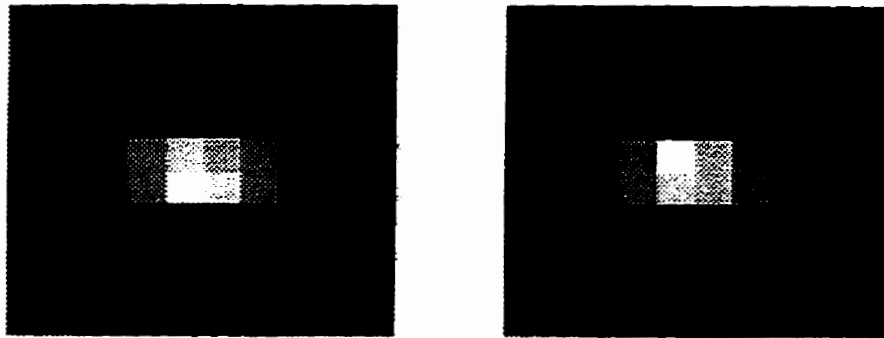
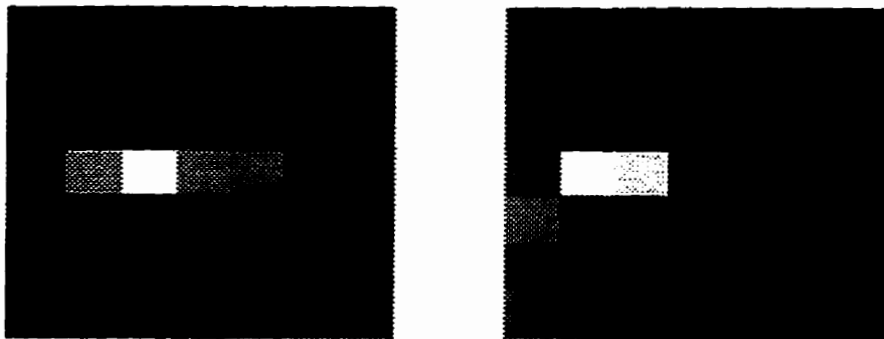


Figure 7-7: Straight and curved rays. The effect of regularization coefficient (resolvability).



(a)



(b)

Figure 7-8: Inversion of laboratory data with regularization: straight (left) and curved (right) rays. (a) Central, high velocity anomaly, 256 rays, $\lambda=10$ (refer to Figure 5-1d) (b) Off-center high velocity anomaly, 49 rays, $\lambda=2$ (refer to Figure 5-1a).

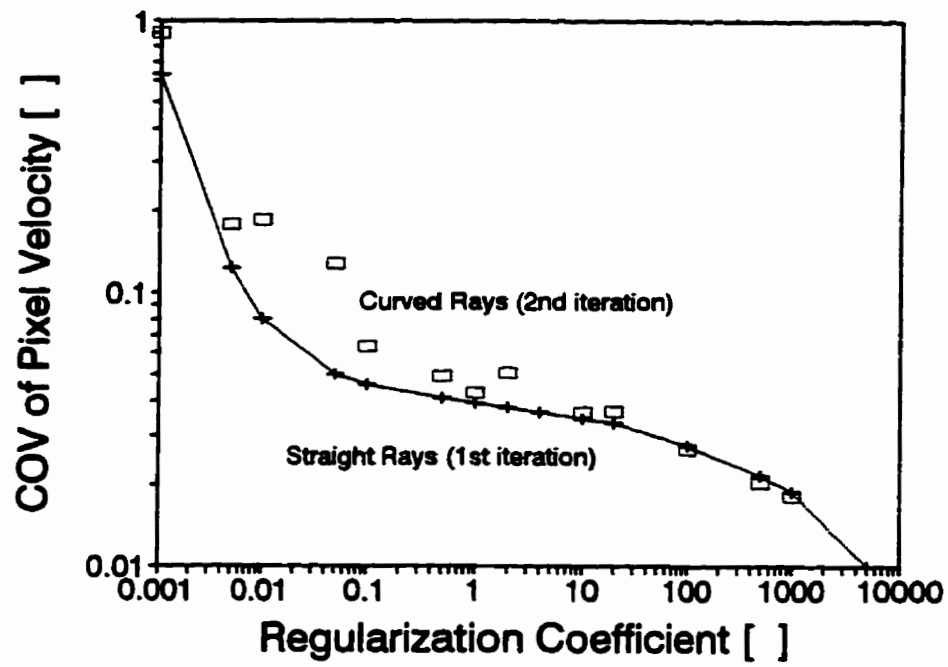
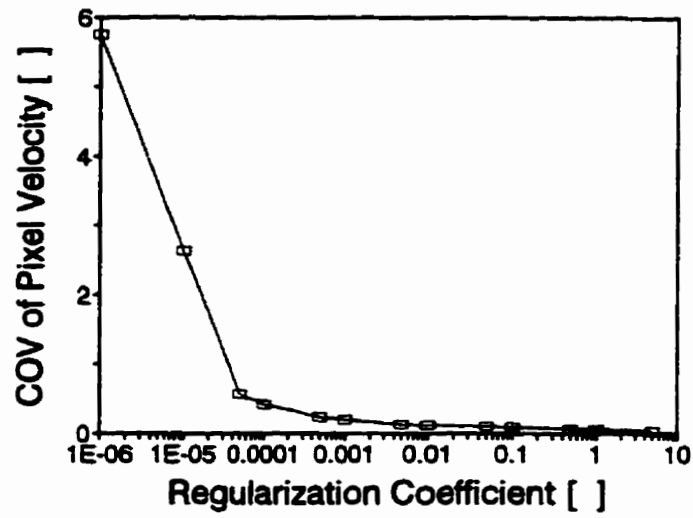
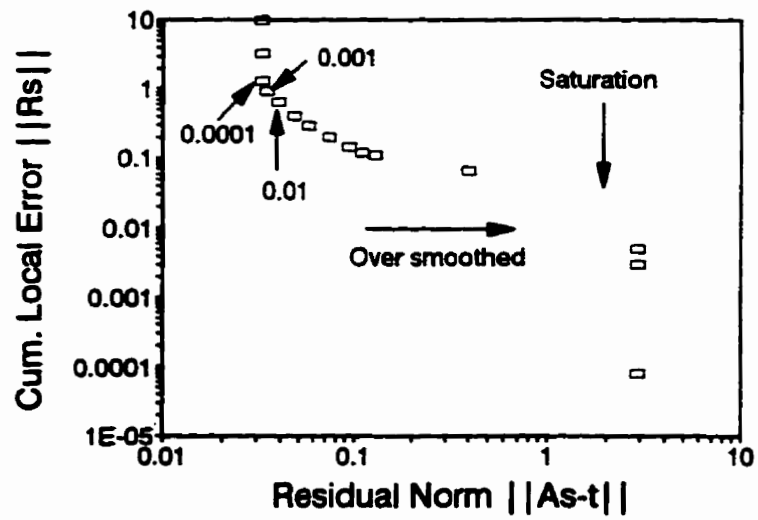


Figure 7-9: Straight and curved rays. The effect of regularization coefficient (variability).

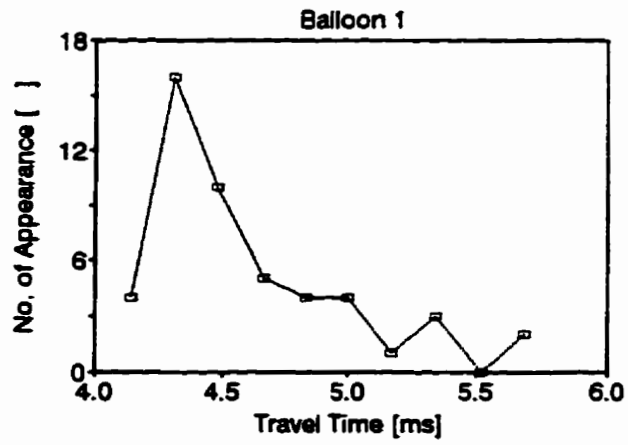


(a)

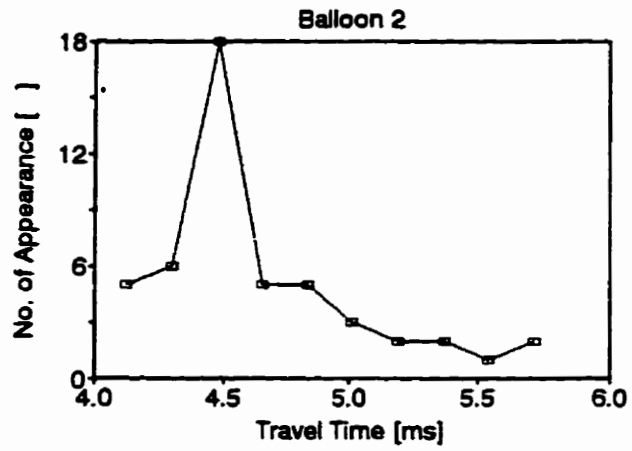


(b)

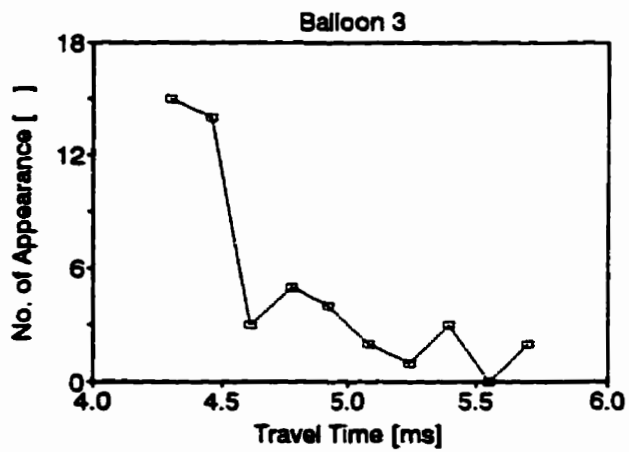
Figure 7-10: Optimization of regularization coefficient.



(a)

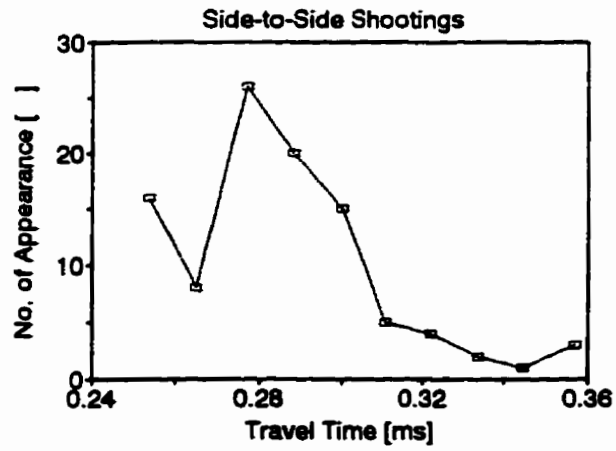


(b)

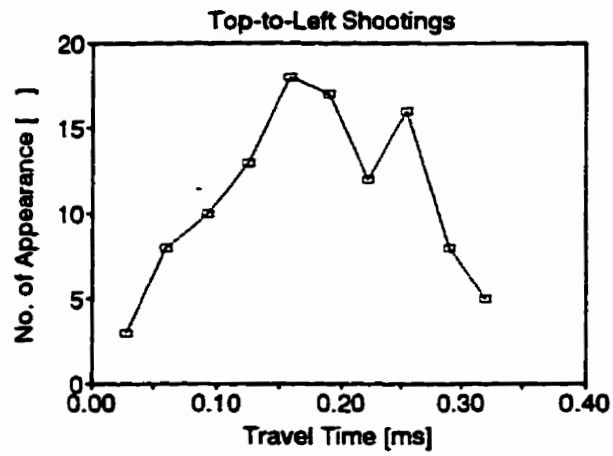


(c)

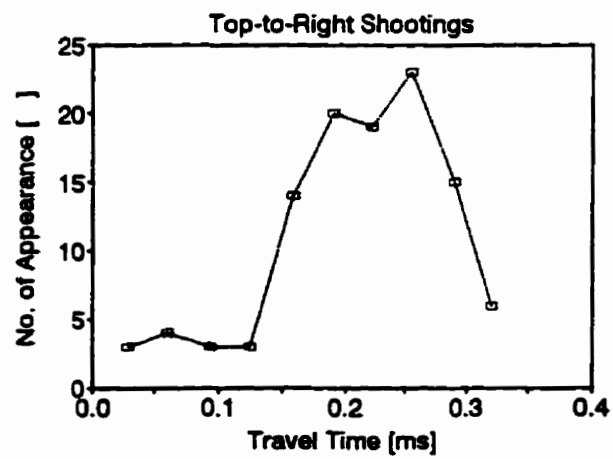
Figure 7-11: Distribution of travel times in small balloons.



(a)

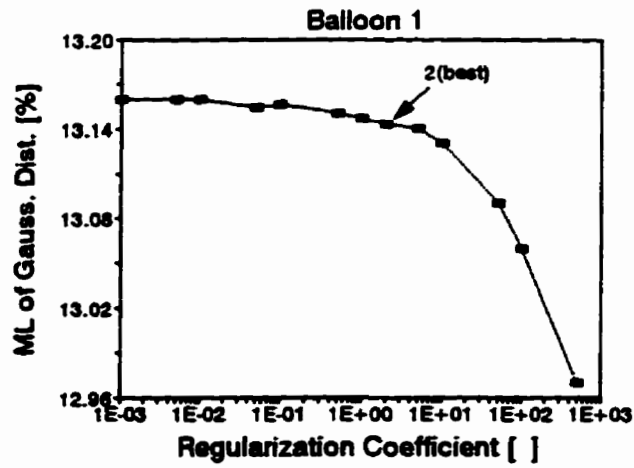


(b)

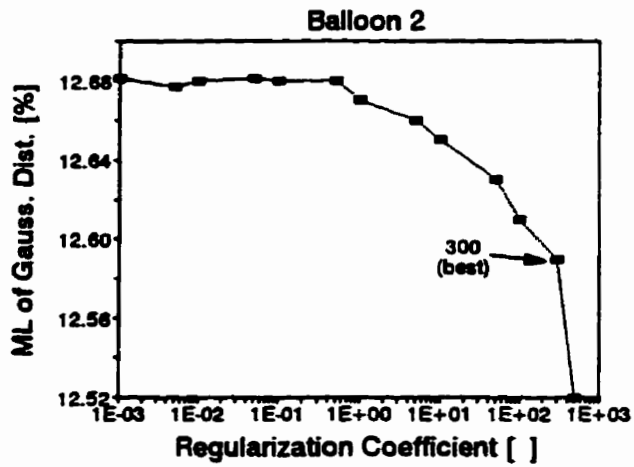


(c)

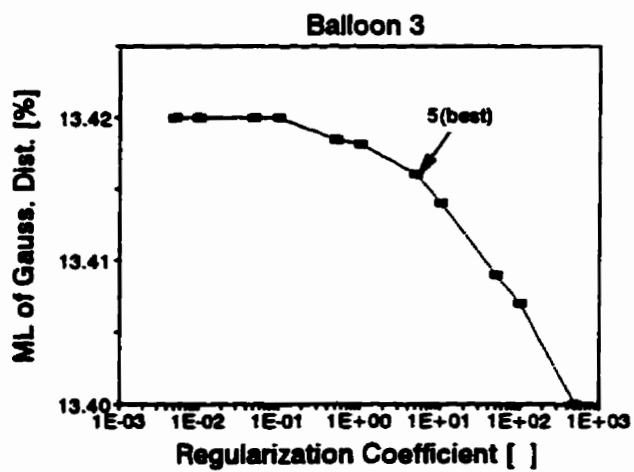
Figure 7-12: Distribution of travel times in concrete crack.



(a)

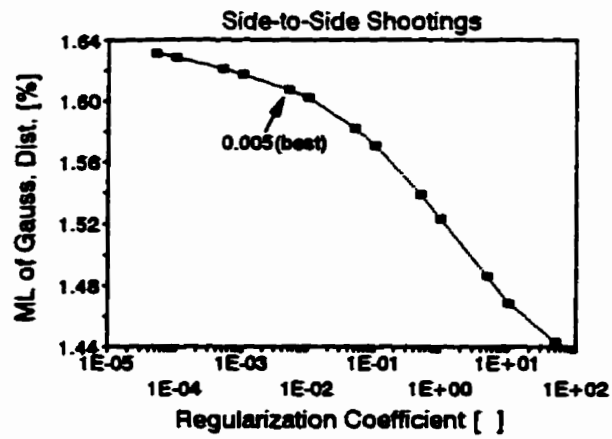


(b)

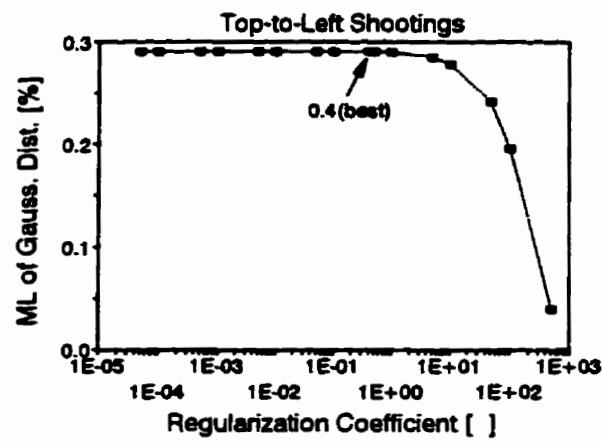


(c)

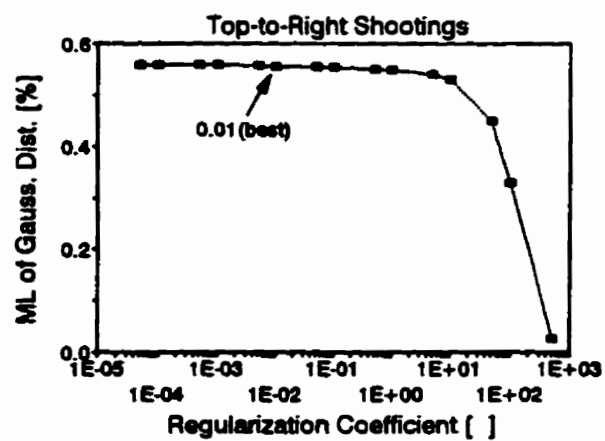
Figure 7-13: Maximum likelihood of small balloons (Gaussian distribution).



(a)



(b)



(c)

Figure 7-14: Maximum likelihood of concrete crack (Gaussian distribution).

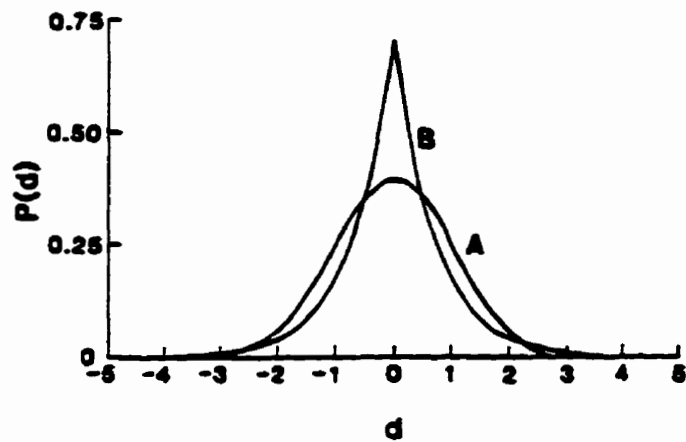
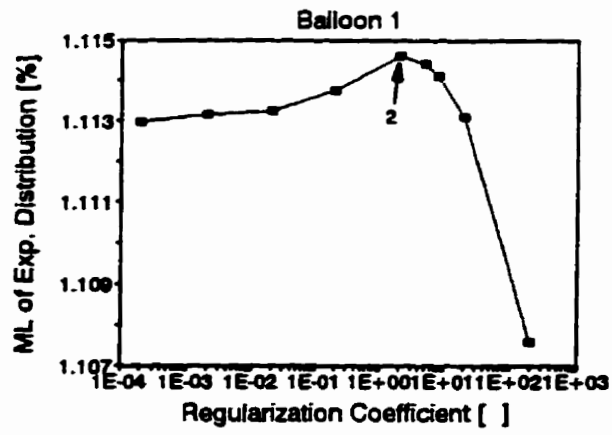
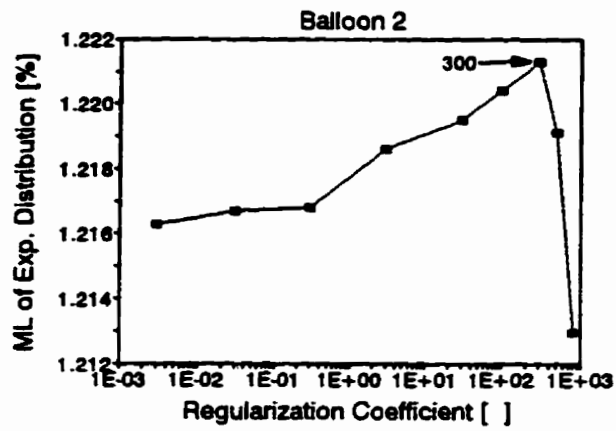


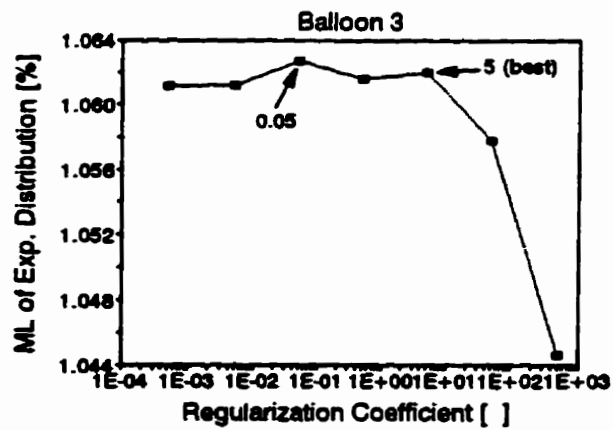
Figure 7-15: Gaussian (curve A) and exponential (curve B) distribution with zero mean and unit variance. The exponential distribution has the longer tail (Menke, 1984).



(a)



(b)



(c)

Figure 7-16: Maximum likelihood of small balloons (Exp. distribution).

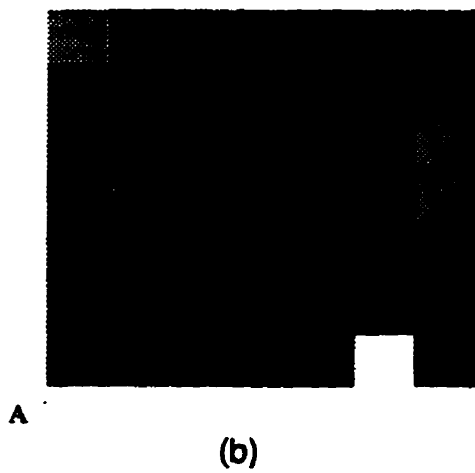
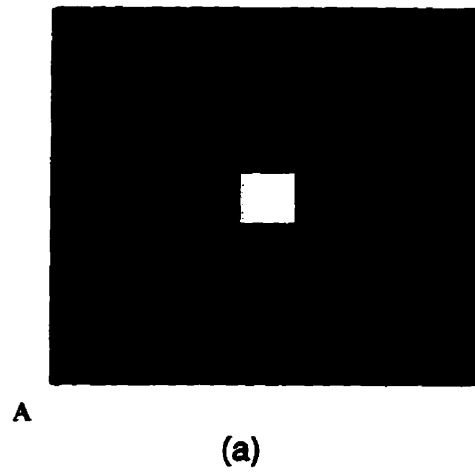
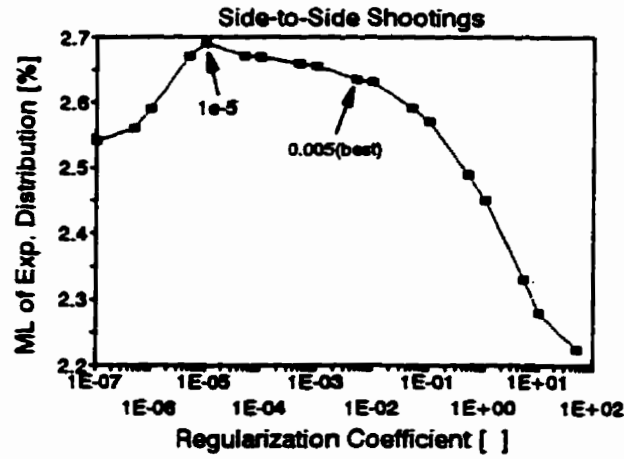
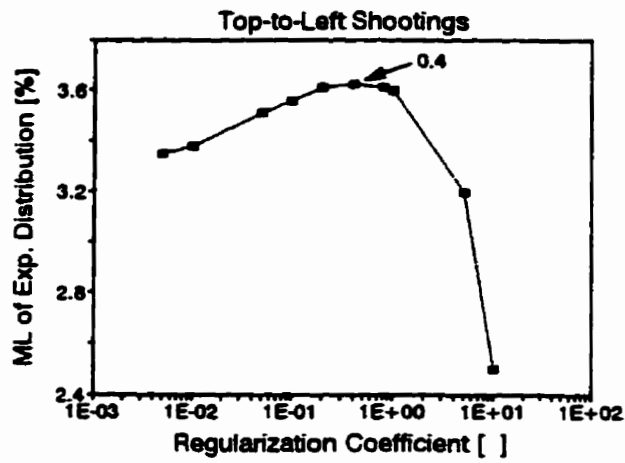


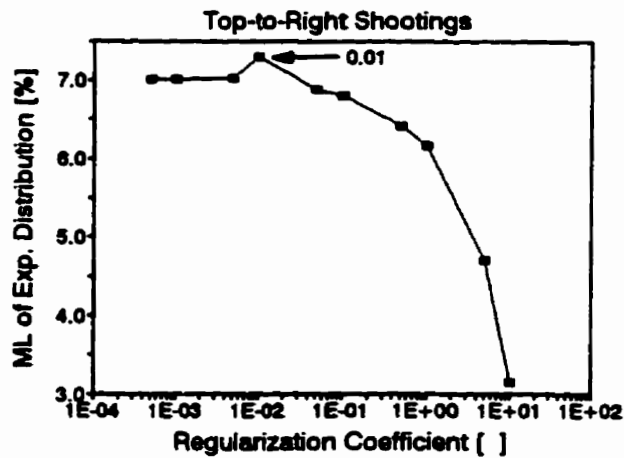
Figure 7-17: Inverted images for Balloon 3 case with (a) optimal $\lambda=5$ and (b) with $\lambda=0.05$ (post peak) (Thresholded, refer to Appendix F).



(a)

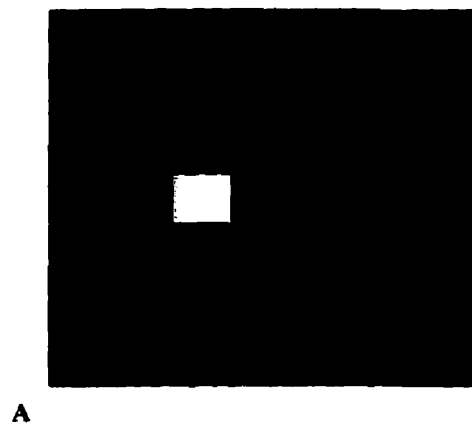


(b)



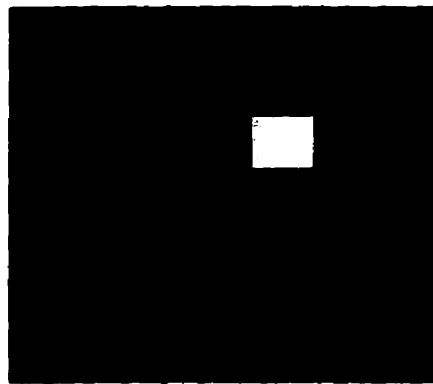
(c)

Figure 7-18: Maximum likelihood of concrete crack (Exp. distribution).



A

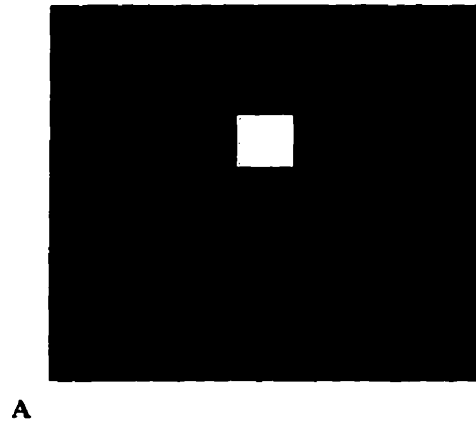
(a)



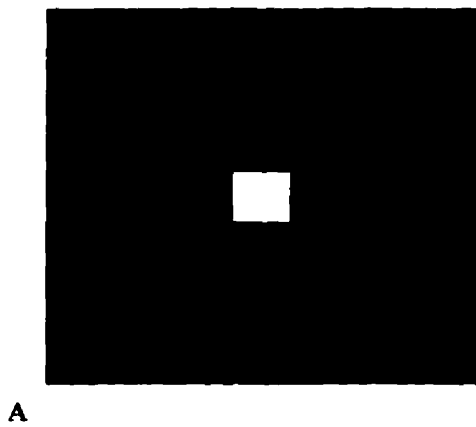
A

(b)

Figure 7-19: Inverted images with optimal regularization coefficient, for (a) Balloon 1 (curved rays) and (b) Balloon 2 (straight rays) (thresholded, refer to Appendix F).

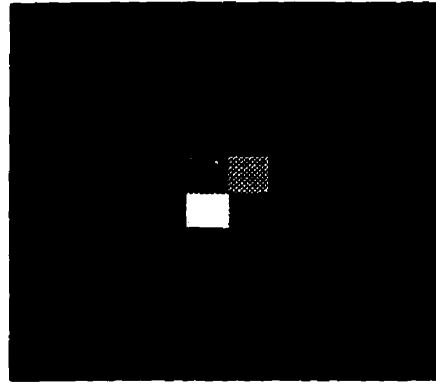


(a)



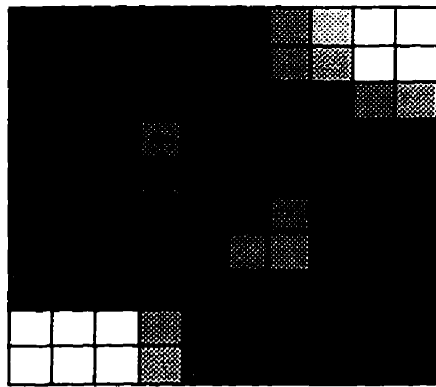
(b)

Figure 7-20: Inverted images with optimal regularization coefficient for (a) Balloon 2 (curved rays) and (b) Balloon 3 (straight rays) (Thresholded, refer to Appendix F).



A

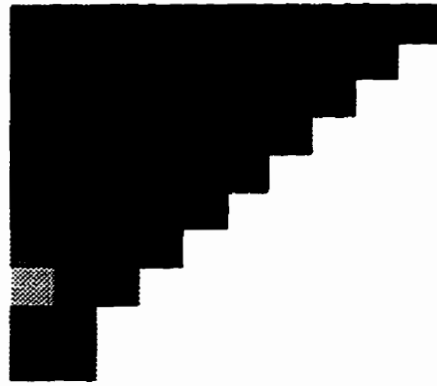
(a)



A

(b)

Figure 7-21: Inverted images with optimal regularization coefficient for (a) Balloon 4 (curved rays) and (b) Side-to-side shootings data of concrete crack (straight rays).



A

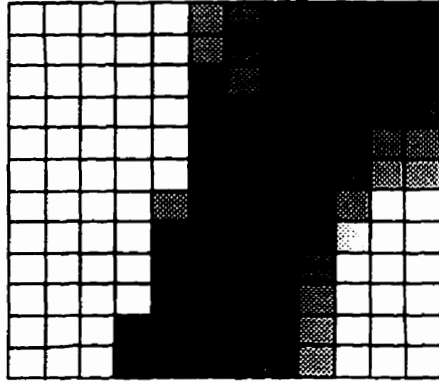
(a)



A

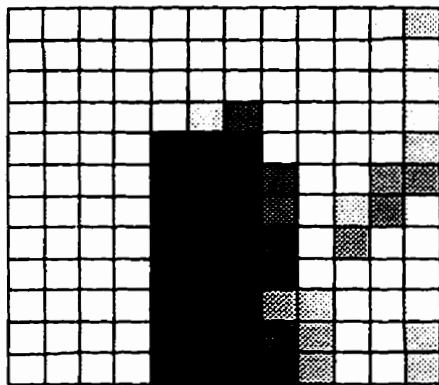
(b)

Figure 7-22: Inverted images with optimal regularization coefficient, using straight rays, for concrete crack (a) Top to left-side shootings and (b) Top to right-side shootings.



A

(a)



A

(b)

Figure 7-23: Inverted images with optimal regularization coefficient for concrete column Using (a) straight rays and (b) Curved rays (Thresholded, refer to Appendix F).



A

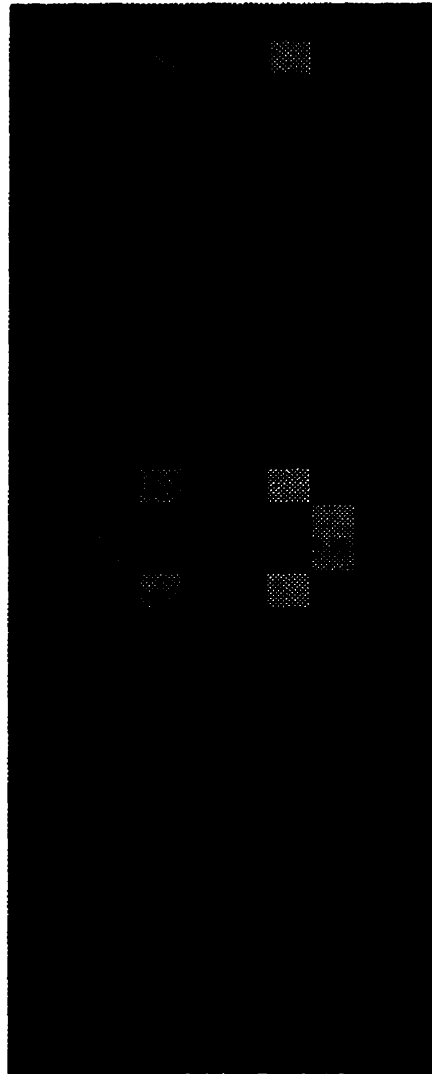
(a)



A

(b)

Figure 7-24: Inverted images with optimal regularization coefficient, using straight rays, for (a) Kosciuzko bridge pier and (b) Chute Hemmings dam data.



A

Figure 7-25: Inverted images with optimal regularization coefficient for Korean Demilitarized Zone data (Thresholded, refer to Appendix F). Same results for both straight and curved rays.

Mathgram 7-1: DLSQ solution (HV-Center model). Random error is added to the data.

Random error is added as: $t = t + md(1)$ initial velocity=10 $\eta = 50$

Definitions: $n := 10$ $i := 1..n+5$ $j := 1..n$
 $ij := 1..n \cdot (n+5)$ $nh := n$ $m := 1..nh$ $k := 1..nh - 1$

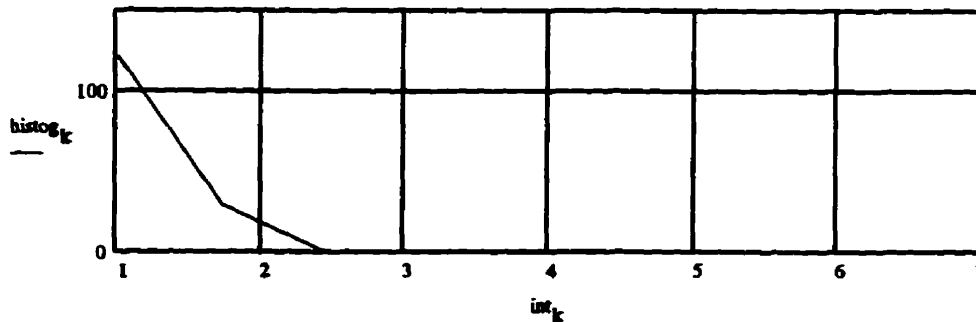
Input File: $V := \text{READPRN}(\text{vd50})$ $V_{\min} := \min(V)$ $V_{\max} := \max(V)$
 $V_{\min} = 1.025$ $V_{\max} = 8.154$ $\text{mean}(V) = 1.929$

Enhancement: $V_{ij} := \text{if}(V_{ij} < V_{\min}, V_{\min}, V_{ij})$ $V_{ij} := \text{if}(V_{ij} > 2., 2., V_{ij})$

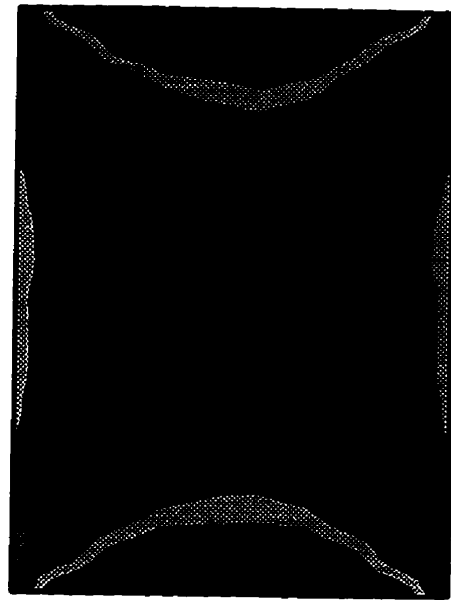
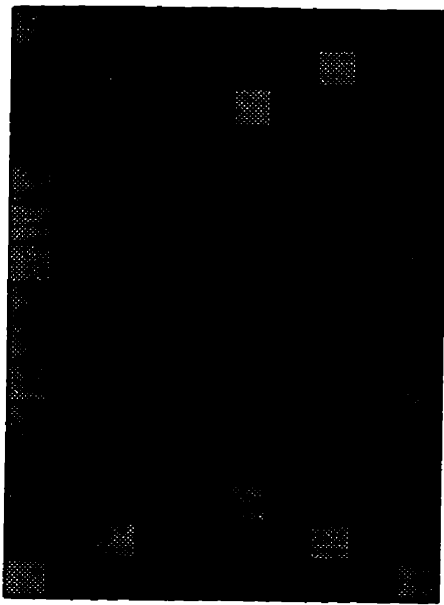
Histogram: $\text{int}_m := V_{\min} + (m - 1) \cdot \frac{V_{\max} - V_{\min}}{nh}$ $\text{histog} := \text{hist}(\text{int}, V)$

2D Image $A_{i,j} := V_{(i-1) \cdot nh + j}$ $B_{j,(n-i+5)+1} := A_{i,j}$

Histogram of the inverted velocity field



Inverted velocity field



Mathgram 7-2: DLSQ solution (HV-Center model). Systematic error is added to the data.

Systematic error is added as: $t = t + 0.5$ initial velocity=10 $\eta = 0.05$

Definitions: $n := 10$ $i := 1..n + 5$ $j := 1..n$
 $ij := 1..n \cdot (n + 5)$ $nh := n$ $m := 1..nh$ $k := 1..nh - 1$

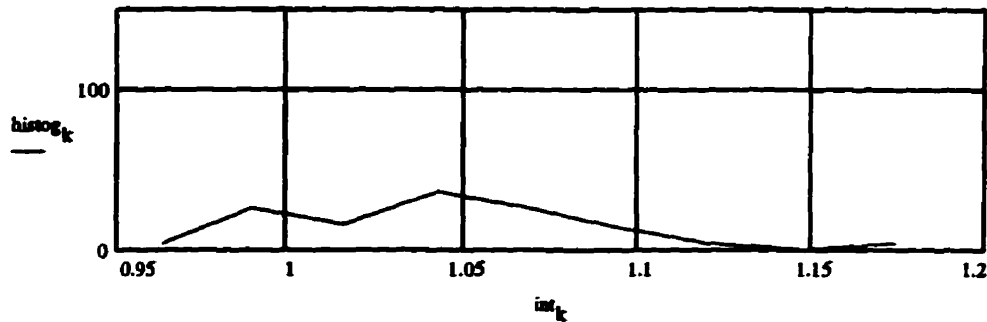
Input File: $V := \text{READPRN}(\text{vd005s})$ $V_{\min} := \min(V)$ $V_{\max} := \max(V)$
 $V_{\min} = 0.964$ $V_{\max} = 1.226$ $\text{mean}(V) = 1.079$

Enhancement: $V_{ij} := \text{if}(V_{ij} < V_{\min}, V_{\min}, V_{ij})$ $V_{ij} := \text{if}(V_{ij} > V_{\max}, V_{\max}, V_{ij})$

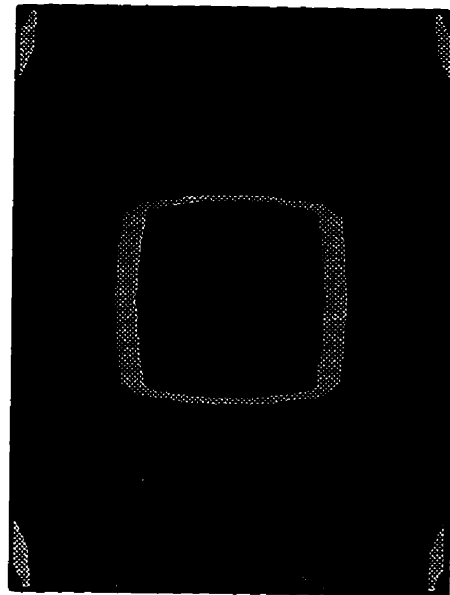
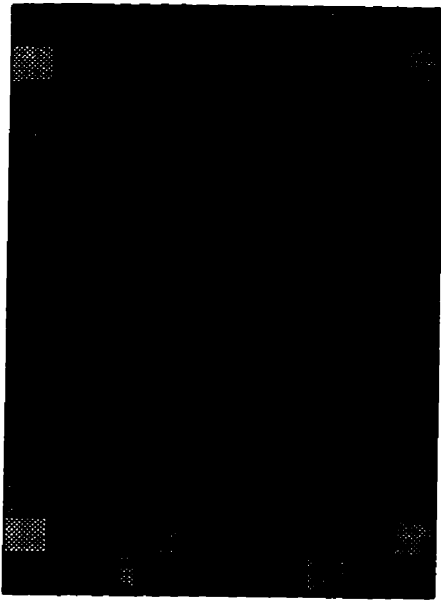
Histogram: $\text{int}_m := V_{\min} + (m - 1) \cdot \frac{V_{\max} - V_{\min}}{nh}$ $\text{histog} := \text{hist}(\text{int}, V)$

2D Image $A_{i,j} := V_{(i-1) \cdot nh + j}$ $B_{j, (n-i+5)+1} := A_{i,j}$

Histogram of the inverted velocity field



Inverted velocity field



Mathgram 7-3: Regularization solution (HV-Center model). Random error is added to the data.

Random error is added as: $t = t + md(1)$

initial velocity=10

$\eta = 5$

Definitions:

$n := 10$

$i := 1..n+5$

$j := 1..n$

$ij := 1..n(n+5)$

$nh := n$

$m := 1..nh$

$k := 1..nh - 1$

Input File:

$V := \text{READPRN}(vr5)$

$Vmin := \min(V)$

$Vmax := \max(V)$

$Vmin = 0.891$

$Vmax = 1.322$

$\text{mean}(V) = 1.064$

Enhancement:

$V_{ij} := \text{if}(V_{ij} < Vmin, Vmin, V_{ij})$

$V_{ij} := \text{if}(V_{ij} > 2., 2., V_{ij})$

Histogram:

$int_m := Vmin + (m - 1) \frac{Vmax - Vmin}{nh}$

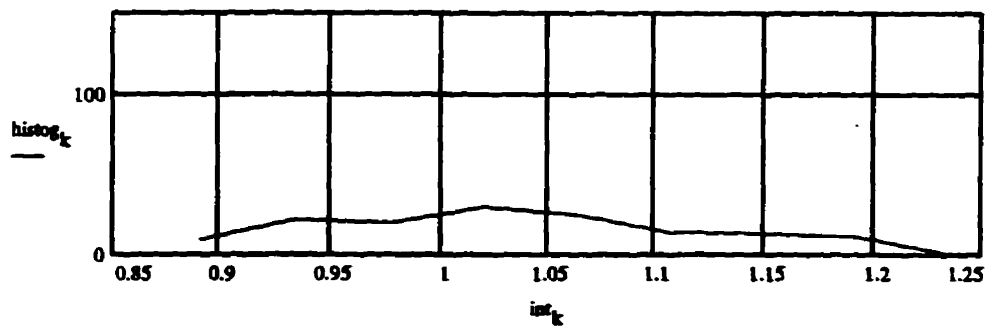
$\text{histog} := \text{hist}(int, V)$

2D Image

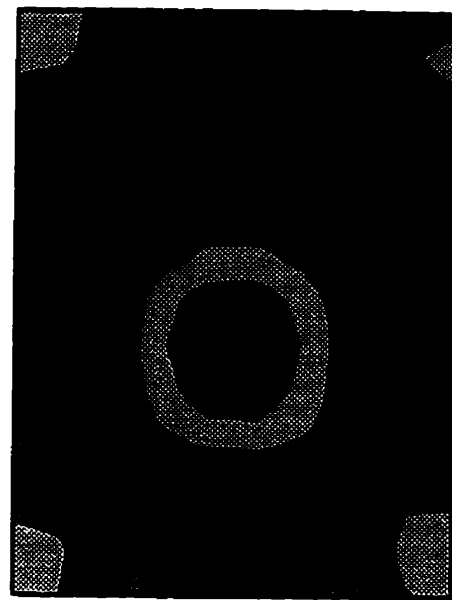
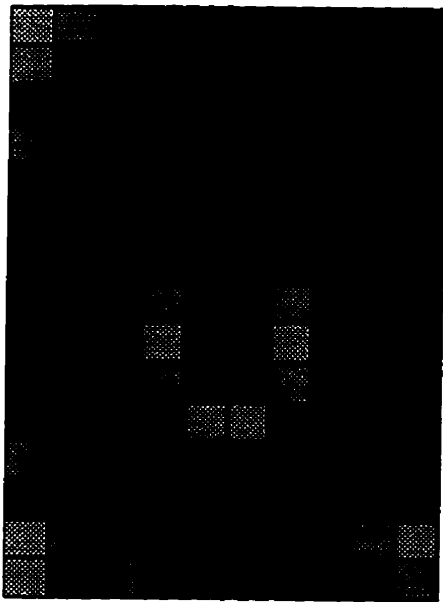
$A_{i,j} := V_{(i-1) \cdot nh + j}$

$B_{j, (n-i+5)+1} := A_{i,j}$

Histogram of the inverted velocity field



Inverted velocity field



Mathgram 7-4: Regularization solution (HV-Center model). Systematic error is added to the data.

Systematic error is added as: $t = t + 0.5$ initial velocity=10 $\lambda = 0.05$

Definitions: $n := 10$ $i := 1..n+5$ $j := 1..n$
 $ij := 1..n \cdot (n+5)$ $nh := n$ $m := 1..nh$ $k := 1..nh - 1$

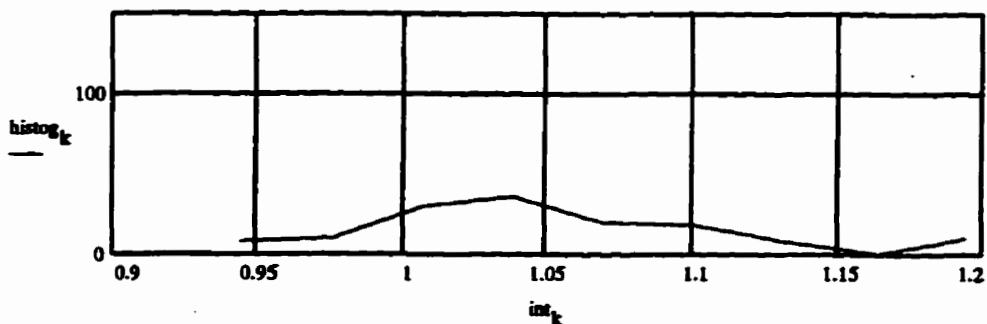
Input File: $V := \text{READPRN}(\text{vr005s})$ $V_{\min} := \min(V)$ $V_{\max} := \max(V)$
 $V_{\min} = 0.945$ $V_{\max} = 1.257$ $\text{mean}(V) = 1.078$

Enhancement: $V_{ij} := \text{if}(V_{ij} < V_{\min}, V_{\min}, V_{ij})$ $V_{ij} := \text{if}(V_{ij} > V_{\max}, V_{\max}, V_{ij})$

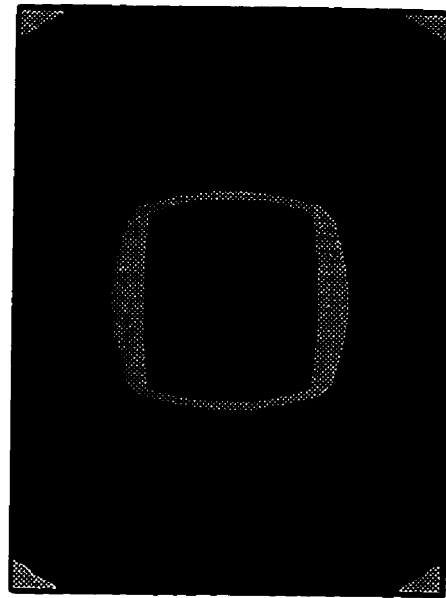
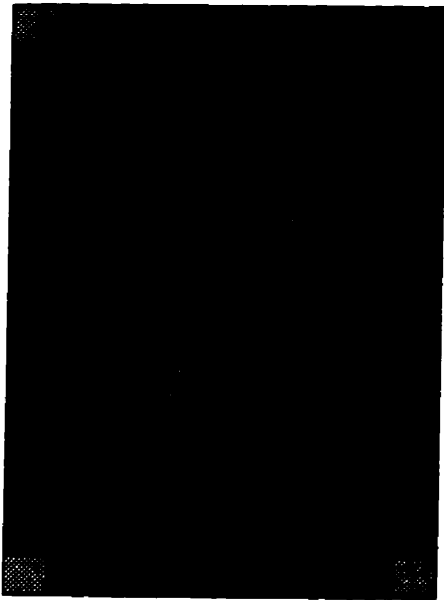
Histogram: $\text{int}_m := V_{\min} + (m - 1) \cdot \frac{V_{\max} - V_{\min}}{nh}$ $\text{histog} := \text{hist}(\text{int}, V)$

2D Image $A_{i,j} := V_{(i-1) \cdot nh + j}$ $B_{j,(n-i+5)+1} := A_{i,j}$

Histogram of the inverted velocity field



Inverted velocity field



CHAPTER VIII

SUMMARY AND CONCLUSIONS

Tomography (tomo: to cut or slice-*Greek*) is the inversion of measurements of multiple planes of a body. CE-tomography is the inversion of boundary measurements to determine the field of a physical parameter within civil engineering systems. Data for seismic CE-tomographic imaging are line integrals of a physical parameter, along a specific path through the medium, e.g. the travel time accumulated along a ray path between a source and a receiver.

The purpose of this research was to assess the potential of tomographic imaging in a variety of civil engineering infrastructures, placing emphasis on matrix-based inversion algorithms. While most prior research in tomography has been based on simulated data, this research centered on case histories gathered under well-controlled, yet realistic field conditions.

All examples given in this document used travel time observations that were inverted to determine the velocity field. However, the method is completely general; any boundary observation that can be defined as a line integral through the medium can be substituted throughout.

8.1 Summary

Inversion

- Several methods have been proposed to solve the inverse tomographic

problem; they can be categorized as: (i) matrix inversion methods, (ii) iterative methods, (iii) transform methods, and (iv) other methods.

- Iterative methods are not stable in ill-conditioned problems. Transform methods are restricted to straight ray projections (space transformations could be invoked to generalize the solution to heterogeneous, anisotropic media). Matrix methods are versatile, computationally efficient, and robust. However, efficient storage and computation are required.
- Matrix inversion methods have been rarely employed in tomographic inversion because of high memory demand and computational efficiency. The coefficient matrix (L) is large and sparse. In a dense $n \times n$ matrix, the order of computation complexity is $O(n^3)$ and $O(n^2)$ for storage. However, efficient iterative algorithms combined with sparse matrix techniques can reduce the order of computational complexity to $O(n^{1.3})$ and storage requirement to $O(n)$.
- Damped least square (DLSQ) and regularization methods are used to avoid the ill-conditioning which is inherent in tomographic inversion problems.
- The coefficient matrix during an inversion process, in both DLSQ and regularization methods, is symmetric and positive definite. Therefore, a conjugate gradient method is used (note that regularization and damped least squares methods produce coefficient matrices with different structures).
- Hybrid solutions can be attempted to enhance the resolvability of an inverted image (e.g., fuzzy logic pre-processing followed by regularization).

Ray Tracing

- The analysis of wave propagation is often simplified to exercises with straight

lines connecting sources and receivers. However, civil engineering problems of interest are not homogeneous and not isotropic. If the velocity contrast in the medium is more than 15 to 20 percent, rays bend toward higher velocity regions. In this case, entries in the coefficient matrix depend on a priori estimates of the velocity field. The inversion problem becomes non-linear, and ray tracing should be implemented during an iterative solution of the tomographic inverse problem. In general, based on Fermat's principle, it is assumed that "picked travel times" correspond to the shortest travel time paths.

- Ray tracing is a two-point boundary value problem: the end points are specified (the source and receiver positions), and the propagation path and time must be determined. Ray theory is used in the development of some ray tracing algorithms. However, there are more general solutions. Ray tracing techniques can be categorized as: One-point methods, Two-point methods, and Whole-field methods.
- One-point methods are efficient and have low memory demands. Yet, they have all the restrictions inherent in ray theory. Furthermore, they may never converge. Two-point methods are flexible and efficient, require low memory storage and can solve travel times in shadow zones and diffracted ray paths. However, they may not be able to find the global minimum. Whole-field methods can identify global minimum travel times, including shadow and diffracted zones. While the solution is computer demanding, all rays from a given shot are solved at once.

Optimization of DLSQ and Regularization Coefficients

- In a tomographic inversion process, under-determination (or mixed-determination) and noise in the data result in ill-conditioned problems. A

solution can be obtained using matrix based, Damped Least Squares (DLSQ) or regularization methods.

- Addition of *a priori* information is one way to decrease the size of the null space by specifying image parameters (unknowns) that reside in the null space.
- The DLSQ method overcomes the singularity of the coefficient matrix. In the case of a mixed-determined problem and noisy data, the regularization method is applied by adding information, in the form of constraints. In both cases, the best solution can be obtained for a certain damping or regularization coefficient. The quality of the image worsens with either lack of or excessive damping or regularization coefficients. These coefficients are not unique but depend on the velocity field.
- One way to determine the size of the null space is to plot the sizes of the singular values against their index numbers. This is the spectrum of the data kernel. This plot also highlights the true amount of information relative to the number of measurements that were conducted.
- As a part of this study, criteria were evaluated to determine the optimal values for DLSQ and regularization coefficients. The selection based on the coefficient of variation (COV) of the whole set of pixel slownesses tends to promote global smoothness. Another alternative approach is to define local measures of variability.
- The maximum likelihood method asserts that the optimum values of the system parameters maximize the probability that the observed data are in fact observed. In this study the maximum likelihood method was used to evaluate the optimal regularization coefficient. Assuming a Gaussian distribution for the travel time data, the optimal regularization coefficient can be obtained from a cumulative number of appearances of the data vs. travel

time data plot. In this case, the method fails to evaluate the optimal coefficients in most cases. However, the optimal coefficients can be evaluated if the intersection point of the two best lines passing through the data points is computed. The results show under-smoothed images similar to the previous methods. Another option is to assume an exponential distribution for the travel times data. In this case, the method has shown certain values for the optimal coefficients in all cases. However, since in some cases a post peak appears, for the purpose of programming, the safe way to evaluate the optimal regularization coefficient is to start with large regularization values. The optimal value is the first available peak. The reason that the exponential distribution gives more accurate results than the Gaussian distribution lies in the relationship between these two distributions and the L norms. The exponential distribution has the same relationship to the L_1 norm as the Gaussian distribution has to the L_2 norm. A high-order norm should be employed for short-tailed data. The tomographic data, and especially side-to-side shootings, appear to have a long-tailed distribution. Therefore, it is more appropriate to use the exponential distribution.

Computational Efficiency and Accuracy in Ray Tracing Methods

As a part of this research, the computational efficiency and accuracy in ray tracing methods were studied. The following are concluded:

- An n step ray is assumed to have a parameter comparable with all ray tracing methods. An example of one-point methods will require $4n$ calculations for each ray to be traced. If the ray path is defined for m shooting angles, then, the number of calculations needed for only primary ray tracing by one-point methods is in the order of $4mn^2$.

- The density of over-head computations varies among methods and it may be a decisive factor (e.g. computation time required for determining shooting angles in one-point method).
- Two rays from a source never cross. Hence, one-point methods and two-point methods can be readily optimized by searching all rays from a given source at once. The reduction in computational demand is proportional to n^3 , shifting curves parallel towards the straight-ray case.
- Travel time is relatively insensitive to variations in ray path. Often, most computational efforts in ray tracing are spent in optimizing travel times to the point that the estimated time error becomes significantly lower than measurements errors. However, optimization alters ray paths and the length rays traverse different cells. This affects tomographic reconstruction. The significance of this effect was evaluated.

Pre-Processing

Data pre-processing can be employed to provide foresight about the medium, and help provide proper constraints for the solution. Selected pre-processors designed during this study are: distribution and amount of information, presence of accidental and systematic errors, degree of heterogeneity and anisotropy, and analysis of shadows. All the pre-processors were tested with all case histories.

WATom-I Software

- A program for tomographic inversion has been written as part of this study. The selected tomographic inversion methods are based on matrix analyses.

To avoid high memory and computational time demands, sparse matrix algorithms are employed. Ray bending and straight rays are two possibilities. The program is in structured form to facilitate future additions and modifications. The Sine-Arc two-point ray tracing method is used for non-linear cases. The conjugate gradients method is used to determine the inverse of the coefficient matrix.

8.2 Conclusions

- Matrix based inversion methods are mathematically robust and facilitate analyzing the available information and adding additional constraints. However, efficient storage and computation are required. Sparse matrix data structures and algorithms were used in the written software (WATOM-I).
- It was shown that while more accurate travel paths can improve the inverted image, the ray paths accuracy does not need to exceed measurement accuracy on travel times, which is usually about 1%.
- The effect of model error was evaluated. Ray tracing optimization alters ray paths and the length that rays traverse different cells. This affects tomographic reconstruction. The significance of this effect was evaluated with simulated data to facilitate comparison. It was shown that only 1% error in time relates to an average 4-pixel widths difference in travel length per pixel (400%); given that the average travel length per pixel is 20 pixel widths, the percent average error is $4/20=20\%$.
- While most tomographic studies are based on simulated data, a data base of case histories with real data was compiled and employed in this study. The inversion of real data is significantly more challenging than would be

expected from the extensive number of studies with simulated data that are found in the literature.

- Before any inversion process, the measurement set can be analyzed to learn about system parameters and trends. Pre-processing methods were employed as a pre-looking into the data and as an integral part of “enhanced inversion”.
- Small singular values can generate large errors in the solution. Regularization adds information in the form of constraints in order to decrease the ill-conditioning of the problem. It is shown that regularization is a robust solution if random or systematic noise is added to the data.
- The number of independent equations in a data set is not equal to the number of data. Singular value decomposition was used to indicate this fact for selected case histories. The size of null space can be improved by regularizing the data.
- Optimal DLSQ and regularization coefficients can be identified on the bases of global and local variability of the inverted image and the error between the measured and predicted travel times. It was concluded that the values of coefficients selected with these approaches is higher than the optimal value.
- The optimal value of regularization coefficient was evaluated based on the maximum correlation (maximum likelihood) of the joint distribution of the observed and calculated travel times. The optimal regularization coefficients were located in most cases. However, multiple solutions were possible in some cases. In those cases, the best way to approach the optimal coefficient is to start with high values of the regularization coefficient. The optimal value is the first maximum value of the probability.

REFERENCES

- Aki, K., and Richards, P. G., 1980, Quantitative Seismology - Theory and Methods, Vols. 1 and 2, Freeman Company, San Francisco, 932 pages.
- Asakawa, E., and Kawanaka, T., 1993, "Seismic Ray Tracing Using Linear Travel Time Interpolation", *Geophysical Prospecting*, Vol. 41, p. 99-111.
- Auld, B. A., 1973, Acoustic Fields and Waves in Solids, A Wiley-Interscience Publication, New York.
- Bracewell, R., and Riddle, A. C., 1967, "Inversion of Fan Beam Scans in Radio Astronomy", *Astronomy*, V. 50, p. 427-434.
- Cerveny, V., Klimes, L., and Psencik, I., 1984, "Paraxial Ray Approximation in the Computation of Seismic Wavefield in Inhomogeneous Media" *Geophys. J. R. astr. Soc.*, Vol. 79, p.89-104.
- Chernov, L. A., 1960, Wave Propagation in a Random Medium, New York, Dover, 168 pages.
- Cormack, A., 1973, "Reconstruction of Densities From Their Projections With Applications in Radiological Physics", *Phys. Med. Biol.*, V. 18, p. 195-207.
- Devaney, A. J., 1984, "Geophysical Diffraction Tomography", *IEEE Trans. Geo. Remote Sens.*, Vol.GE-22, No.1, p. 3-13.
- Dines, K.A., and Lytle, R. J., 1979, "Computerized Geophysical Tomography" *Proce. IEEE*, Vol. 67, No. 7, pp. 1065-1073,
- Dyer, B.C., and Worthington, M. H., 1988, "Seismic Reflection Tomography, A Case Study", *F.B.*, V.6, No. 11, p. 354-366.
- Eliseevnin, V. A., 1965, "Analysis of Waves Propagating in an Inhomogeneous Medium", *Soviet Physics Acoustics*, Vol. 10, p. 242-245.
- Forsythe, G. E., Malcolm, M. A., and Cleve, B. M., 1977, Computer Methods for Mathematical Computation, Prentice-Hall, Inc., 259 pages.
- Geoltarine, S., and Brac, J., 1993, "Can We Image Complex Structures with First-Arrival travel time?", *Geophysics*, Vol. 58, No. 4, p. 564-575.
- Gheshlaghi, F., and Bahavar, M., 1991, "Tomographic Methods and Their Applications in Cross-Hole Data Processing", *Proc. of SEE 1.*, Tehran, Iran.

- Gheshlaghi, F., 1992, "Determination of Earthquake Hypo-Center by Ray Tracing", *Proc. of SEE 1.*, Tehran-Iran.
- Gheshlaghi, F., Santamarina, J. C., Wiese, D., Thomas, M., Polak, M., and Caratin, G., 1995, "Tomographic imaging - Concrete Structures", *Proc. of Non-Destructive Testing in Civil Eng.*, Berlin, Germany.
- Gloub, G.H., and Van Loan, C.F., 1983, Matrix Computations, N. Oxford, Oxford, 642 pages.
- Golubov, B., Efimov, A., and Skvortsov, V., 1991, Walsh Series and Transforms, Theory and Applications, Kluwer Academic Publishers, Dordrecht, 368 pages.
- Gordon, R., 1974, "A Tutorial on ART", *IEEE. Tran. Nucle. Scie.*, Vol. NS-21, p. 78-93.
- Henrique, L. M. dos Reis, 1990, Non-Destructive Testing and Evaluation for Manufacturing and Construction, Hemisphere Publishing Corporation, New York, 368 pages.
- Hansen, P. C., 1992, "Analysis of Discrete Ill-Posed Problems by Means of the L-Curve", *SIAM Rev.*, Vol. 34, No. 4, p. 561-580.
- Hansen, P. C., and, O'leary, D. P., 1993, "The Use of the L-Curve in the Regularization of Discrete Ill-Posed Problems", *SIAM J. Sci. Comput.*, Vol. 14, No. 6, p. 1487-1503.
- Helbig, K., 1994, Foundations of Anisotropy for Exploration Seismics, Elsevier Science, New York, 486 pages.
- Hounsfield, G. N., 1973, "Method and Apparatus for Measuring X or Gamma Radiation Absorption or Transmission at Plural Angles and Analyzing the Data", *U.S.patent* , Vol.6, p.778-614.
- Hryciw, R., 1989, "Ray-Path Curvature in Shallow Seismic Investigations", *ASCM Journal of Geotechnical Engineering*, Vol. 115, p. 1268-1284.
- Ishii, Y., Rokugawa, S., and Suzuki, T., 1988, "On the Various Subsurface Models and ART Methods", *Proceedings of 1988 spring meeting, SEG Japan*, p.23-26.
- Iyer, H. M., and Hirahara, K., 1993, Seismic Tomography, Chapman and Hall, London, 842 pages.
- Julian, B. R., and Gubbins, D., 1977, "Three-Dimensional Seismic Ray Tracing", *Journal of Geophysics*, Vol. 43, p. 95-113.

- Kak, A. C., and Slaney, M., 1988, Principles of Computerized Tomographic imaging, IEEE Press, New York, 329 pages.
- Lee, W. H. K., and Stewart, S. W., 1981, Principles and Applications of Microearthquake Networks, Academic Press, New York, 293 pages.
- Lytle, R. J., and Dines, K. A., 1980, "Iterative Ray Tracing Between Boreholes for Underground Image Reconstruction", *IEEE Trans. Geo. Remo. Sens.*, Vol. GE-18, No. 3, p. 234-240.
- Matsuoka, T., and Ezaka, T., 1990, "Ray Tracing on Reciprocity", 60th SEG meeting, San Francisco, Extended Abstracts, p. 1028-1031.
- McMechan, G.A., 1983, "Seismic Tomography in Boreholes", *Geophys. J. R. Astr. Soc.*, Vol. 74, p.601-612.
- McMechan, G.A., Harris, J.M., and Anderson, M., 1987, "Cross-hole Tomography for Strongly Variable Media with Applications to Scale Model Data", *Boll. Seis. Soci. Am.* , Vol.77, No.6, p.1945-1960.
- Menke, W., 1989, Geophysical Data Analysis, Academic Press, Inc., New York, 285 pages.
- Mersereau, R.M., and Oppenheim, A.V., 1974, "Digital Reconstruction of Multi-Dimensional Signals from Their Projections", *Proc. IEEE.*, Vol.62, No.10, p.210-229.
- Michelena, R.J., 1993, "Singular Value Decomposition for Cross-Well Tomography", *Geophysics*, Vol. 58, No.11, p.1655-1661.
- Morozov, V.A. 1993, Regularization Methods for Ill-Posed Problems, CRC Press, 257 pages.
- Moser, T. J., 1991, "Shortest Path Calculation of Seismic Rays", *Geophysics*, Vol. 56, No. 1, p. 59-67.
- Moser, T. J., 1994, "Migration Using the Shortest Path Method", *Geophysics*, Vol. 59, No. 7, p. 1110-1120.
- Nelder, J. A., and Mead, R., 1965, "A Simplex Method for Function Minimization", *Computer Journal*, Vol. 7, p. 308-313.
- Nilsson, N. J., 1980, Principles of Artificial Intelligence, Tioga Publishing Co., 476 pages.
- Nolet, G., 1987, Seismic Tomography, D. Reidel Publishing company, 386 pages.

- Officer, C. B., 1974, Introduction to Theoretical Geophysics, Springer-Verlag New York Inc., 385 pages.
- Pan, S.X., and Kak, A.C., 1983, "A Computational Study of Reconstruction Algorithms for Diffraction Tomography: Interpretation Versus Filtered Backpropagation", *IEEE Trans. on Acoustics Speech, and Signal Processing*, Vol.ASSP-31, No.5, p.1262-1275.
- Paul, R.J., 1993, "Seismic Detection of Over-Pressuring and Fracturing: An Example from the Qaidam Basin, People's Republic of China", *Geophysics*, Vol.58, No.10, p.1532-1543.
- Peterson, J. E., Paulsson B. N. P., and McEvilly, T. V., 1985, "Applications of Algebraic Reconstruction Technique to Crosshole Seismic Data", *Geophysics*, Vol.50, No.10, p. 1566-1580.
- Podvin, P., and Lecomte, I., 1991, "Finite-Difference Computation of Travel Times in Very Contrasted Velocity Models: a Massively Parallel Approach and Its Associated Tools", *Geophysical J. International*, Vol. 105, p. 271-284.
- Prothero, W. A., Taylor, W. J., and Eickemeyer, J. A., 1988, "A Fast, Two-Point, Three-Dimensional Ray Tracing Algorithm Using a Simple Step Search Method", *Bulletin of the Seismological Society of America*, Vol. 78, No. 3, p. 1190-1198.
- Rechten, R. D., and Ballard, R. F., 1993, "Cross-borehole Seismic Tomographic of Tunnels", *Proc. of the Fourth Tunnel Detection Symposium on Subsurface Exploration Technology*, Golden, Colorado.
- Rhazi, J., 1995, "Tomographic Data: Chute Hemmings Dam", Internal Report, Laval University.
- Sambridge, M. S., and Kennett, B. L. N., 1990, "Boundary Value Ray Tracing in a Heterogeneous Medium: a Simple and Versatile Algorithm", *Geophysical Journal International*, Vol. 101, p. 157-168.
- Santamarina, J.C., 1991, "Imaging with Uncertain Data Using Fuzzy Constraints", *EOS - Transactions American Geophysical Union*, April 23 Issue, p. 194.
- Santamarina, C., Tallin, A., Wakim, T., 1991, "Kosciuzko Bridge Pier - A Tomographic Study", Civil and Environmental Engineering Department, Polytechnic University, New York.
- Santamarina, J. C., Tallin, A., and Wakim, T., 1991, "Imaging a Balloon: A Laboratory Demonstration of Tomographic Techniques", Civil and Environmental Engineering Department, Polytechnic University, New York.

- Santamarina, J. C., 1994, An Introduction to Geotomography, Geophysical Characterization of Sites, Edited R. D. Woods, International Science Publisher, New Hampshire (see also University of Waterloo course notes).
- Santamarina, J. C., and Reed, A. C., 1994, "Ray Tomographic: Errors and Error Functions", *Journal of Applied Geophysics*, Vol. 32, p. 347-355.
- Santamarina, J. C., and Cesare, M. A., 1995, "Tomographic Inversion in Vertically Heterogeneous, Anisotropic media", University of Waterloo Report.
- Santamarina, J. C., and Gheshlaghi, F., 1995, "Tomographic Imaging: Potentials and Limitations", *Proceedings of SPIE*, Oakland, California, Vol. 2457, p. 67-78.
- Sassa, K., *et al.*, 1989, "Improvement in the Accuracy of Seismic Tomography by Use of an Effective Ray-Tracing Algorithm", MMIJ/IMM Joint Symposium Shigaku-Kaikan Kyoto, Japan.
- Scudder, H.J., 1978, "Introduction to Computer Aided Tomography", *Proc. IEEE.*, Vol. 66, p. 628-637.
- Shepp, L.A., and Vardi, Y., 1982, "Maximum Likelihood Reconstruction for Emission Tomography", *IEEE Trans. Medical Im.*, Vol. MI-1, No. 2, p. 113-122.
- Sheriff, R. E., 1978, A First Course in Geophysical Exploration and Interpretation, IHRDC Publishers, 313 pages.
- Sheriff, R. E., 1989, Geophysical Methods, Prentice Hall, Englewood Cliffs, New Jersey, 605 pages.
- Silvey, S. D., 1970, Statistical Inference, Penguin Books, 192 pages.
- Sluis, A., and Vorst, H., 1987, Seismic Tomography, D. Reidel Publishing company, Chapter 3, 386 pages.
- Spencer, C., and Gubbins, D., 1980, "Travel-time Inversion for Simultaneous Earthquake Location and Velocity Structure Determination in Laterally Varying Media", *Geophys. J. R. Astr. Soci.*, Vol. 63, p.95-116.
- Stöckli, R. F., 1984, "Two point Ray Tracing in a Three-Dimensional Medium Consisting of Homogeneous Non isotropic Layers Separated by Plane Interfaces", *Geophysics*, Vol. 49, No. 6, p. 767-770.
- Tallin, A.G., and Santamarina, J.C. (1989), Geotomographic Site Investigation Software, *Proc. 7th Nat. Conf. Microcomputers in Civil Engineering*, Orlando, pp. 219-222.

- Tallin, A.G., and Santamarina, J.C., 1992, "Digital Ray Tracing for Geotomography", *IEEE Trans. Geo. Remote Sens.*, Vol. 30, No. 3, p. 617-619.
- Thurber, C. H., and Ellsworth, W. L., 1980, "Rapid Solution of Ray Tracing Problems in Heterogeneous Media", *Bulletin of the Seismological Society of America*, Vol. 70, No. 4, p. 1137-1148.
- Um, J., and Thurber, C., 1987, "A Fast Algorithm for Two-Point Seismic Ray Tracing", *Bulletin of the Seismological Society of America*, Vol. 77, No. 3, p. 972-986.
- Vidale, J. E., 1988, "Finite-Difference Calculation of Travel Times", *Bulletin of the Seismological Society of America*, Vol. 78, No. 6, p. 2062-2076.
- Vidale, J. E., 1990, "Finite-Difference Calculation of Travel Times in Three Dimensions", *Geophysics*, Vol. 55, No. 5, p. 521-526.
- Williamson, P. R., and Worthington, M. H., 1993, "Resolution Limits in Ray Tomography due to Wave Behavior: Numerical Experiments", *Geophysics*, Vol. 58, No. 5, p. 727-735.
- Witten, A.J., King W.C., and J.R. Ursic, 1993, "Geophysical Techniques for Site and Material Characterization", Workshop report, Atlanta, Georgia, p. 35-49.

**APPENDIX A: Ray Paths and Direction
Cosines**

The relations between α , β , i_0 and azimuth ϕ are based on the Figure (A-1) and the following equations (Gheshlaghi, 1992).

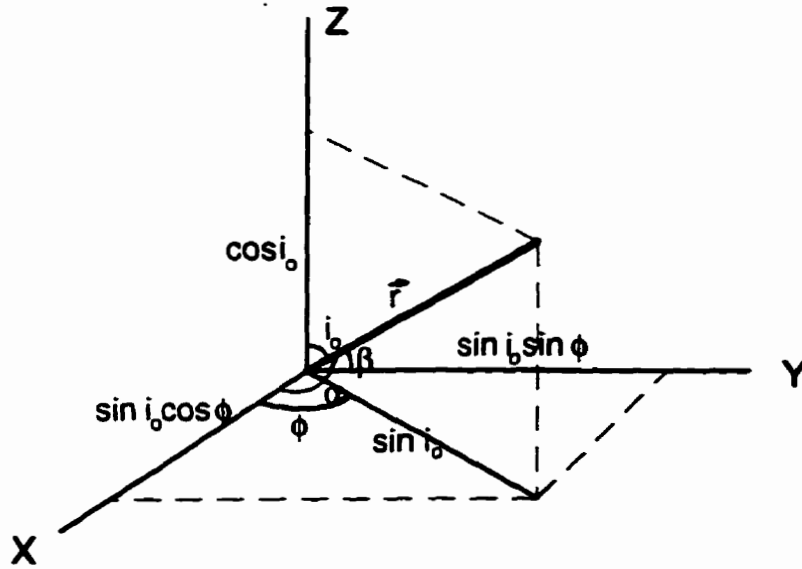


Figure A-1 Graphic relation between the α , β , i_0 and azimuth ϕ .

$$\begin{aligned}
 x &= \vec{r} \cdot \cos \alpha = \vec{r} \cdot \sin i_0 \cdot \cos \phi \\
 y &= \vec{r} \cdot \sin \beta = \vec{r} \cdot \sin i_0 \cdot \sin \phi \\
 z &= \vec{r} \cdot \cos i_0 \\
 \vec{r} &= \sin i_0 \cdot \cos \phi \cdot \hat{i} + \sin i_0 \cdot \sin \phi \cdot \hat{j} + \cos i_0 \cdot \hat{k}
 \end{aligned}
 \tag{A-1}$$

Therefore, the initial value formulation of the ray equation from the eikonal equation may be written as (Eliseevnin, 1965):

$$\begin{aligned}
 \partial_t x &= v \cdot \cos \alpha \\
 \partial_t y &= v \cdot \cos \beta \\
 \partial_t z &= v \cdot \cos i_0
 \end{aligned}
 \tag{A-2a}$$

$$\begin{aligned}
\partial_t \alpha &= \frac{\partial v}{\partial x} \cdot \sin \alpha - \frac{\partial v}{\partial y} \cdot \cot \alpha \cdot \cos \beta - \frac{\partial v}{\partial z} \cdot \cot \alpha \cdot \cos i_o \\
\partial_t \beta &= -\frac{\partial v}{\partial x} \cdot \cos \alpha \cdot \cot \beta + \frac{\partial v}{\partial y} \cdot \sin \beta - \frac{\partial v}{\partial z} \cdot \cot \beta \cdot \cos i_o \\
\partial_t i_o &= -\frac{\partial v}{\partial x} \cdot \cos \alpha \cdot \cot i_o - \frac{\partial v}{\partial y} \cdot \cos \beta \cdot \cot i_o + \frac{\partial v}{\partial z} \cdot \sin i_o
\end{aligned} \tag{A-2b}$$

where ∂_t denotes differentiation with respect to time; x , y , and z describe the endpoint position of the ray at a particular time, $v(x,y,z)$ is the wave velocity; and $\cos \alpha$, $\cos \beta$, and $\cos i_o$ are the local direction cosines related by the expression,

$$\cos^2 \alpha + \cos^2 \beta + \cos^2 i_o = 1 \tag{A-3}$$

Because of the relationship between direction cosines, only five of the equations in (A-2a&b) are independent and therefore only five variables are required to describe the ray at any point of its trajectory. If ϕ and i_o angles are used the following equations can be derived.

$$\begin{aligned}
\partial_t x &= v \cdot \sin i_o \cdot \cos \phi \\
\partial_t y &= v \cdot \sin i_o \cdot \sin \phi \\
\partial_t z &= v \cdot \cos i_o \\
\partial_t i_o &= -\cos i_o \cdot \left(\frac{\partial v}{\partial x} \cdot \cos \phi + \frac{\partial v}{\partial y} \cdot \sin \phi \right) + \frac{\partial v}{\partial z} \cdot \sin i_o, \\
\partial_t \phi &= \frac{1}{\sin i_o} \left(\frac{\partial v}{\partial x} \cdot \sin \phi - \frac{\partial v}{\partial y} \cdot \cos \phi \right).
\end{aligned} \tag{A-4}$$

**APPENDIX B: Lytle and Dines's One-Point
Method ALGOL**

The following steps are involved in a ray tracing algorithm based on the one-point method by Lytle and Dines (1980).

Main program:

1. Choose a shooting angle θ , from an specific source position.
2. Define a parameter "h" as the step length.
3. Go to **subroutine SPLINE** and determine the smoothed local refractive index variation for the next point, based on values of four neighborhood points [(i,j), (i,j+1), (i+1,j), and (i+1,j+1)].
4. Calculate $\Delta\theta_1$, $\Delta\theta_2$, $\Delta\theta_3$, and $\Delta\theta_4$ to obtain four parameters required for the fourth order Runge-Kutta method¹, and determine the next θ value (θ_{i+1}).
5. Repeat steps 3 and 4 until the ray reaches a boundary.
6. Repeat steps 3 to 5 for different lanching angles θ_m ($m=1,2,\dots,n$) from a specific source location.
7. Go to **subroutine ANGLE** and build a continuous function based on the position of exit points and lanching angles.
8. Go to **subroutine ZEROIN** and determine the lanching angle for a given receiver position, using function obtained in the step 7. This is implemented with Newton-Raphson's method.
9. Repeat step 8 for all of the receiver locations.
10. Repeat steps 3 to 9 for all of source locations..

¹ The numerical solution of a differential equation by the Runge-Kutta method avoids the computation of high-order derivatives needed in Taylor Series expansion. Instead, the method uses extra values of the function within the step h.

**APPENDIX C: General Algorithms and
Flowcharts in WATom-I**

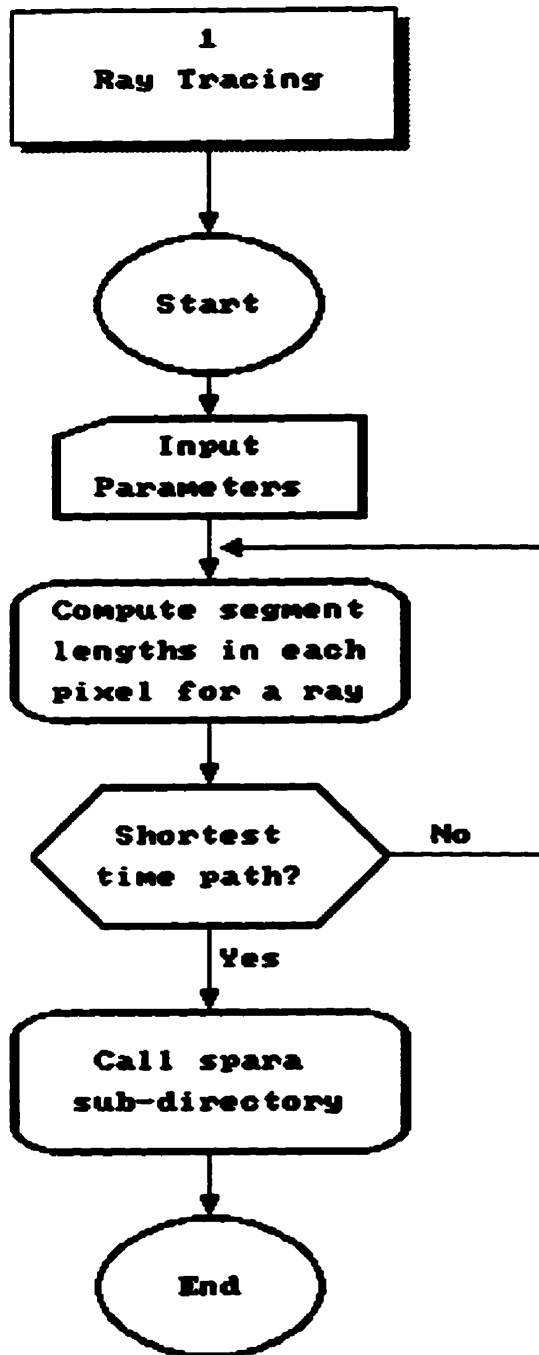


Figure C-1: A general view of the ray tracing algorithm and computation steps for calculating the entries of the "L" matrix.

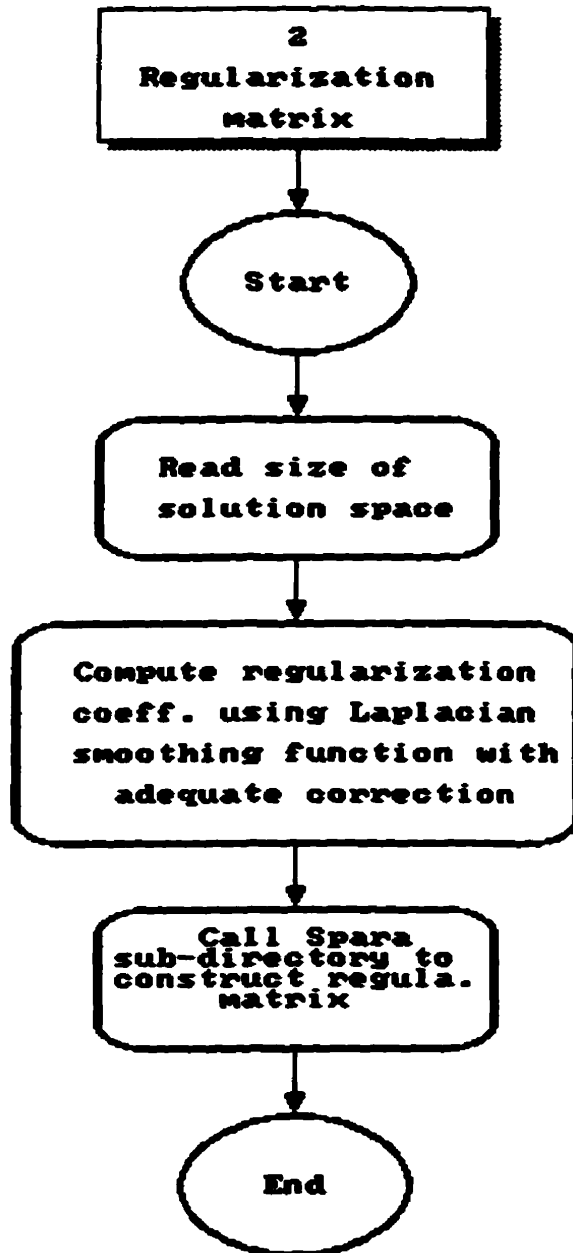


Figure C-2: Computation steps in calculating the entries of the regularization matrix.

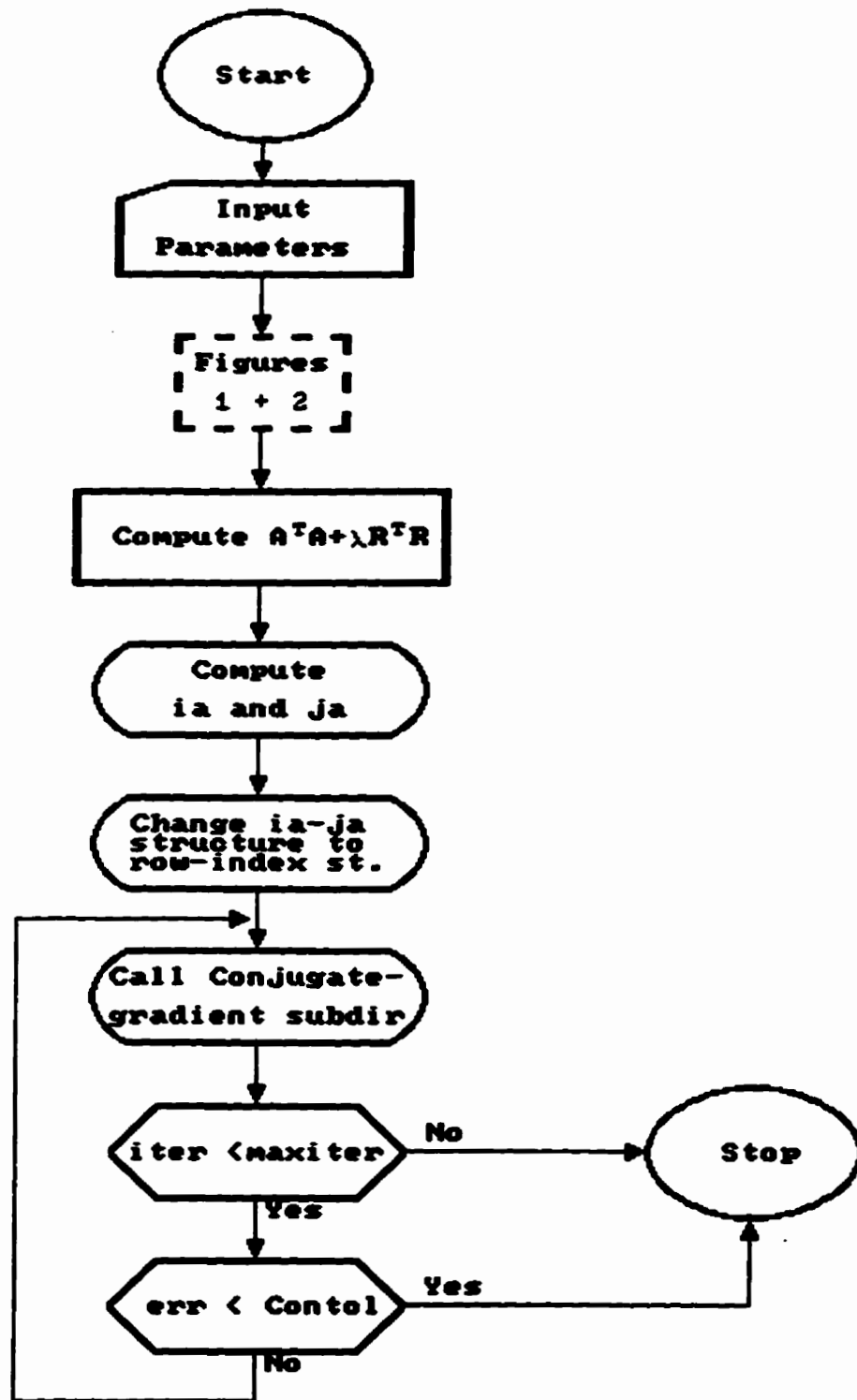


Figure C-3: WATOM-I inversion algorithm (this figure shows only the inversion part). Entries 1+2 refer to the algorithms for ray tracing and regularization (Figures C-1 and C-2).

APPENDIX D: WATom-I Software

```

* .....
C +
C + Tomographic Imaging Using Sparse Matrix Algorithm +
C + and Ray Tracing (WATOM-I) +
C +
* .....

character*20 datf, ray_path, method
character*132 note1

C
integer nray, npix, ndim, sn, m

C
double precision div, add, lambda, w, h
double precision contol, tolcon

C
integer k, n, nja, maxiter, itemax, ikmax

C
C
C -----
C + Parameters Decleration +
C + k = No. of rays, +
C + n = No. of pixels +
C + nja = No. of elements in +
C + matrix A. +
C + maxiter = No. of iterations +
C -----
C
C
parameter(maxiter=50, contol = 1.d-10)

C
write(*, '(7x,a)') 'Input No. of rays and pixels....====>:'
read (*, *) nray, npix

C
nja= nray**2
ndim= nray
if(npix .gt. nray) then
  nja= npix**2
  ndim= npix
endif

C
C -----
C + Input file for initial data +
C -----
C
open(4,file='sdat', status='unknown')

C
ntry=1
ntry1=1
write(*, '(5x,a)') 'No. of Sources and Receivers ....====>:'
read(4, *) sn, m
write(*, '(5x,a)') 'Input No. of rows and Columns ...====>:'
read(4, *) m, ncol
write(*, '(5x,a)') 'Width and Height of the region ..====>:'

```

```

4      read(4,*) w,h
      write(*,'(5x,a)\')(R)egularization or (D)LSQR ..... ==>:'
      read(4,'(a)') method
      if((method .eq. 'R') .or. (method .eq. 'r')) then
      write(*,'(5x,a)\')'Input Regularization coeff. value ==>:'
      read(4,*) lambda
      elseif((method .eq. 'D') .or. (method .eq. 'd')) then
      write(*,'(5x,a)\')'Input DLSQR coeff. value ..... ==>:'
      read(4,*) lambda
      elseif(ntry1 .lt. 3) then
      write(*,'(///10x,a)\')'..... You typed a wrong letter, try R/r
+or D/d .....
          ntry1 = ntry1+1
          write(*,'(///a)\')' '
      goto 4
      else
          stop
      endif
      write(*,'(5x,a)\')'Name of input data file ..... ==>:'
      read(4,'(a)') datf
5      write(*,'(5x,a)\')(S)traight rays or (C)urved rays ==>:'
      read(4,'(a)') ray_path
c
      if((ray_path .eq. 'S') .or. (ray_path .eq. 's')) then
          ikmax=1
          div= 1.
          add= 1.
      elseif((ray_path .eq. 'C') .or. (ray_path .eq. 'c')) then
          read(4,*) ikmax, div, add
          read(4,*) itermax, tolcon
      elseif(ntry .lt. 3) then
      write(*,'(///10x,a)\')'..... You typed a wrong letter, try S/s
+or R/r .....
          ntry = ntry+1
          write(*,'(///a)\')' '
      goto 5
      else
          stop
      endif
c
c
c
c      +      output files      +
c      -----
c
      open( unit=16, file='vlo.out',status='unknown')
      open( unit=18, file='out.out',status='unknown')
c
c
c
      call mainsub(nray, npix, ndim, nja, sn, m,
+          m, ncol, w, h, lambda, datf,
+          ikmax, div, add, ray_path, method,
+          maxiter, itermax, contol, tolcon)

```

```

stop
end

C
C
*
*****
C      +
C      +          MAIN SUBROUTINE          +
C      +
*      *****

C
C
subroutine mainsub(k, n, ndim, nja, sn, m,
+          m, ncol, w, h, lambda, datf,
+          ikmax, div, add, ray_path, method,
+          maxiter, itermax, contol, tolcon)

character*20 datf, ray_path, vlof, method

C
C
integer ia(ndim+1), ja(nja), ier, iconj,
+       ija(nja+1), iat(ndim+1), jat(nja)

C
integer ir(ndim+1), jr(nja)

C
integer i, ii, sn, rn, kk
integer icount, itermax, maxiter, ikmax

C
double precision row(ndim), a(nja), b(n), at(nja),
+       x(n), v(n), btime(k), r(nja),
+       aft(ndim), a2(n,n), sa(nja+1), btem(k)

C
double precision tmpx, avex, veloc, vav
double precision div, add, lambda, w, h
double precision contol, tolcon, tsqrt

C
C
if((ray_path .eq. 'C') .or. (ray_path .eq. 'c')) then
write(*, '(/5x,a)') 'Input velocity file-name ..... ==>:'
read(4, *) vlof
open(1, file=vlof, status='unknown')
read(1, *) (v(jj), jj=1,n)
do i=1,n
v(i)= 1./v(i)
enddo
elseif((ray_path .eq. 'S') .or. (ray_path .eq. 's')) then
write(*, '(/5x,a)') 'Input average velocity ..... ==>:'
read(4, *) vav
do i=1,n
v(i)= 1./vav
enddo

C
endif

C

```

```

write(*,'(///18x,a)')***** ..... PLEASE WAIT ..... *****
C
C
C   icount= 1
1   continue
   tsqrt= 0.
C
C   call ray(k, n, ndim, nja, a, v, btime, at, iat,
+       jat, m, ncol, w, h, lambda, datf, kk,
+       ikmax, div, add, sn, m, btem)
C
C
C   -----
C   + operations with matrices +
C   -----
C
C   call transa(k, n, kk, iat, jat, at,
+       nja, ndim, ia, ja, a)
C
C   iparcham= 0
C   call ata(iparcham, k, n, nja, ndim, ia, ja, a,
+       aft, iat, jat, at)
C
C   call atb(k, n, nja, ndim,
+       ia, ja, a, btime, b)
C
C   if((method .eq. 'D') .or. (method .eq. 'd')) then
C
C       call DLSQR(n, nja, ndim, r, ir, jr)
C
C   elseif((method .eq. 'R') .or. (method .eq. 'r')) then
C
C       call regula(k, m, ncol, n, ndim, nja, a, r, ir, jr, kk)
C
C   else
C       write(*,*) 'Input error in matrix method'
C
C   endif
C
C   -----
C   + constructing matrix rt and irt-jrt +
C   -----
C
C   call transa(k, n, kk, ir, jr, r,
+       nja, ndim, ia, ja, a)
C
C   -----
C   + constructing rtr +
C   -----
C
C   iparcham= 1
C   call ata(iparcham, k, n, nja, ndim, ia, ja, a,
+       aft, ir, jr, r)
C
C   call combin(n, nja, ndim, at, iat, jat,
+       r, ir, jr, aft, row, lambda, a, ia, ja)

```

```

C -----
C + change storage mode for sparse matrix +
C -----
C
C call replc(n, nja, ndim, a, ia, ja, a2)
C
C call sprsin(a2, n, nja, sa, ija)
C
C -----
C + conjugate gradient inversion +
C -----
C
C call linbcg(nja, contol, n, b, v, maxiter,
+       ija, sa, x)
C
C   if((ray_path .eq. 'C') .or. (ray_path .eq. 'c')) then
C     icount= icount+1
C     do i= 1,k
C       tsqrt= tsqrt+(btime(i)-btem(i))**2
C     enddo
C     tsqrt= dsqrt(tsqrt)
C     if((tsqrt .lt. tolcon) .or.
+       (icount .gt. itermax)) then
C       goto 22
C     else
C       do 2 i= 1,n
C         v(i)= 1./x(i)
C       2 continue
C       goto 1
C     endif
C   endif
C
C 22 tmpx= 0.
C
C
C do 3 i= 1, n
C   x(i)= dabs(x(i))
C   tmpx=tmpx+x(i)
C 3 continue
C avex= tmpx/dfloat(n)
C
C do 4 i=1, n
C   if (v(i) .eq. 0.) goto 4
C   if (x(i) .le. 0.) then
C     v(i)= 1./avex
C   else
C     v(i)= 1./x(i)
C   endif
C 4 continue
C
C 5 continue
C do 6 i= 1,n
C   write(16,'(5x,f20.5)'v(i)
C 6 continue
C
C return

```

```

end
C
C
C
C
* .....
* *
C + calculating ray segments in each +
* + pixel, assuming Arc-Sine or Straight paths +
* *
* .....

subroutine ray (k, n, ndim, nja, a, v, btime, at, iat,
+ jat, m, ncol, w, h, lambda, datf, kk,
+ ikmax, div, add, sn, m, btern)

C
character*20 datf
character*100 note_s, note_r, note_t
C
integer iflag, iflag1, sn, m, ns, nr
C
double precision Lnt(n), v(n), plnt(n),
+ sx(sn), sz(sn), rx(m), rz(m)
C
C
real sxtmp, sztmp, rxtmp, rztmp, txtmp, tztmp,
+ xtmp, ztmp, ytmp, ytmp1
C
double precision tem, lambda, tmpt, tmp, x, y, tx, tz,
+ w, h, tmplx, tmpsz, ak, div, add, yy,
+ tmpb, xb, xbh, zbh, pi, txb, tzb, zb,
+ txb1, tzb1, txb2, tzb2, tem1, vav, ln
C
integer k, n, ndim, nja, ij, kj, ij,
+ ii, num, jmax, kj, kk, i, j,
+ ik, ikk, in, im, ikmax
C
double precision a(nja), btime(k), at(nja)
C
integer iat(ndim+1), jat(nja)

xb= w/dfloat(ncol)
xbh= xb/2.
zb= h/dfloat(m)
zbh= zb/2.

C
C
C + intializing +
C
do i= 1,n
plnt(i)= 0.
enddo
C

```

```

do i=1,ndim+1
  iat(i)=0
enddo
c
do i=1,nja
  jat(i)=0
  a(i)=0.
  at(i)=0.
enddo
iat(1)= 1
in= 0
kk= 1
kj= 1
num= 0
jmax= ncol
pi= 3.141592
ic= 1
c
c
c -----
c + Input data-file +
c -----
c
open(2, file=datf, status='unknown')
c
read(2,'(//a)') note_s
do i= 1,sn
  read(2,*)sx(i), sz(i)
  sx(i)= sx(i)/xb
  sz(i)= sz(i)/zb
enddo
c
read(2,'(a)') note_r
do i= 1,m
  read(2,*)rx(i), rz(i)
  rx(i)= rx(i)/xb
  rz(i)= rz(i)/zb
enddo
c
read(2,'(a)') note_t
c
1 continue
c
read(2,*,err=3) ns, nr, btime(kj)
c
ln= 0.
tem= 0.
tmpt= 1.e20
iflag= 0
ytmp1= 1.e20
c
if(sz(ns) .gt. dfloat(m)) then
write(*,*)'warning!!! *source location value out of range*'
pause
endif
c
if(rz(nr) .gt. dfloat(m)) then

```

```

write(*,*)'warning!!! "receiver location value out of range"
pause
endif
c
if (sx(ns) .gt. rx(nr))then
  tmpsx= sx(ns)
  sx(ns)= rx(nr)
  rx(nr)= tmpsx
  tmpsz= sz(ns)
  sz(ns)= rz(nr)
  rz(nr)= tmpsz
  iflag1= 3
endif
c
sxtmp= sx(ns)
sztmp= sz(ns)
rxtmp= rx(nr)
rztmp= rz(nr)
txb= float(ifix(sxtmp))+0.5
tzb= float(ifix(sztmp))+0.5
c
if (sx(ns) .eq. rx(nr)) then
if (sz(ns) .gt. rz(nr)) then
  tmpsx= sx(ns)
  sx(ns)= rx(nr)
  rx(nr)= tmpsx
  tmpsz= sz(ns)
  sz(ns)= rz(nr)
  rz(nr)= tmpsz
  sxtmp= sx(ns)
  sztmp= sz(ns)
  iflag1= 3
  txb= float(ifix(sxtmp))+0.5
  tzb= float(ifix(sztmp))+0.5
endif
do i= 1,n
  Lnt(i)= 0.
enddo
sztmp= sz(ns)
ni= ifix(sztmp)+1
if(ni .ge. m) ni= ifix(sztmp)
rxtmp= rx(nr)
rztmp= rz(nr)
mi= ifix(rztmp)+1
if(mi .ge. m) mi= ifix(rztmp)
do i= ni,mi
  ii= (tzb+0.5)
  iij= (txb+0.5)
  jj= (ii-1)*jmax+iij
  Lnt(jj)= zb
  ln= ln+Lnt(jj)
  tem= tem+Lnt(jj)/v(jj)
  tzb= tzb+1.
  jj= jj+ncol
enddo
c

```

```

tzbn= tzb-0.5
if(abs(rztmp-float(ifix(tzbn))) .gt. 0.) then
  Lnt(jj)= abs(rztmp-float(ifix(tzbn)))
  ln= ln+Lnt(jj)
  tem= tem+Lnt(jj)/v(jj)
endif
tmpt= tem
tem= 0.
do i= 1,n
  a(i)= Lnt(i)
enddo
iflag= 1
goto 143
endif
if(sz(ns) .eq. dfloat(m)) sz(ns)= sz(ns)-0.00001
if(rz(nr) .eq. dfloat(m)) rz(nr)= rz(nr)-0.00001
C
C
do 142 ik= 1,ikmax
do i= 1,n
  Lnt(i)= 0.
enddo
ak=(dfloat(ik)/div)-add
C
C
C
-----
+ if source and receiver located in same pixel +
-----
C
C
+ if((ifix(sztmp) .eq. ifix(rztmp)) .and.
  (ifix(sxtmp) .eq. ifix(rxtmp))) then
  ii= (sztmp+1.)
  ijj= (sxtmp+1.)
  jjr= (ii-1)*jmax+ijj
  Lnt(jjr)= dsqrt(((sz(ns)-rz(nr))**2)*zb**2
+      +((sx(ns)-rx(nr))**2)*xb**2)
  ln= ln+Lnt(jjr)
  tem= tem+Lnt(jjr)/v(jjr)
  iflag= 2
  goto 141
endif
C
C
sxtmp= sx(ns)
sztmp= sz(ns)
txb= float(ifix(sxtmp))+0.5
if(sz(ns) .eq. m) sztmp= m-0.00001
tzb= float(ifix(sztmp))+0.5
tx= sx(ns)
tz= sz(ns)
sxtmp= sx(ns)
il= ifix((sxtmp+1.))
ill= ifix((rxtmp+1.))
if(ill .gt. ncol) ill= ncol
C
do 140 i= il,ill

```

```

130  continue
      x= float(i)
c
c
c
c  -----
c  + Half Sine-Arc "Sin(kx)=Sin(2*pi*x/lambda)" lambda=rx-sx +
c  -----
c
      y= sz(ns)+(x-sx(ns))*((rz(nr)-sz(ns))/(rx(nr)-sx(ns)))
+    +ak*sin(pi*(x-sx(ns))/(rx(nr)-sx(ns)))
c
      if (ak .ne. 0.) then
        if ((y .lt. 0.) .or. (y .gt. m)) goto 142
      endif
c
      ytmp= y
      if(abs(y-float(ifix(ytmp))) .lt. 0.000001) y= y+0.00001
c
      tzbtmp= tzb
      if((y-float(ifix(tzbtmp+0.5))) .gt. 0.000001) then
        yy= y
        y= tzb+0.5
        ytmp1= y
        x= (((y-tz)*(tx-x))/(tz-yy))+tx
        if(x .gt. rx(nr)) then
          x= rx(nr)
          y= rz(nr)
          iflag= 4
        endif
        ii= (tzb+0.5)
        ijj= (txb+0.5)
        jj= (ii-1)*jmax+ijj
        Lnt(jj)= dsqrt((y-tz)*(y-tz)*zb*zb+(x-tx)*(x-tx)*xb*xb)
        ln= ln+Lnt(jj)
        tem= tem+Lnt(jj)/v(jj)
        if((iflag .eq. 4) .or. (x .eq. rx(nr))) goto 141
        tx= x
        tz= y
        tzb= tzb+1.
        jj= jj+ncol
        iflag= 0
        goto 130
      endif
c
      tzbtmp= tzb
      if((y-float(ifix(tzbtmp-0.5))) .LT. 0.000001) then
        yy= y
        y= tzb-0.5
        ytmp1= y
        x= (((y-tz)*(tx-x))/(tz-yy))+tx
        if(x .gt. rx(nr)) then
          x= rx(nr)
          y= rz(nr)
          iflag= 4
        endif
        ii= (tzb+0.5)

```

```

    ij= (txb+0.5)
    jj= (ii-1)*jmax+ijj
    Lnt(jj)= dsqrt((y-tz)*(y-tz)*zb*zb+(x-tx)*(x-tx)*xb*xb)
    ln= ln+Lnt(jj)
    tem= tem+Lnt(jj)/v(jj)
    if((iflag .eq. 4) .or. (x .eq. rx(nr))) goto 141
tx= x
tz= y
tzb= tzb-1.
jj= jj-ncol
iflag= 0
goto 130
endif
c
    ii= (tzb+0.5)
    ij= (txb+0.5)
    jj= (ii-1)*jmax+ijj
    if(x .gt. txb) txb=txb+1.
    Lnt(jj)= dsqrt((y-tz)*(y-tz)*zb*zb+(x-tx)*(x-tx)*xb*xb)
    ln= ln+Lnt(jj)
    tem= tem+Lnt(jj)/v(jj)
    tx= x
    tz= y
    jj= jj+1
140 continue
141 continue
c
-----
c + choosing shortest time path +
c -----
c
if (tem .lt. tmpt) then
    tmpt= tem
    tem= 0.
c
-----
c + using array "a" to store lenghts +
c -----
c
    do i= 1,n
        a(i)= Lnt(i)
    enddo
endif
tem= 0.
if(iflag .eq. 2) goto 143
c
142 continue
143 continue
c
    do i= 1,n
        plnt(i)= plnt(i)+a(i)
    enddo
c
call spara(n, ndim, nja, kk, kj, a, at, iat, jat)
c
if (iflag1 .eq. 3) then

```

```

    rx(nr)= sx(ns)
    sx(ns)= tmplx
    rz(nr)= sz(ns)
    sz(ns)= tmplx
    iflag1= 0
endif
if(kj .ge. k) goto 2
kj= kj+1
iflag= 1
goto 1
2 continue
do i= 1,n
  if (plnt(i) .eq. 0.) then
    v(i)= 0.
  endif
enddo
c
close(2)
return
3 write(*,'(a)')***** error in input file *****
stop
end
c
c
c
c
*
+ .....
c +   Generating a sparse matrix with   +
c +           ia-ja structure           +
* .....

subroutine spara(n, ndim, nja, kk, kj, a, at, iat, jat)

double precision a(nja),at(nja)

integer iat(ndim+1), jat(nja)

integer n, ndim, nja, j, kk, kj

c
iat(1)= 1
do j= 1,n
  if(a(j) .ne. 0.) then
    at(kk)= a(j)
    jat(kk)= j
    kk= kk+1
  endif
enddo
iat(kj+1)= kk

c
return
end
c
c
c
c

```

```

*      +-----+
c      +   constructing transpose   +
c      +         of a matrix         +
*      +-----+

      subroutine transa(k, n, kk, iat, jat, at,
+                nja, ndim, ia, ja, a)

      double precision a(nja),at(nja)

      integer ia(ndim+1), ja(nja),
+            iat(ndim+1), jat(nja)

      integer k, n, ndim, nja, jj, kk,
+            ii, num, i, j, ik, in

      in= 0
      num= 0
      ia(1)= 1
      iat(1)= 1
      do ii= 1,n
      do jj= 1,kk-1
      if(jat(jj) .eq. ii)then
      num= num+1
      a(num)= at(jj)
      endif
      enddo
      ia(ii+1)= num+1
      enddo
c
      if(jat(1) .eq. 1) then
      ja(1)= 1
      in= in+1
      endif
c
      do i= 1,n
      do j= 1,kk-1
      if(jat(j) .eq. i)then
      do ik= 1,k+1
      if (j .lt. iat(ik)) then
      ja(in)= ik-1
      in= in+1
      goto 155
      endif
      enddo
      endif
      continue
155  enddo
      enddo
      return
      end

c
c
c
c
c

```

```

*      .....
C      +   Multiplying a matrix   +
C      +   by its transpos       +
*      .....

      subroutine ata(iparcham, k, n, nja, ndim,
+             ia, ja, a, aft, iat, jat, at)
C
      double precision a(nja), at(nja), aft(ndim)

      double precision tmp

      integer ia(ndim+1),ja(nja),
+             iat(ndim+1),jat(nja)

      integer k, n, ndim, nja, jj, kk,
+             ii, i, j, ik, ikk

      ik= 0
      ikk= 1
      ia(1)= 1
      iat(1)= 1
160  continue
      if(ikk .gt. n) goto 165
      do j= 1,ndim
      aft(j)= 0.
      enddo
C
      do ii= ia(ikk),ia(ikk+1)-1
      aft(ja(ii))= a(ii)
      enddo
C
      do i= 1,n
C
      tmp= 0.
      do ii= ia(i),ia(i+1)-1
      tmp= tmp+a(ii)*aft(ja(ii))
      enddo
C
C      -----
C      +   Determining the best lambda   +
C      -----
C
      if (iparcham.eq.0) then
      write(*,*)tmp
      elseif(iparcham.eq.1)then
      write(*,*)tmp
      else
      write(*,*)iparcham
      pause 'error in iparcham'
      endif
C
      if(tmp .ne. 0.)then
      ik= ik+1
      at(ik)= tmp
      jat(ik)= i

```

```

        endif
    enddo
C
    iat(ikk+1)= ik+1
    ikk= ikk+1
C
    goto 160
165 continue
    return
    end

C
C -----
C +      Multiplying a matrix      +
C +      by a vector                +
C -----

subroutine atb(k, n, nja, ndim,
+           ia, ja, a, btime, b)
C
double precision a(nja), btime(k), b(n), tmpb

integer ia(ndim+1),ja(nja)

integer k, n, ndim, nja,
+       ii, i, j, im

C -----
C + initializing vector +
C -----

do i= 1,n
    b(i)= 0
enddo

C
do i= 1,n
C
    tmpb= 0.
    do ii= ia(i),ia(i+1)-1
        tmpb= tmpb+a(ii)*btime(ja(ii))
    enddo

C
    b(i)= tmpb
enddo
return
end

C
+ -----
C + Generating (aTa + lambda*rTr) +
+ -----
C

Subroutine combin(n, nja, ndim, at, iat, jat,
+       r, ir, jr, aft, row, lambda, a, ia, ja)

```

```

      double precision r(nja), a(nja), at(nja),
+      aft(ndim), row(ndim), lambda
c
      integer ir(ndim+1), jr(ndim), ia(ndim+1), ja(nja),
+      iat(ndim+1), jat(nja)
c
      integer n, nja, ndim, i, ii, kk,
+      jkk, kjk, j
c
      kk= 1
      jkk= 1
      ia(1)= 1
      iat(1)= 1
      do kjk=1, n
c
      do j= 1,ndim
      row(j)= 0.
      aft(j)= 0.
      enddo
c
      do ii= iat(jkk),iat(jkk+1)-1
      aft(jat(ii))= at(ii)
      enddo
c
      do ii= ir(jkk),ir(jkk+1)-1
      row(jr(ii))= r(ii)
      enddo
c
      do i= 1,n
      aft(i)= lambda*row(i)+aft(i)
      enddo

c
c
c
c
-----
+ generating ia-ja structure +
-----

c
      do j= 1,n
      if(aft(j) .ne. 0.) then
      a(kk)= aft(j)
      ja(kk)= j
      kk= kk+1
      endif
      enddo
      ia(jkk+1)= kk
      jkk= jkk+1
      enddo
c
      return
      end

```

```

* .....
* *
* *   Generating identity matrix in ia-ja format   *
* *
* .....

```

Subroutine DLSQR (n, nja, ndim, r, ir, jr)

```

double precision r(nja)
C
integer ir(ndim+1), jr(nja)
C
integer n, nja, i, ii
C

```

```

C -----
C + initialization +
C -----
C

```

```

do i= 1,n
  r(i)= 0.
  jr(i)= 0
enddo
do i= 1,ndim+1
  ir(i)= 0
enddo

```

```

C -----
C + Constructing matrix "I" and ii, ji for DLSQR +
C -----
C

```

```

ii= 1
6 if(ii .le. n) then
  r(ii)= 1.
  jr(ii)= ii
  ii= ii+1
  goto 6
endif
ir(1)= 1
do i= 2,ndim+1
  ir(i)= i
enddo
return
end

```

```

* .....
* *
* *   GENERATING REGULARIZATION MATRIX   *
* *
* .....

```

+ Subroutine regula(k, m, ncol, n, ndim, nja, a,
r, ir, jr, kk)

```

double precision r(nja), a(nja)
C

```

```

integer ir(ndim+1), jr(nja)
c
integer k, n, ndim, nja, jj, kjj, ij, m,
+   ii, num, jmax, kj, kk, i, j, ncol
c
   kk= 1
   kj= 0
   ir(1)= 1
   num= 0
   ikr= 1
   in= 0
   jmax= ncol
c
c
do 4 i= 1,m
do 3 j= 1,ncol
   kj= kj+1
   do ij= 1,n
     a(ij)= 0.
   enddo
   if ((i .eq. 1) .and. (j .eq. 1)) then
     a(1)= -4.
     a(2)= 2.
     a(1+ncol)= 2.
   elseif ((i .eq. m) .and. (j .eq. 1)) then
     jj= (i-1)*jmax+j
     a(jj-ncol)= 2.
     a(jj)= -4.
     a(jj+1)= 2.
   elseif ((i .eq. 1) .and. (j .eq. ncol)) then
     jj= (i-1)*jmax+j
     a(jj-1)= 2.
     a(jj)= -4.
     a(jj+ncol)= 2.
   elseif ((i .eq. m) .and. (j .eq. ncol)) then
     jj= (i-1)*jmax+j
     a(jj-ncol)= 2.
     a(jj)= -4.
     a(jj-1)= 2.
   elseif ((i .gt. 1) .and. (j .eq. 1) .and. (i .lt. m)) then
     jj= (i-1)*jmax+j
     a(jj-ncol)= 1.
     a(jj)= -4.
     a(jj+1)= 2.
     a(jj+ncol)= 1.
   elseif ((i .gt. 1) .and. (j .eq. ncol) .and. (i .lt. m)) then
     jj= (i-1)*jmax+j
     a(jj-ncol)= 1.
     a(jj)= -4.
     a(jj-1)= 2.
     a(jj+ncol)= 1.
   elseif ((j .gt. 1) .and. (i .eq. 1) .and. (j .lt. ncol)) then
     jj= (i-1)*jmax+j
     a(jj-1)= 1.
     a(jj)= -4.

```

```

      a(jj+1)= 1.
      a(jj+ncol)= 2.
    elseif ((j .gt. 1) .and. (i .eq. m) .and. (j .lt. ncol)) then
      jj= (i-1)*jmax+j
      a(jj-1)= 1.
      a(jj)= -4.
      a(jj+1)= 1.
      a(jj-ncol)= 2.
    else
      jj= (i-1)*jmax+j
      a(jj-ncol)= 1.
      a(jj-1)= 1.
      a(jj)= -4.
      a(jj+1)= 1.
      a(jj+ncol)= 1.
    endif
  c
  c
      call spara(n, ndim, nja, kk, kj, a, r, ir, jr)

3  continue
4  continue

      return
      end

```

```

*      *****
+      +      Conjugate gradient      +
*      *****

```

```

SUBROUTINE linbcg(nja, contol, n, b, v, maxiter,
+              ija, sa, x)

  INTEGER iter,maxiter,itol,n,nja,ija(nja+1)
  DOUBLE PRECISION contol, b(n), x(n), eps, v(n), sa(nja+1)
  INTEGER j
  DOUBLE PRECISION ak,akden,bk,bkden,bknum,bnrm,dxnrm,xnrm,zm1nrm,
+              znrm,p(n),pp(n),r(n),rr(n),z(n),zz(n),snrm,err
  parameter (eps=1.d-14)
  iter= 0
  itol= 1
  c
  do i= 1,n
    r(i)= 0.
  enddo
  c
  call atimes(nja,ija,sa,n,v,r,0)
  do 11 j=1,n
    r(j)=b(j)-r(j)
    rr(j)=r(j)
11  continue
  call atimes(nja,ija,sa,n,r,rr,0)
  znrm=1.d0
  if(itol.eq.1) then

```

```

    bnm=snm(n,b,itol)
else if (itol.eq.2) then
    call asolve(nja,ija,sa,n,b,z,0)
    bnm=snm(n,z,itol)
else if (itol.eq.3.or.itol.eq.4) then
    call asolve(nja,ija,sa,n,b,z,0)
    bnm=snm(n,z,itol)
    call asolve(nja,ija,sa,n,r,z,0)
    znm=snm(n,z,itol)
else
    pause 'illegal itol in linbcg'
endif
call asolve(nja,ija,sa,n,r,z,0)
100 if (iter.le.maxiter) then
    iter=iter+1
    zm1nrm=znm
    call asolve(nja,ija,sa,n,rr,zz,1)
    bknum=0.d0
    do 12 j=1,n
        bknum=bknum+z(j)*rr(j)
12    continue
    if(itol.eq.1) then
        do 13 j=1,n
            p(j)=z(j)
            pp(j)=zz(j)
13    continue
    else
        bk=bknum/bkden
        do 14 j=1,n
            p(j)=bk*p(j)+z(j)
            pp(j)=bk*pp(j)+zz(j)
14    continue
    endif
    bkden=bknum
    call atimes(nja,ija,sa,n,p,z,0)
    akden=0.d0
    do 15 j=1,n
        akden=akden+z(j)*pp(j)
15    continue
    ak=bknum/akden
    call atimes(nja,ija,sa,n,pp,zz,1)
    do 16 j=1,n
        x(j)=x(j)+ak*p(j)
        r(j)=r(j)-ak*z(j)
        rr(j)=rr(j)-ak*zz(j)
16    continue
    call asolve(nja,ija,sa,n,r,z,0)
    if(itol.eq.1.or.itol.eq.2)then
        znm=1.d0
        err=snm(n,r,itol)/bnm
    else if(itol.eq.3.or.itol.eq.4)then
        znm=snm(n,z,itol)
        if(abs(zm1nrm-znm).gt.eps*znm) then
            dxnm=dabs(ak)*snm(n,p,itol)
            err=znm/dabs(zm1nrm-znm)*dxnm
        else

```

```

err=znrm/bnrm
goto 100
endif
xnrm=snrm(n,x,itol)
if(err.le.0.5d0*xnrm) then
err=err/xnrm
else
err=znrm/bnrm
goto 100
endif
endif
write (18,*) ' iter=',iter,' err=',err
if(err.gt.contol) goto 100
endif
101 continue
write(18,*)' max error = ', err
C
return
END
C (C) Copr. 1986-92 Numerical Recipes Software

```

```

C *****
C + storing matrix A into a two +
C + dimensional matrix +
C *****

```

```

subroutine replc(n, nja, ndim, a, ia, ja, a2)
integer n, ia(ndim+1), ja(nja)
double precision a(nja), a2(n,n)
C
do i= 1,n
do j= 1,n
a2(i,j)= 0.
enddo
enddo
C
do i= 1,n
do j= ia(i),ia(i+1)-1
a2(i,ja(j))= a(j)
enddo
enddo
return
end

```

```

C *****
C + Norm of a vector +
C *****

```

```

FUNCTION snrm(n,sx,itol)
INTEGER n,itol,i,isamax
DOUBLE PRECISION sx(n),snrm
if (itol.le.3)then
snrm=0.
do 11 i=1,n
snrm=snrm+sx(i)**2

```

```

11  continue
    snrm=dsqrt(snrm)
    else
    isamax=1
    do 12 i=1,n
        if(dabs(sx(i)).gt.dabs(sx(isamax))) isamax=i
12  continue
    snrm=dabs(sx(isamax))
    endif
    return
    END

```

C (C) Copr. 1986-92 Numerical Recipes Software

```

C
C *****
C + Multiplying a matrix by a vector +
C *****

```

```

SUBROUTINE atimes(nja,ija,sa,n,x,r,itnsp)
INTEGER n,itnsp,ija(nja+1),nja
DOUBLE PRECISION x(n),r(n),sa(nja+1)
if (itnsp.eq.0) then
    call dsprsax(nja,sa,ija,n,x,r)
else
    call dsprstx(nja,sa,ija,n,x,r)
endif
return
END

```

C (C) Copr. 1986-92 Numerical Recipes Software

```

C
C *****
C + Multiplying matrix sa by vector x +
C *****

```

```

SUBROUTINE dsprsax(nja,sa,ija,n,x,b)
INTEGER n,ija(nja+1)
DOUBLE PRECISION b(n),sa(nja+1),x(n)
INTEGER i,k
if (ija(1).ne.n+2) pause 'mismatched vector and matrix in dsprsax'
do 12 i=1,n
    b(i)=sa(i)*x(i)
    do 11 k=ija(i),ija(i+1)-1
        b(i)=b(i)+sa(k)*x(ija(k))
11  continue
12  continue
return
END

```

C (C) Copr. 1986-92 Numerical Recipes Software

```

C
C *****
C + Multiplying transpose of a +
C + matrix by a vector +
C *****

```

```

SUBROUTINE dsprstx(nja,sa,ija,n,x,b)
INTEGER n,ija(nja+1)
DOUBLE PRECISION b(n),sa(nja+1),x(n)

```

```

    INTEGER i,j,k
    if(ija(1).ne.n+2) pause 'mismatched vector and matrix in dsprstx'
    do 11 i=1,n
        b(i)=sa(i)*x(i)
11    continue
        do 13 i=1,n
            do 12 k=ija(i),ija(i+1)-1
                j=ija(k)
                b(j)=b(j)+sa(k)*x(i)
12    continue
13    continue
    return
    END

```

```

C (C) Copr. 1986-92 Numerical Recipes Software
C .....
C + changing format of a two dimensional matrix to +
C + row-index sparse format +
C .....

```

```

SUBROUTINE sprsin(a2,n,nja,sa,ija)
    INTEGER n,nja,ija(nja+1)
    double precision a2(n,n),sa(nja+1)
    INTEGER i,j,k
    do 11 j=1,n
        sa(j)=a2(j,j)
11    continue
    ija(1)=n+2
    k=n+1
    do 13 i=1,n
        do 12 j=1,n
            if(dabs(a2(i,j)).gt.0.)then
                if(i.ne.j)then
                    k=k+1
                    if(k.gt.(nja+1))pause 'nja too small in sprsin'
                    sa(k)=a2(i,j)
                    ija(k)=j
                endif
            endif
12    continue
        ija(i+1)=k+1
13    continue
    return
    END

```

```

C (C) Copr. 1986-92 Numerical Recipes Software
C .....
C + Make a division using a matrix +
C + or its transpose +
C .....

```

```

SUBROUTINE asolve(nja,ija,sa,n,b,x,itmsp)
    INTEGER n,itmsp,ija(nja+1),nja,i
    DOUBLE PRECISION x(n),b(n),sa(nja+1)
    do 11 i=1,n
        x(i)=b(i)/sa(i)
11    continue
    return
    END

```

```

C (C) Copr. 1986-92 Numerical Recipes Software

```

**APPENDIX E: Corresponding Input Files for
All Case Histories**

**Hellium Balloon 1, Located in off-center to the left
Locations in inches, Travel times in milliseconds.**

Source locations (X,Z)	Reciver locations (X,Z)
0 3	60.3 3
0 12	60.3 12
0 21	60.3 21
0 30	60.3 30
0 39	60.3 39
0 48	60.3 48
0 57	60.3 57

Source number= Sn, Receiver number= Rn, Travel times= T-T

Sn	Rn	T-T	Sn	Rn	T-T
1	1	4.38	5	1	4.84
1	2	4.42	5	2	4.56
1	3	4.54	5	3	4.38
1	4	4.80	5	4	4.26
1	5	5.06	5	5	4.32
1	6	5.42	5	6	4.44
1	7	5.78	5	7	4.58
2	1	4.50	6	1	5.30
2	2	4.42	6	2	5.00
2	3	4.50	6	3	4.74
2	4	4.62	6	4	4.60
2	5	4.84	6	5	4.46
2	6	5.10	6	6	4.42
2	7	5.36	6	7	4.44
3	1	4.68	7	1	5.86
3	2	4.52	7	2	5.46
3	3	4.46	7	3	5.10
3	4	4.32	7	4	4.82
3	5	4.34	7	5	4.58
3	6	4.52	7	6	4.44
3	7	4.92	7	7	4.36
4	1	4.90			
4	2	4.46			
4	3	4.20			
4	4	4.14			
4	5	4.22			
4	6	4.42			
4	7	4.78			

**Helium Balloon 2, Located in off-center to the top
Locations in inches, Travel times in milliseconds.**

Source locations (X,Z)	Receiver locations (X,Z)
0 3	60.3 3
0 12	60.3 12
0 21	60.3 21
0 30	60.3 30
0 39	60.3 39
0 48	60.3 48
0 57	60.3 57

Source number= Sn, Receiver number= Rn, Travel times= T-T

Sn	Rn	T-T	Sn	Rn	T-T
1	1	4.52	5	1	4.92
1	2	4.56	5	2	4.68
1	3	4.58	5	3	4.56
1	4	4.74	5	4	4.52
1	5	5.06	5	5	4.48
1	6	5.50	5	6	4.50
1	7	5.90	5	7	4.60
2	1	4.54	6	1	5.32
2	2	4.30	6	2	5.08
2	3	4.18	6	3	4.92
2	4	4.32	6	4	4.70
2	5	4.60	6	5	4.56
2	6	5.00	6	6	4.48
2	7	5.56	6	7	4.52
3	1	4.50	7	1	5.80
3	2	4.24	7	2	5.54
3	3	4.12	7	3	5.16
3	4	4.28	7	4	4.88
3	5	4.54	7	5	4.68
3	6	4.82	7	6	4.52
3	7	5.24	7	7	4.42
4	1	4.62			
4	2	4.38			
4	3	4.24			
4	4	4.36			
4	5	4.46			
4	6	4.62			
4	7	4.90			

**Helium Balloon 3, Located in the center
Locations in inches, Travel times in milliseconds.**

Source locations (X,Z)	Receiver locations (X,Z)
0 3	60.3 3
0 12	60.3 12
0 21	60.3 21
0 30	60.3 30
0 39	60.3 39
0 48	60.3 48
0 57	60.3 57

Source number= Sn, Receiver number= Rn, Travel times= T-T

Sn	Rn	T-T	Sn	Rn	T-T
1	1	4.38	5	1	5.14
1	2	4.42	5	2	4.78
1	3	4.58	5	3	4.52
1	4	4.79	5	4	4.42
1	5	5.06	5	5	4.38
1	6	5.38	5	6	4.44
1	7	5.76	5	7	4.60
2	1	4.46	6	1	5.42
2	2	4.40	6	2	5.04
2	3	4.42	6	3	4.74
2	4	4.54	6	4	4.56
2	5	4.76	6	5	4.46
2	6	5.04	6	6	4.42
2	7	5.44	6	7	4.46
3	1	4.58	7	1	5.86
3	2	4.4	7	2	5.46
3	3	4.34	7	3	5.12
3	4	4.39	7	4	4.82
3	5	4.5	7	5	4.58
3	6	4.76	7	6	4.46
3	7	5.08	7	7	4.40
4	1	4.82			
4	2	4.56			
4	3	4.36			
4	4	4.3			
4	5	4.38			
4	6	4.56			
4	7	4.84			

Helium Balloon 4, Located in the center.
Locations in inches, Travel times in milliseconds.

Source locations (X,Z)		Receiver locations (X,Z)	
0.0	5.2501	59.5	5.2500
0.0	8.501	59.5	8.5000
0.0	11.7501	59.5	11.750
0.0	15.001	59.5	15.000
0.0	18.2501	59.5	18.250
0.0	21.501	59.5	21.500
0.0	24.7501	59.5	24.750
0.0	28.001	59.5	28.000
0.0	31.2501	59.5	31.250
0.0	34.501	59.5	34.500
0.0	37.7501	59.5	37.750
0.0	41.001	59.5	41.000
0.0	44.2501	59.5	44.250
0.0	47.501	59.5	47.500
0.0	50.7501	59.5	50.750
0.0	54.001	59.5	54.000

Source number= Sn, Receiver number= Rn, Travel times= T-T

Sn	Rn	T-T	Sn	Rn	T-T
1	1	4.41	9	1	4.71
1	2	4.43	9	2	4.59
1	3	4.44	9	3	4.49
1	4	4.48	9	4	4.41
1	5	4.52	9	5	4.33
1	6	4.58	9	6	4.27
1	7	4.63	9	7	4.24
1	8	4.66	9	8	4.23
1	9	4.71	9	9	4.2
1	10	4.76	9	10	4.22
1	11	4.85	9	11	4.24
1	12	4.92	9	12	4.3
1	13	5.05	9	13	4.35
1	14	5.15	9	14	4.45
1	15	5.32	9	15	4.53
1	16	5.44	9	16	4.69
2	1	4.4	10	1	4.77
2	2	4.4	10	2	4.65
2	3	4.41	10	3	4.55
2	4	4.42	10	4	4.45
2	5	4.47	10	5	4.37
2	6	4.49	10	6	4.31
2	7	4.51	10	7	4.28
2	8	4.52	10	8	4.25
2	9	4.6	10	9	4.21
2	10	4.61	10	10	4.23
2	11	4.73	10	11	4.25
2	12	4.77	10	12	4.29
2	13	4.92	10	13	4.34
2	14	5.00	10	14	4.42

2	15	5.18	10	15	4.55
2	16	5.27	10	16	4.66
3	1	4.41	11	1	4.84
3	2	4.42	11	2	4.73
3	3	4.4	11	3	4.62
3	4	4.42	11	4	4.52
3	5	4.44	11	5	4.42
3	6	4.43	11	6	4.36
3	7	4.44	11	7	4.31
3	8	4.44	11	8	4.29
3	9	4.48	11	9	4.25
3	10	4.53	11	10	4.26
3	11	4.61	11	11	4.26
3	12	4.67	11	12	4.31
3	13	4.88	11	13	4.33
3	14	5.03	11	14	4.44
3	15	5.15	11	15	4.5
3	16	5.2	11	16	4.58
4	1	4.43	12	1	4.97
4	2	4.41	12	2	4.85
4	3	4.4	12	3	4.71
4	4	4.4	12	4	4.63
4	5	4.4	12	5	4.53
4	6	4.34	12	6	4.46
4	7	4.35	12	7	4.40
4	8	4.34	12	8	4.35
4	9	4.41	12	9	4.31
4	10	4.42	12	10	4.33
4	11	4.53	12	11	4.33
4	12	4.56	12	12	4.38
4	13	4.69	12	13	4.39
4	14	4.76	12	14	4.43
4	15	4.92	12	15	4.48
4	16	5.01	12	16	4.51
5	1	4.52	13	1	5.04
5	2	4.47	13	2	4.92
5	3	4.45	13	3	4.77
5	4	4.38	13	4	4.72
5	5	4.37	13	5	4.57
5	6	4.29	13	6	4.55
5	7	4.34	13	7	4.44
5	8	4.29	13	8	4.43
5	9	4.35	13	9	4.34
5	10	4.36	13	10	4.39
5	11	4.45	13	11	4.43
5	12	4.48	13	12	4.41
5	13	4.6	13	13	4.4
5	14	4.67	13	14	4.42
5	15	4.84	13	15	4.43
5	16	4.91	13	16	4.47
6	1	4.57	14	1	5.19
6	2	4.53	14	2	5.09
6	3	4.48	14	3	4.93
6	4	4.36	14	4	4.86
6	5	4.34	14	5	4.71
6	6	4.26	14	6	4.67

6	7	4.29	14	7	4.55
6	8	4.26	14	8	4.56
6	9	4.29	14	9	4.44
6	10	4.31	14	10	4.48
6	11	4.38	14	11	4.41
6	12	4.42	14	12	4.47
6	13	4.51	14	13	4.42
6	14	4.6	14	14	4.41
6	15	4.74	14	15	4.42
6	16	4.83	14	16	4.44
7	1	4.63	15	1	5.32
7	2	4.52	15	2	5.21
7	3	4.45	15	3	5.04
7	4	4.35	15	4	4.96
7	5	4.3	15	5	4.81
7	6	4.24	15	6	4.76
7	7	4.23	15	7	4.65
7	8	4.21	15	8	4.63
7	9	4.24	15	9	4.55
7	10	4.25	15	10	4.58
7	11	4.31	15	11	4.51
7	12	4.35	15	12	4.49
7	13	4.44	15	13	4.43
7	14	4.52	15	14	4.42
7	15	4.65	15	15	4.41
7	16	4.75	15	16	4.42
8	1	4.7	16	1	5.45
8	2	4.53	16	2	5.34
8	3	4.47	16	3	5.18
8	4	4.37	16	4	5.11
8	5	4.31	16	5	4.94
8	6	4.25	16	6	4.89
8	7	4.24	16	7	4.78
8	8	4.2	16	8	4.72
8	9	4.21	16	9	4.63
8	10	4.22	16	10	4.67
8	11	4.29	16	11	4.59
8	12	4.31	16	12	4.54
8	13	4.4	16	13	4.48
8	14	4.46	16	14	4.45
8	15	4.59	16	15	4.43
8	16	4.69	16	16	4.42

Concrete Crack (Side-to-Side shootings)
Locations in meters, Travel times in milliseconds.

Source locations (X,Z)		Receiver locations (X,Z)	
0	0.1	1.2	0.1
0	0.2	1.2	0.2
0	0.3	1.2	0.4
0	0.4	1.2	0.5
0	0.5	1.2	0.6
0	0.6	1.2	0.7
0	0.7	1.2	0.8
0	0.8	1.2	0.9
0	1.0	1.2	1.0
0	1.1	1.2	1.1

Source number= Sn, Receiver number= Rn, Travel times= T-T

Sn	Rn	T-T	Sn	Rn	T-T	Sn	Rn	T-T
1	1	.260	5	1	.272	9	1	.368
1	2	.258	5	2	.266	9	2	.332
1	3	.300	5	3	.288	9	3	.284
1	4	.296	5	4	.282	9	4	.276
1	5	.302	5	5	.282	9	5	.268
1	6	.308	5	6	.286	9	6	.264
1	7	.316	5	7	.290	9	7	.260
1	8	.330	5	8	.296	9	8	.256
1	9	.344	5	9	.302	9	9	.254
1	10	.358	5	10	.310	9	10	.256
2	1	.258	6	1	.282	10	1	.360
2	2	.256	6	2	.272	10	2	.346
2	3	.292	6	3	.286	10	3	.294
2	4	.294	6	4	.280	10	4	.286
2	5	.294	6	5	.280	10	5	.276
2	6	.302	6	6	.282	10	6	.270
2	7	.308	6	7	.286	10	7	.264
2	8	.322	6	8	.290	10	8	.258
2	9	.330	6	9	.296	10	9	.256
2	10	.338	6	10	.302	10	10	.256
3	1	.264	7	1	.290			
3	2	.260	7	2	.278			
3	3	.292	7	3	.290			
3	4	.286	7	4	.286			
3	5	.288	7	5	.282			
3	6	.294	7	6	.284			
3	7	.302	7	7	.286			
3	8	.310	7	8	.288			
3	9	.322	7	9	.294			
3	10	.330	7	10	.300			
4	1	.268	8	1	.300			
4	2	.262	8	2	.288			
4	3	.288	8	3	.300			
4	4	.284	8	4	.294			
4	5	.284	8	5	.288			
4	6	.288	8	6	.290			
4	7	.296	8	7	.290			
4	8	.302	8	8	.294			
4	9	.312	8	9	.296			
4	10	.322	8	10	.304			

Concrete Crack (Top to left-Side shootings)

Locations in meters, Travel times in milliseconds.

Source locations (X,Z) Receiver locations (X,Z)

0.1	0	0	0.1
0.2	0	0	0.2
0.3	0	0	0.3
0.4	0	0	0.4
0.5	0	0	0.5
0.6	0	0	0.6
0.7	0	0	0.7
0.8	0	0	0.8
0.9	0	0	1.0
1.0	0	0	1.1
1.1	0		

Source number= Sn, Receiver number= Rn, Travel times= T-T

Sn	Rn	T-T	Sn	Rn	T-T	Sn	Rn	T-T
1	1	.028	5	1	.113	9	1	.199
1	2	.049	5	2	.115	9	2	.200
1	3	.070	5	3	.123	9	3	.204
1	4	.092	5	4	.138	9	4	.212
1	5	.117	5	5	.153	9	5	.222
1	6	.137	5	6	.170	9	6	.234
1	7	.156	5	7	.185	9	7	.244
1	8	.179	5	8	.206	9	8	.260
1	9	.266	5	9	.278	9	9	.316
1	10	.272	5	10	.288	9	10	.324
2	1	.052	6	1	.136	10	1	.218
2	2	.062	6	2	.137	10	2	.218
2	3	.078	6	3	.144	10	3	.222
2	4	.099	6	4	.155	10	4	.232
2	5	.120	6	5	.169	10	5	.242
2	6	.143	6	6	.186	10	6	.252
2	7	.159	6	7	.200	10	7	.260
2	8	.182	6	8	.216	10	8	.272
2	9	.266	6	9	.286	10	9	.328
2	10	.276	6	10	.294	10	10	.338
3	1	.070	7	1	.157	11	1	.242
3	2	.077	7	2	.158	11	2	.242
3	3	.090	7	3	.163	11	3	.244
3	4	.109	7	4	.174	11	4	.252
3	5	.128	7	5	.186	11	5	.258
3	6	.149	7	6	.200	11	6	.268
3	7	.166	7	7	.212	11	7	.278
3	8	.188	7	8	.232	11	8	.292
3	9	.268	7	9	.294	11	9	.342
3	10	.280	7	10	.306	11	10	.352
4	1	.091	8	1	.176			
4	2	.095	8	2	.178			
4	3	.106	8	3	.182			
4	4	.121	8	4	.192			
4	5	.138	8	5	.202			
4	6	.159	8	6	.216			
4	7	.173	8	7	.228			
4	8	.195	8	8	.242			
4	9	.270	8	9	.302			
4	10	.284	8	10	.314			

Concrete Crack (Top to right-Side shootings)

Locations in meters, Travel times in milliseconds.

Source locations (X,Z) Receiver locations (X,Z)

0.1	0	1.2	0.1
0.2	0	1.2	0.2
0.3	0	1.2	0.3
0.4	0	1.2	0.4
0.5	0	1.2	0.5
0.6	0	1.2	0.6
0.7	0	1.2	0.7
0.8	0	1.2	0.8
0.9	0	1.2	1.0
1.0	0	1.2	1.1
1.1	0		

Source number= Sn, Receiver number= Rn, Travel times= T-T

Sn	Rn	T-T	Sn	Rn	T-T	Sn	Rn	T-T
1	1	.244	5	1	.156	9	1	.070
1	2	.244	5	2	.159	9	2	.080
1	3	.294	5	3	.220	9	3	.172
1	4	.292	5	4	.222	9	4	.174
1	5	.296	5	5	.230	9	5	.186
1	6	.308	5	6	.242	9	6	.204
1	7	.314	5	7	.254	9	7	.220
1	8	.328	5	8	.272	9	8	.242
1	9	.340	5	9	.288	9	9	.258
1	10	.352	5	10	.300	9	10	.274
2	1	.220	6	1	.135	10	1	.049
2	2	.224	6	2	.139	10	2	.063
2	3	.272	6	3	.206	10	3	.163
2	4	.272	6	4	.208	10	4	.171
2	5	.278	6	5	.216	10	5	.184
2	6	.286	6	6	.228	10	6	.200
2	7	.300	6	7	.244	10	7	.216
2	8	.316	6	8	.262	10	8	.238
2	9	.324	6	9	.278	10	9	.256
2	10	.336	6	10	.290	10	10	.274
3	1	.200	7	1	.111	11	1	.028
3	2	.202	7	2	.116	11	2	.048
3	3	.256	7	3	.191	11	3	.162
3	4	.258	7	4	.193	11	4	.167
3	5	.260	7	5	.204	11	5	.179
3	6	.272	7	6	.216	11	6	.199
3	7	.286	7	7	.232	11	7	.216
3	8	.298	7	8	.240	11	8	.242
3	9	.314	7	9	.268	11	9	.252
3	10	.324	7	10	.284	11	10	.270
4	1	.183	8	1	.092			
4	2	.186	8	2	.099			
4	3	.242	8	3	.180			
4	4	.242	8	4	.185			
4	5	.248	8	5	.194			
4	6	.260	8	6	.208			
4	7	.270	8	7	.226			
4	8	.288	8	8	.246			
4	9	.302	8	9	.264			
4	10	.314	8	10	.280			

Concrete Column

Locations in meters, Travel times in milisecond

Source locations (X,Z)		Receiver locations (X,Z)	
0	0.05	1.2	0.05
0	0.1	1.2	0.1
0	0.15	1.2	0.15
0	0.2	1.2	0.2
0	0.25	1.2	0.25
0	0.3	1.2	0.3
0	0.35	1.2	0.35
0	0.4	1.2	0.4
0	0.45	1.2	0.45
0	0.5	1.2	0.5
0	0.55	1.2	0.55
0	0.6	1.2	0.6
0	0.65	1.2	0.65
0	0.7	1.2	0.7
0	0.75	1.2	0.75
0	0.8	1.2	0.8
0	0.85	1.2	0.85
0	0.9	1.2	0.9
0	0.95	1.2	0.95
0	1	1.2	1
0	1.05	1.2	1.05
0	1.1	1.2	1.1
0	1.15	1.2	1.15

Source number= Sn, Receiver number= Rn, Travel times= T-T

Sn	Rn	T-T	Sn	Rn	T-T	Sn	Rn	T-T
1	1	0.258	9	1	0.276	17	1	0.326
1	2	0.256	9	2	0.274	17	2	0.32
1	3	0.256	9	3	0.27	17	3	0.314
1	4	0.258	9	4	0.266	17	4	0.31
1	5	0.258	9	5	0.27	17	5	0.306
1	6	0.258	9	6	0.276	17	6	0.3
1	7	0.262	9	7	0.264	17	7	0.298
1	8	0.264	9	8	0.282	17	8	0.294
1	9	0.266	9	9	0.29	17	9	0.292
1	10	0.274	9	10	0.3	17	10	0.286
1	11	0.278	9	11	0.306	17	11	0.286
1	12	0.278	9	12	0.284	17	12	0.28
1	13	0.288	9	13	0.284	17	13	0.28
1	14	0.294	9	14	0.284	17	14	0.278
1	15	0.304	9	15	0.292	17	15	0.278
1	16	0.308	9	16	0.292	17	16	0.278
1	17	0.318	9	17	0.3	17	17	0.278
1	18	0.328	9	18	0.306	17	18	0.276
1	19	0.334	9	19	0.308	17	19	0.278
1	20	0.344	9	20	0.31	17	20	0.278
1	21	0.35	9	21	0.314	17	21	0.278
1	22	0.358	9	22	0.322	17	22	0.278
1	23	0.364	9	23	0.348	17	23	0.278
2	1	0.26	10	1	0.28	18	1	0.332
2	2	0.26	10	2	0.274	18	2	0.328

2	3	0.26	10	3	0.272	18	3	0.322
2	4	0.256	10	4	0.27	18	4	0.316
2	5	0.258	10	5	0.268	18	5	0.31
2	6	0.258	10	6	0.268	18	6	0.306
2	7	0.262	10	7	0.27	18	7	0.302
2	8	0.264	10	8	0.268	18	8	0.296
2	9	0.266	10	9	0.272	18	9	0.294
2	10	0.27	10	10	0.278	18	10	0.292
2	11	0.276	10	11	0.284	18	11	0.286
2	12	0.28	10	12	0.278	18	12	0.284
2	13	0.286	10	13	0.282	18	13	0.28
2	14	0.29	10	14	0.284	18	14	0.28
2	15	0.3	10	15	0.286	18	15	0.278
2	16	0.314	10	16	0.288	18	16	0.276
2	17	0.316	10	17	0.292	18	17	0.276
2	18	0.326	10	18	0.294	18	18	0.274
2	19	0.334	10	19	0.3	18	19	0.276
2	20	0.342	10	20	0.304	18	20	0.276
2	21	0.35	10	21	0.308	18	21	0.276
2	22	0.358	10	22	0.31	18	22	0.276
2	23	0.358	10	23	0.312	18	23	0.278
3	1	0.262	11	1	0.286	19	1	0.338
3	2	0.26	11	2	0.284	19	2	0.334
3	3	0.256	11	3	0.278	19	3	0.328
3	4	0.258	11	4	0.278	19	4	0.316
3	5	0.258	11	5	0.276	19	5	0.314
3	6	0.26	11	6	0.276	19	6	0.308
3	7	0.264	11	7	0.272	19	7	0.306
3	8	0.264	11	8	0.276	19	8	0.304
3	9	0.27	11	9	0.278	19	9	0.298
3	10	0.27	11	10	0.28	19	10	0.292
3	11	0.274	11	11	0.282	19	11	0.29
3	12	0.276	11	12	0.284	19	12	0.286
3	13	0.284	11	13	0.282	19	13	0.284
3	14	0.286	11	14	0.282	19	14	0.282
3	15	0.298	11	15	0.284	19	15	0.284
3	16	0.306	11	16	0.286	19	16	0.282
3	17	0.314	11	17	0.29	19	17	0.3
3	18	0.322	11	18	0.292	19	18	0.274
3	19	0.328	11	19	0.298	19	19	0.272
3	20	0.336	11	20	0.298	19	20	0.272
3	21	0.34	11	21	0.304	19	21	0.272
3	22	0.35	11	22	0.334	19	22	0.272
3	23	0.35	11	23	0.314	19	23	0.274
4	1	0.26	12	1	0.286	20	1	0.346
4	2	0.26	12	2	0.284	20	2	0.342
4	3	0.258	12	3	0.28	20	3	0.334
4	4	0.256	12	4	0.278	20	4	0.316
4	5	0.256	12	5	0.276	20	5	0.314
4	6	0.256	12	6	0.278	20	6	0.314
4	7	0.262	12	7	0.286	20	7	0.308
4	8	0.262	12	8	0.282	20	8	0.306
4	9	0.264	12	9	0.282	20	9	0.3
4	10	0.268	12	10	0.284	20	10	0.294
4	11	0.27	12	11	0.284	20	11	0.292
4	12	0.278	12	12	0.282	20	12	0.286

4	13	0.296	12	13	0.282	20	13	0.284
4	14	0.29	12	14	0.28	20	14	0.284
4	15	0.3	12	15	0.284	20	15	0.28
4	16	0.306	12	16	0.284	20	16	0.278
4	17	0.314	12	17	0.286	20	17	0.276
4	18	0.322	12	18	0.29	20	18	0.276
4	19	0.356	12	19	0.292	20	19	0.272
4	20	0.328	12	20	0.294	20	20	0.272
4	21	0.344	12	21	0.298	20	21	0.27
4	22	0.344	12	22	0.306	20	22	0.27
4	23	0.35	12	23	0.3	20	23	0.268
5	1	0.264	13	1	0.298	21	1	0.348
5	2	0.258	13	2	0.292	21	2	0.344
5	3	0.256	13	3	0.29	21	3	0.334
5	4	0.256	13	4	0.284	21	4	0.328
5	5	0.256	13	5	0.286	21	5	0.322
5	6	0.256	13	6	0.284	21	6	0.32
5	7	0.258	13	7	0.284	21	7	0.314
5	8	0.26	13	8	0.284	21	8	0.31
5	9	0.262	13	9	0.284	21	9	0.304
5	10	0.266	13	10	0.284	21	10	0.298
5	11	0.27	13	11	0.284	21	11	0.294
5	12	0.276	13	12	0.282	21	12	0.29
5	13	0.282	13	13	0.28	21	13	0.284
5	14	0.292	13	14	0.284	21	14	0.284
5	15	0.298	13	15	0.284	21	15	0.282
5	16	0.306	13	16	0.284	21	16	0.278
5	17	0.314	13	17	0.286	21	17	0.276
5	18	0.316	13	18	0.288	21	18	0.272
5	19	0.322	13	19	0.292	21	19	0.272
5	20	0.328	13	20	0.292	21	20	0.27
5	21	0.328	13	21	0.292	21	21	0.27
5	22	0.336	13	22	0.294	21	22	0.27
5	23	0.37	13	23	0.298	21	23	0.27
6	1	0.266	14	1	0.302	22	1	0.358
6	2	0.264	14	2	0.298	22	2	0.35
6	3	0.262	14	3	0.296	22	3	0.344
6	4	0.26	14	4	0.292	22	4	0.336
6	5	0.258	14	5	0.292	22	5	0.334
6	6	0.256	14	6	0.292	22	6	0.328
6	7	0.26	14	7	0.29	22	7	0.32
6	8	0.262	14	8	0.286	22	8	0.314
6	9	0.264	14	9	0.286	22	9	0.308
6	10	0.266	14	10	0.284	22	10	0.302
6	11	0.27	14	11	0.284	22	11	0.298
6	12	0.276	14	12	0.284	22	12	0.292
6	13	0.282	14	13	0.282	22	13	0.288
6	14	0.286	14	14	0.284	22	14	0.284
6	15	0.294	14	15	0.282	22	15	0.282
6	16	0.298	14	16	0.284	22	16	0.28
6	17	0.306	14	17	0.282	22	17	0.278
6	18	0.306	14	18	0.282	22	18	0.276
6	19	0.312	14	19	0.284	22	19	0.27
6	20	0.316	14	20	0.286	22	20	0.27
6	21	0.322	14	21	0.286	22	21	0.27
6	22	0.328	14	22	0.29	22	22	0.268

6	23	0.334	14	23	0.298	22	23	0.27
7	1	0.268	15	1	0.31	23	1	0.364
7	2	0.264	15	2	0.306	23	2	0.358
7	3	0.264	15	3	0.3	23	3	0.35
7	4	0.262	15	4	0.298	23	4	0.344
7	5	0.26	15	5	0.296	23	5	0.336
7	6	0.258	15	6	0.294	23	6	0.328
7	7	0.258	15	7	0.292	23	7	0.322
7	8	0.258	15	8	0.288	23	8	0.316
7	9	0.262	15	9	0.286	23	9	0.314
7	10	0.27	15	10	0.284	23	10	0.306
7	11	0.282	15	11	0.282	23	11	0.3
7	12	0.314	15	12	0.278	23	12	0.294
7	13	0.336	15	13	0.278	23	13	0.292
7	14	0.286	15	14	0.278	23	14	0.286
7	15	0.292	15	15	0.278	23	15	0.284
7	16	0.294	15	16	0.278	23	16	0.282
7	17	0.3	15	17	0.278	23	17	0.278
7	18	0.306	15	18	0.28	23	18	0.272
7	19	0.31	15	19	0.282	23	19	0.272
7	20	0.316	15	20	0.284	23	20	0.27
7	21	0.322	15	21	0.284	23	21	0.268
7	22	0.322	15	22	0.284	23	22	0.268
7	23	0.328	15	23	0.29	23	23	0.27
8	1	0.274	16	1	0.316			
8	2	0.268	16	2	0.312			
8	3	0.264	16	3	0.306			
8	4	0.264	16	4	0.304			
8	5	0.26	16	5	0.3			
8	6	0.262	16	6	0.296			
8	7	0.262	16	7	0.292			
8	8	0.264	16	8	0.288			
8	9	0.266	16	9	0.288			
8	10	0.27	16	10	0.284			
8	11	0.276	16	11	0.284			
8	12	0.28	16	12	0.28			
8	13	0.286	16	13	0.278			
8	14	0.29	16	14	0.28			
8	15	0.292	16	15	0.278			
8	16	0.298	16	16	0.278			
8	17	0.3	16	17	0.278			
8	18	0.306	16	18	0.278			
8	19	0.308	16	19	0.278			
8	20	0.314	16	20	0.282			
8	21	0.33	16	21	0.282			
8	22	0.35	16	22	0.276			
8	23	0.354	16	23	0.284			

Kosciuszko bridge pier
 Locations in inches, Travel times in milisecond.

Source locations (X,Z)		Receiver locations (X,Z)	
187.1	202.6	30.4	14.8
167.0	217.5	50.5	0
156.5	217.5	61.0	0
146.0	217.5	71.5	0
135.5	217.5	82.0	0
125.0	217.5	92.5	0
114.5	217.5	103.0	0
104.0	217.5	113.5	0
93.5	217.5	124.0	0
83.0	217.5	134.5	0
72.5	217.5	145.0	0
62.0	217.5	155.5	0
51.5	217.5	166.0	0
30.4	202.6	187.1	14.8
14.8	187.1	202.6	30.4
0	167.0	217.5	50.5
0	156.5	217.5	61.0
0	146.0	217.5	71.5
0	135.5	217.5	82.0
0	125.0	217.5	92.5
0	114.5	217.5	103.0
0	104.0	217.5	113.5
0	93.5	217.5	124.0
0	83.0	217.5	134.5
0	72.5	217.5	145.0
0	62.0	217.5	155.5
0	51.5	217.5	166.0
14.8	30.4	202.6	187.1

Source number= Sn, Receiver number= Rn, Travel times= T-T

Sn	Rn	T-T	Sn	Rn	T-T	Sn	Rn	T-T
1	1	1.49	1	11	1.22	1	21	0.60
2	1	1.34	2	11	1.27	2	21	0.68
3	1	1.46	3	11	1.29	3	21	0.71
4	1	1.33	4	11	1.28	4	21	0.85
5	1	1.30	5	11	1.25	5	21	0.77
6	1	1.27	6	11	1.32	6	21	0.85
7	1	1.26	7	11	1.31	7	21	1.04
8	1	1.19	8	11	1.27	8	21	1.21
9	1	1.25	9	11	1.29	9	21	1.09
10	1	1.22	10	11	1.28	10	21	1.21
11	1	1.25	11	11	1.35	11	21	1.21
12	1	1.15	12	11	1.34	12	21	1.32
13	1	1.17	13	11	1.34	13	21	1.34
14	1	1.09	14	11	1.34	14	21	1.45
15	1	0.99	15	11	1.34	15	21	1.44
16	1	0.91	16	11	1.28	16	21	1.51
17	1	0.84	17	11	1.30	17	21	1.48
18	1	0.76	18	11	1.17	18	21	1.47
19	1	0.78	19	11	1.32	19	21	1.42
20	1	0.68	20	11	1.11	20	21	1.35

21	1	0.57	21	11	1.03	21	21	1.32
22	1	0.51	22	11	1.01	22	21	1.43
23	1	0.45	23	11	0.97	23	21	1.29
24	1	0.48	24	11	0.96	24	21	1.28
25	1	0.35	25	11	0.93	25	21	1.29
26	1	0.32	26	11	0.90	26	21	1.31
27	1	0.27	27	11	0.88	27	21	1.26
28	1	0.10	28	11	0.76	28	21	1.43
1	2	1.45	1	12	1.21	1	22	0.60
2	2	1.47	2	12	1.28	2	22	0.67
3	2	1.44	3	12	1.34	3	22	0.64
4	2	1.36	4	12	1.32	4	22	0.74
5	2	1.35	5	12	1.29	5	22	0.77
6	2	1.30	6	12	1.44	6	22	0.76
7	2	1.29	7	12	1.38	7	22	0.92
8	2	1.28	8	12	1.38	8	22	0.94
9	2	1.32	9	12	1.40	9	22	1.03
10	2	1.29	10	12	1.32	10	22	1.22
11	2	1.29	11	12	1.48	11	22	1.01
12	2	1.24	12	12	1.39	12	22	1.09
13	2	1.25	13	12	1.38	13	22	1.18
14	2	1.18	14	12	1.39	14	22	1.26
15	2	1.13	15	12	1.41	15	22	1.25
16	2	1.02	16	12	1.33	16	22	1.33
17	2	0.98	17	12	1.39	17	22	1.29
18	2	0.91	18	12	1.23	18	22	1.30
19	2	0.90	19	12	1.41	19	22	1.31
20	2	0.80	20	12	1.21	20	22	1.31
21	2	0.70	21	12	1.09	21	22	1.22
22	2	0.63	22	12	1.08	22	22	1.27
23	2	0.58	23	12	1.02	23	22	1.25
24	2	0.57	24	12	1.05	24	22	1.26
25	2	0.49	25	12	1.01	25	22	1.25
26	2	0.45	26	12	0.88	26	22	1.29
27	2	0.42	27	12	0.88	27	22	1.31
28	2	0.24	28	12	0.86	28	22	1.31
1	3	1.45	1	13	1.24	1	23	0.57
2	3	1.41	2	13	1.30	2	23	0.61
3	3	1.42	3	13	1.32	3	23	0.62
4	3	1.30	4	13	1.31	4	23	0.71
5	3	1.30	5	13	1.28	5	23	0.74
6	3	1.29	6	13	1.37	6	23	0.75
7	3	1.23	7	13	1.40	7	23	0.88
8	3	1.24	8	13	1.36	8	23	0.91
9	3	1.30	9	13	1.35	9	23	1.02
10	3	1.24	10	13	1.37	10	23	1.16
11	3	1.31	11	13	1.45	11	23	1.03
12	3	1.22	12	13	1.43	12	23	1.08
13	3	1.22	13	13	1.44	13	23	1.25
14	3	1.16	14	13	1.43	14	23	1.27
15	3	1.10	15	13	1.44	15	23	1.23
16	3	1.00	16	13	1.40	16	23	1.31
17	3	0.97	17	13	1.42	17	23	1.33
18	3	0.91	18	13	1.29	18	23	1.33
19	3	0.90	19	13	1.48	19	23	1.35
20	3	0.78	20	13	1.25	20	23	1.29

21	3	0.71	21	13	1.16	21	23	1.28
22	3	0.64	22	13	1.11	22	23	1.31
23	3	0.58	23	13	1.14	23	23	1.30
24	3	0.58	24	13	1.11	24	23	1.29
25	3	0.50	25	13	1.06	25	23	1.31
26	3	0.45	26	13	1.05	26	23	1.35
27	3	0.46	27	13	1.02	27	23	1.38
28	3	0.28	28	13	0.93	28	23	1.35
1	4	1.40	1	14	1.10	1	24	0.55
2	4	1.37	2	14	1.22	2	24	0.63
3	4	1.38	3	14	1.25	3	24	0.59
4	4	1.30	4	14	1.21	4	24	0.73
5	4	1.28	5	14	1.24	5	24	0.70
6	4	1.29	6	14	1.33	6	24	0.73
7	4	1.24	7	14	1.34	7	24	0.90
8	4	1.23	8	14	1.35	8	24	0.89
9	4	1.27	9	14	1.33	9	24	1.05
10	4	1.26	10	14	1.36	10	24	1.16
11	4	1.28	11	14	1.42	11	24	1.01
12	4	1.20	12	14	1.39	12	24	1.06
13	4	1.23	13	14	1.45	13	24	1.22
14	4	1.18	14	14	1.42	14	24	1.24
15	4	1.12	15	14	1.43	15	24	1.23
16	4	1.03	16	14	1.38	16	24	1.34
17	4	1.00	17	14	1.46	17	24	1.27
18	4	0.93	18	14	1.35	18	24	1.34
19	4	0.92	19	14	1.52	19	24	1.32
20	4	0.81	20	14	1.27	20	24	1.27
21	4	0.73	21	14	1.23	21	24	1.31
22	4	0.67	22	14	1.17	22	24	1.32
23	4	0.63	23	14	1.16	23	24	1.27
24	4	0.63	24	14	1.21	24	24	1.25
25	4	0.55	25	14	1.14	25	24	1.29
26	4	0.52	26	14	1.11	26	24	1.33
27	4	0.49	27	14	1.12	27	24	1.36
28	4	0.32	28	14	1.01	28	24	1.34
1	5	1.37	1	15	0.95	1	25	0.42
2	5	1.35	2	15	1.06	2	25	0.46
3	5	1.42	3	15	1.09	3	25	0.48
4	5	1.31	4	15	1.19	4	25	0.58
5	5	1.31	5	15	1.12	5	25	0.59
6	5	1.27	6	15	1.18	6	25	0.62
7	5	1.25	7	15	1.19	7	25	0.75
8	5	1.24	8	15	1.29	8	25	0.78
9	5	1.24	9	15	1.33	9	25	0.91
10	5	1.27	10	15	1.31	10	25	1.01
11	5	1.30	11	15	1.30	11	25	0.91
12	5	1.24	12	15	1.35	12	25	0.96
13	5	1.24	13	15	1.41	13	25	1.09
14	5	1.21	14	15	1.42	14	25	1.16
15	5	1.15	15	15	1.41	15	25	1.21
16	5	1.08	16	15	1.46	16	25	1.30
17	5	1.05	17	15	1.35	17	25	1.28
18	5	0.96	18	15	1.34	18	25	1.28
19	5	0.99	19	15	1.41	19	25	1.31
20	5	0.84	20	15	1.29	20	25	1.31

21	5	0.77	21	15	1.25	21	25	1.29
22	5	0.73	22	15	1.37	22	25	1.30
23	5	0.68	23	15	1.23	23	25	1.28
24	5	0.68	24	15	1.18	24	25	1.28
25	5	0.60	25	15	1.20	25	25	1.30
26	5	0.58	26	15	1.23	26	25	1.34
27	5	0.57	27	15	1.14	27	25	1.38
28	5	0.41	28	15	1.06	28	25	1.41
1	6	1.34	1	16	0.87	1	26	0.38
2	6	1.33	2	16	0.99	2	26	0.43
3	6	1.35	3	16	1.01	3	26	0.44
4	6	1.29	4	16	1.14	4	26	0.55
5	6	1.23	5	16	1.07	5	26	0.58
6	6	1.24	6	16	1.11	6	26	0.59
7	6	1.21	7	16	1.14	7	26	0.73
8	6	1.23	8	16	1.26	8	26	0.76
9	6	1.25	9	16	1.28	9	26	0.88
10	6	1.25	10	16	1.27	10	26	0.98
11	6	1.28	11	16	1.30	11	26	0.88
12	6	1.23	12	16	1.37	12	26	0.94
13	6	1.24	13	16	1.40	13	26	1.03
14	6	1.20	14	16	1.41	14	26	1.15
15	6	1.16	15	16	1.42	15	26	1.21
16	6	1.10	16	16	1.47	16	26	1.29
17	6	1.05	17	16	1.42	17	26	1.28
18	6	1.01	18	16	1.38	18	26	1.32
19	6	1.00	19	16	1.42	19	26	1.33
20	6	0.87	20	16	1.32	20	26	1.32
21	6	0.81	21	16	1.32	21	26	1.28
22	6	0.76	22	16	1.42	22	26	1.33
23	6	0.72	23	16	1.29	23	26	1.32
24	6	0.72	24	16	1.27	24	26	1.32
25	6	0.64	25	16	1.26	25	26	1.33
26	6	0.63	26	16	1.27	26	26	1.39
27	6	0.61	27	16	1.23	27	26	1.41
28	6	0.47	28	16	1.19	28	26	1.43
1	7	1.36	1	17	0.81	1	27	0.31
2	7	1.36	2	17	0.90	2	27	0.37
3	7	1.37	3	17	0.96	3	27	0.40
4	7	1.30	4	17	1.05	4	27	0.50
5	7	1.24	5	17	1.02	5	27	0.51
6	7	1.27	6	17	1.08	6	27	0.55
7	7	1.25	7	17	1.11	7	27	0.65
8	7	1.20	8	17	1.24	8	27	0.72
9	7	1.29	9	17	1.24	9	27	0.83
10	7	1.28	10	17	1.23	10	27	0.93
11	7	1.34	11	17	1.25	11	27	0.85
12	7	1.25	12	17	1.31	12	27	0.90
13	7	1.25	13	17	1.39	13	27	1.00
14	7	1.24	14	17	1.38	14	27	1.11
15	7	1.22	15	17	1.40	15	27	1.18
16	7	1.14	16	17	1.41	16	27	1.28
17	7	1.11	17	17	1.36	17	27	1.29
18	7	1.05	18	17	1.36	18	27	1.31
19	7	1.07	19	17	1.43	19	27	1.36
20	7	0.92	20	17	1.33	20	27	1.36

21	7	0.87	21	17	1.30	21	27	1.31
22	7	0.82	22	17	1.45	22	27	1.34
23	7	0.77	23	17	1.27	23	27	1.32
24	7	0.77	24	17	1.29	24	27	1.33
25	7	0.71	25	17	1.30	25	27	1.36
26	7	0.67	26	17	1.30	26	27	1.38
27	7	0.67	27	17	1.25	27	27	1.45
28	7	0.53	28	17	1.18	28	27	1.45
1	8	1.29	1	18	0.75	1	28	0.19
2	8	1.29	2	18	0.83	2	28	0.29
3	8	1.33	3	18	0.90	3	28	0.35
4	8	1.26	4	18	1.00	4	28	0.37
5	8	1.25	5	18	0.95	5	28	0.47
6	8	1.26	6	18	1.02	6	28	0.45
7	8	1.25	7	18	1.07	7	28	0.71
8	8	1.23	8	18	1.18	8	28	0.73
9	8	1.23	9	18	1.18	9	28	0.85
10	8	1.24	10	18	1.19	10	28	0.88
11	8	1.30	11	18	1.20	11	28	0.84
12	8	1.29	12	18	1.27	12	28	0.91
13	8	1.27	13	18	1.35	13	28	1.02
14	8	1.25	14	18	1.33	14	28	1.14
15	8	1.23	15	18	1.36	15	28	1.19
16	8	1.15	16	18	1.38	16	28	1.33
17	8	1.18	17	18	1.35	17	28	1.37
18	8	1.03	18	18	1.36	18	28	1.43
19	8	1.22	19	18	1.40	19	28	1.30
20	8	0.97	20	18	1.33	20	28	1.48
21	8	0.88	21	18	1.29	21	28	1.44
22	8	0.85	22	18	1.41	22	28	1.30
23	8	0.80	23	18	1.25	23	28	1.37
24	8	0.80	24	18	1.26	24	28	1.31
25	8	0.76	25	18	1.26	25	28	1.34
26	8	0.74	26	18	1.28	26	28	1.37
27	8	0.72	27	18	1.22	27	28	1.44
28	8	0.60	28	18	1.19	28	28	1.44
1	9	1.24	1	19	0.71			
2	9	1.29	2	19	0.78			
3	9	1.32	3	19	0.84			
4	9	1.28	4	19	0.97			
5	9	1.22	5	19	0.91			
6	9	1.28	6	19	1.09			
7	9	1.26	7	19	1.05			
8	9	1.23	8	19	1.12			
9	9	1.25	9	19	1.11			
10	9	1.24	10	19	1.15			
11	9	1.31	11	19	1.19			
12	9	1.30	12	19	1.24			
13	9	1.30	13	19	1.31			
14	9	1.29	14	19	1.29			
15	9	1.24	15	19	1.32			
16	9	1.20	16	19	1.37			
17	9	1.23	17	19	1.33			
18	9	1.07	18	19	1.30			
19	9	1.25	19	19	1.38			
20	9	1.01	20	19	1.28			

21	9	0.92	21	19	1.27
22	9	0.92	22	19	1.40
23	9	0.84	23	19	1.24
24	9	0.83	24	19	1.24
25	9	0.85	25	19	1.25
26	9	0.79	26	19	1.26
27	9	0.78	27	19	1.25
28	9	0.65	28	19	1.22
1	10	1.27	1	20	0.63
2	10	1.31	2	20	0.72
3	10	1.31	3	20	0.77
4	10	1.31	4	20	0.89
5	10	1.29	5	20	0.80
6	10	1.35	6	20	0.89
7	10	1.32	7	20	1.07
8	10	1.27	8	20	1.25
9	10	1.30	9	20	1.08
10	10	1.30	10	20	1.20
11	10	1.36	11	20	1.24
12	10	1.32	12	20	1.30
13	10	1.36	13	20	1.36
14	10	1.35	14	20	1.43
15	10	1.32	15	20	1.39
16	10	1.26	16	20	1.48
17	10	1.30	17	20	1.44
18	10	1.18	18	20	1.43
19	10	1.36	19	20	1.48
20	10	1.14	20	20	1.36
21	10	1.06	21	20	1.35
22	10	1.04	22	20	1.39
23	10	0.98	23	20	1.35
24	10	0.99	24	20	1.32
25	10	1.01	25	20	1.27
26	10	0.98	26	20	1.38
27	10	1.01	27	20	1.23
28	10	0.75	28	20	1.29

Chute Hemmings Dam, Locations in meters, Times in ms (only 164 rays)
 Data is revised. Locations are originated to zero W=10.5, H=14.5

Source locations (X,Z)		Receiver locations (X,Z)	
0	0	2.36	0
0	1	2.36	1
0	2	2.96	1.8
0	3	3.56	2.6
0	4	4.16	3.4
0	5	4.76	4.2
0	6	5.36	5
0	7	5.96	5.8
0	8	6.56	6.6
0	9	7.16	7.4
0	10	7.76	8.2
0	11	8.36	9
0	12	8.96	9.8
0	13	9.6	10.6
0	14	10.2	11.4

Source number= Sn, Receiver number= Rn, Travel times= T-T

Sn	Rn	T-T	Sn	Rn	T-T
1	1	0.889	8	2	2.20
1	2	0.94	8	3	2.04
1	3	1.21	8	4	1.43
1	4	1.45	8	5	1.50
1	5	1.80	8	6	1.67
1	6	2.11	8	7	1.56
1	7	2.05	8	8	1.42
1	8	2.32	8	9	1.51
1	9	2.39	8	10	1.67
1	10	2.57	8	11	1.78
1	11	4.18	8	12	2.00
1	13	4.47	8	13	2.17
2	1	0.90	8	14	2.61
2	2	0.78	8	15	4.19
2	3	0.97	9	2	2.49
2	4	1.20	9	3	2.41
2	5	1.40	9	4	2.06
2	6	1.19	9	5	2.02
2	7	1.49	9	6	1.92
2	8	1.88	9	7	1.39
2	9	2.08	9	8	1.43
2	10	2.30	9	9	1.48
3	1	1.35	9	10	1.60
3	2	0.933	9	11	1.63
3	3	0.979	9	12	1.79
3	4	1.17	9	13	1.98
3	5	1.38	9	14	2.15
3	6	1.06	9	15	2.86
3	7	2.23	10	2	2.47
3	8	2.12	10	3	2.38
3	9	2.33	10	4	2.07
3	10	2.46	10	5	2.01
3	11	2.98	10	6	2.68

3	12	2.75	10	7	1.89
3	13	3.15	10	8	1.70
3	14	3.31	10	9	1.71
4	1	1.63	10	10	1.78
4	2	1.21	10	11	1.66
4	3	1.21	10	12	1.80
4	4	1.21	10	13	1.99
4	5	1.32	10	14	2.16
4	6	1.37	10	15	2.75
4	7	1.65	11	4	2.63
4	8	1.81	11	7	2.05
4	9	2.02	11	8	1.72
4	10	2.09	11	9	1.79
4	11	2.64	11	10	1.76
4	12	2.79	11	11	1.80
4	13	2.88	11	12	1.95
4	14	2.75	11	13	2.17
4	15	2.97	11	14	2.28
5	2	1.32	11	15	2.85
5	3	1.25	12	6	1.95
5	4	1.12	12	9	1.70
5	5	1.23	12	11	1.87
5	6	1.25	12	12	1.99
5	9	1.76	12	13	2.15
5	11	2.31	12	14	2.57
5	12	2.75	12	15	2.79
5	13	3.19	13	5	3.38
5	14	3.42	13	7	2.12
6	2	1.83	13	11	1.94
6	3	1.55	13	12	2.04
6	4	1.31	13	13	2.04
6	5	1.41	13	14	2.14
6	6	1.16	13	15	2.49
6	7	1.14	14	11	2.02
6	8	1.27	14	12	2.18
6	9	1.41	14	13	2.29
6	10	1.63	14	14	3.22
6	11	1.93	14	15	2.56
6	12	2.17	15	11	2.21
6	13	2.38	15	12	2.23
6	15	2.45	15	13	2.28
7	1	3.02	15	15	2.75
7	2	2.41			
7	3	2.11			
7	4	1.88			
7	5	1.74			
7	6	1.50			
7	7	1.00			
7	8	1.08			
7	9	1.29			
7	10	1.50			
7	11	1.93			
7	12	2.01			
7	13	2.58			
7	14	2.71			
7	15	3.20			

Korean Demilitarized Zone

Locations in meters, Travel times in seconds.

S.L.= Source Locations, R.L.= Receiver Locations

S. L. (X,Z)	R. L. (X,Z)	S. L. (X,Z)	R. L. (X,Z)	S. L. (X,Z)	R. L. (X,Z)
0 10	15.2 10	0 22	15.2 13.1	0 26	15.2 30.1
0 10.2	15.2 10.2	0 22.2	15.2 13.3	0 26.2	15.2 30.3
0 10.4	15.2 10.4	0 22.4	15.2 13.5	0 26.4	15.2 30.5
0 10.6	15.2 10.6	0 22.6	15.2 13.7	0 26.6	15.2 30.7
0 10.8	15.2 10.8	0 22.8	15.2 13.9	0 26.8	15.2 30.9
0 11	15.2 11	0 23	15.2 14.1	0 27	15.2 31.1
0 11.2	15.2 11.2	0 23.2	15.2 14.3	0 27.2	15.2 31.3
0 11.4	15.2 11.4	0 23.4	15.2 14.5	0 27.4	15.2 31.5
0 11.6	15.2 11.6	0 23.6	15.2 14.7	0 27.6	15.2 31.7
0 11.8	15.2 11.8	0 23.8	15.2 14.9	0 27.8	15.2 31.9
0 12	15.2 12	0 24	15.2 15.1	0 28	15.2 32.1
0 12.2	15.2 12.2	0 24.2	15.2 15.3	0 28.2	15.2 32.3
0 12.4	15.2 12.4	0 24.4	15.2 15.5	0 28.4	15.2 32.5
0 12.6	15.2 12.6	0 24.6	15.2 15.7	0 28.6	15.2 32.7
0 12.8	15.2 12.8	0 24.8	15.2 15.9	0 28.8	15.2 32.9
0 13	15.2 13	0 25	15.2 16.1	0 29	15.2 33.1
0 13.2	15.2 13.2	0 25.2	15.2 16.3	0 29.2	15.2 33.3
0 13.4	15.2 13.4	0 25.4	15.2 16.5	0 29.4	15.2 33.5
0 13.6	15.2 13.6	0 25.6	15.2 16.7	0 29.6	15.2 33.7
0 13.8	15.2 13.8	0 25.8	15.2 16.9	0 29.8	15.2 33.9
0 14	15.2 14	0 26	15.2 17.1	0 30	15.2 34.1
0 14.2	15.2 14.2	0 26.2	15.2 17.3	0 30.2	15.2 34.3
0 14.4	15.2 14.4	0 26.4	15.2 17.5	0 30.4	15.2 34.5
0 14.6	15.2 14.6	0 26.6	15.2 17.7	0 30.6	15.2 34.7
0 14.8	15.2 14.8	0 26.8	15.2 17.9	0 30.8	15.2 34.9
0 15	15.2 15	0 27	15.2 18.1	0 31	15.2 35.1
0 15.2	15.2 15.2	0 27.2	15.2 18.3	0 31.2	15.2 35.3
0 15.4	15.2 15.4	0 27.4	15.2 18.5	0 31.4	15.2 35.5
0 15.6	15.2 15.6	0 27.6	15.2 18.7	0 31.6	15.2 35.7
0 15.8	15.2 15.8	0 27.8	15.2 18.9	0 31.8	15.2 35.9
0 16	15.2 16	0 28	15.2 19.1	0 32	15.2 36.1
0 16.2	15.2 16.2	0 28.2	15.2 19.3	0 32.2	15.2 36.3
0 16.4	15.2 16.4	0 28.4	15.2 19.5	0 32.4	15.2 36.5
0 16.6	15.2 16.6	0 28.6	15.2 19.7	0 32.6	15.2 36.7
0 16.8	15.2 16.8	0 28.8	15.2 19.9	0 32.8	15.2 36.9
0 17	15.2 17	0 29	15.2 20.1	0 33	15.2 37.1
0 17.2	15.2 17.2	0 29.2	15.2 20.3	0 33.2	15.2 37.3
0 17.4	15.2 17.4	0 29.4	15.2 20.5	0 33.4	15.2 37.5
0 17.6	15.2 17.6	0 29.6	15.2 20.7	0 33.6	15.2 37.7
0 17.8	15.2 17.8	0 29.8	15.2 20.9	0 33.8	15.2 37.9
0 18	15.2 18	0 30	15.2 21.1	0 34	15.2 38.1
0 18.2	15.2 18.2	0 30.2	15.2 21.3	0 34.2	15.2 38.3
0 18.4	15.2 18.4	0 30.4	15.2 21.5	0 34.4	15.2 38.5
0 18.6	15.2 18.6	0 30.6	15.2 21.7	0 34.6	15.2 38.7
0 18.8	15.2 18.8	0 30.8	15.2 21.9	0 34.8	15.2 38.9
0 19	15.2 19	0 31	15.2 22.1	0 35	15.2 39.1
0 19.2	15.2 19.2	0 31.2	15.2 22.3	0 35.2	15.2 39.3
0 19.4	15.2 19.4	0 31.4	15.2 22.5	0 35.4	15.2 39.5
0 19.6	15.2 19.6	0 31.6	15.2 22.7	0 35.6	15.2 39.7
0 19.8	15.2 19.8	0 31.8	15.2 22.9	0 35.8	15.2 39.9

S. L. (X,Z)	R. L. (X,Z)	S. L. (X,Z)	R. L. (X,Z)	S. L. (X,Z)	R. L. (X,Z)
0 20	15.2 20	0 32	15.2 23.1	0 4	15.2 13.1
0 20.2	15.2 20.2	0 32.2	15.2 23.3	0 4.2	15.2 13.3
0 20.4	15.2 20.4	0 32.4	15.2 23.5	0 4.4	15.2 13.5
0 20.6	15.2 20.6	0 32.6	15.2 23.7	0 4.6	15.2 13.7
0 20.8	15.2 20.8	0 32.8	15.2 23.9	0 4.8	15.2 13.9
0 21	15.2 21	0 33	15.2 24.1	0 5	15.2 14.1
0 21.2	15.2 21.2	0 33.2	15.2 24.3	0 5.2	15.2 14.3
0 21.4	15.2 21.4	0 33.4	15.2 24.5	0 5.4	15.2 14.5
0 21.6	15.2 21.6	0 33.6	15.2 24.7	0 5.6	15.2 14.7
0 21.8	15.2 21.8	0 33.8	15.2 24.9	0 5.8	15.2 14.9
0 22	15.2 22	0 34	15.2 25.1	0 6	15.2 15.1
0 22.2	15.2 22.2	0 34.2	15.2 25.3	0 6.2	15.2 15.3
0 22.4	15.2 22.4	0 34.4	15.2 25.5	0 6.4	15.2 15.5
0 22.6	15.2 22.6	0 34.6	15.2 25.7	0 6.6	15.2 15.7
0 22.8	15.2 22.8	0 34.8	15.2 25.9	0 6.8	15.2 15.9
0 23	15.2 23	0 35	15.2 26.1	0 7	15.2 16.1
0 23.2	15.2 23.2	0 35.2	15.2 26.3	0 7.2	15.2 16.3
0 23.4	15.2 23.4	0 35.4	15.2 26.5	0 7.4	15.2 16.5
0 23.6	15.2 23.6	0 35.6	15.2 26.7	0 7.6	15.2 16.7
0 23.8	15.2 23.8	0 35.8	15.2 26.9	0 7.8	15.2 16.9
0 24	15.2 24	0 36	15.2 27.1	0 8	15.2 17.1
0 24.2	15.2 24.2	0 36.2	15.2 27.3	0 8.2	15.2 17.3
0 24.4	15.2 24.4	0 36.4	15.2 27.5	0 8.4	15.2 17.5
0 24.6	15.2 24.6	0 36.6	15.2 27.7	0 8.6	15.2 17.7
0 24.8	15.2 24.8	0 36.8	15.2 27.9	0 8.8	15.2 17.9
0 25	15.2 25	0 37	15.2 28.1	0 9	15.2 18.1
0 25.2	15.2 25.2	0 37.2	15.2 28.3	0 9.2	15.2 18.3
0 25.4	15.2 25.4	0 37.4	15.2 28.5	0 9.4	15.2 18.5
0 25.6	15.2 25.6	0 37.6	15.2 28.7	0 9.6	15.2 18.7
0 25.8	15.2 25.8	0 37.8	15.2 28.9	0 9.8	15.2 18.9
0 26	15.2 26	0 38	15.2 29.1	0 10	15.2 19.1
0 26.2	15.2 26.2	0 38.2	15.2 29.3	0 10.2	15.2 19.3
0 26.4	15.2 26.4	0 38.4	15.2 29.5	0 10.4	15.2 19.5
0 26.6	15.2 26.6	0 38.6	15.2 29.7	0 10.6	15.2 19.7
0 26.8	15.2 26.8	0 38.8	15.2 29.9	0 10.8	15.2 19.9
0 27	15.2 27	0 39	15.2 30.1	0 11	15.2 20.1
0 27.2	15.2 27.2	0 39.2	15.2 30.3	0 11.2	15.2 20.3
0 27.4	15.2 27.4	0 39.4	15.2 30.5	0 11.4	15.2 20.5
0 27.6	15.2 27.6	0 39.6	15.2 30.7	0 11.6	15.2 20.7
0 27.8	15.2 27.8	0 39.8	15.2 30.9	0 11.8	15.2 20.9
0 28	15.2 28	0 40	15.2 31.1	0 12	15.2 21.1
0 28.2	15.2 28.2	0 40.2	15.2 31.3	0 12.2	15.2 21.3
0 28.4	15.2 28.4	0 40.4	15.2 31.5	0 12.4	15.2 21.5
0 28.6	15.2 28.6	0 40.6	15.2 31.7	0 12.6	15.2 21.7
0 28.8	15.2 28.8	0 40.8	15.2 31.9	0 12.8	15.2 21.9
0 29	15.2 29	0 41	15.2 32.1	0 13	15.2 22.1
0 29.2	15.2 29.2	0 41.2	15.2 32.3	0 13.2	15.2 22.3
0 29.4	15.2 29.4	0 41.4	15.2 32.5	0 13.4	15.2 22.5
0 29.6	15.2 29.6	0 41.6	15.2 32.7	0 13.6	15.2 22.7
0 29.8	15.2 29.8	0 41.8	15.2 32.9	0 13.8	15.2 22.9
0 30	15.2 30	0 15	15.2 0.1	0 14	15.2 23.1
0 30.2	15.2 30.2	0 15.2	15.2 0.3	0 14.2	15.2 23.3
0 30.4	15.2 30.4	0 15.4	15.2 0.5	0 14.4	15.2 23.5

S. L. (X,Z)	R. L. (X,Z)	S. L. (X,Z)	R. L. (X,Z)	S. L. (X,Z)	R. L. (X,Z)
0 30.6	15.2 30.6	0 15.6	15.2 0.7	0 14.6	15.2 23.7
0 30.8	15.2 30.8	0 15.8	15.2 0.9	0 14.8	15.2 23.9
0 31	15.2 31	0 16	15.2 1.1	0 15	15.2 24.1
0 31.2	15.2 31.2	0 16.2	15.2 1.3	0 15.2	15.2 24.3
0 31.4	15.2 31.4	0 16.4	15.2 1.5	0 15.4	15.2 24.5
0 31.6	15.2 31.6	0 16.6	15.2 1.7	0 15.6	15.2 24.7
0 31.8	15.2 31.8	0 16.8	15.2 1.9	0 15.8	15.2 24.9
0 32	15.2 32	0 17	15.2 2.1	0 16	15.2 25.1
0 32.2	15.2 32.2	0 17.2	15.2 2.3	0 16.2	15.2 25.3
0 32.4	15.2 32.4	0 17.4	15.2 2.5	0 16.4	15.2 25.5
0 32.6	15.2 32.6	0 17.6	15.2 2.7	0 16.6	15.2 25.7
0 32.8	15.2 32.8	0 17.8	15.2 2.9	0 16.8	15.2 25.9
0 33	15.2 33	0 18	15.2 3.1	0 17	15.2 26.1
0 33.2	15.2 33.2	0 18.2	15.2 3.3	0 17.2	15.2 26.3
0 33.4	15.2 33.4	0 18.4	15.2 3.5	0 17.4	15.2 26.5
0 33.6	15.2 33.6	0 18.6	15.2 3.7	0 17.6	15.2 26.7
0 33.8	15.2 33.8	0 18.8	15.2 3.9	0 17.8	15.2 26.9
0 34	15.2 34	0 19	15.2 4.1	0 18	15.2 27.1
0 34.2	15.2 34.2	0 19.2	15.2 4.3	0 18.2	15.2 27.3
0 34.4	15.2 34.4	0 19.4	15.2 4.5	0 18.4	15.2 27.5
0 34.6	15.2 34.6	0 19.6	15.2 4.7	0 18.6	15.2 27.7
0 34.8	15.2 34.8	0 19.8	15.2 4.9	0 18.8	15.2 27.9
0 35	15.2 35	0 20	15.2 5.1	0 19	15.2 28.1
0 35.2	15.2 35.2	0 20.2	15.2 5.3	0 19.2	15.2 28.3
0 35.4	15.2 35.4	0 20.4	15.2 5.5	0 19.4	15.2 28.5
0 35.6	15.2 35.6	0 20.6	15.2 5.7	0 19.6	15.2 28.7
0 35.8	15.2 35.8	0 20.8	15.2 5.9	0 19.8	15.2 28.9
0 36	15.2 36	0 21	15.2 6.1	0 20	15.2 29.1
0 36.2	15.2 36.2	0 21.2	15.2 6.3	0 20.2	15.2 29.3
0 36.4	15.2 36.4	0 21.4	15.2 6.5	0 20.4	15.2 29.5
0 36.6	15.2 36.6	0 21.6	15.2 6.7	0 20.6	15.2 29.7
0 36.8	15.2 36.8	0 21.8	15.2 6.9	0 20.8	15.2 29.9
0 37	15.2 37	0 22	15.2 7.1	0 21	15.2 30.1
0 37.2	15.2 37.2	0 22.2	15.2 7.3	0 21.2	15.2 30.3
0 37.4	15.2 37.4	0 22.4	15.2 7.5	0 21.4	15.2 30.5
0 37.6	15.2 37.6	0 22.6	15.2 7.7	0 21.6	15.2 30.7
0 37.8	15.2 37.8	0 22.8	15.2 7.9	0 21.8	15.2 30.9
0 38	15.2 38	0 23	15.2 8.1	0 22	15.2 31.1
0 38.2	15.2 38.2	0 23.2	15.2 8.3	0 22.2	15.2 31.3
0 38.4	15.2 38.4	0 23.4	15.2 8.5	0 22.4	15.2 31.5
0 38.6	15.2 38.6	0 23.6	15.2 8.7	0 22.6	15.2 31.7
0 38.8	15.2 38.8	0 23.8	15.2 8.9	0 22.8	15.2 31.9
0 39	15.2 39	0 24	15.2 9.1	0 23	15.2 32.1
0 39.2	15.2 39.2	0 24.2	15.2 9.3	0 23.2	15.2 32.3
0 39.4	15.2 39.4	0 24.4	15.2 9.5	0 23.4	15.2 32.5
0 39.6	15.2 39.6	0 24.6	15.2 9.7	0 23.6	15.2 32.7
0 39.8	15.2 39.8	0 24.8	15.2 9.9	0 23.8	15.2 32.9
0 10	15.2 6.1	0 25	15.2 10.1	0 24	15.2 33.1
0 10.2	15.2 6.3	0 25.2	15.2 10.3	0 24.2	15.2 33.3
0 10.4	15.2 6.5	0 25.4	15.2 10.5	0 24.4	15.2 33.5
0 10.6	15.2 6.7	0 25.6	15.2 10.7	0 24.6	15.2 33.7
0 10.8	15.2 6.9	0 25.8	15.2 10.9	0 24.8	15.2 33.9
0 11	15.2 7.1	0 26	15.2 11.1	0 25	15.2 34.1

S. L. (X,Z)	R. L. (X,Z)	S. L. (X,Z)	R. L. (X,Z)	S. L. (X,Z)	R. L. (X,Z)
0 11.2	15.2 7.3	0 26.2	15.2 11.3	0 25.2	15.2 34.3
0 11.4	15.2 7.5	0 26.4	15.2 11.5	0 25.4	15.2 34.5
0 11.6	15.2 7.7	0 26.6	15.2 11.7	0 25.6	15.2 34.7
0 11.8	15.2 7.9	0 26.8	15.2 11.9	0 25.8	15.2 34.9
0 12	15.2 8.1	0 27	15.2 12.1	0 26	15.2 35.1
0 12.2	15.2 8.3	0 27.2	15.2 12.3	0 26.2	15.2 35.3
0 12.4	15.2 8.5	0 27.4	15.2 12.5	0 26.4	15.2 35.5
0 12.6	15.2 8.7	0 27.6	15.2 12.7	0 26.6	15.2 35.7
0 12.8	15.2 8.9	0 27.8	15.2 12.9	0 26.8	15.2 35.9
0 13	15.2 9.1	0 28	15.2 13.1	0 27	15.2 36.1
0 13.2	15.2 9.3	0 28.2	15.2 13.3	0 27.2	15.2 36.3
0 13.4	15.2 9.5	0 28.4	15.2 13.5	0 27.4	15.2 36.5
0 13.6	15.2 9.7	0 28.6	15.2 13.7	0 27.6	15.2 36.7
0 13.8	15.2 9.9	0 28.8	15.2 13.9	0 27.8	15.2 36.9
0 14	15.2 10.1	0 29	15.2 14.1	0 28	15.2 37.1
0 14.2	15.2 10.3	0 29.2	15.2 14.3	0 28.2	15.2 37.3
0 14.4	15.2 10.5	0 29.4	15.2 14.5	0 28.4	15.2 37.5
0 14.6	15.2 10.7	0 29.6	15.2 14.7	0 28.6	15.2 37.7
0 14.8	15.2 10.9	0 29.8	15.2 14.9	0 28.8	15.2 37.9
0 15	15.2 11.1	0 30	15.2 15.1	0 29	15.2 38.1
0 15.2	15.2 11.3	0 30.2	15.2 15.3	0 29.2	15.2 38.3
0 15.4	15.2 11.5	0 30.4	15.2 15.5	0 29.4	15.2 38.5
0 15.6	15.2 11.7	0 30.6	15.2 15.7	0 29.6	15.2 38.7
0 15.8	15.2 11.9	0 30.8	15.2 15.9	0 29.8	15.2 38.9
0 16	15.2 12.1	0 31	15.2 16.1	0 30	15.2 39.1
0 16.2	15.2 12.3	0 31.2	15.2 16.3	0 30.2	15.2 39.3
0 16.4	15.2 12.5	0 31.4	15.2 16.5	0 30.4	15.2 39.5
0 16.6	15.2 12.7	0 31.6	15.2 16.7	0 30.6	15.2 39.7
0 16.8	15.2 12.9	0 31.8	15.2 16.9	0 30.8	15.2 39.9
0 17	15.2 13.1	0 32	15.2 17.1	0 31	15.2 40.1
0 17.2	15.2 13.3	0 32.2	15.2 17.3	0 31.2	15.2 40.3
0 17.4	15.2 13.5	0 32.4	15.2 17.5	0 31.4	15.2 40.5
0 17.6	15.2 13.7	0 32.6	15.2 17.7	0 31.6	15.2 40.7
0 17.8	15.2 13.9	0 32.8	15.2 17.9	0 31.8	15.2 40.9
0 18	15.2 14.1	0 33	15.2 18.1	0 32	15.2 41.1
0 18.2	15.2 14.3	0 33.2	15.2 18.3	0 32.2	15.2 41.3
0 18.4	15.2 14.5	0 33.4	15.2 18.5	0 32.4	15.2 41.5
0 18.6	15.2 14.7	0 33.6	15.2 18.7	0 32.6	15.2 41.7
0 18.8	15.2 14.9	0 33.8	15.2 18.9	0 32.8	15.2 41.9
0 19	15.2 15.1	0 34	15.2 19.1	0 33	15.2 42.1
0 19.2	15.2 15.3	0 34.2	15.2 19.3	0 33.2	15.2 42.3
0 19.4	15.2 15.5	0 34.4	15.2 19.5	0 33.4	15.2 42.5
0 19.6	15.2 15.7	0 34.6	15.2 19.7	0 33.6	15.2 42.7
0 19.8	15.2 15.9	0 34.8	15.2 19.9	0 33.8	15.2 42.9
0 20	15.2 16.1	0 35	15.2 20.1	0 1	15.2 16.1
0 20.2	15.2 16.3	0 35.2	15.2 20.3	0 1.2	15.2 16.3
0 20.4	15.2 16.5	0 35.4	15.2 20.5	0 1.4	15.2 16.5
0 20.6	15.2 16.7	0 35.6	15.2 20.7	0 1.6	15.2 16.7
0 20.8	15.2 16.9	0 35.8	15.2 20.9	0 1.8	15.2 16.9
0 21	15.2 17.1	0 36	15.2 21.1	0 2	15.2 17.1
0 21.2	15.2 17.3	0 36.2	15.2 21.3	0 2.2	15.2 17.3
0 21.4	15.2 17.5	0 36.4	15.2 21.5	0 2.4	15.2 17.5
0 21.6	15.2 17.7	0 36.6	15.2 21.7	0 2.6	15.2 17.7

S. L. (X,Z)	R. L. (X,Z)	S. L. (X,Z)	R. L. (X,Z)	S. L. (X,Z)	R. L. (X,Z)
0 21.8	15.2 17.9	0 36.8	15.2 21.9	0 2.8	15.2 17.9
0 22	15.2 18.1	0 37	15.2 22.1	0 3	15.2 18.1
0 22.2	15.2 18.3	0 37.2	15.2 22.3	0 3.2	15.2 18.3
0 22.4	15.2 18.5	0 37.4	15.2 22.5	0 3.4	15.2 18.5
0 22.6	15.2 18.7	0 37.6	15.2 22.7	0 3.6	15.2 18.7
0 22.8	15.2 18.9	0 37.8	15.2 22.9	0 3.8	15.2 18.9
0 23	15.2 19.1	0 38	15.2 23.1	0 4	15.2 19.1
0 23.2	15.2 19.3	0 38.2	15.2 23.3	0 4.2	15.2 19.3
0 23.4	15.2 19.5	0 38.4	15.2 23.5	0 4.4	15.2 19.5
0 23.6	15.2 19.7	0 38.6	15.2 23.7	0 4.6	15.2 19.7
0 23.8	15.2 19.9	0 38.8	15.2 23.9	0 4.8	15.2 19.9
0 24	15.2 20.1	0 39	15.2 24.1	0 5	15.2 20.1
0 24.2	15.2 20.3	0 39.2	15.2 24.3	0 5.2	15.2 20.3
0 24.4	15.2 20.5	0 39.4	15.2 24.5	0 5.4	15.2 20.5
0 24.6	15.2 20.7	0 39.6	15.2 24.7	0 5.6	15.2 20.7
0 24.8	15.2 20.9	0 39.8	15.2 24.9	0 5.8	15.2 20.9
0 25	15.2 21.1	0 40	15.2 25.1	0 6	15.2 21.1
0 25.2	15.2 21.3	0 40.2	15.2 25.3	0 6.2	15.2 21.3
0 25.4	15.2 21.5	0 40.4	15.2 25.5	0 6.4	15.2 21.5
0 25.6	15.2 21.7	0 40.6	15.2 25.7	0 6.6	15.2 21.7
0 25.8	15.2 21.9	0 40.8	15.2 25.9	0 6.8	15.2 21.9
0 26	15.2 22.1	0 41	15.2 26.1	0 7	15.2 22.1
0 26.2	15.2 22.3	0 41.2	15.2 26.3	0 7.2	15.2 22.3
0 26.4	15.2 22.5	0 41.4	15.2 26.5	0 7.4	15.2 22.5
0 26.6	15.2 22.7	0 41.6	15.2 26.7	0 7.6	15.2 22.7
0 26.8	15.2 22.9	0 41.8	15.2 26.9	0 7.8	15.2 22.9
0 27	15.2 23.1	0 42	15.2 27.1	0 8	15.2 23.1
0 27.2	15.2 23.3	0 42.2	15.2 27.3	0 8.2	15.2 23.3
0 27.4	15.2 23.5	0 42.4	15.2 27.5	0 8.4	15.2 23.5
0 27.6	15.2 23.7	0 42.6	15.2 27.7	0 8.6	15.2 23.7
0 27.8	15.2 23.9	0 42.8	15.2 27.9	0 8.8	15.2 23.9
0 28	15.2 24.1	0 43	15.2 28.1	0 9	15.2 24.1
0 28.2	15.2 24.3	0 43.2	15.2 28.3	0 9.2	15.2 24.3
0 28.4	15.2 24.5	0 43.4	15.2 28.5	0 9.4	15.2 24.5
0 28.6	15.2 24.7	0 43.6	15.2 28.7	0 9.6	15.2 24.7
0 28.8	15.2 24.9	0 43.8	15.2 28.9	0 9.8	15.2 24.9
0 29	15.2 25.1	0 44	15.2 29.1	0 10	15.2 25.1
0 29.2	15.2 25.3	0 44.2	15.2 29.3	0 10.2	15.2 25.3
0 29.4	15.2 25.5	0 44.4	15.2 29.5	0 10.4	15.2 25.5
0 29.6	15.2 25.7	0 44.6	15.2 29.7	0 10.6	15.2 25.7
0 29.8	15.2 25.9	0 44.8	15.2 29.9	0 10.8	15.2 25.9
0 30	15.2 26.1	0 6	15.2 10.1	0 11	15.2 26.1
0 30.2	15.2 26.3	0 6.2	15.2 10.3	0 11.2	15.2 26.3
0 30.4	15.2 26.5	0 6.4	15.2 10.5	0 11.4	15.2 26.5
0 30.6	15.2 26.7	0 6.6	15.2 10.7	0 11.6	15.2 26.7
0 30.8	15.2 26.9	0 6.8	15.2 10.9	0 11.8	15.2 26.9
0 31	15.2 27.1	0 7	15.2 11.1	0 12	15.2 27.1
0 31.2	15.2 27.3	0 7.2	15.2 11.3	0 12.2	15.2 27.3
0 31.4	15.2 27.5	0 7.4	15.2 11.5	0 12.4	15.2 27.5
0 31.6	15.2 27.7	0 7.6	15.2 11.7	0 12.6	15.2 27.7
0 31.8	15.2 27.9	0 7.8	15.2 11.9	0 12.8	15.2 27.9
0 32	15.2 28.1	0 8	15.2 12.1	0 13	15.2 28.1
0 32.2	15.2 28.3	0 8.2	15.2 12.3	0 13.2	15.2 28.3

S. L. (X,Z)	R. L. (X,Z)	S. L. (X,Z)	R. L. (X,Z)	S. L. (X,Z)	R. L. (X,Z)
0 32.4	15.2 28.5	0 8.4	15.2 12.5	0 13.4	15.2 28.5
0 32.6	15.2 28.7	0 8.6	15.2 12.7	0 13.6	15.2 28.7
0 32.8	15.2 28.9	0 8.8	15.2 12.9	0 13.8	15.2 28.9
0 33	15.2 29.1	0 9	15.2 13.1	0 14	15.2 29.1
0 33.2	15.2 29.3	0 9.2	15.2 13.3	0 14.2	15.2 29.3
0 33.4	15.2 29.5	0 9.4	15.2 13.5	0 14.4	15.2 29.5
0 33.6	15.2 29.7	0 9.6	15.2 13.7	0 14.6	15.2 29.7
0 33.8	15.2 29.9	0 9.8	15.2 13.9	0 14.8	15.2 29.9
0 34	15.2 30.1	0 10	15.2 14.1	0 15	15.2 30.1
0 34.2	15.2 30.3	0 10.2	15.2 14.3	0 15.2	15.2 30.3
0 34.4	15.2 30.5	0 10.4	15.2 14.5	0 15.4	15.2 30.5
0 34.6	15.2 30.7	0 10.6	15.2 14.7	0 15.6	15.2 30.7
0 34.8	15.2 30.9	0 10.8	15.2 14.9	0 15.8	15.2 30.9
0 35	15.2 31.1	0 11	15.2 15.1	0 16	15.2 31.1
0 35.2	15.2 31.3	0 11.2	15.2 15.3	0 16.2	15.2 31.3
0 35.4	15.2 31.5	0 11.4	15.2 15.5	0 16.4	15.2 31.5
0 35.6	15.2 31.7	0 11.6	15.2 15.7	0 16.6	15.2 31.7
0 35.8	15.2 31.9	0 11.8	15.2 15.9	0 16.8	15.2 31.9
0 36	15.2 32.1	0 12	15.2 16.1	0 17	15.2 32.1
0 36.2	15.2 32.3	0 12.2	15.2 16.3	0 17.2	15.2 32.3
0 36.4	15.2 32.5	0 12.4	15.2 16.5	0 17.4	15.2 32.5
0 36.6	15.2 32.7	0 12.6	15.2 16.7	0 17.6	15.2 32.7
0 36.8	15.2 32.9	0 12.8	15.2 16.9	0 17.8	15.2 32.9
0 37	15.2 33.1	0 13	15.2 17.1	0 18	15.2 33.1
0 37.2	15.2 33.3	0 13.2	15.2 17.3	0 18.2	15.2 33.3
0 37.4	15.2 33.5	0 13.4	15.2 17.5	0 18.4	15.2 33.5
0 37.6	15.2 33.7	0 13.6	15.2 17.7	0 18.6	15.2 33.7
0 37.8	15.2 33.9	0 13.8	15.2 17.9	0 18.8	15.2 33.9
0 38	15.2 34.1	0 14	15.2 18.1	0 19	15.2 34.1
0 38.2	15.2 34.3	0 14.2	15.2 18.3	0 19.2	15.2 34.3
0 38.4	15.2 34.5	0 14.4	15.2 18.5	0 19.4	15.2 34.5
0 38.6	15.2 34.7	0 14.6	15.2 18.7	0 19.6	15.2 34.7
0 38.8	15.2 34.9	0 14.8	15.2 18.9	0 19.8	15.2 34.9
0 39	15.2 35.1	0 15	15.2 19.1	0 20	15.2 35.1
0 39.2	15.2 35.3	0 15.2	15.2 19.3	0 20.2	15.2 35.3
0 39.4	15.2 35.5	0 15.4	15.2 19.5	0 20.4	15.2 35.5
0 39.6	15.2 35.7	0 15.6	15.2 19.7	0 20.6	15.2 35.7
0 39.8	15.2 35.9	0 15.8	15.2 19.9	0 20.8	15.2 35.9
0 12	15.2 3.1	0 16	15.2 20.1	0 21	15.2 36.1
0 12.2	15.2 3.3	0 16.2	15.2 20.3	0 21.2	15.2 36.3
0 12.4	15.2 3.5	0 16.4	15.2 20.5	0 21.4	15.2 36.5
0 12.6	15.2 3.7	0 16.6	15.2 20.7	0 21.6	15.2 36.7
0 12.8	15.2 3.9	0 16.8	15.2 20.9	0 21.8	15.2 36.9
0 13	15.2 4.1	0 17	15.2 21.1	0 22	15.2 37.1
0 13.2	15.2 4.3	0 17.2	15.2 21.3	0 22.2	15.2 37.3
0 13.4	15.2 4.5	0 17.4	15.2 21.5	0 22.4	15.2 37.5
0 13.6	15.2 4.7	0 17.6	15.2 21.7	0 22.6	15.2 37.7
0 13.8	15.2 4.9	0 17.8	15.2 21.9	0 22.8	15.2 37.9
0 14	15.2 5.1	0 18	15.2 22.1	0 23	15.2 38.1
0 14.2	15.2 5.3	0 18.2	15.2 22.3	0 23.2	15.2 38.3
0 14.4	15.2 5.5	0 18.4	15.2 22.5	0 23.4	15.2 38.5
0 14.6	15.2 5.7	0 18.6	15.2 22.7	0 23.6	15.2 38.7
0 14.8	15.2 5.9	0 18.8	15.2 22.9	0 23.8	15.2 38.9

S. L. (X,Z)	R. L. (X,Z)	S. L. (X,Z)	R. L. (X,Z)	S. L. (X,Z)	R. L. (X,Z)
0 15	15.2 6.1	0 19	15.2 23.1	0 24	15.2 39.1
0 15.2	15.2 6.3	0 19.2	15.2 23.3	0 24.2	15.2 39.3
0 15.4	15.2 6.5	0 19.4	15.2 23.5	0 24.4	15.2 39.5
0 15.6	15.2 6.7	0 19.6	15.2 23.7	0 24.6	15.2 39.7
0 15.8	15.2 6.9	0 19.8	15.2 23.9	0 24.8	15.2 39.9
0 16	15.2 7.1	0 20	15.2 24.1	0 25	15.2 40.1
0 16.2	15.2 7.3	0 20.2	15.2 24.3	0 25.2	15.2 40.3
0 16.4	15.2 7.5	0 20.4	15.2 24.5	0 25.4	15.2 40.5
0 16.6	15.2 7.7	0 20.6	15.2 24.7	0 25.6	15.2 40.7
0 16.8	15.2 7.9	0 20.8	15.2 24.9	0 25.8	15.2 40.9
0 17	15.2 8.1	0 21	15.2 25.1	0 26	15.2 41.1
0 17.2	15.2 8.3	0 21.2	15.2 25.3	0 26.2	15.2 41.3
0 17.4	15.2 8.5	0 21.4	15.2 25.5	0 26.4	15.2 41.5
0 17.6	15.2 8.7	0 21.6	15.2 25.7	0 26.6	15.2 41.7
0 17.8	15.2 8.9	0 21.8	15.2 25.9	0 26.8	15.2 41.9
0 18	15.2 9.1	0 22	15.2 26.1	0 27	15.2 42.1
0 18.2	15.2 9.3	0 22.2	15.2 26.3	0 27.2	15.2 42.3
0 18.4	15.2 9.5	0 22.4	15.2 26.5	0 27.4	15.2 42.5
0 18.6	15.2 9.7	0 22.6	15.2 26.7	0 27.6	15.2 42.7
0 18.8	15.2 9.9	0 22.8	15.2 26.9	0 27.8	15.2 42.9
0 19	15.2 10.1	0 23	15.2 27.1	0 28	15.2 43.1
0 19.2	15.2 10.3	0 23.2	15.2 27.3	0 28.2	15.2 43.3
0 19.4	15.2 10.5	0 23.4	15.2 27.5	0 28.4	15.2 43.5
0 19.6	15.2 10.7	0 23.6	15.2 27.7	0 28.6	15.2 43.7
0 19.8	15.2 10.9	0 23.8	15.2 27.9	0 28.8	15.2 43.9
0 20	15.2 11.1	0 24	15.2 28.1	0 29	15.2 44.1
0 20.2	15.2 11.3	0 24.2	15.2 28.3	0 29.2	15.2 44.3
0 20.4	15.2 11.5	0 24.4	15.2 28.5	0 29.4	15.2 44.5
0 20.6	15.2 11.7	0 24.6	15.2 28.7	0 29.6	15.2 44.7
0 20.8	15.2 11.9	0 24.8	15.2 28.9	0 29.8	15.2 44.9
0 21	15.2 12.1	0 25	15.2 29.1	0 30	15.2 45.1
0 21.2	15.2 12.3	0 25.2	15.2 29.3	0 30.2	15.2 45.3
0 21.4	15.2 12.5	0 25.4	15.2 29.5	0 30.4	15.2 45.5
0 21.6	15.2 12.7	0 25.6	15.2 29.7	0 30.6	15.2 45.7
0 21.8	15.2 12.9	0 25.8	15.2 29.9	0 30.8	15.2 45.9

Source number= Sn, Receiver number= Rn, Travel times= T-T

Sn	Rn	T-T	Sn	Rn	T-T	Sn	Rn	T-T
1	1	0.003610	351	351	0.003856	701	701	0.003542
2	2	0.003618	352	352	0.003854	702	702	0.003555
3	3	0.003603	353	353	0.003869	703	703	0.003567
4	4	0.003588	354	354	0.003869	704	704	0.003570
5	5	0.003578	355	355	0.003876	705	705	0.003570
6	6	0.003562	356	356	0.003887	706	706	0.003570
7	7	0.003555	357	357	0.003887	707	707	0.003575
8	8	0.003552	358	358	0.003894	708	708	0.003575
9	9	0.003542	359	359	0.003899	709	709	0.003570
10	10	0.003542	360	360	0.003899	710	710	0.003570
11	11	0.003534	361	361	0.003887	711	711	0.003555
12	12	0.003532	362	362	0.003879	712	712	0.003545
13	13	0.003534	363	363	0.003874	713	713	0.003540
14	14	0.003542	364	364	0.003876	714	714	0.003534
15	15	0.003542	365	365	0.003879	715	715	0.003529

Sn	Rn	T-T	Sn	Rn	T-T	Sn	Rn	T-T
16	16	0.003550	366	366	0.003854	716	716	0.003522
17	17	0.003552	367	367	0.003838	717	717	0.003517
18	18	0.003562	368	368	0.003843	718	718	0.003514
19	19	0.003562	369	369	0.003836	719	719	0.003514
20	20	0.003567	370	370	0.003838	720	720	0.003514
21	21	0.003575	371	371	0.003838	721	721	0.003512
22	22	0.003580	372	372	0.003841	722	722	0.003509
23	23	0.003585	373	373	0.003846	723	723	0.003509
24	24	0.003583	374	374	0.003856	724	724	0.003509
25	25	0.003585	375	375	0.003866	725	725	0.003507
26	26	0.003583	376	376	0.003869	726	726	0.003507
27	27	0.003588	377	377	0.003879	727	727	0.003507
28	28	0.003590	378	378	0.003894	728	728	0.003504
29	29	0.003588	379	379	0.003897	729	729	0.003496
30	30	0.003585	380	380	0.003904	730	730	0.003496
31	31	0.003585	381	381	0.003899	731	731	0.003481
32	32	0.003583	382	382	0.003907	732	732	0.003476
33	33	0.003588	383	383	0.003907	733	733	0.003466
34	34	0.003588	384	384	0.003914	734	734	0.003453
35	35	0.003588	385	385	0.003909	735	735	0.003451
36	36	0.003583	386	386	0.003907	736	736	0.003448
37	37	0.003578	387	387	0.003904	737	737	0.003443
38	38	0.003583	388	388	0.003899	738	738	0.003446
39	39	0.003593	389	389	0.003899	739	739	0.003448
40	40	0.003585	390	390	0.003902	740	740	0.003443
41	41	0.003583	391	391	0.003904	741	741	0.003443
42	42	0.003567	392	392	0.003894	742	742	0.003443
43	43	0.003562	393	393	0.003879	743	743	0.003446
44	44	0.003565	394	394	0.003871	744	744	0.003451
45	45	0.003565	395	395	0.003859	745	745	0.003451
46	46	0.003562	396	396	0.003851	746	746	0.003446
47	47	0.003552	397	397	0.003859	747	747	0.003443
48	48	0.003550	398	398	0.003849	748	748	0.003446
49	49	0.003542	399	399	0.003831	749	749	0.003451
50	50	0.003534	400	400	0.003826	750	750	0.003443
51	51	0.003527	401	401	0.003813	751	751	0.004120
52	52	0.003519	402	402	0.003788	752	752	0.004130
53	53	0.003512	403	403	0.003740	753	753	0.004137
54	54	0.003512	404	404	0.003742	754	754	0.004143
55	55	0.003507	405	405	0.003729	755	755	0.004130
56	56	0.003506	406	406	0.003724	756	756	0.004132
57	57	0.003509	407	407	0.003719	757	757	0.004143
58	58	0.003501	408	408	0.003719	758	758	0.004143
59	59	0.003502	409	409	0.003714	759	759	0.004132
60	60	0.003496	410	410	0.003722	760	760	0.004122
61	61	0.003491	411	411	0.003722	761	761	0.004125
62	62	0.003491	412	412	0.003719	762	762	0.004120
63	63	0.003494	413	413	0.003719	763	763	0.004110
64	64	0.003496	414	414	0.003722	764	764	0.004107
65	65	0.003491	415	415	0.003724	765	765	0.004112
66	66	0.003496	416	416	0.003729	766	766	0.004105
67	67	0.003501	417	417	0.003737	767	767	0.004089
68	68	0.003496	418	418	0.003747	768	768	0.004089

Sn	Rn	T-T	Sn	Rn	T-T	Sn	Rn	T-T
69	69	0.003504	419	419	0.003745	769	769	0.004084
70	70	0.003502	420	420	0.003745	770	770	0.004074
71	71	0.003504	421	421	0.003745	771	771	0.004061
72	72	0.003534	422	422	0.003752	772	772	0.004056
73	73	0.003557	423	423	0.003750	773	773	0.004049
74	74	0.003570	424	424	0.003750	774	774	0.004041
75	75	0.003583	425	425	0.003755	775	775	0.004028
76	76	0.003603	426	426	0.003752	776	776	0.004028
77	77	0.003590	427	427	0.003750	777	777	0.004013
78	78	0.003575	428	428	0.003747	778	778	0.004008
79	79	0.003565	429	429	0.003747	779	779	0.004003
80	80	0.003545	430	430	0.003737	780	780	0.003998
81	81	0.003540	431	431	0.003737	781	781	0.004001
82	82	0.003532	432	432	0.003742	782	782	0.003998
83	83	0.003524	433	433	0.003745	783	783	0.003996
84	84	0.003522	434	434	0.003745	784	784	0.003990
85	85	0.003522	435	435	0.003745	785	785	0.003998
86	86	0.003514	436	436	0.003734	786	786	0.004001
87	87	0.003514	437	437	0.003737	787	787	0.004006
88	88	0.003507	438	438	0.003734	788	788	0.004023
89	89	0.003504	439	439	0.003737	789	789	0.004034
90	90	0.003496	440	440	0.003732	790	790	0.004049
91	91	0.003486	441	441	0.003724	791	791	0.004054
92	92	0.003479	442	442	0.003724	792	792	0.004054
93	93	0.003474	443	443	0.003704	793	793	0.004054
94	94	0.003469	444	444	0.003704	794	794	0.004054
95	95	0.003453	445	445	0.003707	795	795	0.004054
96	96	0.003436	446	446	0.003709	796	796	0.004051
97	97	0.003433	447	447	0.003702	797	797	0.004049
98	98	0.003420	448	448	0.003707	798	798	0.004056
99	99	0.003410	449	449	0.003709	799	799	0.004064
100	100	0.003405	450	450	0.003704	800	800	0.004084
101	101	0.003405	451	451	0.004813	801	801	0.004092
102	102	0.003403	452	452	0.004808	802	802	0.004105
103	103	0.003398	453	453	0.004808	803	803	0.004127
104	104	0.003395	454	454	0.004803	804	804	0.004127
105	105	0.003397	455	455	0.004793	805	805	0.004140
106	106	0.003394	456	456	0.004793	806	806	0.004143
107	107	0.003389	457	457	0.004790	807	807	0.004148
108	108	0.003393	458	458	0.004793	808	808	0.004148
109	109	0.003398	459	459	0.004798	809	809	0.004148
110	110	0.003395	460	460	0.004796	810	810	0.004148
111	111	0.003393	461	461	0.004801	811	811	0.004145
112	112	0.003395	462	462	0.004796	812	812	0.004148
113	113	0.003400	463	463	0.004793	813	813	0.004153
114	114	0.003398	464	464	0.004785	814	814	0.004153
115	115	0.003400	465	465	0.004783	815	815	0.004155
116	116	0.003398	466	466	0.004780	816	816	0.004155
117	117	0.003400	467	467	0.004778	817	817	0.004163
118	118	0.003394	468	468	0.004783	818	818	0.004155
119	119	0.003390	469	469	0.004780	819	819	0.004153
120	120	0.003390	470	470	0.004788	820	820	0.004132
121	121	0.003390	471	471	0.004790	821	821	0.004117

Sn	Rn	T-T	Sn	Rn	T-T	Sn	Rn	T-T
122	122	0.003387	472	472	0.004785	822	822	0.004099
123	123	0.003390	473	473	0.004783	823	823	0.004087
124	124	0.003392	474	474	0.004773	824	824	0.004056
125	125	0.003389	475	475	0.004765	825	825	0.004039
126	126	0.003389	476	476	0.004768	826	826	0.004011
127	127	0.003380	477	477	0.004768	827	827	0.004008
128	128	0.003377	478	478	0.004768	828	828	0.004001
129	129	0.003369	479	479	0.004763	829	829	0.003957
130	130	0.003367	480	480	0.004755	830	830	0.003960
131	131	0.003361	481	481	0.004757	831	831	0.003950
132	132	0.003356	482	482	0.004768	832	832	0.003925
133	133	0.003354	483	483	0.004775	833	833	0.003925
134	134	0.003359	484	484	0.004773	834	834	0.003927
135	135	0.003354	485	485	0.004770	835	835	0.003927
136	136	0.003346	486	486	0.004775	836	836	0.003925
137	137	0.003351	487	487	0.004773	837	837	0.003912
138	138	0.003356	488	488	0.004768	838	838	0.003919
139	139	0.003356	489	489	0.004755	839	839	0.003927
140	140	0.003356	490	490	0.004745	840	840	0.003919
141	141	0.003339	491	491	0.004735	841	841	0.003927
142	142	0.003339	492	492	0.004666	842	842	0.003930
143	143	0.003339	493	493	0.004719	843	843	0.003927
144	144	0.003341	494	494	0.004722	844	844	0.003930
145	145	0.003338	495	495	0.004714	845	845	0.003932
146	146	0.003333	496	496	0.004712	846	846	0.003932
147	147	0.003323	497	497	0.004709	847	847	0.003932
148	148	0.003323	498	498	0.004699	848	848	0.003930
149	149	0.003326	499	499	0.004694	849	849	0.003927
150	150	0.003323	500	500	0.004689	850	850	0.003919
151	151	0.003625	501	501	0.004687	851	851	0.003917
152	152	0.003622	502	502	0.004681	852	852	0.003925
153	153	0.003620	503	503	0.004681	853	853	0.003922
154	154	0.003630	504	504	0.004681	854	854	0.003927
155	155	0.003630	505	505	0.004679	855	855	0.003925
156	156	0.003620	506	506	0.004681	856	856	0.003927
157	157	0.003627	507	507	0.004687	857	857	0.003927
158	158	0.003620	508	508	0.004684	858	858	0.003927
159	159	0.003622	509	509	0.004676	859	859	0.003925
160	160	0.003620	510	510	0.004676	860	860	0.003919
161	161	0.003617	511	511	0.004674	861	861	0.003919
162	162	0.003627	512	512	0.004674	862	862	0.003917
163	163	0.003637	513	513	0.004679	863	863	0.003925
164	164	0.003625	514	514	0.004676	864	864	0.003927
165	165	0.003640	515	515	0.004684	865	865	0.003935
166	166	0.003643	516	516	0.004674	866	866	0.003942
167	167	0.003643	517	517	0.004671	867	867	0.003935
168	168	0.003678	518	518	0.004674	868	868	0.003919
169	169	0.003668	519	519	0.004676	869	869	0.003914
170	170	0.003665	520	520	0.004666	870	870	0.003919
171	171	0.003655	521	521	0.004666	871	871	0.003914
172	172	0.003648	522	522	0.004674	872	872	0.003902
173	173	0.003650	523	523	0.004664	873	873	0.003899
174	174	0.003668	524	524	0.004664	874	874	0.003889

Sn	Rn	T-T	Sn	Rn	T-T	Sn	Rn	T-T
175	175	0.003655	525	525	0.004664	875	875	0.003881
176	176	0.003650	526	526	0.004669	876	876	0.003884
177	177	0.003627	527	527	0.004676	877	877	0.003884
178	178	0.003627	528	528	0.004676	878	878	0.003879
179	179	0.003627	529	529	0.004679	879	879	0.003879
180	180	0.003627	530	530	0.004684	880	880	0.003866
181	181	0.003637	531	531	0.004674	881	881	0.003861
182	182	0.003632	532	532	0.004674	882	882	0.003861
183	183	0.003637	533	533	0.004671	883	883	0.003859
184	184	0.003635	534	534	0.004669	884	884	0.003861
185	185	0.003632	535	535	0.004669	885	885	0.003864
186	186	0.003622	536	536	0.004666	886	886	0.003874
187	187	0.003610	537	537	0.004651	887	887	0.003871
188	188	0.003607	538	538	0.004649	888	888	0.003869
189	189	0.003607	539	539	0.004649	889	889	0.003869
190	190	0.003599	540	540	0.004656	890	890	0.003869
191	191	0.003589	541	541	0.004654	891	891	0.003874
192	192	0.003579	542	542	0.004654	892	892	0.003874
193	193	0.003572	543	543	0.004636	893	893	0.003884
194	194	0.003582	544	544	0.004628	894	894	0.003887
195	195	0.003569	545	545	0.004608	895	895	0.003884
196	196	0.003554	546	546	0.004598	896	896	0.003879
197	197	0.003546	547	547	0.004600	897	897	0.003879
198	198	0.003544	548	548	0.004598	898	898	0.003866
199	199	0.003559	549	549	0.004585	899	899	0.003869
200	200	0.003539	550	550	0.004578	900	900	0.003866
201	201	0.003541	551	551	0.004565	901	901	0.004812
202	202	0.003546	552	552	0.004565	902	902	0.004807
203	203	0.003546	553	553	0.004565	903	903	0.004802
204	204	0.003539	554	554	0.004555	904	904	0.004784
205	205	0.003551	555	555	0.004537	905	905	0.004779
206	206	0.003554	556	556	0.004517	906	906	0.004769
207	207	0.003559	557	557	0.004504	907	907	0.004751
208	208	0.003564	558	558	0.004496	908	908	0.004761
209	209	0.003574	559	559	0.004494	909	909	0.004744
210	210	0.003584	560	560	0.004481	910	910	0.004736
211	211	0.003589	561	561	0.004479	911	911	0.004746
212	212	0.003589	562	562	0.004471	912	912	0.004731
213	213	0.003615	563	563	0.004471	913	913	0.004728
214	214	0.003627	564	564	0.004474	914	914	0.004718
215	215	0.003637	565	565	0.004461	915	915	0.004721
216	216	0.003630	566	566	0.004453	916	916	0.004716
217	217	0.003620	567	567	0.004441	917	917	0.004708
218	218	0.003617	568	568	0.004438	918	918	0.004708
219	219	0.003607	569	569	0.004425	919	919	0.004708
220	220	0.003599	570	570	0.004433	920	920	0.004703
221	221	0.003597	571	571	0.004431	921	921	0.004693
222	222	0.003587	572	572	0.004433	922	922	0.004703
223	223	0.003579	573	573	0.004438	923	923	0.004703
224	224	0.003587	574	574	0.004436	924	924	0.004708
225	225	0.003569	575	575	0.004433	925	925	0.004703
226	226	0.003554	576	576	0.004436	926	926	0.004701
227	227	0.003564	577	577	0.004436	927	927	0.004693

Sn	Rn	T-T	Sn	Rn	T-T	Sn	Rn	T-T
228	228	0.003564	578	578	0.004438	928	928	0.004693
229	229	0.003564	579	579	0.004443	929	929	0.004688
230	230	0.003566	580	580	0.004466	930	930	0.004690
231	231	0.003574	581	581	0.004464	931	931	0.004696
232	232	0.003574	582	582	0.004469	932	932	0.004690
233	233	0.003579	583	583	0.004464	933	933	0.004693
234	234	0.003572	584	584	0.004481	934	934	0.004690
235	235	0.003577	585	585	0.004481	935	935	0.004690
236	236	0.003574	586	586	0.004469	936	936	0.004693
237	237	0.003554	587	587	0.004474	937	937	0.004696
238	238	0.003551	588	588	0.004479	938	938	0.004690
239	239	0.003551	589	589	0.004494	939	939	0.004690
240	240	0.003546	590	590	0.004484	940	940	0.004716
241	241	0.003526	591	591	0.004489	941	941	0.004711
242	242	0.003511	592	592	0.004499	942	942	0.004713
243	243	0.003513	593	593	0.004496	943	943	0.004708
244	244	0.003513	594	594	0.004486	944	944	0.004711
245	245	0.003506	595	595	0.004481	945	945	0.004708
246	246	0.003498	596	596	0.004476	946	946	0.004708
247	247	0.003488	597	597	0.004486	947	947	0.004723
248	248	0.003488	598	598	0.004476	948	948	0.004736
249	249	0.003480	599	599	0.004466	949	949	0.004731
250	250	0.003470	600	600	0.004466	950	950	0.004736
251	251	0.003465	601	601	0.003814	951	951	0.004739
252	252	0.003452	602	602	0.003791	952	952	0.004749
253	253	0.003450	603	603	0.003793	953	953	0.004756
254	254	0.003457	604	604	0.003781	954	954	0.004764
255	255	0.003457	605	605	0.003778	955	955	0.004761
256	256	0.003445	606	606	0.003770	956	956	0.004756
257	257	0.003445	607	607	0.003768	957	957	0.004741
258	258	0.003447	608	608	0.003760	958	958	0.004739
259	259	0.003455	609	609	0.003758	959	959	0.004744
260	260	0.003455	610	610	0.003763	960	960	0.004746
261	261	0.003447	611	611	0.003770	961	961	0.004746
262	262	0.003440	612	612	0.003770	962	962	0.004766
263	263	0.003430	613	613	0.003775	963	963	0.004777
264	264	0.003432	614	614	0.003773	964	964	0.004787
265	265	0.003435	615	615	0.003765	965	965	0.004805
266	266	0.003440	616	616	0.003755	966	966	0.004805
267	267	0.003432	617	617	0.003750	967	967	0.004807
268	268	0.003437	618	618	0.003743	968	968	0.004805
269	269	0.003435	619	619	0.003740	969	969	0.004784
270	270	0.003435	620	620	0.003745	970	970	0.004784
271	271	0.003435	621	621	0.003750	971	971	0.004769
272	272	0.003427	622	622	0.003753	972	972	0.004716
273	273	0.003427	623	623	0.003763	973	973	0.004701
274	274	0.003447	624	624	0.003773	974	974	0.004701
275	275	0.003457	625	625	0.003770	975	975	0.004678
276	276	0.003445	626	626	0.003778	976	976	0.004668
277	277	0.003445	627	627	0.003778	977	977	0.004640
278	278	0.003445	628	628	0.003775	978	978	0.004625
279	279	0.003440	629	629	0.003770	979	979	0.004625
280	280	0.003435	630	630	0.003758	980	980	0.004619

Sn	Rn	T-T	Sn	Rn	T-T	Sn	Rn	T-T
281	281	0.003425	631	631	0.003750	981	981	0.004614
282	282	0.003432	632	632	0.003737	982	982	0.004614
283	283	0.003437	633	633	0.003737	983	983	0.004609
284	284	0.003430	634	634	0.003730	984	984	0.004609
285	285	0.003430	635	635	0.003725	985	985	0.004609
286	286	0.003419	636	636	0.003720	986	986	0.004602
287	287	0.003397	637	637	0.003705	987	987	0.004597
288	288	0.003399	638	638	0.003699	988	988	0.004589
289	289	0.003394	639	639	0.003697	989	989	0.004584
290	290	0.003397	640	640	0.003687	990	990	0.004587
291	291	0.003399	641	641	0.003681	991	991	0.004584
292	292	0.003402	642	642	0.003687	992	992	0.004584
293	293	0.003394	643	643	0.003687	993	993	0.004581
294	294	0.003381	644	644	0.003687	994	994	0.004576
295	295	0.003379	645	645	0.003689	995	995	0.004576
296	296	0.003366	646	646	0.003702	996	996	0.004569
297	297	0.003361	647	647	0.003712	997	997	0.004574
298	298	0.003364	648	648	0.003712	998	998	0.004569
299	299	0.003349	649	649	0.003709	999	999	0.004566
300	300	0.003349	650	650	0.003709	1000	1000	0.004566
301	301	0.003932	651	651	0.003717	1001	1001	0.004564
302	302	0.003937	652	652	0.003717	1002	1002	0.004564
303	303	0.003945	653	653	0.003727	1003	1003	0.004569
304	304	0.003937	654	654	0.003737	1004	1004	0.004559
305	305	0.003930	655	655	0.003732	1005	1005	0.004556
306	306	0.003930	656	656	0.003732	1006	1006	0.004556
307	307	0.003930	657	657	0.003732	1007	1007	0.004549
308	308	0.003940	658	658	0.003725	1008	1008	0.004554
309	309	0.003950	659	659	0.003725	1009	1009	0.004554
310	310	0.003957	660	660	0.003722	1010	1010	0.004559
311	311	0.003952	661	661	0.003730	1011	1011	0.004549
312	312	0.003950	662	662	0.003752	1012	1012	0.004541
313	313	0.003952	663	663	0.003750	1013	1013	0.004541
314	314	0.003947	664	664	0.003752	1014	1014	0.004538
315	315	0.003942	665	665	0.003763	1015	1015	0.004531
316	316	0.003945	666	666	0.003763	1016	1016	0.004533
317	317	0.003942	667	667	0.003760	1017	1017	0.004521
318	318	0.003942	668	668	0.003742	1018	1018	0.004521
319	319	0.003940	669	669	0.003722	1019	1019	0.004518
320	320	0.003940	670	670	0.003702	1020	1020	0.004526
321	321	0.003945	671	671	0.003681	1021	1021	0.004523
322	322	0.003945	672	672	0.003674	1022	1022	0.004516
323	323	0.003947	673	673	0.003664	1023	1023	0.004516
324	324	0.003950	674	674	0.003661	1024	1024	0.004516
325	325	0.003940	675	675	0.003656	1025	1025	0.004511
326	326	0.003940	676	676	0.003651	1026	1026	0.004511
327	327	0.003932	677	677	0.003643	1027	1027	0.004513
328	328	0.003930	678	678	0.003628	1028	1028	0.004518
329	329	0.003930	679	679	0.003626	1029	1029	0.004518
330	330	0.003930	680	680	0.003621	1030	1030	0.004518
331	331	0.003925	681	681	0.003616	1031	1031	0.004523
332	332	0.003930	682	682	0.003608	1032	1032	0.004516
333	333	0.003922	683	683	0.003598	1033	1033	0.004511

Sn	Rn	T-T	Sn	Rn	T-T	Sn	Rn	T-T
334	334	0.003907	684	684	0.003595	1034	1034	0.004511
335	335	0.003907	685	685	0.003588	1035	1035	0.004516
336	336	0.003902	686	686	0.003575	1036	1036	0.004511
337	337	0.003892	687	687	0.003570	1037	1037	0.004518
338	338	0.003894	688	688	0.003560	1038	1038	0.004518
339	339	0.003894	689	689	0.003552	1039	1039	0.004513
340	340	0.003884	690	690	0.003547	1040	1040	0.004505
341	341	0.003884	691	691	0.003547	1041	1041	0.004511
342	342	0.003876	692	692	0.003537	1042	1042	0.004503
343	343	0.003879	693	693	0.003529	1043	1043	0.004500
344	344	0.003876	694	694	0.003524	1044	1044	0.004495
345	345	0.003879	695	695	0.003529	1045	1045	0.004493
346	346	0.003874	696	696	0.003522	1046	1046	0.004503
347	347	0.003866	697	697	0.003524	1047	1047	0.004508
348	348	0.003861	698	698	0.003524	1048	1048	0.004503
349	349	0.003856	699	699	0.003529	1049	1049	0.004505
350	350	0.003854	700	700	0.003540	1050	1050	0.004503

**APPENDIX F: Corresponding Inversion
Mathcad Files for All Case
Histories**

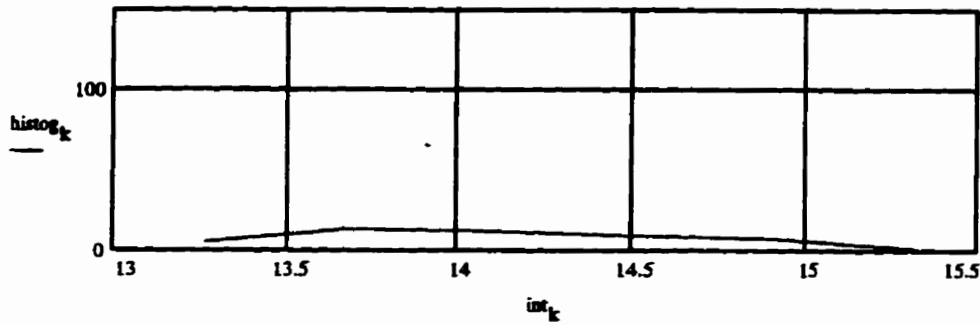
Inverting Velocity Field (Balloon 1): $\lambda = 2$

Definitions $n := 7$ $i := 1..n$ $j := 1..n$
 $ij := 1..n \cdot n$ $nh := n$ $m := 1..nh$ $k := 1..nh - 1$

Input File $V := \text{READPRN}(\text{vb1sc})$ $V_{\min} := \min(V)$ $V_{\max} := \max(V)$
 $V_{\min} = 13.262$ $V_{\max} = 16.137$ $\text{mean}(V) = 14.384$

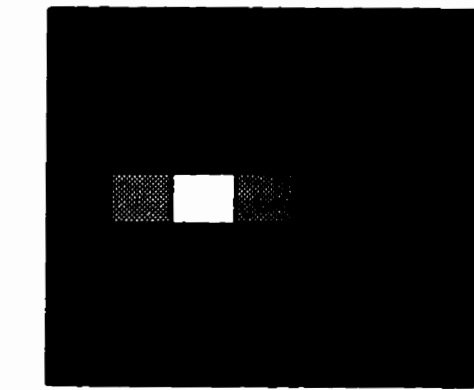
Histogram $\text{int}_m := V_{\min} + (m - 1) \cdot \frac{V_{\max} - V_{\min}}{nh}$ $\text{histog} := \text{hist}(\text{int}, V)$

Histogram of the inverted velocity field



2D Image $A_{i,j} := V_{(i-1) \cdot nh + j}$ $B_{j,(n-i)+1} := A_{i,j}$

Inverted velocity field



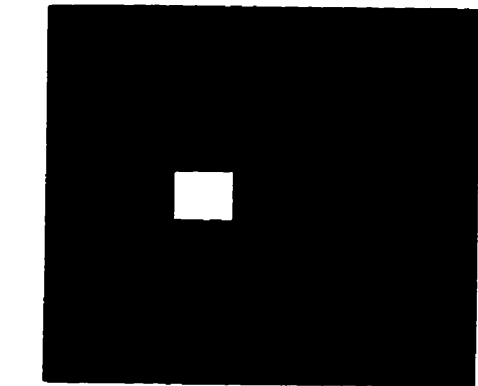
A



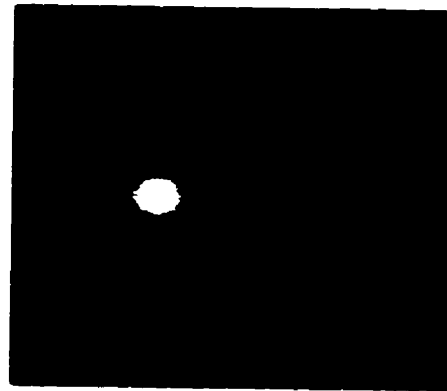
B

Enhancement	$V_{ij} := \text{if}(V_{ij} < 15.8, 15.8, V_{ij})$	$V_{ij} := \text{if}(V_{ij} > V_{\text{max}}, V_{\text{max}}, V_{ij})$
2D Image	$A_{i,j} := V_{(i-1) \cdot m + j}$	$B_{j, (n-i)+1} := A_{i,j}$

Enhanced inverted velocity field



A

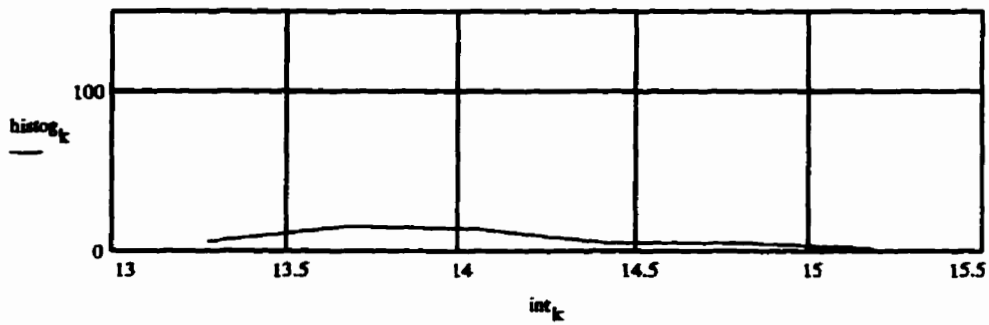


B

Inverting Velocity Field (Balloon 2): $\lambda = 300$

Definitions	$n := 7$	$i := 1..n$	$j := 1..n$
$ij := 1..n-n$	$nh := n$	$m := 1..nh$	$k := 1..nh - 1$
Input File	$V := \text{READPRN}(\text{vb2sc})$	$V_{\min} := \min(V)$	$V_{\max} := \max(V)$
	$V_{\min} = 13.277$	$V_{\max} = 15.94$	$\text{mean}(V) = 14.253$
Histogram	$\text{int}_m := V_{\min} + (m - 1) \cdot \frac{V_{\max} - V_{\min}}{nh}$		$\text{histog} := \text{hist}(\text{int}, V)$

Histogram of the inverted velocity field

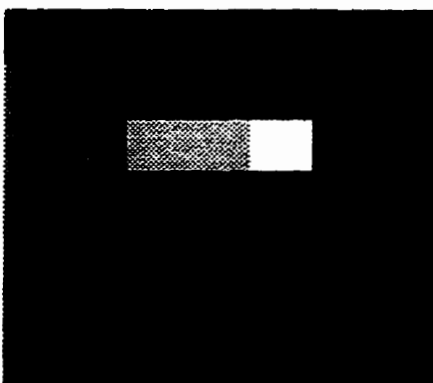


2D Image

$$A_{i,j} := V_{(i-1) \cdot nh + j}$$

$$B_{j,(n-i)+1} := A_{i,j}$$

Inverted velocity field



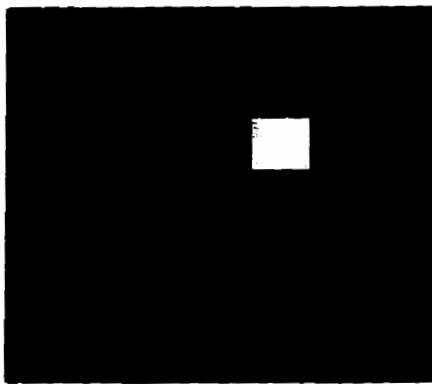
A



B

Enhancement $V_{ij} := \text{if}(V_{ij} < 15.8, 15.8, V_{ij})$ $V_{ij} := \text{if}(V_{ij} > V_{\text{max}}, V_{\text{max}}, V_{ij})$
 2D Image $A_{i,j} := V_{(i-1) \cdot m + j}$ $B_{j,(n-i)+1} := A_{i,j}$

Enhanced inverted velocity field



A



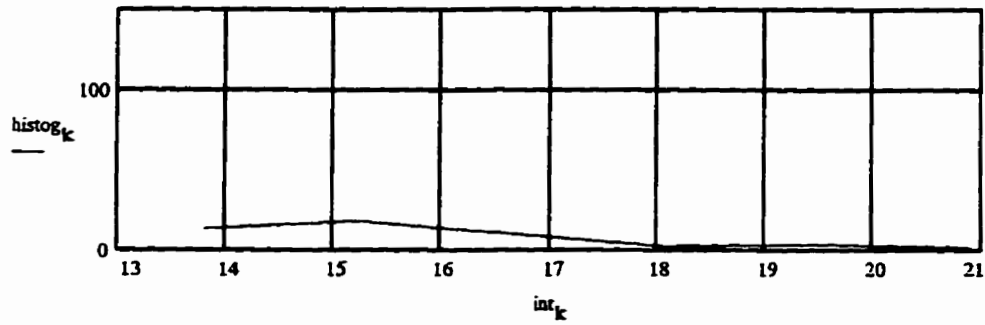
B

Inverting Velocity Field (Balloon 2): $\lambda = 300$

Ray Tracing (Second Iteration)

Definitions	$n := 7$	$i := 1..n$	$j := 1..n$
	$nh := n$	$m := 1..nh$	$k := 1..nh - 1$
Input File	$V := \text{READPRN}(\text{vb2scr})$	$V_{\min} := \min(V)$	$V_{\max} := \max(V)$
	$V_{\min} = 13.8$	$V_{\max} = 23.73$	$\text{mean}(V) = 16.729$
Histogram	$\text{int}_m := V_{\min} + (m - 1) \cdot \frac{V_{\max} - V_{\min}}{nh}$		$\text{histog} := \text{hist}(\text{int}, V)$

Histogram of the inverted velocity field

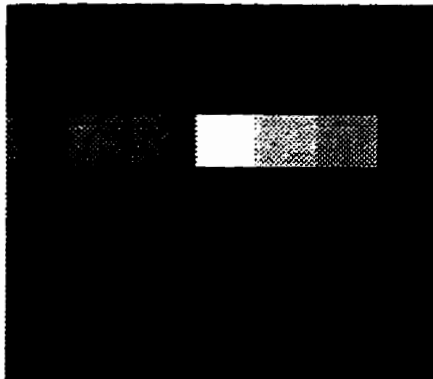


2D Image

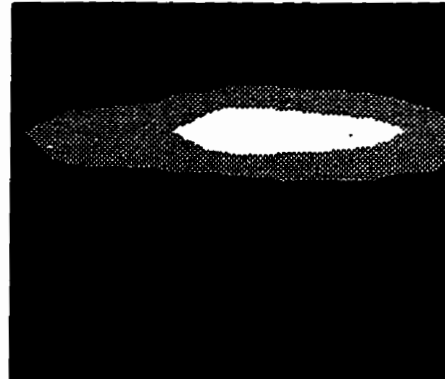
$$A_{i,j} := V_{(i-1) \cdot nh + j}$$

$$B_{j,(n-i)+1} := A_{i,j}$$

Inverted velocity field



A



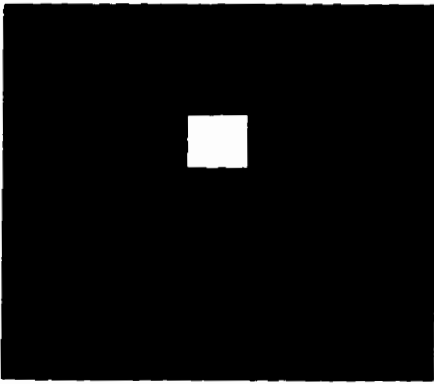
B

The chop-off threshold value is selected based on computed value for the highest velocity in the medium.

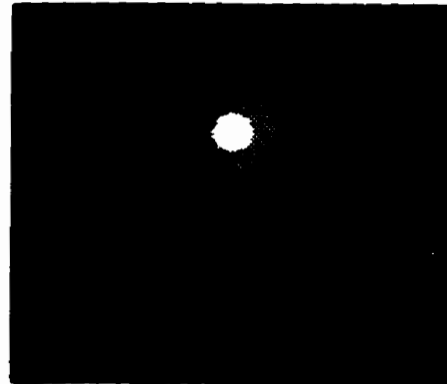
Enhancement $V_{ij} := \text{if}(V_{ij} < 23.5, 23.5, V_{ij})$ $V_{ij} := \text{if}(V_{ij} > V_{\text{max}}, V_{\text{max}}, V_{ij})$

2D Image $A_{i,j} := V_{(i-1) \cdot m + j}$ $B_{j,(n-i)+1} := A_{i,j}$

Enhanced inverted velocity field



A



B

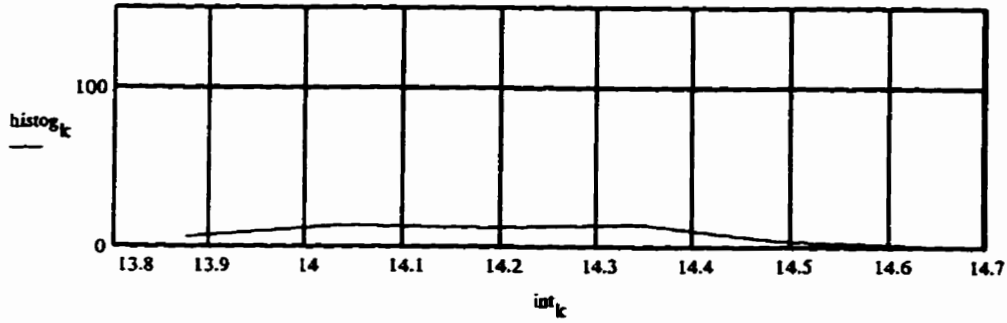
Inverting Velocity Field (Balloon 3): $\lambda = 5$

Definitions $n := 7$ $i := 1..n$ $j := 1..n$
 $ij := 1..n-n$ $nh := n$ $m := 1..nh$ $k := 1..nh - 1$

Input File $V := \text{READPRN}(\text{vb3sc})$ $V_{\min} := \min(V)$ $V_{\max} := \max(V)$
 $V_{\min} = 13.875$ $V_{\max} = 14.969$ $\text{mean}(V) = 14.27$

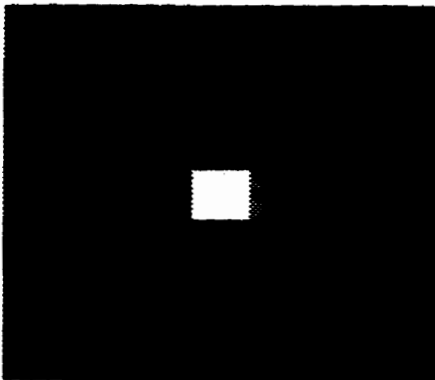
Histogram $\text{int}_m := V_{\min} + (m - 1) \cdot \frac{V_{\max} - V_{\min}}{nh}$ $\text{histog} := \text{hist}(\text{int}, V)$

Histogram of the inverted velocity field

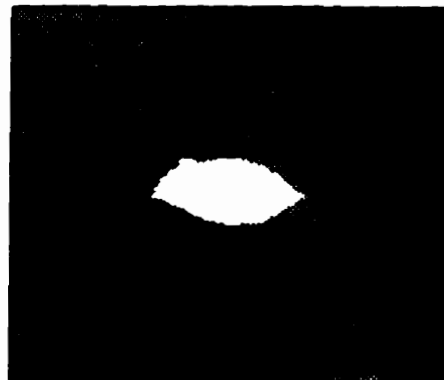


2D Image $A_{i,j} := V_{(i-1) \cdot nh + j}$ $B_{j,(n-i)+1} := A_{i,j}$

Inverted velocity field



A

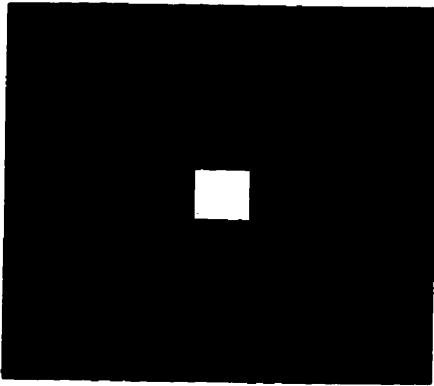


B

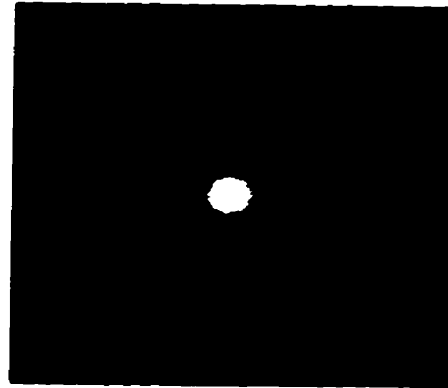
Enhancement $V_{ij} := \text{if}(V_{ij} < 14.8, 14.8, V_{ij})$ $V_{ij} := \text{if}(V_{ij} > V_{\text{max}}, V_{\text{max}}, V_{ij})$

2D Image $A_{i,j} := V_{(i-1) \cdot m + j}$ $B_{j,(n-i)+1} := A_{i,j}$

Enhanced inverted velocity field



A



B

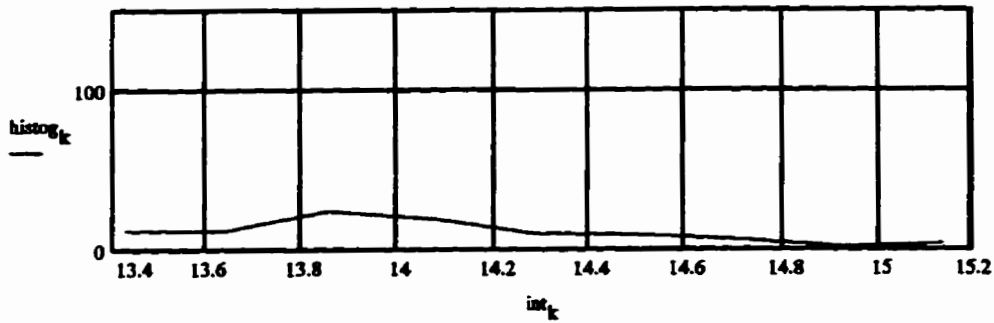
Inverting Velocity Field (Balloon 4): $\lambda = 10$

Definitions $n := 10$ $i := 1..n$ $j := 1..n$
 $ij := 1..n \cdot n$ $nh := n$ $m := 1..nh$ $k := 1..nh - 1$

Input File $V := \text{READPRN}(\text{vb16})$ $V_{\min} := \min(V)$ $V_{\max} := \max(V)$
 $V_{\min} = 13.429$ $V_{\max} = 15.564$ $\text{mean}(V) = 14.194$

Histogram $\text{int}_m := V_{\min} + (m - 1) \cdot \frac{V_{\max} - V_{\min}}{nh}$ $\text{histog} := \text{hist}(\text{int}, V)$

Histogram of the inverted velocity field

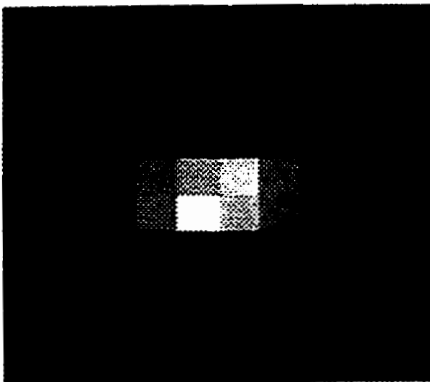


2D Image

$$A_{i,j} := V_{(i-1) \cdot nh + j}$$

$$B_{j,(n-i)+1} := A_{i,j}$$

Inverted velocity field



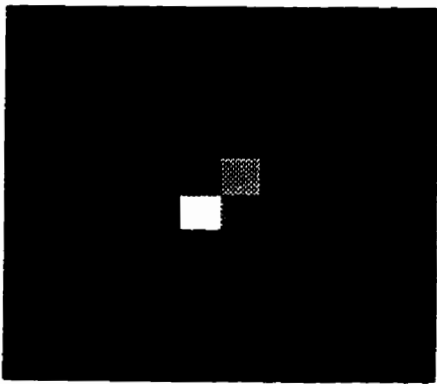
A



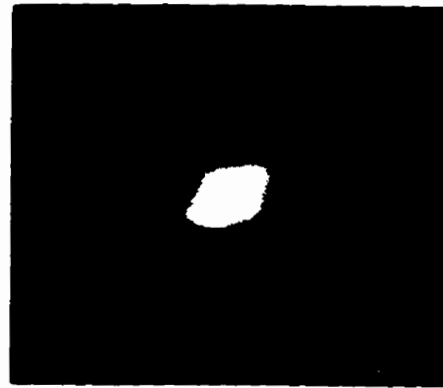
B

Enhancement $V_{ij} := \text{if}(V_{ij} < 15.2, 15.2, V_{ij})$ $V_{ij} := \text{if}(V_{ij} > V_{\text{max}}, V_{\text{max}}, V_{ij})$
 2D Image $A_{i,j} := V_{(i-1) \cdot m + j}$ $B_{j,(n-i)+1} := A_{i,j}$

Enhanced inverted velocity field



A



B

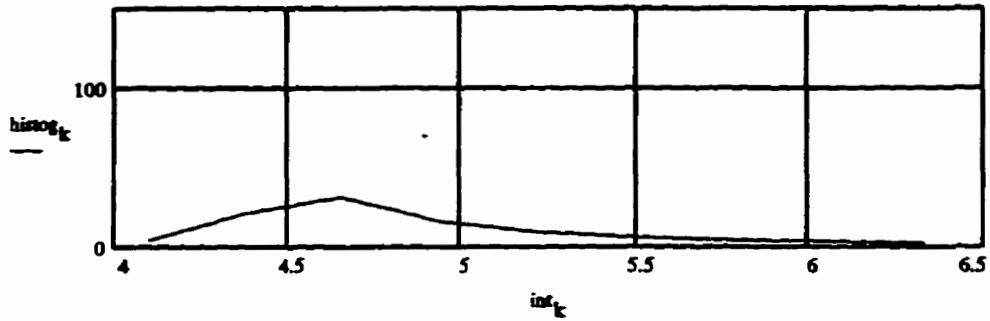
Inverting Velocity Field (Concrete Crack Side-to-Side Shootings): $\lambda = 0.005$

Definitions $n := 10$ $i := 1..n$ $j := 1..n$
 $ij := 1..n \cdot n$ $nh := n$ $m := 1..nh$ $k := 1..nh - 1$

Input File $V := \text{READPRN}(\text{vrckss})$ $V_{\min} := \min(V)$ $V_{\max} := \max(V)$
 $V_{\min} = 4.098$ $V_{\max} = 6.894$ $\text{mean}(V) = 5.065$

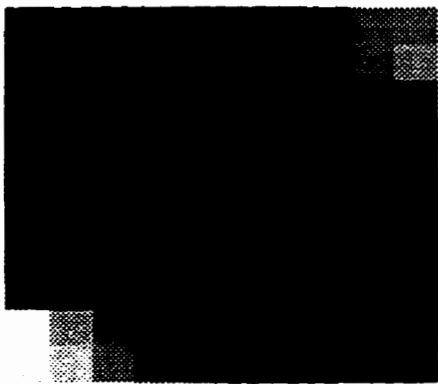
Histogram $\text{int}_m := V_{\min} + (m - 1) \cdot \frac{V_{\max} - V_{\min}}{nh}$ $\text{histog} := \text{hist}(\text{int}, V)$

Histogram of the inverted velocity field



2D Image $A_{i,j} := V_{(i-1) \cdot nh + j}$ $B_{j,(n-i)+1} := A_{i,j}$

Inverted velocity field



A



B

Enhancement

$$V_{ij} := \text{if}(V_{ij} < V_{\min}, V_{\min}, V_{ij})$$

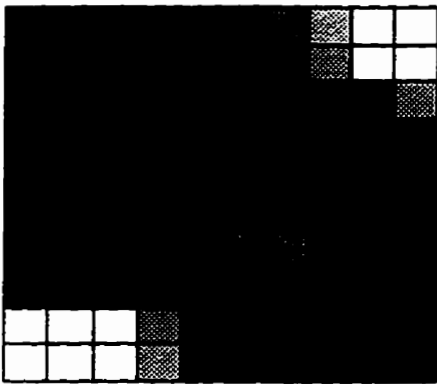
$$V_{ij} := \text{if}(V_{ij} > 6., 6., V_{ij})$$

2D Image

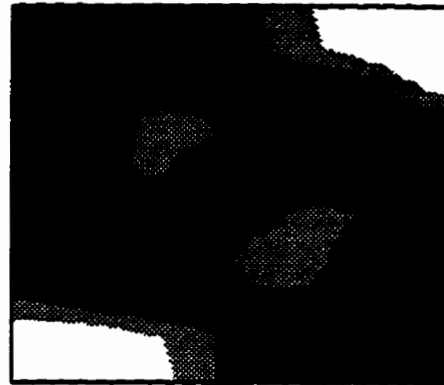
$$A_{i,j} := V_{(i-1) \cdot m + j}$$

$$B_{j,(n-i)+1} := A_{i,j}$$

Enhanced inverted velocity field



A



B

Inverting Velocity Field (Concrete Crack Top to Left-Side Shooting)

$\lambda = 0.4$ Initial velocity = 400

Definitions $n := 10$ $i := 1..n$ $j := 1..n$
 $ij := 1..n \cdot n$ $nh := n$ $m := 1..nh$ $k := 1..nh - 1$

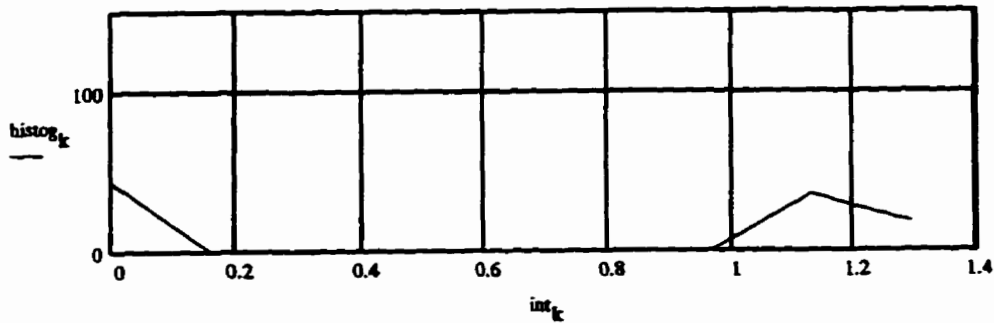
Input File $V := \text{READPRN}(\text{vcrkl})$ $V_{\min} := \min(V)$ $V_{\max} := \max(V)$
 $V_{\min} = 0$ $V_{\max} = 1.613$ $\text{mean}(V) = 0.724$

Enhancement $V_{ij} := \text{if}(V_{ij} < V_{\min}, V_{\min}, V_{ij})$ $V_{ij} := \text{if}(V_{ij} > V_{\max}, V_{\max}, V_{ij})$

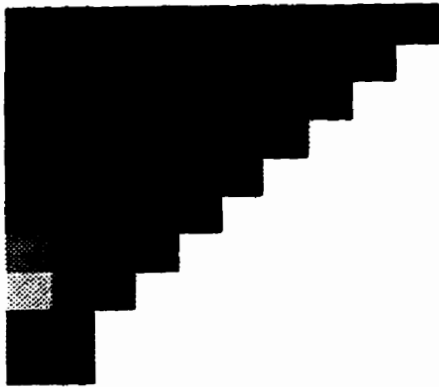
Histogram $\text{int}_m := V_{\min} + (m - 1) \cdot \frac{V_{\max} - V_{\min}}{nh}$ $\text{histog} := \text{hist}(\text{int}, V)$

2D Image $A_{i,j} := V_{(i-1) \cdot nh + j}$ $A_{i,j} := \text{if}[V_{(i-1) \cdot nh + j} \neq 0., 1.65, A_{i,j}]$ $B_{j, (n-i)+1} := A_{i,j}$

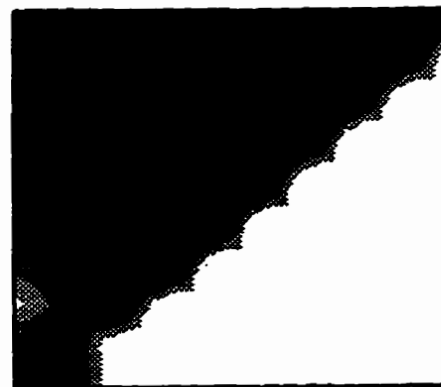
Histogram of the inverted velocity field



Inverted velocity field



A



B

Inverting Velocity Field (Concrete Crack Top to Right-Side Shooting)

$\lambda = 0.01$ Initial velocity = 400

Definitions $n := 10$ $i := 1..n$ $j := 1..n$
 $ij := 1..n \cdot n$ $nh := n$ $m := 1..nh$ $k := 1..nh - 1$

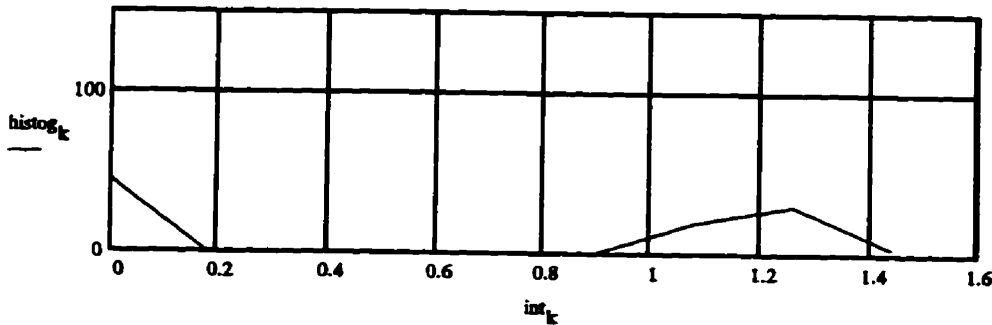
Input File $V := \text{READPRN}(\text{vcrktr})$ $V_{\min} := \min(V)$ $V_{\max} := \max(V)$
 $V_{\min} = 0$ $V_{\max} = 1.797$ $\text{mean}(V) = 0.728$

Enhancement $V_{ij} := \text{if}(V_{ij} < V_{\min}, V_{\min}, V_{ij})$ $V_{ij} := \text{if}(V_{ij} > V_{\max}, V_{\max}, V_{ij})$

Histogram $\text{int}_m := V_{\min} + (m - 1) \cdot \frac{V_{\max} - V_{\min}}{nh}$ $\text{histog} := \text{hist}(\text{int}, V)$

2D Image $A_{i,j} := V_{(i-1) \cdot nh + j}$ $A_{i,j} := \text{if}[V_{(i-1) \cdot nh + j} \approx 0., 1.8, A_{i,j}]$ $B_{j,(n-i)+1} := A_{i,j}$

Histogram of the inverted velocity field



Inverted velocity field



A



B

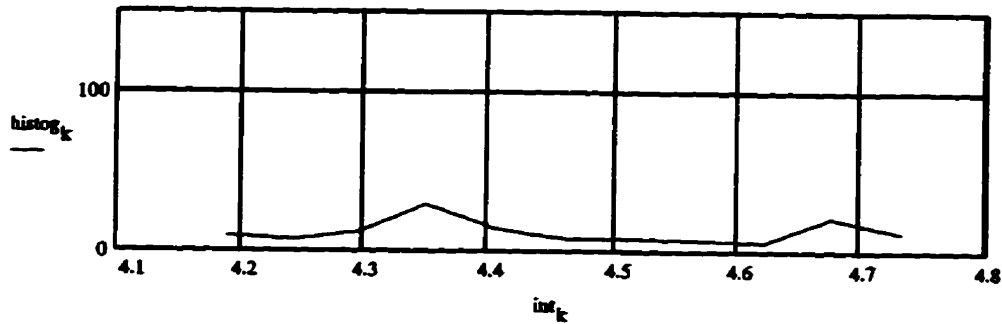
Inverting Velocity Field (Concrete Column): $\lambda = 0.2$

Definitions $n := 12$ $i := 1..n$ $j := 1..n$
 $ij := 1..n-n$ $nh := n$ $m := 1..nh$ $k := 1..nh - 1$

Input File $V := \text{READPRN}(vconc)$ $V_{\min} := \min(V)$ $V_{\max} := \max(V)$
 $V_{\min} \approx 4.189$ $V_{\max} \approx 4.84$ $\text{mean}(V) \approx 4.514$

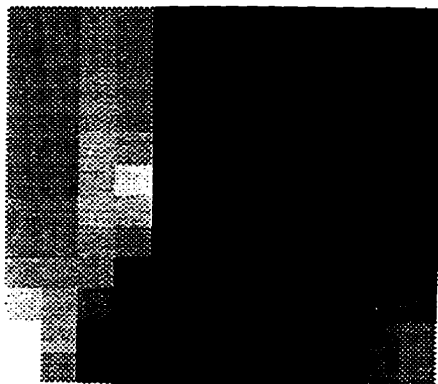
Histogram $\text{int}_m := V_{\min} + (m - 1) \cdot \frac{V_{\max} - V_{\min}}{nh}$ $\text{histog} := \text{hist}(\text{int}, V)$

Histogram of the inverted velocity field



2D Image $A_{i,j} := V_{(i-1) \cdot nh + j}$ $B_{(n-i)+1,j} := A_{i,j}$

Inverted velocity field



A



B

Enhancement

$$V_{ij} := \text{if}(V_{ij} < 4.2, 4.2, V_{ij})$$

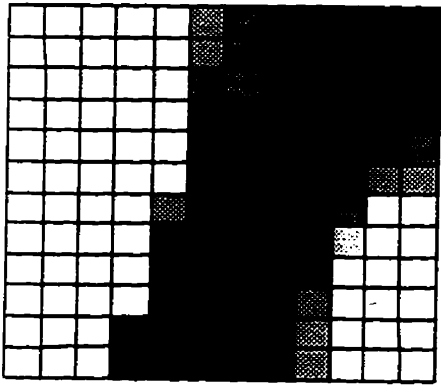
$$V_{ij} := \text{if}(V_{ij} > 4.5, 4.5, V_{ij})$$

2D Image

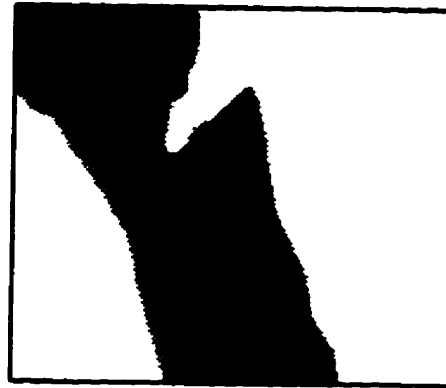
$$A_{i,j} := V_{(i-1) \cdot m + j}$$

$$B_{(n-i)+1,j} := A_{i,j}$$

Enhanced inverted velocity field



A



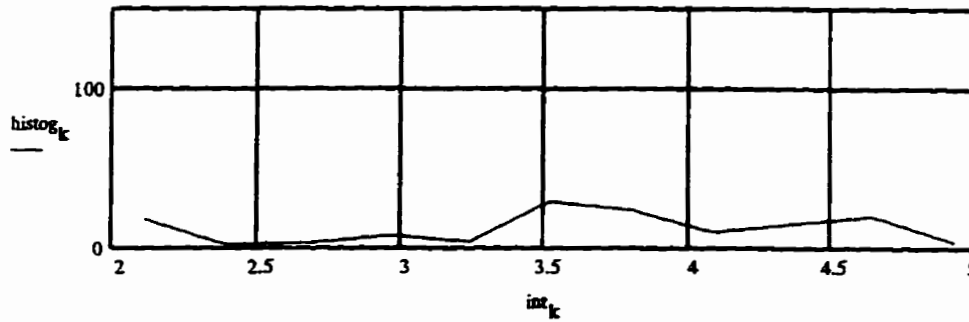
B

Inverting Velocity Field (Concrete Column): $\lambda = 0.2$

Ray Tracing (Second Iteration)

Definitions	$n := 12$	$i := 1..n$	$j := 1..n$
	$ij := 1..n \cdot n$	$nh := n$	$m := 1..nh$
			$k := 1..nh - 1$
Input File	$V := \text{READPRN}(v)$	$V_{\min} := \min(V)$	$V_{\max} := \max(V)$
	$V_{\min} = 2.119$	$V_{\max} = 5.486$	$\text{mean}(V) = 3.867$
Histogram	$\text{int}_m := V_{\min} + (m - 1) \frac{V_{\max} - V_{\min}}{nh}$		$\text{histog} := \text{hist}(\text{int}, V)$

Histogram of the inverted velocity field

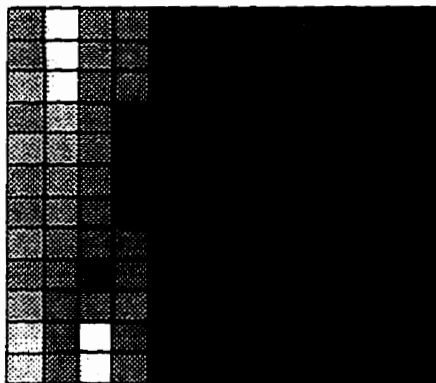


2D Image

$$A_{i,j} := V_{(i-1) \cdot nh + j}$$

$$B_{(n-i)+1,j} := A_{i,j}$$

Inverted velocity field



A



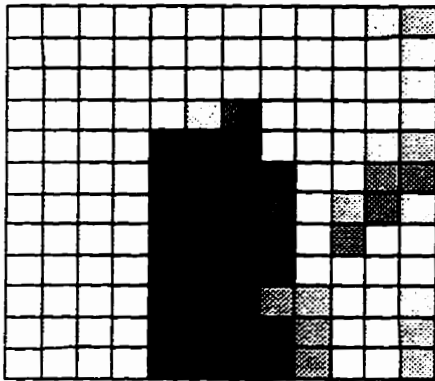
B

The chop-off threshold value is selected based on computed average velocity and assuming that the wave velocity in the confine concrete is more than 3.5 km/s.

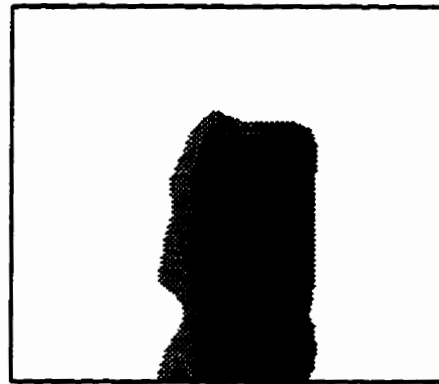
Enhancement $V_{ij} := \text{if}(V_{ij} < V_{\text{min}}, V_{\text{min}}, V_{ij})$ $V_{ij} := \text{if}(V_{ij} > 3.7, 3.7, V_{ij})$

2D Image $A_{i,j} := V_{(i-1) \cdot mh + j}$ $B_{(n-i)+1,j} := A_{i,j}$

Enhanced inverted velocity field



A

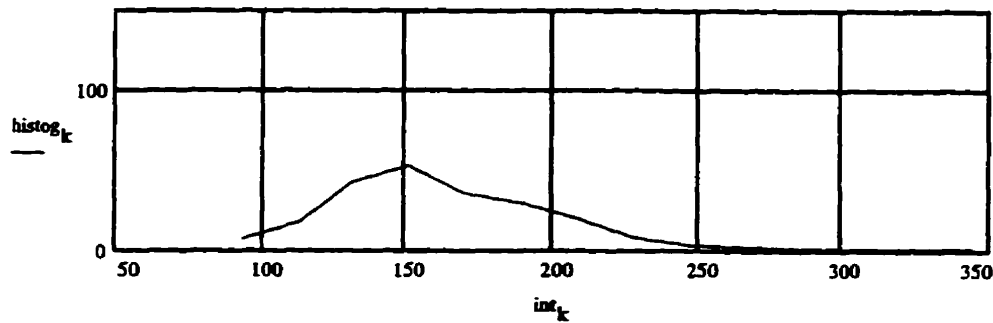


B

Inverting Velocity Field (Kosciuzko Bridge Pier) $\lambda = 1000$

Initial velocity = 400

Definitions	$n := 15$	$i := 1..n$	$j := 1..n$
	$ij := 1..n-n$	$nh := n$	$m := 1..nh$
			$k := 1..nh - 1$
Input File	$V := \text{READPRN}(vkos)$	$V_{\min} := \min(V)$	$V_{\max} := \max(V)$
	$V_{\min} = 93.13$	$V_{\max} = 383.08$	$\text{mean}(V) = 174.225$
Enhancement	$V_{ij} := \text{if}(V_{ij} < V_{\min}, V_{\min}, V_{ij})$		$V_{ij} := \text{if}(V_{ij} > V_{\max}, V_{\max}, V_{ij})$
Histogram	$\text{int}_m := V_{\min} + (m - 1) \cdot \frac{V_{\max} - V_{\min}}{nh}$		$\text{histog} := \text{hist}(\text{int}, V)$
2D Image	$A_{j,i} := V_{(i-1) \cdot nh + j}$		$B_{j,(n-i)+1} := A_{i,j}$

Histogram of the inverted velocity field**Inverted velocity field**

A



R

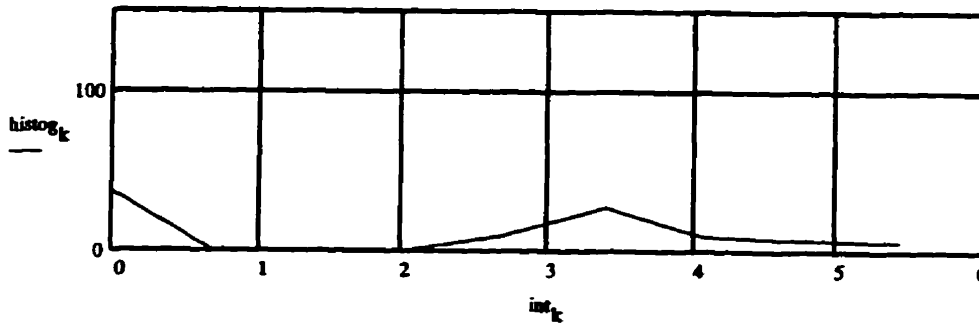
Inverting Velocity Field (Chute Hemming Dam)

$\lambda = 1000$

initial velocity=400

Definitions	$n := 10$	$i := 1..n$	$j := 1..n$
	$ij := 1..n-n$	$nh := n$	$m := 1..nh$
			$k := 1..nh - 1$
Input File	$V := \text{READPRN}(vhem)$	$Vmin := \min(V)$	$Vmax := \max(V)$
	$Vmin = 0$	$Vmax = 6.79$	$\text{mean}(V) = 2.705$
Enhancement	$V_{ij} := \text{if}(V_{ij} < Vmin, Vmin, V_{ij})$		$V_{ij} := \text{if}(V_{ij} > Vmax, Vmax, V_{ij})$
Histogram	$\text{int}_m := Vmin + (m - 1) \cdot \frac{Vmax - Vmin}{nh}$		$\text{histog} := \text{hist}(\text{int}, V)$
2D Image	$A_{i,j} := V_{(i-1) \cdot nh + j}$	$A_{i,j} := \text{if}[V_{(i-1) \cdot nh + j} \approx 0., 6.8, A_{i,j}]$	$B_{j, (n-i) + 1} := A_{i,j}$

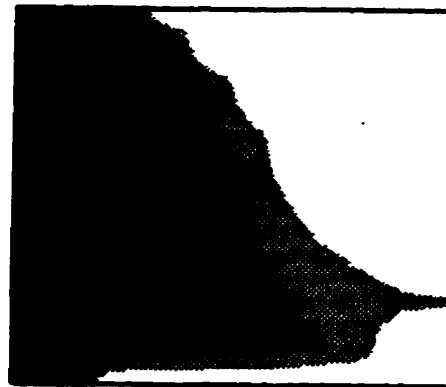
Histogram of the inverted velocity field



Inverted velocity field



A



B

Inverting Velocity Field (Korean DMZ)

$\lambda = 50000$

Initial velocity = 400

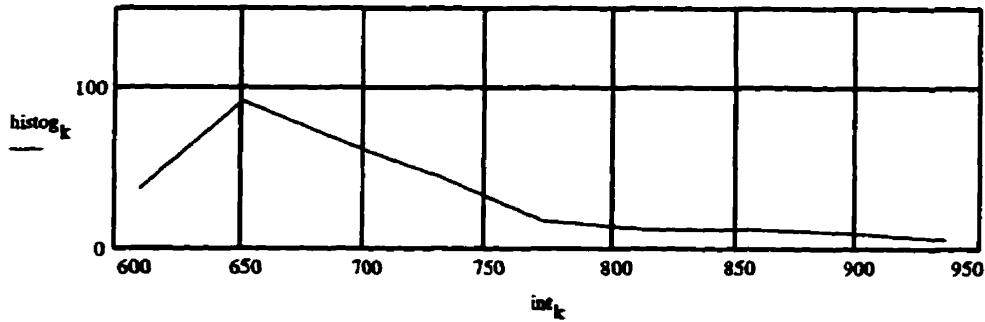
Same results for Straight and Ray tracing

Definitions $n := 10$ $i := 1..n + 20$ $j := 1..n$
 $ij := 1..n \cdot (n + 20)$ $nh := n$ $m := 1..nh$ $k := 1..nh - 1$

Input File $V := \text{READPRN}(vkor)$ $V_{\min} := \min(V)$ $V_{\max} := \max(V)$
 $V_{\min} = 609.749$ $V_{\max} = 1.018 \cdot 10^3$ $\text{mean}(V) = 726.737$

Histogram $\text{int}_m := V_{\min} + (m - 1) \cdot \frac{V_{\max} - V_{\min}}{nh}$ $\text{histog} := \text{hist}(\text{int}, V)$

Histogram of the inverted velocity field

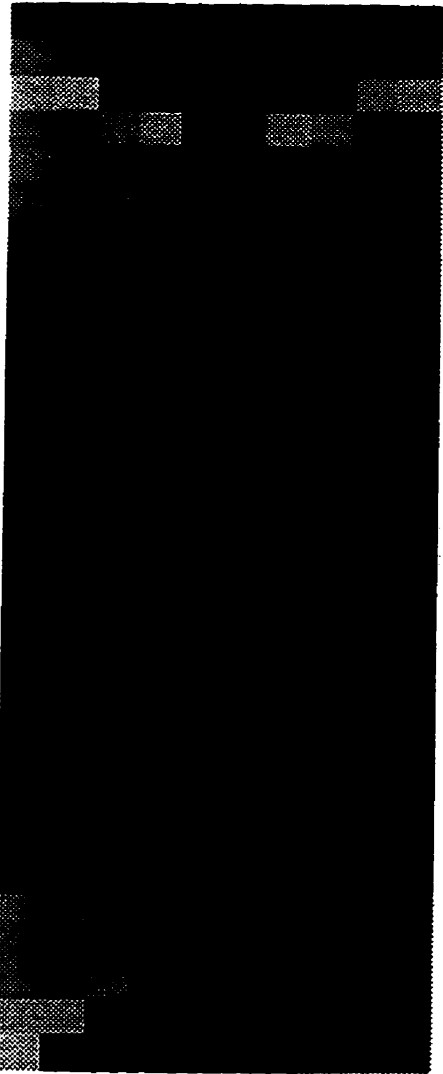


2D Image

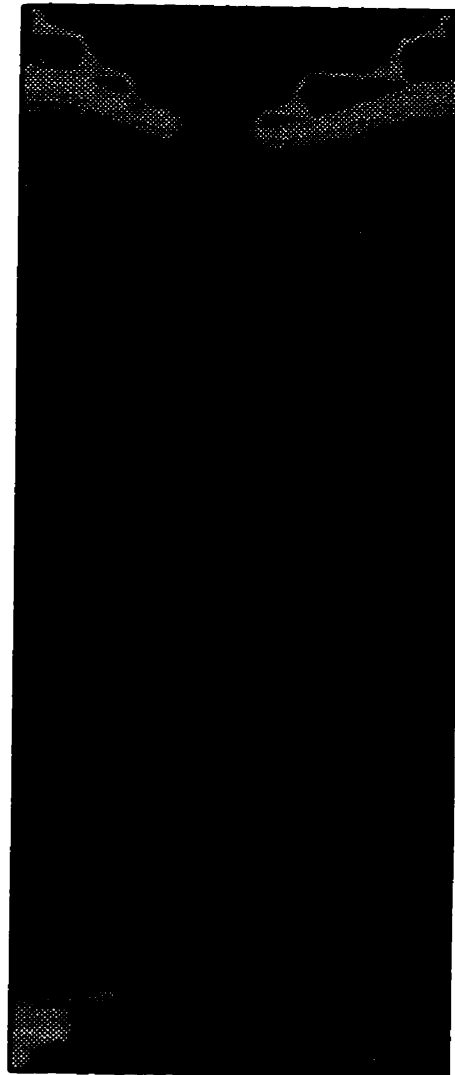
$$A_{i,j} := V_{(i-1) \cdot m + j}$$

$$B_{j, (n+20-i)+1} := A_{i,j}$$

Inverted velocity field



A



B

Enhancement

$$V_{ij} := \text{if}(V_{ij} < 600., 600., V_{ij})$$

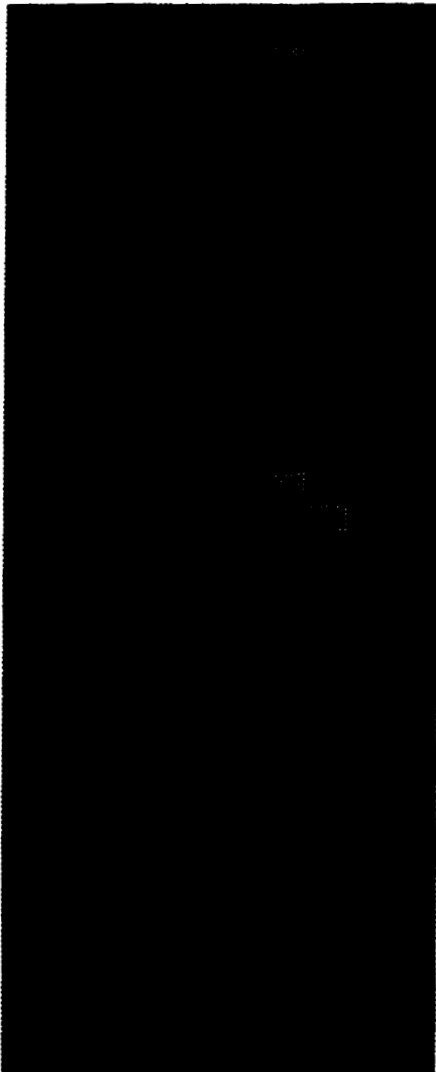
$$V_{ij} := \text{if}(V_{ij} > 650., 650., V_{ij})$$

2D Image

$$A_{i,j} := V_{(i-1) \cdot nb + j}$$

$$B_{j, (n+20-i)+1} := A_{i,j}$$

Enhanced inverted velocity field



A



B